

DISS. ETH NO. 17036

Calibration of a Terrestrial Laser Scanner for Engineering Geodesy

A dissertation submitted to

ETH ZURICH

for the degree of

Doctor of Sciences

presented by

THORSTEN SCHULZ

Dipl.-Ing., Technical University of Berlin

born 24.02.1977

citizen of Germany

accepted on the recommendation of

Prof. Dr. Hilmar Ingensand, examiner

Prof. Dr.-Ing. habil. Thomas Wunderlich, co-examiner

2007

Abstract

For several years now, terrestrial laser scanning has become an additional surveying technique in geodesy. Recent developments have improved several aspects of terrestrial laser scanners, e.g. the data acquisition rate, accuracy, and range. Since such instruments are relatively new and constructed by manufacturers who do not have advanced experience in surveying instruments, investigations are needed to assess the quality of the instrumental characteristics and the acquired data. In this way, manufacturers will understand the needs of geodesists and in turn enable geodesists to provide the necessary support in the development of improvements. This thesis has three objectives, the calibration and investigation of a terrestrial laser scanner, the post-processing of point clouds acquired by laser scanners, and applications of terrestrial laser scanning.

The first objective is a comprehensive calibration and investigation of a specific laser scanner, the Imager 5003 of Zoller+Fröhlich GmbH (Germany). The investigation and calibration procedures shall give a general impulse for all users of terrestrial laser scanning regarding instrumental and non-instrumental errors, the assessment of the quality of distance and angle measurements, and the influencing parameters. Laser scanners are a black box instrument that produces a huge number of 3D points in the form of a point cloud in a short time. However, it is the surveyor, who has to assess the reliability and quality of the resulting data. Therefore, the potential and the limitations of laser scanner systems must be identified. This is particularly important when a distance measurement is influenced by several parameters that can bias the data. Since laser scanning is an active surveying method, mostly independent of lighting conditions, distance measurements do not require prisms. Thus, surveying of almost every object is conceivable.

The second objective involves post-processing of the point clouds. Terrestrial laser scanning consists not only of data acquisition, but also processing of the acquired 3D data, which include an intensity value of the reflected laser beam. The point clouds define the objects and the data contains nearly all the information about the objects due to the high sampling interval of laser scanners. To produce the final result, data processing needs to be completed and this can be quite involving, e.g. registration, data filtering, noise reduction, triangulation, and modeling. The ratio between post-processing and data acquisition can be 10:1 or greater, which means ten (or more) days of post-processing follow one day of data acquisition. This aspect of post-processing applies for both static laser scanning and kinematic laser scanning. The only difference is that kinematic laser scanning requires a unique method of registration and geo-referencing.

The third objective examines the applications of terrestrial laser scanning. Laser scanning can be used in different fields of applications, e.g. industrial metrology, cultural heritage, reverse engineering, and engineering geodesy. Due to the increased requirements regarding accuracy engineering geodesy appears to be a challenging field. Therefore, three different applications are presented which verify the successful use of terrestrial laser scanning in engineering geodesy. The first application involves the field of urban water management. A road surface was scanned to derive catchment areas and water flow directions. The second application covers the field of engineering geology. A tunnel during and after excavation was scanned to characterize rock mass structures and to derive displacement maps of surfaces and object points. Since the first two applications are based on static laser scanning, which means the laser scanner did not change in position and orientation during scanning, the third application is a kinematic one, which means the laser scanner was in motion during scanning. Such kinematic applications are of great interest since the performance of laser scanning can be increased significantly. Tunnels and roads are especially appropriate for kinematic laser scanning. The potential of kinematic laser scanning is tested by moving the laser scanner along a track line. The quality is assessed by scanning reference points.

Zusammenfassung

Seit einigen Jahren hat sich das terrestrische Laserscanning als eine zusätzliche Datenerfassungstechnik in der Geodäsie behaupten können. Die Entwicklungen in der nahen Vergangenheit haben terrestrische Laserscanner in vielerlei Hinsicht verbessern können, z.B. bezüglich der Aufnahmegeschwindigkeit, der Genauigkeit und der Reichweite. Da solche Instrumente jedoch einerseits relativ neu sind und andererseits von Herstellern produziert werden, die keine langjährige Erfahrung bezüglich geodätischer Instrumente aufweisen, ist es erforderlich, die Qualität sowohl seitens der Konstruktion der Laserscanner als auch von den erfaßten Daten zu beurteilen. Das Ziel ist es, den Herstellern die Wünsche und Bedürfnisse der Geodäten zu vermitteln und sie mit Ideen für Verbesserungen und Entwicklungen zu unterstützen. Die vorliegende Arbeit hat drei Zielsetzungen, die Kalibrierung und Untersuchung eines Laserscanners, die Datenbearbeitung und Datenauswertung von Punktwolken sowie Anwendungsmöglichkeiten von terrestrischem Laserscanning.

Die erste Zielsetzung umfaßt eine eingehende Kalibrierung und Untersuchung eines bestimmten Laserscanners, des Imager 5003 von Zoller+Fröhlich GmbH (Deutschland). Die vorgestellten Untersuchungen und Kalibrierungen sollen einen Denkanstoß für all diejenigen geben, die sich mit terrestrischem Laserscanning beschäftigen. Diese umfassen instrumentelle Fehler wie nicht-instrumentelle Fehler als auch die Beurteilung der Qualität der Distanz- und Winkelmessungen sowie anderer Einflussfaktoren. Der Laserscanner repräsentiert eine Black-Box, die in kurzer Zeit eine grosse Anzahl von 3D Daten erfaßt, die Punktwolken genannt werden. Der Geodät sollte jedoch in der Lage sein, diese erfaßten Daten zu beurteilen bezüglich Zuverlässigkeit und Qualität. Dazu muss er die Stärken und Schwächen eines Laserscanner-Systems identifizieren. Besonders die Distanzmessung ist von mehreren Parametern beeinflusst, die verrauschte Daten erzeugen. Da es sich beim Laserscanning um eine aktive Datenerfassung handelt, ist es nahezu unabhängig von der Umgebungsbeleuchtung und basiert auf reflektorloser Distanzmessung. Damit ist es möglich, nahezu jedes Objekt zu erfassen.

Die zweite Zielsetzung beschäftigt sich mit den Aspekten der Datenbearbeitung und Datenauswertung, denn terrestrisches Laserscanning bedeutet nicht nur Datenaufnahme. Die erfaßten 3D Daten inklusive einem Intensitätswert des reflektierten Laserstrahls müssen aufbereitet werden. Zwar definieren die Punktwolken das Objekt und jede Information kann aus der Punktwolke entnommen werden aufgrund der hohen Abtastrate des Laserscanners. Aber es gibt darüber hinaus jede Menge Arbeit, um die Daten zu prozessieren und das Endprodukt abzuleiten, z.B. die Registrierung, die Datenfilterung, die Reduzierung des Messrauschens, die Dreiecksvermaschung, die Modellierung. Das Verhältnis zwischen Datenaufbereitung und Datenauswertung einerseits und der Datenaufnahme andererseits kann bis zu einem Verhältnis von 10:1 ansteigen; dies bedeutet, daß zehn Tage mit Datenaufbereitung und Datenauswertung von einem Tag Datenerfassung anfallen. Der Aspekt der Datenaufbereitung gilt dabei sowohl für statische Laserscanning-Aufnahmen als auch kinematische Laserscanning-Aufnahmen. Der einzige Unterschied liegt in der speziellen Art der Registrierung und Georeferenzierung bei kinematisch erfaßten Laserscanning-Daten.

Die dritte Zielsetzung umfaßt die Anwendungsmöglichkeiten des terrestrischen Laserscannings. Laserscanning wird für verschiedenste Bereiche genutzt, z.B. industrielle Meßtechnik, Denkmalschutz und Kulturgüter, Flächenrückführung und Nachbau und Ingenieurvermessung. Aufgrund der hohen Genauigkeitsforderungen stellt die Ingenieurvermessung eine interessante Herausforderung dar. Daher werden drei verschiedene Beispiele aus dem Bereich der Ingenieurvermessung vorgestellt, in denen terrestrisches Laserscanning erfolgreich angewendet wurde. Das erste Beispiel kommt aus dem Bereich der Siedlungswasserwirtschaft. Die Oberfläche einer Straße wurde gescannt und anschließend wurden Einzugsbereiche und Fließrichtungen der Abflußströme vom Regenwasser abgeleitet. Das zweite Beispiel kommt aus dem Bereich der Ingenieurgeologie. Ein Tunnel wurde während und nach dem Ausbruch mittels terrestrischem La-

serscanning aufgenommen. Basierend auf diesen Daten wurden Strukturen verschiedener Gesteinsschichten sowie Deformationen des Tunnels flächenhaft und in diskreten Punkten abgeleitet. Während die ersten beiden Beispiele statische Applikationen darstellen, d.h. der Laserscanner wurde während der Datenerfassung nicht bewegt, stellt das dritte Beispiel eine kinematische Anwendung dar, d.h. der Laserscanner wurde während der Datenerfassung bewegt. Solche kinematischen Anwendungen sind von großem Interesse, da die Arbeitsleistung beträchtlich gesteigert werden kann. Speziell für Tunnels und Straßen ist kinematisches Laserscanning geeignet. Das Potential für kinematische Anwendungen wurde getestet, indem der Laserscanner auf einer Messbahn entlang bewegt wurde. Die Qualität wurde mittels Referenzpunkten beurteilt.

Contents

Abstract	iii
Zusammenfassung	v
1 Introduction	1
1.1 Terrestrial Laser Scanning	1
1.2 Motivation	3
1.3 Outline	4
2 Components of Terrestrial Laser Scanner	7
2.1 Distance and Reflectance Measurement System	7
2.1.1 Electromagnetic Waves	8
2.1.2 Laser	9
2.1.3 Direct Time-of-Flight	13
2.1.4 Amplitude-Modulated Continuous Wave (AMCW)	13
2.1.5 Frequency-Modulated Continuous Wave (FMCW)	15
2.1.6 Overview of Distance Measurement Techniques in Terrestrial Laser Scanners	16
2.1.7 Avalanche Photo Diode (APD)	16
2.1.8 Reflection Principles	17
2.1.9 Reflectance Models	17
2.2 Angle Measurement System	18
2.2.1 Incremental Encoding	19
2.2.2 Binary Encoding	20
2.3 Deflection System	20
2.3.1 Oscillating Mirror	21
2.3.2 Rotating Mirror	22
2.3.3 Overview of Deflection Techniques in Terrestrial Laser Scanners	22
3 Calibration of Terrestrial Laser Scanner	23
3.1 Laboratories and Tools for Calibration	26
3.1.1 Calibration Track Line	26
3.1.2 Test Field of Control Points	27
3.1.3 Test Field of Observation Pillars	28
3.1.4 Electronic Unit for Frequency Measurement	28
3.1.5 Calibration of Spheres	29
3.2 Distance Measurement System	31
3.2.1 Static Mode	32
3.2.2 Scanning Mode	35
3.2.3 Long-Term Stability	39
3.2.4 Frequency Stability	40
3.3 Angle Measurement System	42
3.3.1 Horizontal Encoder	44
3.3.2 Vertical Encoder	45

3.3.3	Angular Resolution	46
3.4	Instrumental Errors	48
3.4.1	Eccentricity of Scan Center	49
3.4.2	Wobble of Vertical axis	52
3.4.3	Error of Collimation Axis	58
3.4.4	Error of Horizontal Axis	63
3.5	Non-Instrumental Errors	64
3.5.1	Intensity of Laser Beam	64
3.5.2	Angle of Incidence	65
3.5.3	Surface Properties of Materials	67
3.6	Precision and Accuracy of Terrestrial Laser Scanner Data	69
3.6.1	Single Point Precision	70
3.6.2	Accuracy of Modeled Objects (Spheres)	70
4	Static Laser Scanning	73
4.1	Data Processing	73
4.1.1	Blunder Detection	73
4.1.2	Mixed Pixel	74
4.1.3	Range/Intensity Crosstalk	75
4.1.4	Multipath	76
4.1.5	Noise Reduction	77
4.2	Registration	78
4.2.1	Target-Based Registration	80
4.2.2	Point Cloud Registration	81
4.3	Modeling and Visualization	82
4.3.1	Geometrical Primitives	83
4.3.2	Triangulation	83
4.3.3	NURBS	84
4.3.4	CAD	85
4.3.5	Rendering and Texture Mapping	85
5	Kinematic Laser Scanning	87
5.1	Test Trolley on Calibration Track Line	88
5.1.1	Relative Position and Orientation	89
5.1.2	Absolute Position and Orientation	90
5.2	Rotation Time of Rotating Mirror of Laser Scanner	92
5.2.1	Direct Method	93
5.2.2	Indirect Method	99
5.2.3	Discussion and Comparison	101
5.3	Position-Fixing Using Total Station	102
5.3.1	Blunder Detection and Smoothing	102
5.3.2	Polynomial Interpolation	103
5.3.3	Regression Line	104
5.3.4	Kalman Filtering	105
5.4	Synchronisation	108
6	Applications of Terrestrial Laser Scanning	109
6.1	Static Application: Road Surface Analysis	109
6.1.1	Introduction	109
6.1.2	Method	110

6.1.3	Results	111
6.2	Static Application: Rock Engineering Applications	114
6.2.1	Introduction	114
6.2.2	Method	115
6.2.3	Results	118
6.3	Kinematic Application: Test Tunnel	121
6.3.1	Introduction	121
6.3.2	Kinematic Model: Regression Line	122
6.3.3	Kinematic Model: Kalman Filter	123
6.3.4	Results	126
7	Summary	131
7.1	Conclusions	131
7.2	Outlook	132
A	Imaging System of Imager 5003 of Zoller+Fröhlich	135
B	Technical Data of Imager 5003 of Zoller+Fröhlich	137
C	Adjustment of Sphere	139
D	Electronic Circuit for Determining Rotation Time	143
	Bibliography	145
	List of Figures	153
	List of Tables	157
	Acknowledgement	159
	Curriculum Vitae	161

Introduction

1.1 Terrestrial Laser Scanning

For several years now, terrestrial laser scanning (TLS) has become an additional data acquisition technique in geodesy. The development of laser scanners is in its infancy. Therefore, the scanners do not have the same properties, e.g. accuracy, precision, reproducibility, repeatability, and reliability, as traditional geodetic instruments, e.g. automated total station and global positioning systems (GPS). However, further technological developments will lead to advanced instruments in the near future. The interests of geodesists regarding centering, levelling, real time processing of data (and not only in-situ controlling of acquired data), etc. require close cooperation with manufacturers. Nowadays, the second to third generation of such instruments is available on the market. Geodesists are not the only ones interested in laser scanning. The use of terrestrial laser scanners is widespread in production lines, plants, cultural heritage, industrial metrology etc. The application area is growing nearly everyday. In geology, crime scene investigation and engineering geodesy, terrestrial laser scanning is relatively new.

Terrestrial laser scanning technology has been strongly influenced by the development of LiDAR, an acronym for light detecting and ranging, which started in the 1970's. LiDAR has been successfully used for more than 30 years in airborne and remote sensing applications. The delay in adopting LiDAR in terrestrial instruments involves providing for short ranges, i.e. less than one kilometer, and increased accuracy, i.e. less than one decimeter. These have been made possible by technological developments since the 1990's, such as:

- improvements in microchip laser technology
- manufacturing of optical elements
- development of micro-electro-mechanical systems
- improvements in computer technology
- data processing algorithms

Consequently, the performance of data capturing, the accuracy in range measurement, the reliability of acquired data etc. have increased and the instrumental design, i.e. weight and dimensions, the costs etc. have decreased.

A LiDAR unit consists roughly of an emitter, a receiver and a detector system. The carrier is a laser, which contains the modulated information required for detecting the travel time from emitter to objects and back. Lasers differ in power and wavelength, with power limited to a maximum value for eye safety. The method for solving the range is based on continuous waveforms or direct time-of-flight. Scattered light is received at fixed time intervals. For detecting the laser beam, highly sensitive diodes have to be implemented. The

diodes are either PIN diodes or avalanche photo diodes (APD). Each LiDAR system deflects the laser beam to objects. Therefore, a deflection unit is required, which is able to align the laser beam towards the desired direction. It is distinguished between rotating mirrors and oscillating mirrors. Depending on the deflection principle, the field of view is defined. Due to this deflection of the laser beam, laser scanning provides nearly continuous scanning of the environment instead of discrete surveying. The objects are described by an arbitrary point cloud, which means a laser scanner cannot survey specific points, e.g. edges or corners.

A LiDAR has the ability to acquire more than the 3D coordinates of the environment. Due to the detection of the reflected laser beam by a diode, the amplitude or intensity of the laser beam contains additional information and can be used as a fourth dimension. Thus, a LiDAR system acquires not only 3D coordinates but also an intensity value. Even though the intensity is dependent on several aspects, e.g. the range to the object, surface properties of the object, and the angle of incidence, defined by the angle between incident laser beam and surface normal, the information is helpful in interpretations and classifications of laser scanning data. Thus, the acquired point clouds of LiDAR systems can be interpreted as range images, as intensity images, or as 3D data.

Some terrestrial laser scanners are shown in Figure 1.1. Most of the manufacturers have a range of products that include several types of laser scanners. Terrestrial laser scanners are a surveying instrument that is neither an automated total station nor a digital camera. Development of surveying instruments have envisioned an 'all-in-one' instrument that includes the functionality of automated total station, digital camera, GPS, and level. Nowadays, the fusion between automated total station and GPS is not wishful thinking, it is reality. Since photogrammetry and laser scanning have complementary characteristics, e.g. high detailed intensity information and high detailed geometry information, a fusion is not only conceivable but also required [Przybilla, 2005]. Most of the laser scanners can be equipped with a digital camera.



Figure 1.1: Overview of terrestrial laser scanners.

The operating range and the precision of LiDAR systems depend on the distance measurement technique. Figure 1.2 shows the typical distance technologies, cf. Section 2.1, and their range-precision-dependency. Triangulation is used for close ranges, the frequency-modulated continuous wave method (FMCW) is categorized between close ranges and medium ranges, the amplitude-modulated continuous wave method (AMCW) operates in medium ranges and the direct time-of-flight method (TOF) is for medium ranges up to long ranges. Precision decreases as the range increases. Some typical applications are also given and categorized with respect to the range in Figure 1.2.

Terrestrial laser scanning is a promising technique and has the potential to be accepted as additional surveying technology. Recent developments regarding performance, range and accuracy have opened up new application areas for laser scanning. This is especially the case in the field of engineering geodesy. Since the first laser scanners showed several drawbacks and were not appropriate for geodesists, the next generations of terrestrial laser scanners have also taken into account the needs of geodesists, e.g. feasibility for levelling, centering, and orienting. The data acquisition is also an integral part of terrestrial laser scanning.

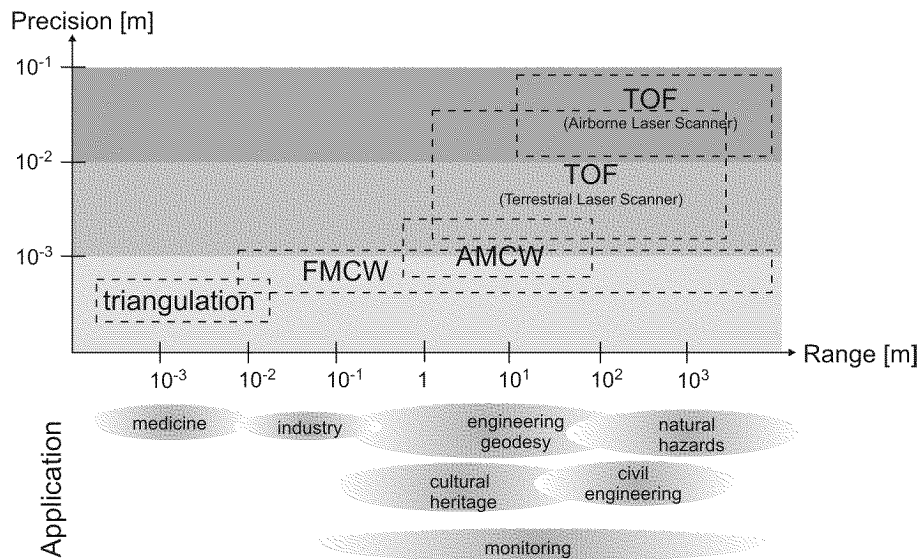


Figure 1.2: Distance measurement technologies used in LiDAR systems, their operating range and their precision. Some typical applications are given with respect to the range.

The acquired points have to be processed by using software packages. Although, this post-processing can be time-consuming, it is an important part. Thus, terrestrial laser scanning is defined as the combination of hardware, i.e. the laser scanner, and software.

1.2 Motivation

Each surveying instrument has to be investigated and calibrated regarding instrumental errors and non-instrumental errors. Furthermore, the precision and the accuracy of the single measurement components, i.e. the distance and the angles, should be known. In traditional surveying instruments, e.g. total station, GPS receiver, level, these components are well-known. Thus, for several decades, this knowledge has led to the proper design of the traditional instruments. At the conception of GPS, the acceptance of the technique as well as the instrument were reserved. Nowadays, GPS is well-accepted and state-of-the-art.

Terrestrial laser scanning can be viewed in a similar way. The technology is relatively new, but the laser scanner is on its way to becoming integrated in the geodesists' world. The performance is impressive regarding the data acquisition rate and the accuracy is in the range of centimeters or less. The premises have been laid for the use and acceptance of terrestrial laser scanning, also in the field of engineering geodesy. The first generation of terrestrial laser scanners were developed several years ago by companies, who did not understand the needs of geodesists, but recent developments have ignited the interests of geodesists in these instruments. Laser scanners have now come into the focal point of geodesy and have a high potential for complementing the geodesists' instruments. The investigation and calibration from the point of geodesists have started. Within the last few years, studies have been initiated by independent institutions for a better understanding of the performance, the potentials and the limitations of terrestrial laser scanners.

One important aspect is to make laser scanners comparable with each other. Due to the different principles regarding deflection of the laser beam, distance measurement technology, working range, and data acquisition rate, it is nearly impossible to make comparisons. The question is not which laser scanner is the best but which laser scanner is the best-suited for a specific application. Also, the experimental setup for testing a laser scanner has to be chosen according to the characteristics of the laser scanner.

[Böhler et al., 2003] developed a test procedure to assess the quality of measurements obtained by different laser scanners, e.g. noise and systematic offsets in range measurements. Based on the results, the laser scanners can be compared. This performance evaluation is both an important and essential aspect in understanding the limitations and characteristics of the scanners. As performance evaluation does not analyze systematic and methodological errors in detail, investigations and calibrations are required. In photogrammetry, camera calibration is applied by estimating several influencing parameters, e.g. camera constant deviation, lens distortion. Considering laser scanners, the calibration procedure can be carried out by a system calibration (self-calibration) or a calibration of components, cf. Chapter 3.

[Rietdorf et al., 2004] introduced a system calibration by using a test field of planes for estimating a set of parameters, e.g. additive constant for range measurements, vertical index error, horizontal collimation error. The planes guarantee both a laser scanner system and software independence. The significance of the parameters are identified by standard hypothesis testing. The high redundancy rate illustrates the reliability. One drawback can be defined by the limited test field dimensions of only several meters. Similar calibration procedures were done by [Reshetyuk, 2006b] and [Lichti et al., 2005a]. They established indoor calibration rooms using different types of targets (planar coded black and white targets, retro-reflective targets). [Reshetyuk, 2006b] could specify range drifts, angular accuracy and angular precision for three different laser scanners (Callidus 1.1, Leica HDS 2500 and Leica HDS 3000). [Lichti et al., 2005a] used the FARO 880 (former IQSun 880) laser scanner. They identified several range-dependent parameters, i.e. additive constant, amplitude of sinusoidal error, collimation axis error, trunnion axis error, vertical index error, and found time-dependent behaviour in most of these parameters. [Kersten et al., 2005] established a system calibration using a 3D indoor test field with both planar targets and spherical targets. They evaluated a significant difference between the two types of targets regarding nominal distances and measured distances.

Since laser scanners are based on prismless distance measurements, the influence of different materials and colours on the acquired data becomes an important aspect. The materials can cause systematic effects as well as increasing noise in the data. It was found that not only the materials have to be considered but also the combination of the laser scanner, i.e. wavelength of the laser light, and the materials. Results of different laser scanner systems and different materials and colours can be found in various contributions, e.g. [Reshetyuk, 2006a], [Kersten et al., 2005] and [Böhler et al., 2003].

This thesis has two main aspects. The first involves verifying knowledge and performance of the single components of terrestrial laser scanners. Therefore, the experimental setups have to be designed such that the single components are separable, e.g. the distance measurement system has to be uncoupled from the angle measurement system. The second involves testing terrestrial laser scanners in different applications to examine the potential and the limitation of these instruments in the branch of engineering geodesy.

1.3 Outline

The thesis is organized according to the following chapters:

- Chapter 2: Components of Terrestrial Laser Scanner
This chapter examines the main components of a terrestrial laser scanner in acquiring 3D point clouds. In detail, the distance and reflectance measurement system and the angle measurement system are discussed. Since a laser scanner acquires information about the environment, the orientation of the laser beam has to be changed. Thus, a deflection system is required.
- Chapter 3: Calibration of Terrestrial Laser Scanner
This chapter forms the main chapter of the thesis. It involves a comprehensive calibration and investigation of several parameters, which have to be taken into account for precise measurements. Terres-

terrestrial laser scanners are up to now not well-known and are manufactured by companies, who do not have advanced knowledge of surveying instruments. Several important aspects are discussed in detail and should give new findings for terrestrial laser scanners. The chapter begins with an overview of the laboratories and tools for the calibration of laser scanners. Subsequently, the investigation of the distance and angle measurement system, the influence of instrumental and non-instrumental errors and finally, the accuracy of laser scanner data are discussed.

- Chapter 4: Static Laser Scanning

This chapter examines the processing of laser scanning point clouds. Laser scanning consists of two parts data acquisition and post-processing of point clouds. The main aspects of processing point clouds are presented. The chapter also covers the topics of data processing, registration as well as modeling and visualization.

- Chapter 5: Kinematic Laser Scanning

This chapter outlines some of the requirements for kinematic applications. The laser scanner is mounted on a test trolley, which is moved along a test tunnel. The laser scanner is operated in the so-called profiler mode and the rotation time was used for an internal time stamp of the laser scanner data. The absolute position of the moving trolley is surveyed by a total station. The specialties of data processing of kinematic applications are presented for laser scanner data and total station data, respectively.

- Chapter 6: Applications of Terrestrial Laser Scanning

This chapter introduces three different applications of terrestrial laser scanning which involve the field of engineering geodesy. Two static applications are presented, one deals with the analysis of road surfaces, and the other deals with applications for rock engineering. The third example examines the suitability of terrestrial laser scanning for kinematic applications, as performed in a test tunnel.

- Chapter 7: Conclusions and Outlook

This chapter summarizes the findings of the thesis and gives an outlook to future work and developments.

Components of Terrestrial Laser Scanner

A terrestrial laser scanner defines an instrument for generating 3D coordinates. The core components for describing each acquired point by three coordinates and an intensity value as a fourth dimension are the distance and reflectance measurement system and the angle measurement system. In the following, these components are briefly discussed with respect to understanding laser scanners. Since the laser scanners are operating within a field of view, the laser beam has to be deflected in two directions, horizontally and vertically, respectively. Thus, the deflection system is the second important component of a laser scanner.

2.1 Distance and Reflectance Measurement System

The core component of a terrestrial laser scanner is the distance measurement system. The distance measurement system defines not only the depth resolution, i.e. the range, but depending on the technique used, additional properties can also be defined:

- the range
- the precision of distance measurements
- the performance of repeated distance measurements

Optical distance measurement methods used in terrestrial laser scanners can be technically divided into three categories [Bosch and Lescure, 1995]: interferometry, time-of-flight methods and triangulation, cf. Figure 2.1. Since interferometry and triangulation are not widely used in terrestrial laser scanners¹ and are more related to remote sensing and close-range applications, the focus is on the time-of-flight methods.

The time-of-flight methods are based on measuring the time it takes for a pulse or pattern of energy emitted by the laser scanner to travel and strike a surface and to return. The range s to be measured can be identified by [Rüeger, 1996]

$$s = c \cdot \frac{\Delta t}{2} \quad (2.1)$$

where c is the speed of light and Δt the round-trip time of the laser energy. The speed of light is a natural constant and well-defined for a vacuum². If the travel time is also known, the range can be calculated. The determination of the time can be achieved either by a direct time measurement, e.g. direct time-of-flight, or by an indirect time measurement, e.g. amplitude-modulated continuous wave, frequency-modulated

¹Close-range scanners based on triangulation are also terrestrial laser scanners, but due to the limited working range of up to only a few meters, here they are not categorized in the same group of terrestrial laser scanners.

²Due to atmospheric conditions and turbulence, the speed of light varies and thus, is not a constant. However, the variations can be estimated by mathematical models.

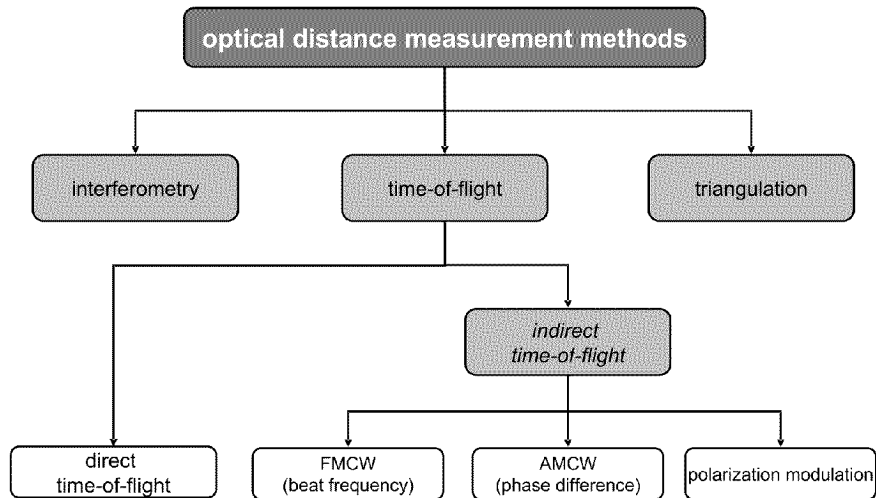


Figure 2.1: Optical distance measurement methods in terrestrial laser scanners.

continuous wave, polarisation modulation. The direct time-of-flight method and the amplitude-modulated continuous wave method are widely-used in terrestrial laser scanners, whereas the frequency-modulated continuous wave method and the polarisation modulation method are rarely used in terrestrial laser scanners.

The intensity of the reflected laser beam defines a fourth dimension, in addition to the 3D coordinates. The reflected laser beam is detected by a photodiode, i.e. PIN diode or avalanche photo diode (APD), and the amplitude of the detected signal corresponds directly to the intensity of the received laser beam. The intensity of the laser beam is dependent on several parameters, such as the range, the angle of incidence and the surface properties, e.g. colour, roughness. Unfortunately, the physical significance of this information is often not exactly defined by the manufacturers [Lichti et al., 2002a]. Therefore, the intensity can relate to either the amplitude or the energy of the received signal. For avoiding noise caused by ambient light, additional filters are used, e.g. IR Filter.

Since laser scanning is an active and prismless method for surveying the environment, it is necessary to comment on some aspects of the reflection principles. Often, the results of laser scanning are 3D-models, which have to be illuminated within the software packages. Thus, the section is completed by utilizing some methods for modeling the reflectance. This is especially the case in computer graphics, where several models are used for shading the digital models to achieve a realistic appearance with respect to illumination. The term reflectance is defined as the ratio of the amount of electromagnetic radiation, usually light, reflected from a surface to the amount originally striking the surface.

2.1.1 Electromagnetic Waves

Electromagnetic radiation contains a broad spectrum from cosmic radiation with very short wavelengths ($\lambda < 10^{-14}\text{m}$) up to radio waves ($\lambda > 10^6\text{m}$). Electromagnetic waves are used as carrier waves for transmitting signals, which show varying forms, e.g. impulses, patterns. The specific wavelength that is used depends on the layer of the atmosphere, e.g. troposphere, ionosphere, and on the range to be measured. Delays during the transmission of the electromagnetic wave between emitter and receiver caused by different conditions of the atmosphere have to be taken into account. Variations in temperature, air pressure, humidity, and other parameters influence the speed of light and the propagation of the electromagnetic wave. Thus, the speed of light is not a constant and has to be corrected by applying atmospheric conditions.

For geodetic applications, the most widely-used electromagnetic waves are the electro-optical waves. Electro-optical radiation ($0.4\mu\text{m} < \lambda < 1.3\mu\text{m}$) represents only a small bandwidth of the whole electromagnetic spectrum. They are appropriate for surveying due to their advantageous properties in the atmospheric layer close to the earth surface. These waves offer the best compromise in minimizing the absorption in the atmosphere and maximizing both the possibility of bundling and transmission [Hinderling, 2004].

Exemplarily, the transmission of the atmosphere for electromagnetic waves with wavelengths from $0.4\mu\text{m}$ up to $1.6\mu\text{m}$ is shown in Figure 2.2. Transmission is based on the mathematical low resolution transmission model (LOWTRAN). Further information of LOWTRAN can be found in [Richter, 1985]. The maximum transmission is reached by wavelengths of more than $1.5\mu\text{m}$. The shorter the wavelength, the less the transmission. Furthermore, there are some wavelengths with significantly lower transmissions. Based on such models, the best possible wavelengths for the range and the atmospheric layer in question can be found.

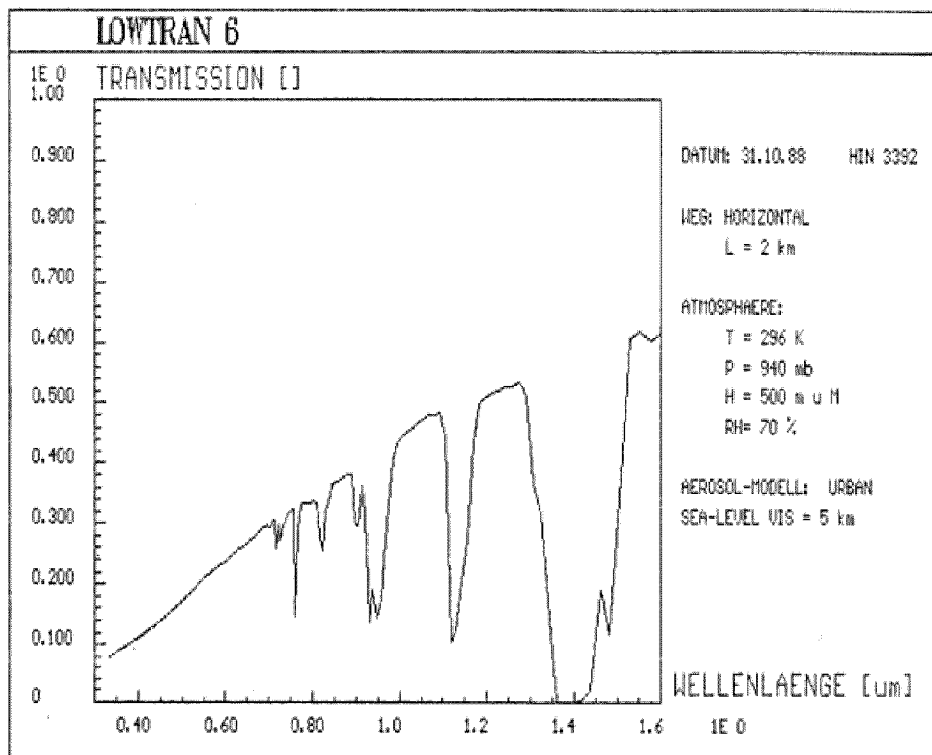


Figure 2.2: Transmission of electromagnetic waves based on LOWTRAN 6.

2.1.2 Laser

Signals for determining distances, e.g. impulses, frequencies, are modulated on electromagnetic waves. A laser³ emits a specific type of electromagnetic radiation. The emission of a laser is very intense monochromatic radiation that travels as a very narrow beam with high energy. Considering the electromagnetic spectrum, lasers fit in the optical region that extends from the infra-red through the visible to the ultraviolet regions. The principle of lasers can be found in various literature, e.g. [Gerthsen and Vogel, 1993], [Henderson, 1997], [Kneubühl, 1982] and [Young, 1984]. Concerning terrestrial laser scanners, the wavelengths vary from 500 nm (green) to 800 nm (near infra-red). For example, the laser diode of a continuous wave laser is shown in Figure 2.3. The chip is based on semiconductor materials.

³Laser is an acronym for light amplification by stimulated emission of radiation

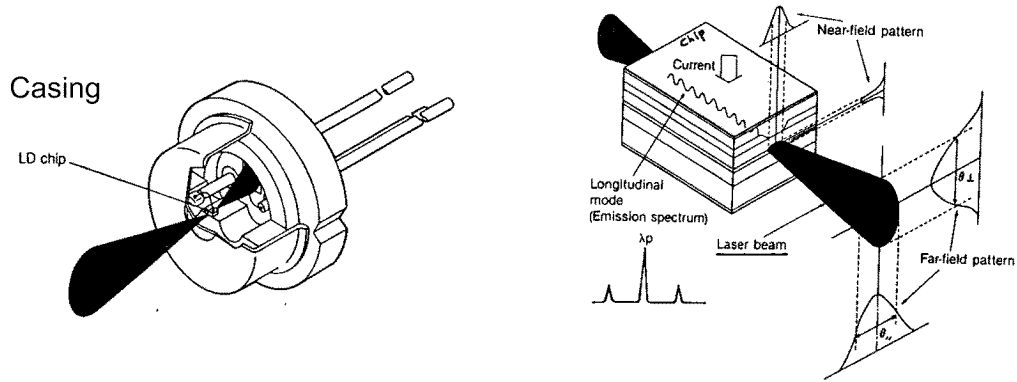


Figure 2.3: Casing (left) and structure (right) of a laser diode, adapted from [Hinderling, 2004].

Laser Beam Propagation

The propagation of optical and infrared waves can be described by various models. These models use basic geometries, such as [Andrews and Phillips, 1998] and [Meschede, 2004]:

- Plane wave: An unbounded wave with constant amplitude and constant phase. A plane wave model is defined as a model in which the phase fronts form parallel planes. This model is used to describe the properties of starlight and other exo-atmospheric sources at a ground-based receiver.
- Spherical wave: An unbounded wave associated with a point source. The spherical wave model is characterized by concentric spheres forming the phase fronts. This model is sometimes used for a small-aperture source within or near turbulent mediums.
- Gaussian-beam wave: A wave of finite extent with focusing capabilities. This model is used in most beam wave analysis.

The medium of propagation is in most cases the turbulent atmosphere, which changes the conditions permanently. These fluctuations of the atmosphere, which have an influence on the refraction index along the propagation path of the laser beam, cause a variety of deleterious effects in the wave, e.g. disruption of the coherence, broadening of the beam, redistribution of the beam energy [Andrews and Phillips, 1998].

Considering diffraction, a natural wave phenomenon of all light waves, the propagation of the laser beam is disturbed in many ways. The beam diameter is changed and thus, the amount of energy within any spot size inside the beam diameter deteriorates. The amount of beam spreading varies depending on the wavelength, the shape of the phase front, and the size of the emitting aperture [Andrews and Phillips, 1998]. An estimation on the amount of beam spreading at large distances from the beam waist is given by the beam divergence angle Θ_B , cf. Figure 2.4. Therefore, the minimum value for the spot size is assumed to be at the beam waist. Beyond the beam waist, the beam diverges according to [Weichel, 1990]:

$$w_z = w_0 \sqrt{1 + \left(\frac{\lambda \cdot z}{\pi \cdot w_0^2} \right)^2} \quad (2.2)$$

where w_z is the beam radius at range z , w_0 is the beam waist and λ is the wavelength. The geometrical form of the laser footprint can have various forms. The most common forms are cyclical and elliptical. Within the footprints, the irradiance, i.e. the power per unit, is not uniform but Gaussian, according to the Gaussian-beam wave [Andrews and Phillips, 1998]. The beam divergence is assumed to be linear as defined by the beam divergence angle Θ_B . Furthermore, the beam diameter also depends on the wavelength.

Concerning terrestrial laser scanners, the spot size of the laser beam is a function of the wavelength, the beam waist and the range. The minimum spot size is not at the emitting laser diode but also somewhere along the path of the laser beam. But, the beam waist can be shifted along the path by means of focussing in order to minimize the spot size according to the object range.

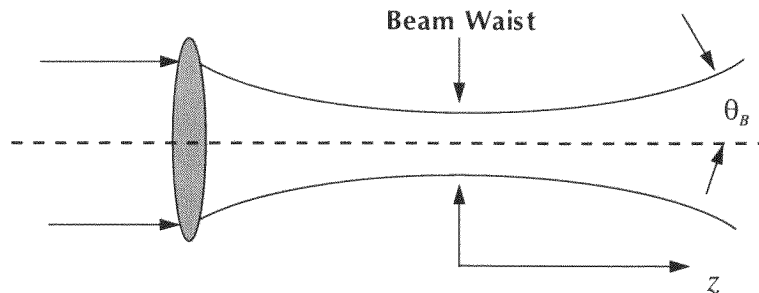


Figure 2.4: *Beam waist and divergence angle of a laser beam according to [Andrews and Phillips, 1998].*

Refraction, Scintillation and Dispersion

An electromagnetic wave, which propagates through a random medium, e.g. the atmosphere, is influenced by varying conditions, e.g. temperature, pressure, humidity. Thus, propagation characteristics change with respect to the geometry and the intensity. The varying geometry is caused by refraction, which makes the beam move or quiver. The beam propagation is no longer a straight line but a curve. In addition, the variation in the intensity of the laser beam caused by the varying atmosphere is called scintillation. Furthermore, these intensity fluctuations are affected by optical turbulence. Optical turbulence can be defined as the fluctuations in the refractive index resulting from atmospheric turbulence [Beland, 1993].

Another effect is known as dispersion. Dispersion here is defined as the dependence of the propagation velocity on the wavelength.⁴ Since each laser light consists of a narrow spectrum, which is so close that the laser light can be considered monochromatic, the propagation velocity is defined by the group velocity of differing frequencies or wavelengths. Consequently, a group refractive coefficient must be considered. Depending on the group refractive coefficient, the distance to be measured has to be corrected and this is known as the first velocity correction. Further details concerning atmospheric influences on the propagation of electromagnetic waves can be found in [Joeckel and Stober, 1991] and [Rüeger, 1996].

The described influences are relatively small for short ranges and can be neglected. However, for long range laser scanners covering distances of up to several hundreds of meters, the influences due to the atmosphere and the refractive index have to be taken into account. They affect the distances in a systematic way and cause methodological errors.

Laser Safety

Due to power density, most lasers are dangerous and can cause damage to the skin or the eyes. Depending on the wavelength of the laser, different elements of the eyes are affected. Lasers are generally categorized into four classes according to the laser's ability to cause damage to the eyes. The eye transmission can be seen in Figure 2.5. For the visible area and some infrared frequencies, the eye has a transmission characteristic of nearly 100 %.

The classification procedure of lasers is carried out in a specific setup as defined in [IEC, 2001]. The laser beam is focused on an aperture located in a predefined distance. A detector is placed just behind the

⁴Dispersion is used in different ways: For example, in optics, dispersion is the separation of a wave into its spectral components depending on the wavelength

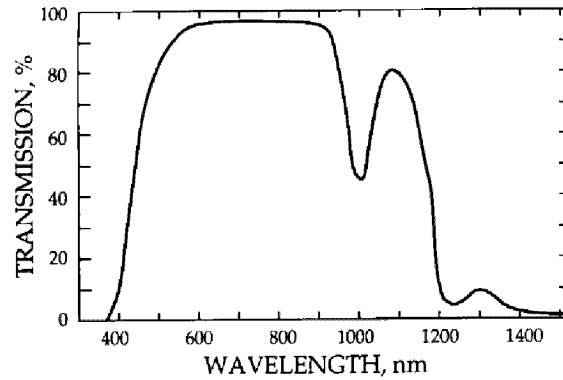


Figure 2.5: Eye transmission for electromagnetic waves.

aperture and records the highest output power level of the laser beam. Due to the detected power level, lasers are classified. Table 2.1 shows the different laser classes and their characteristics. More information concerning laser safety can be found in [Henderson, 1997] and [Young, 1984].

Table 2.1: Overview of Laser Safety Classes according to IEC 60825-1 and EN 60825-1.

Class	Description
1	Eye-safe under all operating conditions
1M	Safe for viewing directly with the naked eye, but may be hazardous to view with the aid of optical instruments. In general, the use of magnifying glasses increases the hazard from a widely-diverging beam, e.g. LEDs and bare laser diodes, and binoculars or telescopes increase the hazard from a wide, collimated beam; such as those used in open-beam telecommunications systems.
2	These are visible lasers. This class is safe for accidental viewing under all operating conditions. However, it may not be safe for a person who deliberately stares into the laser beam for longer than 0.25 s, by overcoming their natural aversion response to the very bright light.
2M	These are visible lasers. This class is safe for accidental viewing with the naked eye, as long as the natural aversion response is not overcome as with Class 2, but may be hazardous, even for accidental viewing, when viewed with the aid of optical instruments, as with class 1M.
3R	Radiation in this class is considered low risk but potentially hazardous. The class limit for 3R is 5 times the applicable class limit for Class 1 (for invisible radiation) or class 2 (for visible radiation). Hence, continuous wave visible lasers emitting between 1 and 5 mW are normally Class 3R. Visible class 3R is similar to class IIIA in US regulations.
3B	Radiation in this class is very likely to be dangerous. For a continuous wave laser the maximum output into the eye must not exceed 500 mW. The radiation can be a hazard to the eye or skin. However, viewing of the diffuse reflection is safe.
4	This is the highest class of laser radiation. Radiation in this class is very dangerous, and viewing of the diffuse reflection may be dangerous. Class 4 laser beams are capable of setting fire to materials onto which they are projected.

Most of the terrestrial laser scanners fit in class 3, e.g. HDS Leica Geosystems (Switzerland), Trimble (USA), Zoller+Fröhlich GmbH (Germany), FARO Technologies Inc. (USA), I-Site Pty Ltd. (Australia), 3rd Tech Inc. (USA). The laser scanners of Callidus Precision Systems GmbH (Germany), Optech Inc. (Canada) and Riegler Laser Measurement Systems GmbH (Austria) are categorized as class 1. However, for all laser scanners, eye safety is frequently guaranteed since the operation of laser scanners in the scanning mode deflects the laser beam at a high speed. The laser beam does not hit the eyes long enough to cause damage due to the

rotation. Additionally, if the laser beam describes a constant line without rotation, eye contact has to be avoided. It is then not only recommended but also prescribed to wear safety goggles.

2.1.3 Direct Time-of-Flight

The direct time-of-flight method determines the travel time Δt of an impulse to a surface and back by

$$s = \frac{c}{2} \cdot \Delta t \quad (2.3)$$

where s is the distance to the surface at which the impulse was reflected and c is the speed of light. The temporal accuracy has to be high due to fast speed of light ($c \approx 3 \cdot 10^8$ m/s). If the range has to be solved to 1 mm, a time resolution is required of

$$\Delta t = \frac{2 \cdot \Delta s}{c} = \frac{2 \cdot 0.001 \text{ m}}{3 \cdot 10^8 \text{ m/s}} = 6.7 \cdot 10^{-12} \text{ s} = 6.7 \text{ ps}. \quad (2.4)$$

Due to the time resolution required for distance measurements within the millimeter scale, the electronic units have to produce short pulses or patterns and have to operate very quickly. Since a single timed pulse is not very accurate, a large number of pulses is used and averaged to give a more accurate distance. Often the direct time-of-flight technique is able to distinguish between a first pulse and a last pulse, which are detected and belong to the same emitted laser pulse. It can be decided whether the first pulse or the last pulse is of interest. Furthermore, problems caused at edges and by multipath effects result in biased data that can be avoided in the direct time-of-flight technique.

The advantage of the direct time-of-flight technique in terrestrial laser scanners is the ability to cover long ranges up to several hundreds of meters or even up to a kilometer. The emitted laser may have high energy for traveling a long distance because the energy of the received signal for measuring the travel time has to be sufficiently high. Since the emitted pulses cannot be generated in a short time, the minimum time interval between two laser pulses for determining distances is limited. Thus, the frequency of measuring distances is defined and characterizes the sampling frequency of a laser scanner. Typical sampling frequencies for laser scanners are between 1 kHz and 30 kHz. As discussed before, the range resolution is limited according to the time resolution. Generally, a distance accuracy for a single distance measurement below 1 cm is rarely achievable. Figure 2.6 shows schematically the direct time-of-flight principle.

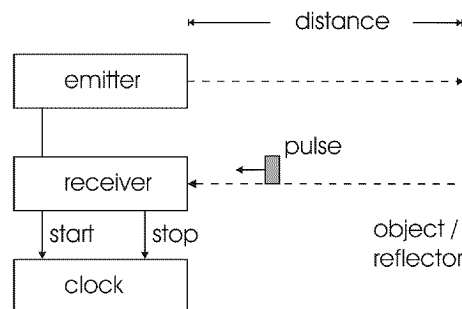


Figure 2.6: Direct time-of-flight principle schematically according to [Zetsche, 1979].

2.1.4 Amplitude-Modulated Continuous Wave (AMCW)

The amplitude-modulated continuous wave method (AMCW) modulates the carrier sinusoidally or rectangularly. The returned energy waveform is delayed by the travel time Δt and appears proportionately phase-shifted in comparison to the emitted energy. The range s is proportional to the phase shift $\Delta\phi$:

$$s = \frac{c}{2} \cdot \frac{\Delta\phi}{2\pi f}, \quad (2.5)$$

where f is the frequency of the sine wave. Instead of determining the time Δt directly, compared to Equation (2.3), the travel time is replaced by

$$\Delta t = \frac{\Delta\phi}{2\pi f}. \quad (2.6)$$

If the wave defining the maximum interval is fulfilling more than one period, a multiple N of the wavelength λ has to be added to the range, which is computed by the phase shift $\Delta\phi$. Thus, the equation for determining the absolute range s is [Hinderling, 2004]:

$$s = \frac{1}{2} \left(N \cdot \lambda + \lambda \frac{\Delta\phi}{2\pi} \right) \quad \text{with} \quad \lambda = \frac{c}{f}. \quad (2.7)$$

The resolution of the range s not only depends on the determination of Δt but also on the determination of $\Delta\phi$. The range s is more precise with higher frequencies or with more precise determinations of $\Delta\phi$. Generally, the phase angle $\Delta\phi$ can be solved from $1/4000$ and up to $1/8000$ of the wavelength, cf. [Rüeger, 1996] and [Kahmen, 1997]. The common way for determining longer ranges is to use more than one frequency. The lowest frequency defines the maximum range and the higher frequencies are used for improving the coarse range provided by the lowest frequency within the desired precision. In practice, objects at farer distances than the period of the lowest frequency are shifted within the period of the lowest frequency. This ambiguity is of importance and has to be taken into account.

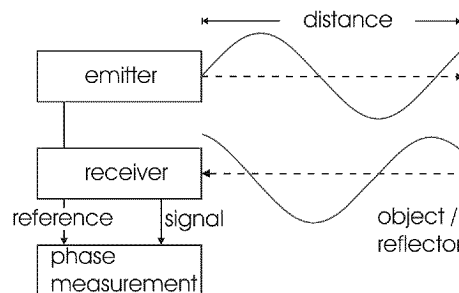


Figure 2.7: Amplitude-modulated continuous wave: phase difference principle according to [Zetsche, 1979].

The range interval for laser scanners operating with AMCW-method is limited up to nearly 100 m since the intensity of the modulated signal, e.g. sine wave and square wave, is decreasing and the phase shift $\Delta\phi$ cannot be reliably detected. However, electronic units allow fast determinations of the range, thereby increasing the data acquisition rate. Typical sampling frequencies of laser scanners operating with the AMCW-method reach values of 100 kHz and up to 700 kHz. The distance accuracy for one single measurement can be increased within some millimeters. Unfortunately, each phase measurement represents a single shot, which means no distinction can be made regarding first pulses and last pulses. Especially at edges, the AMCW-method produces erroneous data that result in mixed pixels, cf. Section 4.1.2. Figure 2.7 shows schematically the AMCW-method.

The modulation is not only based on one frequency. The modulation of two or more simultaneous frequencies is also possible. For example, the laser scanner 'Imager 5003' of Zoller+Fröhlich is based on bi-modulation using two frequencies. In Figure 2.8, the AMCW of the 'Imager 5003', representing the high frequency signal 'hfs' and the low frequency signal 'lfs' (close), cf. Section 3.2, can be seen. Based on this figure, the period of the 'hfs' is of about 180 ns and the period of the 'lfs' is of about 22 ns and therefore, fit the nominal values.

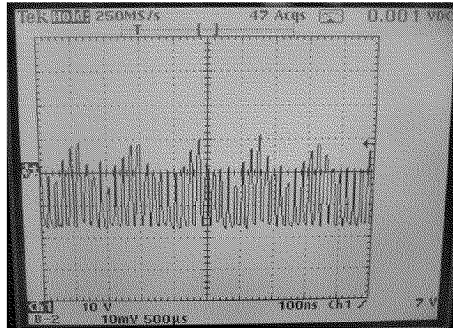


Figure 2.8: Zoller+Fröhlich laser scanner: the high frequency signal 'hfs' and the low frequency signal 'lfs' (close) of the amplitude-modulated continuous wave.

2.1.5 Frequency-Modulated Continuous Wave (FMCW)

The frequency-modulated continuous wave method (FMCW) is based on the modulation of a signal by varying the frequency. The emitted signal is modulated by a sine wave at varying frequencies and mixed with the reflected frequency. The mixed frequency is low-pass filtered and the generated signal is referred to as the beat signal. The range can be estimated by measuring the resulting beat frequency which follows a periodic waveform with a period T_r . The distance to the object is proportional to the (maximum) beat frequency B , i.e. the absolute difference in frequency Δf between the received signal and the emitted signal [Hancock, 1999]:

$$s = \frac{c}{2} \cdot \frac{BT_r}{2\Delta f}. \quad (2.8)$$

The FMCW technique is not widely-used in terrestrial laser scanners and is more related to radar systems, i.e. long range applications. More information can be found in [Hinderling, 2004].

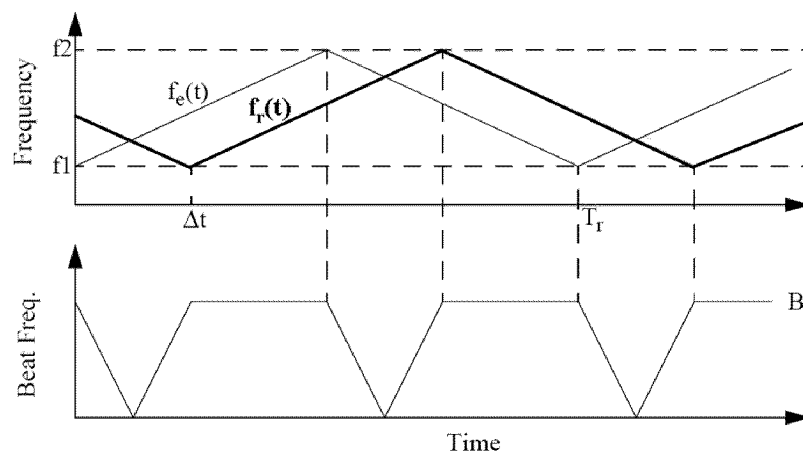


Figure 2.9: Typical chirped waveforms and beat frequency for an FMCW laser. $f_e(t)$ is the emitted frequency, and $f_r(t)$ is the received frequency. B is the peak beat frequency for a measurement. Δt is the delay in the reflected signal and T_r is the period of the frequency chirp (adapted from [Hancock, 1999]).

2.1.6 Overview of Distance Measurement Techniques in Terrestrial Laser Scanners

Table 2.2 gives an overview of the distance techniques that are used in terrestrial laser scanners. The correlation between the distance measurement technique on one hand and the range and data acquisition rate on the other can be seen.

Table 2.2: Overview of distance measurement techniques in terrestrial laser scanners. The data acquisition rate, i.e. frequency, and the range depend on the distance measurement technique.

Laser Scanner	Manufacturer	Distance Technique	Range [m]	Frequency [kHz]
CPW 8000	Callidus	direct TOF	80	28
LS 880	FARO	AMCW	76	120
HDS 3000	Leica Geosystems	direct TOF	300	1.8
LMS-Z420i	Riegl	direct TOF	800	12
GX	Trimble	direct TOF	350	5
Imager 5003	Zoller+Fröhlich	AMCW	53	625

2.1.7 Avalanche Photo Diode (APD)

An avalanche photodiode (APD) is a photodiode that internally amplifies the photocurrent by an avalanche process. A large reverse-bias voltage, typically over 100 volts, is applied across the active region. This voltage causes the electrons initially generated by the incident photons to accelerate as they move through the APD active region. As these electrons collide with other electrons in the semiconductor material, they cause a fraction of them to become part of the photocurrent. This process is known as avalanche multiplication. Avalanche multiplication continues to occur until the electrons move out of the active area of the APD.

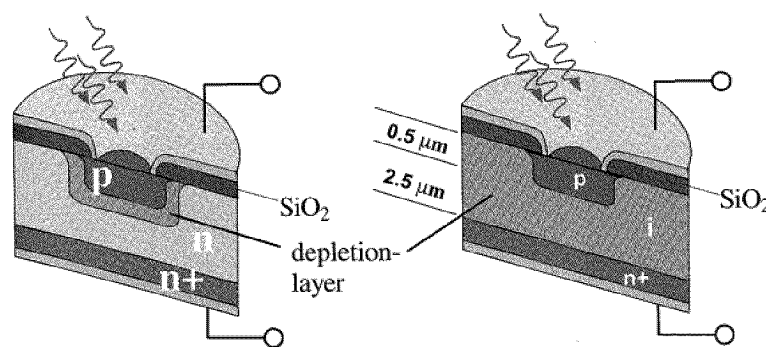


Figure 2.10: Layout of silicon photodiodes: conventional design (left) and pin layout (right) according to [Meschede, 2004].

The gain of the APD can be changed by changing the reverse-bias voltage. A larger reverse-bias voltage results in a larger gain. However, a larger reverse-bias voltage also results in increased noise levels. Excess noise resulting from the avalanche multiplication process places a limit on the useful gain of the APD. The avalanche process introduces excess noise because every photo-generated carrier does not undergo the same multiplication.

An APD is compact and immune to magnetic fields, requires low currents, is difficult to overload and has high quantum efficiency that can reach 90%. The noise properties of an APD are affected by the materials that the APD is made of. Typical semiconductor materials used in the construction of low-noise APDs include silicon (Si), indium gallium arsenide (InGaAs) and germanium (Ge). More information concerning photons and APD can be found in [Saleh and Teich, 1991] and [Meschede, 2004].

2.1.8 Reflection Principles

The reflection of electro-optical waves is based on different types of reflection. It is distinguished between:

- specular, i.e. mirror-like, reflection
- diffuse, i.e. Lambertian, reflection

The specular or mirror-like reflection is characterized so that the angle of reflection θ_r is identical to the angle of incidence θ_i with respect to the surface normal

$$\theta_r = \theta_i. \quad (2.9)$$

The incoming ray is reflected in only one single direction. The specular reflection appears if the roughness of the surface is relatively small in comparison to the wavelength of the incoming ray [Gerthsen and Vogel, 1993]. The specular reflection is illustrated in Figure 2.11 (left). The complement to specular reflection is the diffuse reflection, as illustrated in Figure 2.11 (middle). The incoming ray fans out as a bundle of reflecting rays, covering the hemisphere surrounding the surface of the object. This reflection requires that the roughness of the surface be uneven or granular with respect to the wavelength of the incoming ray. If a surface is completely non-specular, the reflected light will spread over the hemisphere surrounding the surface.

The combination of specular reflection and diffuse reflection leads to a mixed reflection. The incoming ray is divided into several reflecting rays covering the hemisphere surrounding the surface of the object. However, the intensity of the ray, with its angle of reflection equalling the angle of incidence, mirrored at the surface normal, is the largest. One approximation of a mixed reflection is shown in Figure 2.11 (right). Some surfaces exhibit retroreflection. The structure of these surfaces is such that light is returned in the direction from which it came regardless of the angle of incidence. Such reflection is caused by prisms, which are used for precise distance measurements of total stations.

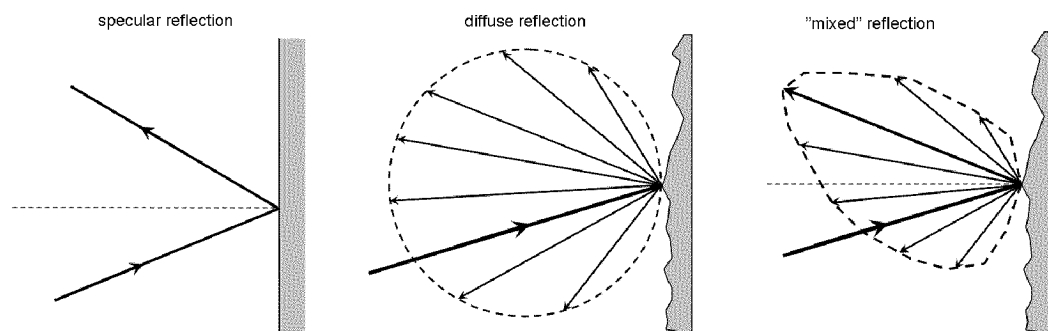


Figure 2.11: Types of reflection: specular reflection (left), diffuse reflection (middle) and mixed reflection, consisting of combined diffuse-specular reflection (right).

2.1.9 Reflectance Models

Specular reflection and diffuse reflection are simple approximations. In reality, surfaces exhibit various types of reflection. Other properties of electromagnetic waves, e.g. polarization, influence the way of reflection and complicate a mathematical description. In computer graphics several models were developed for describing the reflectance. In the following, three models are introduced: the Lambertian reflectance

model, the Phong model and the Torrance-Sparrow model. More information concerning reflection models can be found in [Luhmann et al., 2006], [Janser et al., 1996] and [Tönnies and Lemke, 1994].

Lambertian Reflectance Model

One common model for diffuse reflection is Lambertian reflectance, where the light is reflected with equal luminance in all directions according to Lambert's cosine law [Gerthsen and Vogel, 1993]. Lambert's cosine law states that the reflected or transmitted luminous intensity in any direction J from an element of a perfectly diffusing surface varies as the cosine of the angle α between that direction and the normal vector of the surface:

$$J = J_0 \cos(\alpha), \quad (2.10)$$

where J_0 is the intensity radiation in normal direction. As a consequence, the luminance of the surface is the same regardless of the viewing angle and the angle of incidence.

Phong Model

Phong's model is one of the most common lighting models in computer graphics. The intention of the Phong reflection model is to produce a 3D model with a certain degree of realism. Therefore, it combines the common reflection principles, specular and diffuse, with ambient lighting. In Figure 2.12, the image and the Phong model of a sphere can be seen. The modeled sphere becomes a realistic illustration of a real sphere. More information can be found in [Phong, 1975].

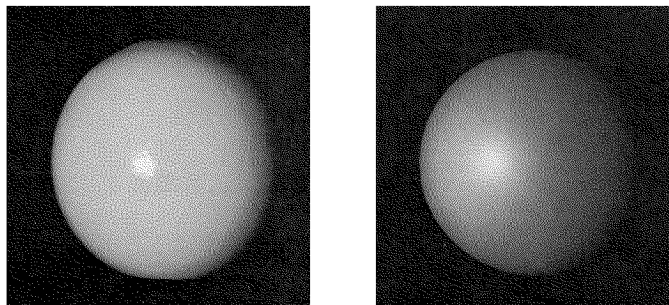


Figure 2.12: Phong model: Picture of a sphere (left) and sphere displayed by Phong model (right), adapted from [Phong, 1975].

Torrance-Sparrow Reflectance Model

The Torrance and Sparrow reflectance model is close to the Phong illumination model with some differences. These differences are that the intensity of the specular reflection varies with the direction of the light source and the angle of peak specular reflection is not always exactly at the angle of incidence [Torrance and Sparrow, 1967].

2.2 Angle Measurement System

The orientation of the laser beam in terrestrial laser scanners is measured electro-optically by encoders with respect to a horizontal and a vertical direction. The electro-optical method is based on transmitted light or on reflected light. A glass arc with diameters of 5 cm to 7 cm is coded by a pattern of alternate opaque and transparent areas. Incident light from an internal source falls on the glass arc and photodiodes convert

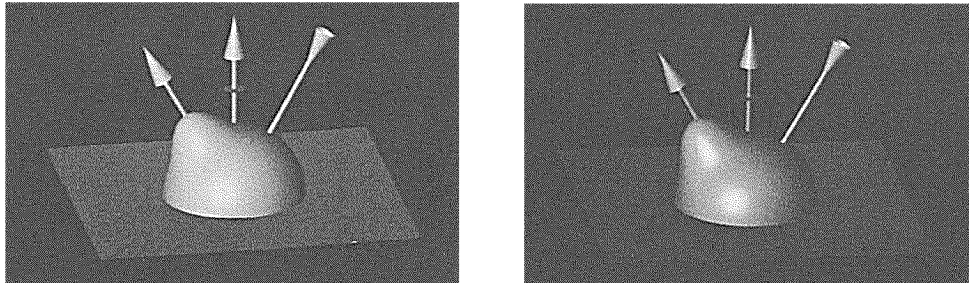


Figure 2.13: Comparison between Phong model (left) and Torrance and Sparrow model (right), adapted from [Blinn, 1977].

the light energy transmitted by or reflected from the pattern into electrical energy, e.g. pulses or pixel information. The digital signal then has to be converted from an analog signal to a digital output readable as a decimal number, cf. Figure 2.14.

In most terrestrial laser scanners, binary encoding is implemented since an initialization is not required and the angular resolution is sufficiently high for laser scanning. However, for higher resolution, within some milligons, incremental encoding has to be used.

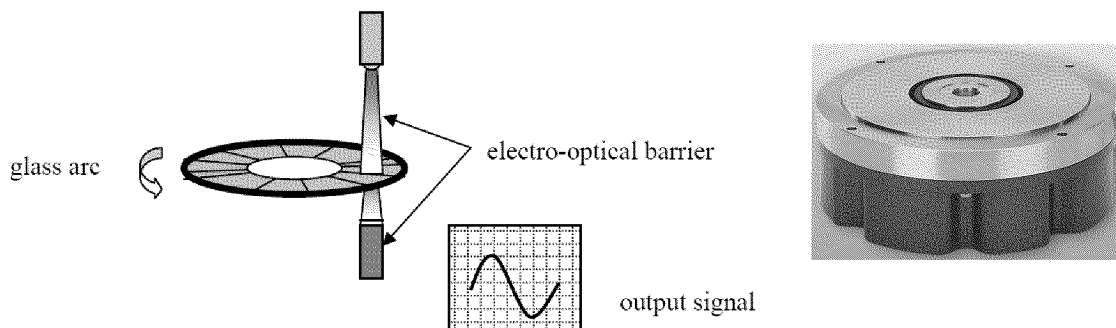


Figure 2.14: Glass arc, electro-optical barrier and output signal schematically (left) and angle transmitter of Heidenhain GmbH, Germany (right).

2.2.1 Incremental Encoding

Incremental encoding is also called the relative method since the reference base is not marked on the circle. Using this method, only a relative rotation of the glass circle is measurable. Light from a source is passed through the graduated glass circle prepared by transparent and opaque strips of equal width. The smallest graduation unit is defined by the width of one strip. The quantity of light received by the photodiode depends on the rotation and changes are nearly sinusoidal. The periods of the sinusoidal oscillation can be counted and the amount of rotation can be determined. Incremental encoding requires an initialisation. Therefore, the glass arc is marked with an additional code that differs from the pattern containing the angle information. The additional code has to pass the electro-optical barrier and the counter is then initialized.

The determination of the angle is carried out by a coarse measurement and a fine measurement. The coarse measurement counts the number of passing transparent and opaque strips. Therefore, the output signal of the photo diode is triggered and the number of pulses, i.e. transitions between positive and negative states, are counted. Due to the pattern consisting of up to 20,000 elements, the rotation angle has a resolution up to 0.02 gon. The fine measurement uses the Moiré effect. The pattern of several opaque and transparent

strips of up to 200 is overlapped by the corresponding diametrically opposed pattern. Based on the Moiré pattern, the resolution can be increased by measuring the phase. Therefore, the reading index has to be positioned within the last period of the Moiré pattern. Further details can be found in [Ingensand, 1998] and [Schlemmer, 1996].

2.2.2 Binary Encoding

The binary encoding method is also called the absolute method since the reference base is physically marked on the graduated glass circle. Light from a light source passes through the encoded glass circle, which is marked with the number of the graduation in a binary code. Each corresponding digit of the binary code is represented by a transparent or an opaque element.

The glass circle contains either coded rings or is marked by an absolute code, which can be read by an array of CCD⁵ sensors. In Figure 2.15, a glass circle with coded rings (left) and an absolute code (right) can be seen. The required resolution can be achieved by interpolation algorithms. Further details can be found in [Ingensand, 1998] and [Schlemmer, 1996].

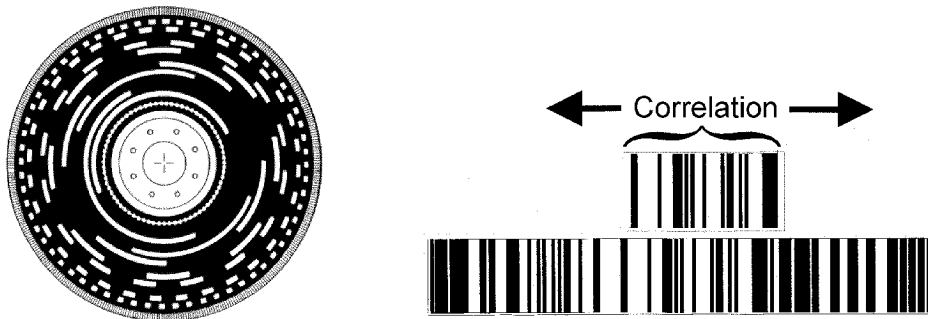


Figure 2.15: *Binary encoding with absolute orientation according to [Ingensand, 1998]. Coded rings (left) and absolute code (right).*

2.3 Deflection System

Scanning the environment requires the deflection of the laser beam in two directions, horizontally and vertically, respectively. Due to constant angle increments the result is a grid of points defining a point cloud. The horizontal deflection step width is often forced to equal the vertical deflection step width. The points are arranged in vertical profiles and shifted by a discrete horizontal angle increment.

The deflection can be separated into a primary deflection and in a secondary deflection for two-mirror-systems, cf. Section 2.3.1. Each mirror rotates about one specific axis to deflect the laser beam in a 2D plane. A common practice is to perform a primary deflection in the vertical direction to generate a vertical profile. The secondary deflection then shifts the laser beam horizontally to acquire the next vertical profile adjacent to the previous profile. In the case of a one-mirror system, the laser beam is deflected by a rotating mirror, which is moving about two perpendicular axes, cf. Section 2.3.2. The dimensions of the environment that can be scanned depends on the principle used for deflecting the laser beam. This field of view is either limited by a section, i.e. camera scanner, or covers a full view, i.e. panorama scanner, cf. Figure 2.16.

There are different techniques for deflecting the laser beam. A detailed discussion is given in [Kern, 2003], where it is distinguished between a deflection using plane mirrors, polygon mirrors, and prisms. Another possibility is the distinction regarding the motion of the mirrors. They can either oscillate or simply rotate.

⁵CCD: Charged Coupled Device

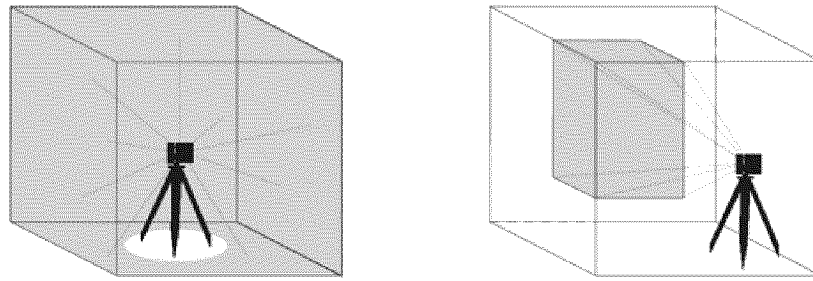


Figure 2.16: Different types of terrestrial laser scanners classified by field of view according to [Runne et al., 2001]: panorama scanner (left) and camera scanner (right).

In the following, a distinction is made between a rotating beam deflection unit and an oscillating beam deflection unit.

The deflection of the laser beam implemented in laser scanners is often a combination of different deflection methods. The primary rotation is faster than the secondary rotation. Considering the panorama scanner, e.g. laser scanners of Callidus, Faro, Riegl, Zoller+Fröhlich, the primary deflection is performed by a fast-rotating mirror. The secondary deflection involves a rotation of the complete deflection unit instead of rotating only the mirror. Appendix A shows the imaging system of the laser scanner Imager 5003 of Zoller+Fröhlich.

2.3.1 Oscillating Mirror

The primary rotation is described by a mirror that oscillates about an axis. The sampling interval is defined by the minimum increment of the encoder unit which causes the mirror to oscillate to the next position. The encoder position and the distance correspond with each other. Since the oscillation is not as fast as the rotation, the synchronisation is not as crucial as it is for the rotating mirror. The combination of two oscillation mirrors deflects the laser beam in the desired directions. The vertical and horizontal sampling intervals are defined by the minimum increment of the encoder controlling the oscillations of the mirrors. The main drawbacks of oscillating mirrors are the limited field of view and the performance of the deflection.

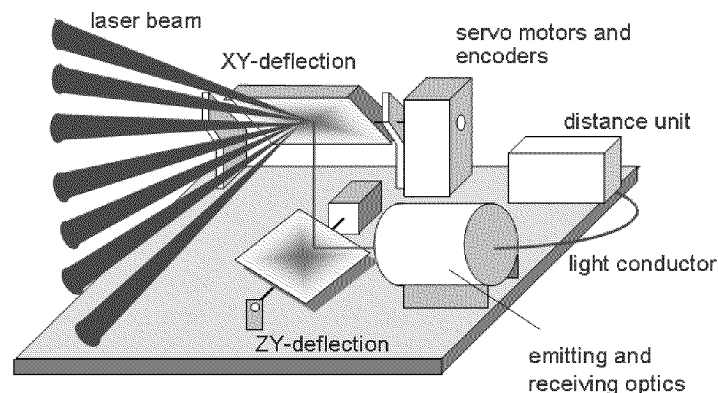


Figure 2.17: Oscillating mirrors according to [Schlemmer, 2004].

2.3.2 Rotating Mirror

The primary rotation is described by a mirror that rotates about an axis. The rotation axis of this primary rotation is often a horizontal axis. Thus, the laser beam is deflected in a vertical profile. The secondary rotation is carried out by the rotation of the laser scanner about a vertical axis to deflect the laser beam in a horizontal profile. The vertical sampling interval is defined by the frequency of detecting distances and the encoder resolution. The distance acquisition has to be synchronized with the corresponding orientation of the rotating mirror. Since the mirror is rotating permanently and quickly, up to 33 rotations per second, the synchronization and the rotation time of the rotating mirror are important aspects.

2.3.3 Overview of Deflection Techniques in Terrestrial Laser Scanners

The following Table 2.3 gives an overview of the deflection techniques that are used in terrestrial laser scanners. The trend is to construct panorama scanners since the advantage of a larger field of view is obvious. The panorama scanners also include the possibility of surveying a user-defined area instead of a full panorama.

Table 2.3: *Overview of deflection techniques in terrestrial laser scanners.*

Laser Scanner	Manufacturer	Deflection Technique
CPW 8000	Callidus	rotating mirror
LS 880	FARO	rotating mirror
HDS 3000	Leica Geosystems	oscillating mirror
LMS-Z420i	Riegl	rotating polygonal mirror wheel
GX	Trimble	scanning optical system (patented)
Imager 5003	Zoller+Fröhlich	rotating mirror

Calibration of Terrestrial Laser Scanner

The conception of an instrument assumes specific constraints between the different components. Due to mechanical imperfections, it is impossible to design an instrument exactly to theoretical planning. There are discrepancies between the real instrument and the ideal instrument, and these are called instrumental errors. The knowledge of instrumental errors is essential in acquiring reliable measurements. The more one is aware of the systematic errors, the better one is able to correct for the real instrument with respect to its ideal construction by applying mathematical models. However, these mathematical models require precise knowledge of the instrument and its components. Furthermore, the calibration of an instrument necessitates the stability and the time constance of the calibration parameters. If these requirements are not fulfilled, calibration is nearly impossible.

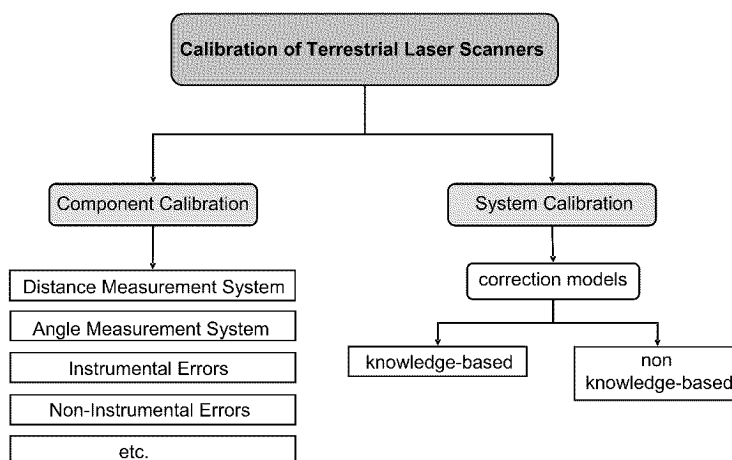


Figure 3.1: Calibration of terrestrial laser scanners, categorized by component calibration and system calibration.

Normally, a distinction can be made between a system calibration and a component calibration [Hennes and Ingensand, 2000]. Figure 3.1 shows the calibration procedures. The system calibration derives either a mathematical model or a correction function, without knowledge of each single instrumental error and its influence, by appropriate observation of control points or known objects, e.g. spheres, planes. The component calibration is mostly based on knowledge-based modeling of the instrument and its instrumental errors. Each single error is investigated separately in a specific experimental setup. The latter has been applied to the laser scanner, Imager 5003 of Zoller+Fröhlich, cf. Table 3.1.

Before starting with the discussion of the calibration procedures applied on the laser scanner, some terms and definitions need to be clarified. There is often a misunderstanding between calibration, performance assessment/evaluation, and certification. They are similar in meaning and are often used synonymously [NIST, 2002]. However, there are slight differences in the nuances of these terms. One formal definition of **calibration** is given by [VIM, 1993]:

Table 3.1: *Specifications of terrestrial laser scanner, Imager 5003 of Zoller+Fröhlich.*

manufacturer :	Zoller+Fröhlich GmbH (Wangen i.A., Germany)
type name :	Imager 5003
type number :	53500
serial number :	161
laser number :	09014
laser class :	3R
production year :	2003

Calibration is a set of operations that establish, under specified conditions, the relationship between values of quantities indicated by a measuring instrument or measuring system, or values represented by a material measure or a reference material, and the corresponding values realized by standards.

Notes:

- (1) *The result of a calibration permits either the assignment of values of measurands to the indications or the determination of corrections with respect to indications.*
- (2) *A calibration may also determine other metrological properties such as the effect of influence quantities.*
- (3) *The result of a calibration may be recorded in a document, sometimes called a calibration certificate or a calibration report.*

Performance assessment/evaluation is a voluntary assessment and would be conducted to determine how well the instrument and the processing software meet a user's specific requirements [NIST, 2002]. **Certification** has legal connotations and would involve testing the instrument in accordance with a set of protocols and measuring the results against a metric pass/fail [NIST, 2002]. The testing would, in general, be conducted in a certified laboratory.

The procedures of calibration and performance assessment/evaluation deal with the investigation of measuring systems. Investigating measuring systems, e.g. automated total stations, digital levels, cameras, laser scanners, usually require many measurements to derive measurands as well as to assess the results. For the assessment of measurements, several standard definitions were developed by different organisations and institutes, such as the International Organization for Standardization (ISO), the American National Standards Institute (ANSI) and the American Society of Testing and Materials (ASTM International). Furthermore, [Heister, 2006] introduced parameters to assess the accuracy of laser scanners and to make them comparable.

The standard definitions cover a wide range of terms. Unfortunately, there are some terms for which standard definitions are missing. Such terms are related to the topic of laser scanners. The reasons for this are due to the relatively young age of the instrument developments and the differing working principles they were based on. Examples of such missing terms include sample rate, horizontal resolution and vertical resolution. Each vendor uses different definitions and specifications for qualifying the characteristics of its laser scanner. To avoid misunderstanding, definitions for two pairs of confusable but important terms are given. They are precision versus accuracy and repeatability versus reproducibility.

Precision is defined as the closeness of the agreement between independent test results obtained under stipulated conditions [ASTM E456-02, 2002]. Usually, precision is expressed numerically by measures of imprecision, such as standard deviation, variance, or coefficient of variation [ASTM E456-02, 2002]. The notes included with the definition also states that precision depends on random errors and does not relate to the true value. The precision can be described by the empirical standard deviation [Möser et al., 2000]:

$$s = \sqrt{\frac{1}{n-1} \sum_{i=1}^n (\mu - x_i)^2} \quad (3.1)$$

$$\mu = \frac{1}{n} \sum_{i=1}^n x_i \quad (3.2)$$

where μ is the mean, x_i represents the test results (data) and n describes the number of data.

Accuracy is defined as the closeness of the agreement between the result of a measurement and a true value of the measurand and is a qualitative concept [VIM, 1993]. Accuracy can be described by the root mean square (RMS) [Deakin and Kildea, 1999]:

$$RMS = \sqrt{\frac{1}{n} \sum_{i=1}^n (a - x_i)^2} \quad (3.3)$$

where a is a constant, x_i represents the test results (data) and n describes the number of data. Therefore, the constant a represents a true or nominal value which is based on surveying with high accuracy. Accuracy can also be expressed by a deviation Δ between the nominal value a , i.e. constant, and the real value μ , resulting in a bias (comparison principle):

$$\Delta = a - \mu. \quad (3.4)$$

In the following, numeric values describing the accuracy refer to the comparison principle expressed by Equation (3.4).

Repeatability is defined as the closeness of the agreement between the results of successive measurements of the same measurand carried out under the same conditions of measurement, e.g. expressed by dispersion parameters [VIM, 1993]. **Reproducibility** is defined as the closeness of the agreement between the results of measurements of the same measurand carried out under changed conditions of measurements [VIM, 1993]. This is important since frequently the conditions under which the instrument is operated differ from those under which the instrument was originally evaluated or calibrated.

Several lab calibration facilities at the IGP (Institute of Geodesy and Photogrammetry, ETH Zurich, Switzerland) allow for the performance of component calibration procedures. These installations include a calibration track line with a length of approx. 52 m, an electronic unit for frequency measurements, test field of observation pillars, 3D test fields, etc. They facilitate the investigation and calibration of instruments regarding various properties. The following sections introduce the different types of installations followed by the discussion of the calibration procedures applied on the different components of the terrestrial laser scanner. The focus is on the two main system components defining a surveying instrument to measure distances and angles, the distance measurement system and the angle measurement system, respectively. Furthermore, additional instrumental and non-instrumental errors affecting both the distance measurement system and the angle measurement system are discussed. Finally, an overall precision for a single point and an accuracy for modeled objects that can be achieved by the laser scanner are derived.

The discussed calibration procedures give an idea of the possible errors that can influence the precision and the accuracy of terrestrial laser scanners and their measurements, respectively. The completeness of all possible influencing parameters is not guaranteed and is not the aim of this research. Different researchers and institutions deal with the investigation of terrestrial laser scanners to achieve a better understanding of these sensors and to establish their use in geodetic applications.

3.1 Laboratories and Tools for Calibration

The IGP is equipped with various kinds of laboratory facilities, test fields, etc. Thus, geodetic instruments can be calibrated regarding different aspects. In the following, some laboratory facilities and test fields, which play an important role in the calibration of the terrestrial laser scanner, are introduced.

3.1.1 Calibration Track Line

The calibration track line at the IGP has a length of roughly 52 m. A trolley moves on the track line, either automatically or manually, cf. Figure 3.2. This trolley is tracked by a laser metric system (HP 5529A dynamic calibrator), which is based on interferometry. Thus, the position of the test trolley on this track line can be located within a high accuracy of less than 0.1 mm^1 . Atmospheric conditions, i.e. air temperature, air pressure and air humidity, are also collected as they are required for atmospheric correction of distances measured by the interferometer to guarantee high accuracy. Therefore, lab conditions are temperature-stabilized by air conditioning within a temperature range of $20^\circ\text{C} \pm 0.5^\circ\text{C}$. The distance measurement system of geodetic instruments can be calibrated by comparing the measured distances acquired by the instrument to be calibrated with the nominal distances provided by the interferometer. Therefore, the instrument to be calibrated is set up at the beginning of the track line in a way that the instrument is aligned in extension with the track line. An observation pillar is installed and facilitates the required setup easily. On the test trolley, a target can be mounted to measure the distances between the test trolley and the instrument. The additive constant between the mechanical zero point of the track line and the observation pillar is calibrated and well-known. Thus, relative as well as absolute distance measurements can be performed.

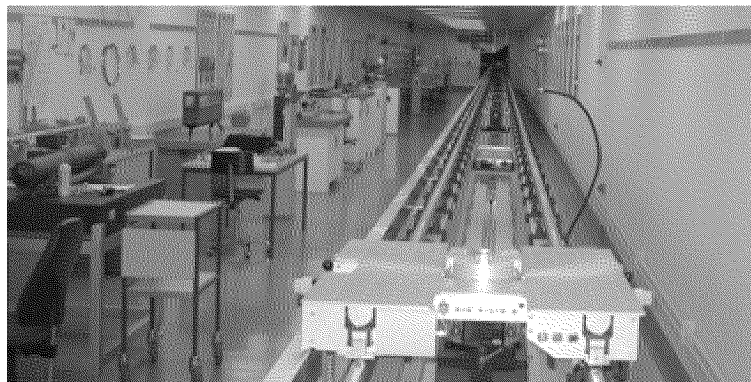


Figure 3.2: Calibration track line with a length of 52 m including the test trolley moving on the track line.

The 3D trajectory of the calibration track line is checked periodically. The optimal track can be approximated by a line that should run straight horizontally and vertically. Since an optimal straight line can rarely be established, the real run of the track line has to be identified. Generally, three different parameters are required: the straightness of alignment, the verticality of alignment and the cant, i.e. transverse gradient. The trajectory of the calibration track line regarding these parameters are shown in Figure 3.3. In the upper figure, the straightness of alignment and the verticality of alignment can be seen. The variation in the vertical direction shows a maximum relative value of 1 mm. According to Abbes comparator principle, the laser beam of the interferometer and the measurement beam of the instrument to be checked has to be in a straight line. Since this constraint can rarely be met with the design of the calibration track line the verticality of alignment is of great importance. But the maximum change in the vertical direction can

¹This accuracy represents for the resulting accuracy of the mechanical zero point of the calibration track line, the orientation of the test trolley, and the accuracy of the laser interferometer. The accuracy of the HP interferometer is given by $0.2 \mu\text{m} + 0.5 \cdot 10^{-6} \cdot D$, where D is the distance in [m]; the resolution is given by $0.1 \mu\text{m}$.

be stated by a value of 0.5 mm in 2 m, cf. Figure 3.3. Since the vertical offset between interferometer and instrument is far below 2 m, this influence can be neglected. The variation in the straightness of alignment shows an increasing deviation up to 3 mm in a range of 50 m. The influence of this deviation on the desired straight distance is far below the desired distance accuracy. In the lower figure, the cant of the track can be seen and is relatively small and thus, negligible. In summary, the track line is well-adjusted regarding the straightness of alignment, the verticality of alignment and the cant. Thus, this track line is well-suited for calibration procedures that will result in a high accuracy.

The trajectory of the calibration track line is not of importance to the calibration of the distance measurement systems of geodetic instruments in static applications. The small variations of the track do not influence the operation of the laser interferometer and does not significantly influence the ranges measured by the geodetic instruments. In addition, for kinematic applications, the 3D trajectory of the moving instrument has to be known in terms of the position (x, y, z) and in terms of the attitude angles $(\omega, \varphi, \kappa)$. If the trajectory is not well-known, additional instruments have to be used to acquire the necessary information, e.g. inclination sensors. However, the trajectory of the calibration track line is well-known and is prepared not only for static applications but also for kinematic applications.

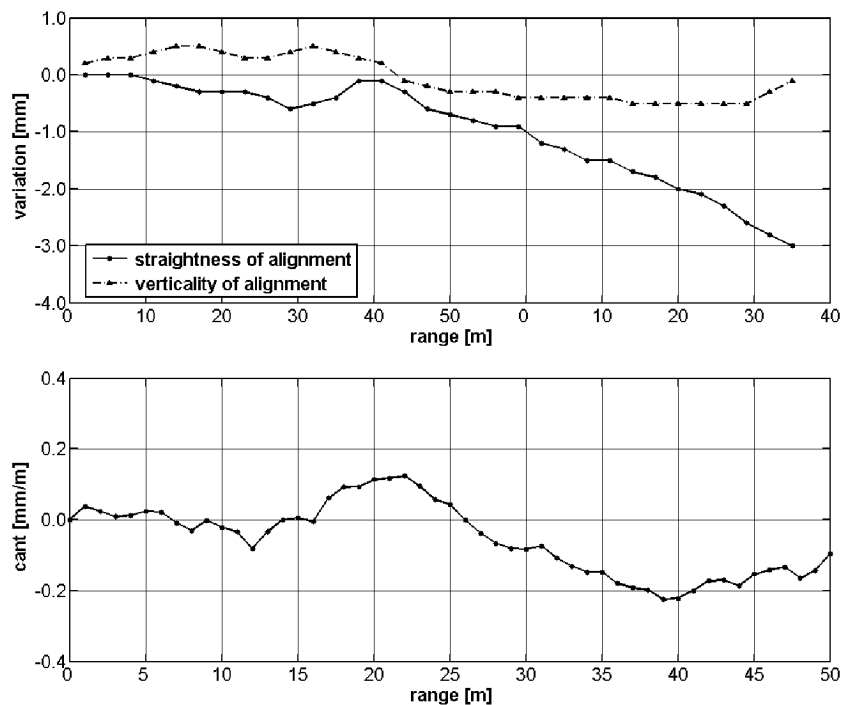


Figure 3.3: Trajectory of the calibration track line. In the upper figure, the straightness of alignment and the verticality of alignment can be seen. In the lower figure, the cant of the track is shown.

The wall behind the interferometer of the calibration track line, cf. Figure 3.10, is covered with a dark velvet curtain to avoid reflections from the background, which would result in mixed pixels, blunders or multipaths.

3.1.2 Test Field of Control Points

Along the calibration track line, a test field of control points was installed. It consists of observation pillars located beside the track line and bolts drilled into concrete walls. These control points are located along the calibration track line at both sides and at different heights. The location of the points can be seen in Figure 3.4. The coordinate system is oriented in such a way that the track of the test trolley defines the x-axis.

The origin is defined by the observation pillar on the track line (pillar number 2000) and the orientation of the x-axis is along the track line towards pillar number 1000. The coordinates of all control points were surveyed with total station from different observation pillars to achieve both high redundancy and high accuracy. All points show an accuracy in the horizontal position of less than 0.7 mm and in the vertical position of less than 0.2 mm.

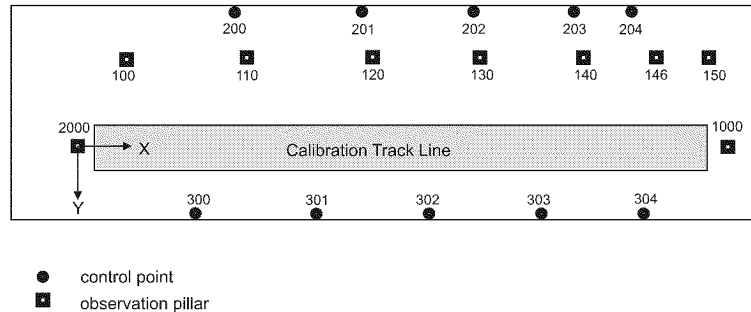


Figure 3.4: Configuration of the control points. The control points are aligned along the calibration track line on both sides and at different heights. The track line defines the x-axis.

3.1.3 Test Field of Observation Pillars

The test field of observation pillars consists of 3×3 pillars. They span an area of approximately $11 \text{ m} \times 5 \text{ m}$. The pillars can be equipped with tribrachs and allows for mounting several kinds of targets and instruments. Figure 3.5 shows the situation of the observation pillars. The 3D coordinates were periodically surveyed with respect to a relative reference frame with a high degree of accuracy. The achieved accuracy in the horizontal position is less than 0.5 mm and in the vertical position less than 0.05 mm.



Figure 3.5: Situation of the observation pillars. The observation pillars are aligned in a 3×3 pattern and span an area of approximately $11 \text{ m} \times 5 \text{ m}$.

3.1.4 Electronic Unit for Frequency Measurement

The unit for frequency measurement allows for the verification of a modulation frequency via knowledge of its nominal frequency. For this purpose a frequency counter with a high degree of accuracy regarding an absolute time base has to be derived. Therefore, the clock frequency of a frequency counter (HP 53131A²) is controlled by a standardized frequency. This standardized frequency is emitted by long wave sources

²A two-channel counter that is capable of producing a frequency resolution of ten digits per second and a bandwidth of 225 MHz. The time interval resolution is specified at 500 ps. An optional third channel provides frequency measurements of up to 3 GHz, 5 GHz, or 12.4 GHz. Standard measurements include frequency, period, ratio, time interval, pulse width, rise/fall time, phase angle, duty cycle, totalize, and peak voltage.

and can be received by the frequency measurement unit. Based on this received standardized frequency, an absolute time base for the frequency counter can be defined.

The modulation frequency of a sensor is transmitted to an APD. The detected signal is amplified and demodulated. The frequency counter calculates the detected modulation frequency. Additionally, the demodulated signal can also be visualized by an oscilloscope. The electronic unit for frequency measurement is shown in Figure 3.6. The APD, the frequency counter, the amplifier and the oscilloscope can also be seen in this figure.

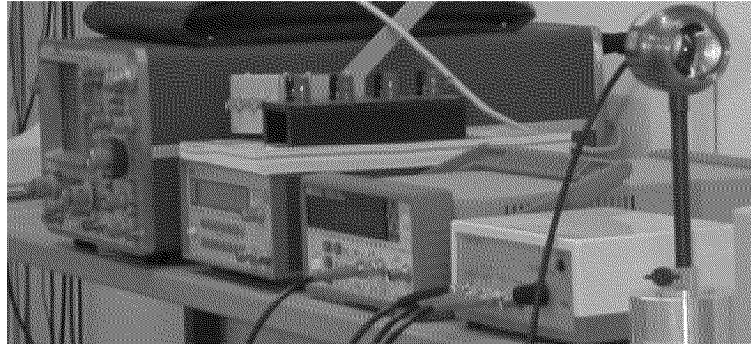


Figure 3.6: *Electronic unit for frequency measurement including an APD, an amplifier, a frequency counter, and an oscilloscope (from right to left).*

3.1.5 Calibration of Spheres

In contrast to traditional geodetic instruments, e.g. total station, GPS, levels, a laser scanner does not support the direct determination of coordinates of discrete points. For the calibration purposes of a laser scanner, it is essential to work with discrete points to derive the coordinates of these points. Several geometrical objects are suitable for laser scanning, e.g. planar coded targets, cylinders and spheres. The most appropriate object for laser scanning in terms of deriving coordinates of a discrete point is a sphere. The advantages of a sphere are manifold. First, each sphere is absolutely defined in 3D by the coordinates of the center point and its diameter. Second, a sphere is featured by a homogenous surface and is invariant regarding the viewing angle. Thus, spheres are well-suited for use as targets for laser scanning. However, there is one major disadvantage. The angle of incidence worsens with increasing distance from the center and vice versa. The introduction of weights can reduce this problem. However, these points are essential as they define the geometry of the sphere.

Consequently, massive wooden spheres in two sizes were prepared as targets for laser scanning. The diameters are of approximately twelve and fifteen centimeters. Adapters were fixed on the spheres for attaching them to prism holders. When installing the adapters, caution was taken to avoid an offset in position and in height between the prisms and the spheres. Furthermore, the spheres were painted with a white colour for achieving high intensity values for the reflected laser beams. Overall, each sphere had to be calibrated with respect to

- the diameter and the symmetry of the diameter, in horizontal and vertical direction,
- the central position of the adapter, and
- the vertical offset between prism center and sphere center.

The calibration process was performed by using a theodolite (Wild T 2000). The theodolite and the sphere were set up on two pillars of the test field of observation pillars, cf. Section 3.1.3. By knowing the distance

between the sphere or the prism, one centimeter deviation in distance does not affect the desired parameters significantly, and the theodolite, calibration parameters can be derived by using the vertical and horizontal angle measurements and simple geometrical relations.

Each sphere has different calibration parameters. The closeness of the calibration parameters of all the spheres allowed for the derivation of two sets of mean values for the diameter and the vertical offset (for the two different sizes). All results showed that the symmetry of the diameter and the central position of the attached adapter are sufficiently adequate. Thus, the spheres, cf. Figure 3.7, can be used for the calibration of the laser scanner.

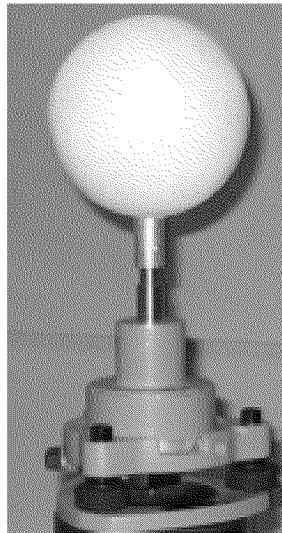


Figure 3.7: Sphere used as target for laser scanning. The diameter of the shown sphere is approximately 12 cm. The sphere is attached to a prism holder.

The center point of a sphere can be calculated easily. Normally, a minimum number of four points satisfy the definition of a sphere and with laser scanning, many more points than necessary for defining a sphere are generated. The resulting redundancy allows for the derivation of the center point via an adjustment. Therefore, the diameter of the spheres can be introduced either as an unknown parameter or as a known constant. Within the adjustment procedure, blunders are detected automatically. Blunders are present if the normal distances from each point to the sphere surface exceed a user-defined limit, e.g. 5 mm. This parameter is the same as using normalized residuals and is introduced because it can be interpreted geometrically. More information concerning the adjustment procedure can be found in Appendix C. The adjustment is iterated until either all points lie within a maximum distance to the surface of the sphere, e.g. 5 mm, or until the unknowns, i.e. coordinates of the center points and the diameter, change below a limit, e.g. 0.1 mm.

The diameters of the two spheres (12 cm and 15 cm) were chosen with respect to practical aspects and with respect to the minimum angle increments and to the beam divergence of the laser scanner, respectively. On one hand, the spheres should be small and lightweight enough to be moved and transported during field work. On the other hand, the spheres have to be large enough to be scanned from distances adapted to the range interval of the laser scanner. Thus, the aforementioned diameters for the spheres were chosen. Additionally, the best possible value for the optimal diameter of the spheres can be derived mathematically. [Reshetyuk et al., 2005] found that the optimal diameter for the laser scanners, HDS 3000 of HDS Leica Geosystems and Imager 5003 of Zoller+Fröhlich, has a value of 14 cm.

3.2 Distance Measurement System

The distance measurement system of the laser scanner Imager 5003 of Zoller+Fröhlich is based on the propagation of the modulated laser light. If the laser beam hits an object in the environment, then the laser beam is partially reflected and can be detected by an APD. This photodiode is coupled with a signal amplifier and provides a dynamic range in reflectivity from 5 % up to 99 % [Fröhlich et al., 2000]. The method used for determining distances is the phase difference principle, cf. Section 2.1.4. Because of the ambiguity in signals, e.g. sine signals, a maximum range by means of a modulated wavelength λ_{\max} has to be defined. The challenge by defining λ_{\max} is to achieve both a long range interval and a high resolution in the distance measurement. Therefore, a resolution of up to $1/8000$ of λ_{\max} is possible, cf. [Rüeger, 1996] and [Kahmen, 1997]. To guarantee long range as well as high resolution, the emitted laser signal is simultaneously intensity-modulated with two different sinusoidal frequencies [Fröhlich et al., 2000]. These two frequencies define a coarse channel component, i.e. low frequency signal ‘lfs’, and a fine channel component, i.e. high frequency signal ‘hfs’. The detected laser light contains the phase shifts of both modulation frequencies: ‘lfs’ limits the maximum range and provides a coarse value for the desired distance and ‘hfs’ delivers a precise but ambiguous range. Depending on the desired maximum range for ‘hfs’, two different modes can be chosen: mode ‘close’ ($\lambda_{\text{lfs}} \approx 54$ m), and mode ‘far’ ($\lambda_{\text{lfs}} \approx 108$ m). Thus, the distance between the scanner and the object is limited to 27 m and 54 m, respectively. ‘hfs’ has a wavelength of $\lambda_{\text{hfs}} \approx 6.7$ m and allows for a resolution of less than 1 mm. The carrier wave of the emitted laser light is in the near infrared ($\lambda \approx 700$ nm). Based on constant emitter signals, the intensity of the detected light is equivalent to the reflectivity value of the object. The simultaneous detection of both range and reflectance values guarantees that they correspond directly to the same data point in 3D. Furthermore, it has to be mentioned that this distance measurement system is (mostly) independent of the lighting condition, e.g. ambient light, because of the active illumination of the laser light.

The reflectivity of an object is not the only parameter which influences the intensity of the reflected laser signal. Other parameters also affect the reflectivity value (I), such as [Gerthsen and Vogel, 1993]:

- distance d , which is inversely proportional to the square of the distance: $I \sim 1/d^2$
- angle of incidence
- surface properties, e.g. colour, roughness, reflectance

The laser scanner can operate in two different modes: a so called ‘scanning mode’ and a so called ‘static mode’. The ‘scanning mode’ means that the deflection unit is rotating. In contrast, the deflecting unit in the ‘static mode’ is not rotating and the laser beam can be aligned manually. The usual operation mode for the laser scanner is the ‘scanning mode’. Therefore, the laser beam is deflected by the rotating deflection unit and is scanning the 3D environment. The ‘static mode’ should only be used for investigation and calibration purposes and for some specific applications because the laser beam is permanently aligned in one direction and is reflected by the same object point in the environment. In ‘static mode’, the laser beam is dangerous for the human eyes since the laser class is 3R and can cause permanent damage to the retina, cf. Section 2.1.2. The operator as well as people involved in the surrounding have to wear safety goggles according to laser safety instructions to avoid irreparable accidents concerning human vision. However, some important aspects can be gained in ‘static mode’, for example:

- precision and accuracy
- long-run behaviour
- frequency stability, e.g. caused by thermal drifts

3.2.1 Static Mode

The manufacturer defines for the distance measurement system two remaining errors after range calibration³: the linearity error and the range noise. The linearity error means that all deviations between the nominal value, i.e. nominal distance, and the measured value, i.e. measured distance, lie within a limit. Because of the presence of random noise and blunders in distance measurements, the measured value is replaced by the mean value of several repeated measurements, e.g. 10,000 measurements. The result is a non-linear curve called a linearity error curve, where its magnitude should be independent of the distance. The range noise describes the measurement noise of repeated measurements against the mean value and corresponds to the empirical standard deviation, i.e. precision. In contrast to the linearity error the range noise is dependent of both the object range and the object reflectivity. Thus, characteristic errors of a distance measurement system, the additive constant and the scale factor, should be eliminated by calibration.

The calibration procedure of the distance measurement system in the 'static mode' includes several targets which differ in reflectivity. The selection of different targets are limited to three reflectivity values, cf. Figure 3.8:

- reflectivity 90% (white)
- reflectivity 60% (grey)
- reflectivity 20% (dark grey)

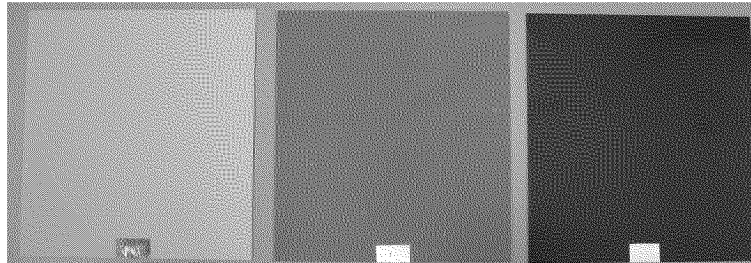


Figure 3.8: Targets with varying reflectivity values used for investigating the distance measurement system. Left target: reflectivity 90% (white), middle target: reflectivity 60% (grey), right target: reflectivity 20% (dark grey).

The targets are painted with a white colour defining a reflectivity of $\approx 95\%$. Subsequently, the targets are covered by transparent papers with defined reflectivity. Thus, the given values are approximations and represent a system-related reflectivity, cf. Section 3.5.1.

The targets are mounted on the telescope of a theodolite (Kern DKM1). The telescope can be aligned precisely in the vertical direction as well as in the horizontal direction. Furthermore, the telescope can be oriented in user-defined directions for aligning the targets in different ways with respect to the laser beam, representing different angles of incidence, cf. Section 3.5.2. The theodolite Kern DKM1 used for the alignment of the targets with respect to the laser beam with a target mounted on the telescope can be seen in Figure 3.9.

The system consisting of the theodolite and the target is calibrated with respect to an additive constant and the uprightness between the top of the target plane and the center of the theodolite. The system is recognized as being constructed accurately without a significant additive constant. Furthermore, the planes used as targets were proven as being flat to a maximum deviation of 0.5 mm.

³Range calibration is defined by applying an error correction function or a look up table derived by residuals between nominal distances and measured distances, i.e. mean values, as defined by several calibration procedures [Mettenleiter, 2004].

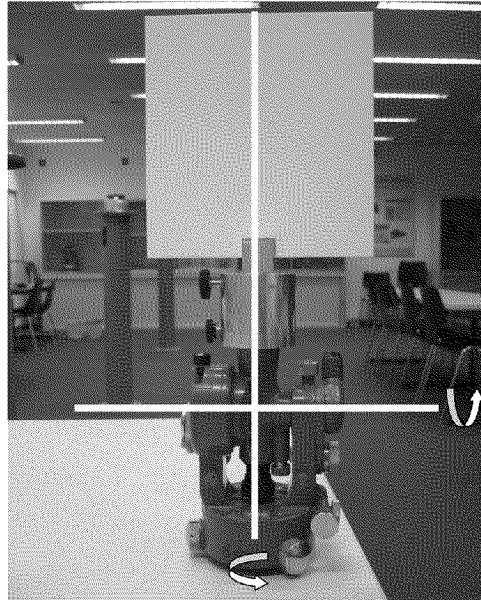


Figure 3.9: Kern theodolite DKM1 used as a target holder for investigating the distance measurement system of the laser scanner. The telescope is turned upright and the target planes can be attached.

The calibration of the distance measurement system in the ‘static mode’ was performed on the calibration track line. The laser scanner was set up on the observation pillar located in extension with the track line (pillar number 2000, cf. Figure 3.4). The different planar targets were mounted on the test trolley by using the theodolite DKM1, cf. Figure 3.9, including centering and levelling. The targets were aligned in such way that the laser beam was horizontal and hit the target plane at a normal angle. Therefore, the theodolite can be rotated and the target can be shifted in height. Based on this alignment, the targets were oriented with respect to the laser beam using the theodolite. This is of importance with respect to the influence of the angle of incidence on the distance measurement system, cf. Section 3.5.2. The calibration procedure is shown schematically in Figure 3.10. All investigations of the distance measurement system in the ‘static mode’ were performed with the following settings⁴:

range mode : far
 filter frequency : 125,000 points/sec
 points per line : 10,000

The chosen range mode and filter frequency correspond to the common settings applied during the ‘scanning mode’⁵. The number of points per line influences the mean value and the empirical standard deviation, i.e. precision, since these parameters are based on the number of acquired measurements.

Repeatability

The repeatability of the distance measurement system allows for the evaluation of systematic effects concerning the additive constant and the scale factor. The determination of such parameters are only meaningful if they are repeatable. Therefore, the same measurement procedure is repeated within a short time and is based on the identical measurement setup. The target that was used is white in colour and is defined by a reflectivity value of 90%. The laser beam hits the target orthogonally.

⁴It is of importance to refer to the settings made for the distance measurement. This is especially the case for the range mode and the filter frequency as they may influence the distances to be measured.

⁵The filter frequency depends on the selected scanning modes. The frequency goes from 125,000 points/sec for the scanning modes ‘preview’ and ‘middle’ to over 250,000 points/sec in the mode ‘high’ and up to 500,000 points/sec for the scanning mode ‘superhigh’

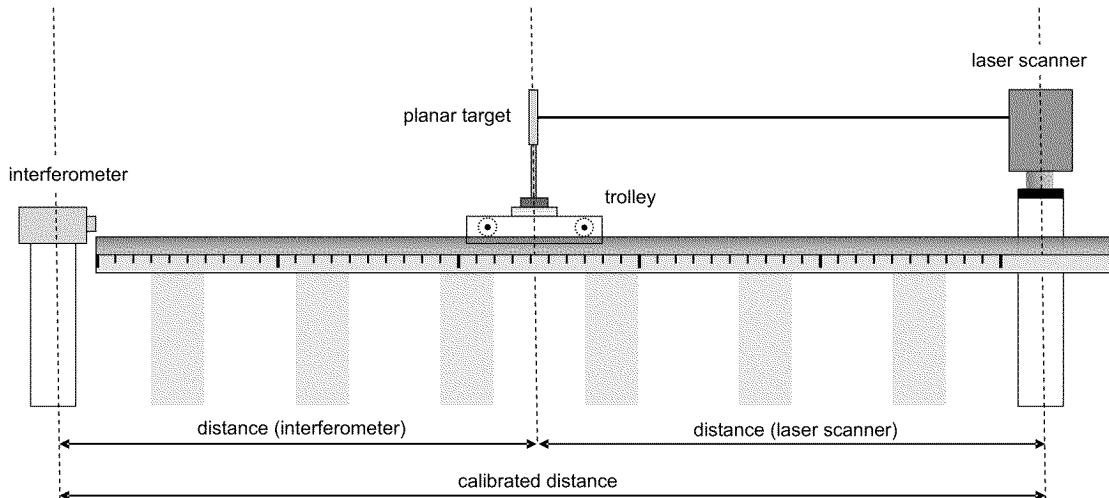


Figure 3.10: Calibration setup for the distance measurement system in the 'static mode' of the laser scanner using planar targets.

Figure 3.11 shows the deviation between the derived mean value acquired by the laser scanner and the nominal value provided by the interferometer. The results are three lines representing the accuracy of the distance measurement system. First, an overall and reproducible systematic trend caused by an additive constant and a scale factor cannot be seen. Second, specific sections showing a similar behaviour can be assumed but without trustworthy results. Calibration curves based on harmonic oscillations can be derived and can be applied for improving the curves of the mean values. However, the more important aspect is that all three lines are within ± 5 mm according to the manufacturers' specifications on the linearity error. These results were confirmed by additional investigations.

It should be mentioned that the calibration curves are dependent on several parameters, e.g. the reflectivity and the angle of incidence. Calibration curves have to be defined regarding these parameters for the sake of completeness. In previous investigations, multipath effects, which were caused by the background, were seen, cf. [Ingensand et al., 2003]. The divergence of the laser beam enlarged the footprint to the point of overtopping at a specific distance. To avoid these affects in following investigations, a velvet curtain was installed in the background. Furthermore, an upgrade of the laser scanner in February, 2004 narrowed the beam divergence.

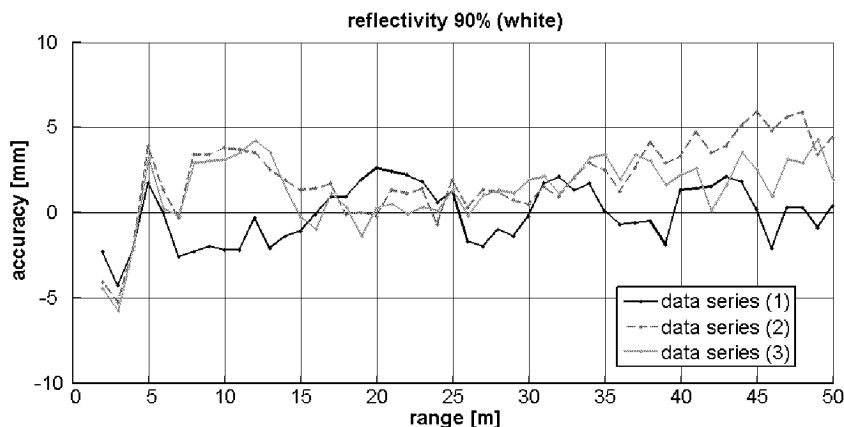


Figure 3.11: Repeatability of the distance measurement system based on the 'static mode'. Three repeated data series on a white target (reflectivity 90%) are plotted and refer to the same setup.

Accuracy

The accuracy of the distance measurement system based on different reflectivity values for the targets has already been analyzed. The question is is there a systematic deviation of the distance measurement system for a specific reflectivity?

The results for specific reflectivity values are shown in Figure 3.12. The curves are similar to the results obtained by the investigation for repeatability. The conclusion is that the reflectivity does not influence the mean value of the distance measurement system. Furthermore, the accuracy meets the requirement of the manufacturer for covering the full measuring range of 50 m. However, the corresponding mean values do not mean that the noise of the measurements, i.e. the precision, is also similar.

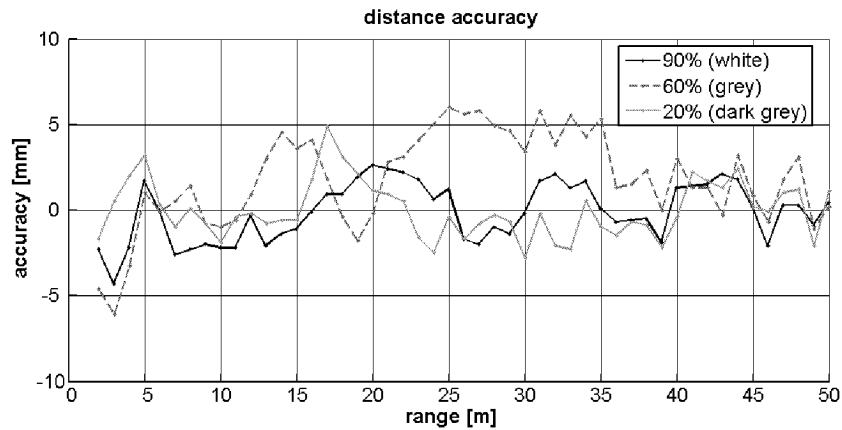


Figure 3.12: Accuracy of the distance measurement system based on the ‘static mode’. The targets used have different values of reflectivity, namely 90% (white), 60% (grey) and 20% (dark grey).

Precision

The precision defines the noise of a sensor. In terms of the laser scanner, the precision of the distance measurement system gives an estimation for the empirical standard deviation of a single distance measurement. The precision is a reliable parameter since it defines the imprecision of a single shot that occurred during a scanning process and helps to assess each single point in the point cloud.

Figure 3.13 shows the standard deviation over the measuring range of 50 m for the three targets with different reflectivity values. It can be seen that up to a range of 10 m, the curves are close to each other with a precision of less than 2 mm. As the lines diverge, a difference between the reflectivity values is clearly visible. Since the standard deviation represents 1σ noise, the area covering each measurement, i.e. 99.9%, has to be multiplied by a factor of three. The increasing noise is correlated to the decreasing intensity in the reflected laser beam and defines the signal-to-noise ratio (SNR). Comparing these results to the specifications of the manufacturer, it can be concluded that the specifications have been met, cf. Appendix B.

3.2.2 Scanning Mode

The investigation of the ‘scanning mode’ was performed on the calibration track line similar to the investigation of the ‘static mode’. The targets used for scanning had the property of a definitely defined center. This is of importance for deriving horizontal distances between the laser scanner and the target. These distances are then compared with nominal distances since the horizontal distance cannot be acquired directly. In Section 3.1.5, spheres were introduced as being well-suited for laser scanning since they have a well-defined center point.

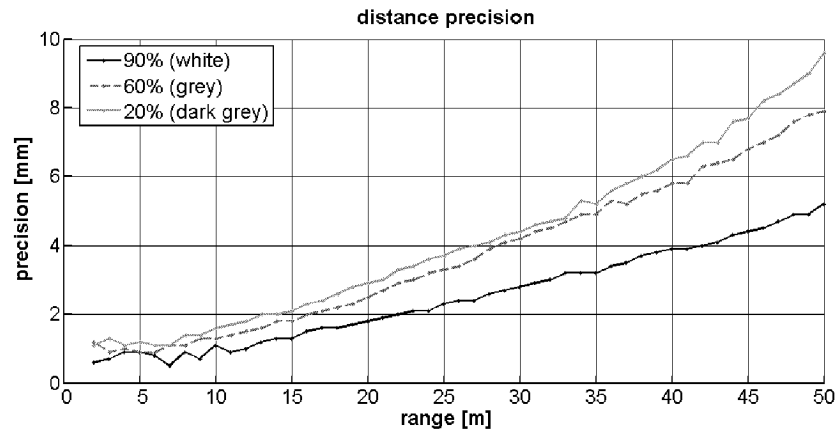


Figure 3.13: Precision of the distance measurement system based on the 'static mode'. The targets used have different values for reflectivity, namely 90% (white), 60% (grey) and 20% (dark grey).

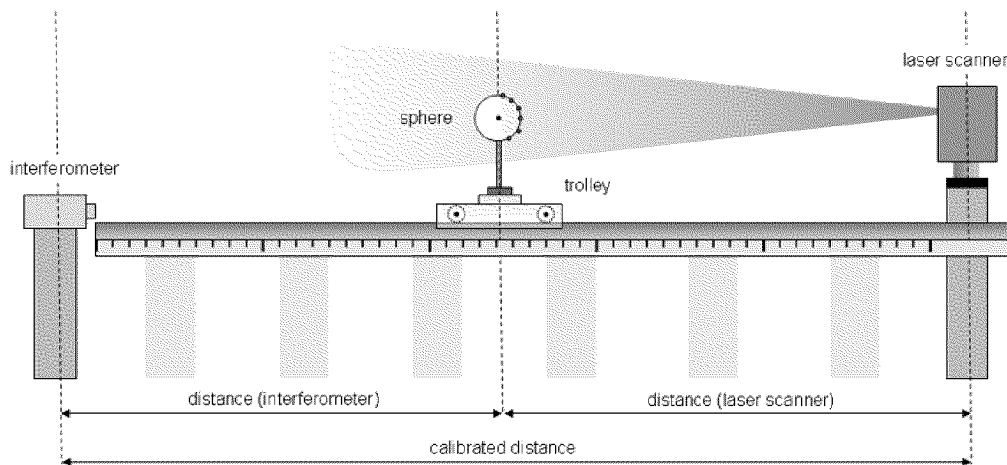


Figure 3.14: Calibration setup for the distance measurement system in the 'scanning mode' of the laser scanner using spheres.

The calibration procedure is performed in all provided scanning modes: 'superhigh', 'high', 'middle', and 'preview'. These modes differ in the resolution of the point cloud since the point-spacing in the horizontal and vertical directions decrease from 'superhigh' to 'preview'. For the scanning process, the operator can choose additional settings to modify the range mode⁶ and the noise⁷. The area containing the sphere to be scanned is selected manually based on a preview scan acquired by the lowest resolution, which is made within a short time. The laser scanner was set up on the observation pillar, which is located in extension with the track line (pillar number 2000, cf. Figure 3.4). The spheres were positioned by the trolley along the calibration track line and the nominal distances were provided by the interferometer to high degree of accuracy, cf. Figure 3.14. The results obtained by this investigation help to assess the distance measurement system regarding:

⁶Referring to Section 3.2 one can choose between the range modes, 'close' and 'far'. What has been recommended is the range mode, 'far', since this mode operates with the full laser power. On the contrary, the mode 'close' only uses half of the laser power

⁷The noise differs between 'default' and 'low'. In the operating mode 'low', the scan time increases and the noise decreases in accordance with the manufacturers' specifications. In the investigation procedures, no significant improvement concerning the quality of the point clouds have been seen.

- systematic effects
- differences between the common three scanning modes 'superhigh', 'high' and 'middle' (the lowest resolution is not considered since it is only adapted for preview scans)
- influence of the knowledge of parameters defining the geometry of objects, e.g. diameter of a sphere

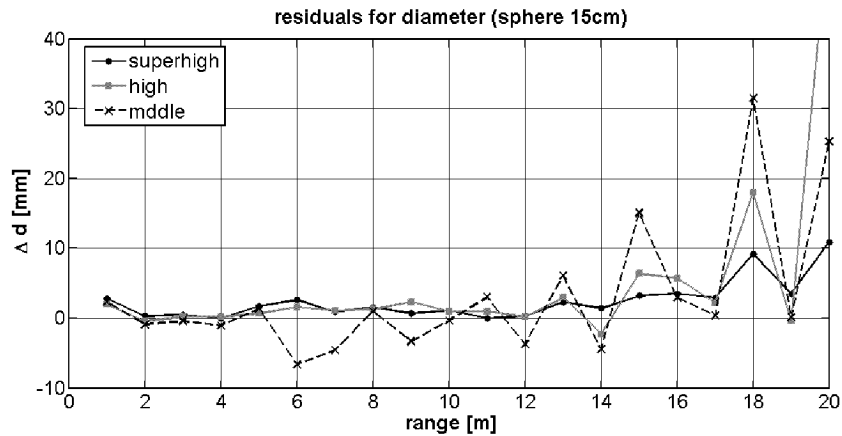


Figure 3.15: Residuals between estimated diameter and nominal diameter of a sphere (15 cm) for the scanning modes 'superhigh', 'high' and 'middle'.

First, the 'scanning modes' are assessed by comparing the computed diameter of the two different spheres against its nominal diameter in different ranges. The results of the sphere with a diameter of 15cm are plotted in Figure 3.15. It can be seen that the estimated diameter based on the scanning mode 'superhigh' fits best followed by 'high' and 'middle'. This result agrees with the assumption that the point density influences the quality of the fitted sphere, especially at farther distances. Thus, the diameter value worsens as the range approaches 15 m and beyond. The scanning modes 'superhigh' and 'high' are well-adapted for precise modeling operations based on the acquired point cloud of up to 15 m concerning the geometry of the derived object. The results obtained by the sphere with a diameter of 12 cm confirm these conclusions.

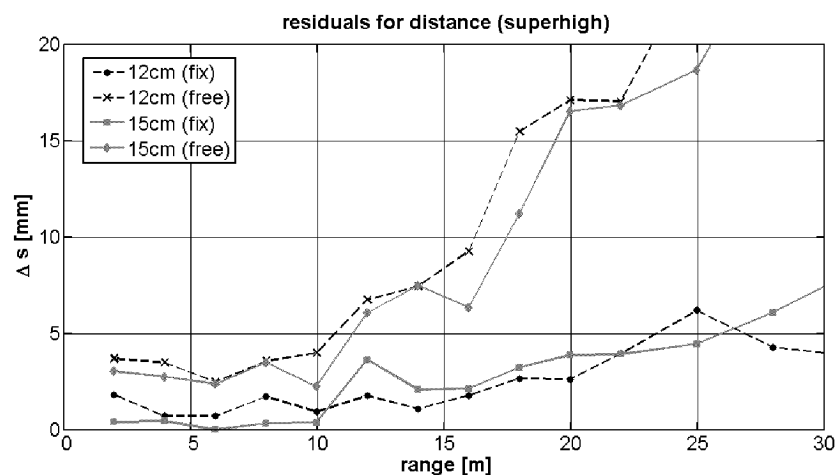


Figure 3.16: Residuals between derived horizontal distances and the nominal distances in the scanning mode 'superhigh'. The center point of the spheres are computed by a 'free' adjustment and a 'fix' adjustment.

Second, the influence of the nominal diameter of the spheres is estimated by comparing the distances to the center points derived by adjustments using the diameter as unknown, termed 'free' adjustment, and using the diameter as well-known constant, termed 'fix' adjustment. Figure 3.16 shows the deviations between

the derived horizontal distances to the computed spheres and the nominal horizontal distances provided by the interferometer for the ‘free’ adjustment and for the ‘fix’ adjustment and for both diameters of 12 cm and 15 cm. The point cloud, from which the spheres were calculated, were acquired by the scanning mode ‘superhigh’. The figure shows that the results obtained by ‘fix’ adjustment are much better than these obtained by ‘free’ adjustment. It can be assumed that the results of the ‘free’ adjustment can be improved by applying an additive constant because all distances are 3 mm to 4 mm to short⁸. The deviations increase significantly for the ‘free’ adjustment from 10 m and thus agree with the results of the diameters comparison. The results based on the scanning modes ‘high’ and ‘middle’ confirm the findings. Considering the ‘free’ adjustment, the range from which the deviations grow strongly decreases from 10 m up to several meters.

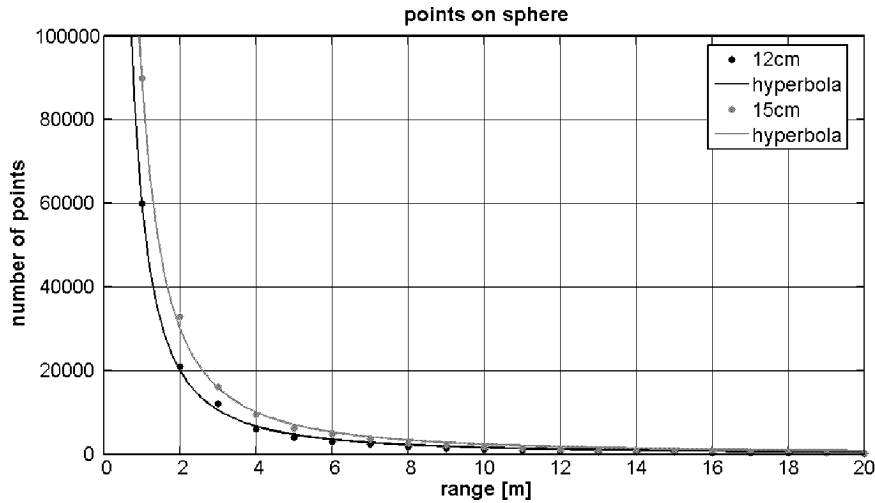


Figure 3.17: Development of the number of points defining a sphere acquired by scanning at different ranges. Spheres with diameters of 12 cm and 15 cm were scanned by the scanning mode ‘superhigh’. The curves define a hyperbola.

The spheres to be modeled are based on a point cloud which vary in the quantity of points. The quantity of the laser points decreases with the range and with the scanning modes from ‘superhigh’ to ‘preview’. In Figure 3.17 the number of points belonging to the spheres with 12 cm and 15 cm are shown and include the corresponding adjustment hyperbolae for the scanning mode ‘superhigh’. The adjustment hyperbolae are based on the mathematical formula [Bronstein and Semendjajew, 1999]:

$$f(x) = a \cdot x^b. \quad (3.5)$$

It can be seen that the number of points decreases rapidly according to the angle increment of the horizontal and the vertical encoder. The parameters of the adjustment hyperbola are summarized in Table 3.2. Therefore, the power b of both hyperbolae fit each other, which means the gradients of the lines are identical and the hyperbola decreases similarly. The scale factor a states for the number of points according to the range of 1 m, which have to be different for the spheres because of the different diameters. Considering the other scanning modes, ‘high’ and ‘middle’, the number of points is lowered by a factor of four and sixteen, respectively. This reduction in the number of points is based on a sub-sampling, which means only each n^{th} pixel in the horizontal and vertical directions is stored depending on the highest angle resolution. For the scanning mode ‘high’, the sub-sampling is $n = 2$ and for the scanning modes ‘middle’ and ‘preview’, the sub-sampling is $n = 4$ and $n = 16$, respectively. Thus, the number of points hitting a sphere and the maximum distance for scanning a sphere can be estimated.

⁸Since the spheres to be scanned are not only aligned in the x-direction or in the y-direction with respect to the local scanner system the resulting Cartesian coordinates of the spheres based on the azimuth and the horizontal distance corrected by the additive constant has to be calculated. This procedure can be applied also on slope distances in 3D-space.

Table 3.2: Parameters of the hyperbola showing the development of the number of points belonging to the sphere according to the scanning mode 'superhigh'.

Sphere Diameter [m]	Scale Factor a	Power b
12 cm	60,320	-1.591
15 cm	90,590	-1.587

Quantity is not the only aspect of importance. The quality also has a strong influence since the quality defines the geometry of the objects. The following Figure 3.18 shall demonstrate the importance of both the quantity and the quality of the point cloud.

Depending on the handling of the point cloud, the appropriate scanning mode has to be chosen carefully. For documentation purposes the scanning modes 'middle' and possibly 'preview' provide the necessary and desired information. In addition, if a high degree of accuracy and precision is of importance, then the scanning modes 'high' and 'superhigh' have to be used. The range for scanning objects, e.g. spheres, has to be limited according to the accuracy. The knowledge of the parameters defining the geometry of objects improve the accuracy of distances significantly. Based on the desired resolution of the point cloud and the mean range to the object, the most appropriate scanning mode should be selected. However, more points and a denser point cloud do not mean a better accuracy. This is especially the case if the point spacing is smaller than the noise of the point cloud. Furthermore, other parameters influence the quality of the point cloud considerably (cf. Section 3.4 and Section 3.5).

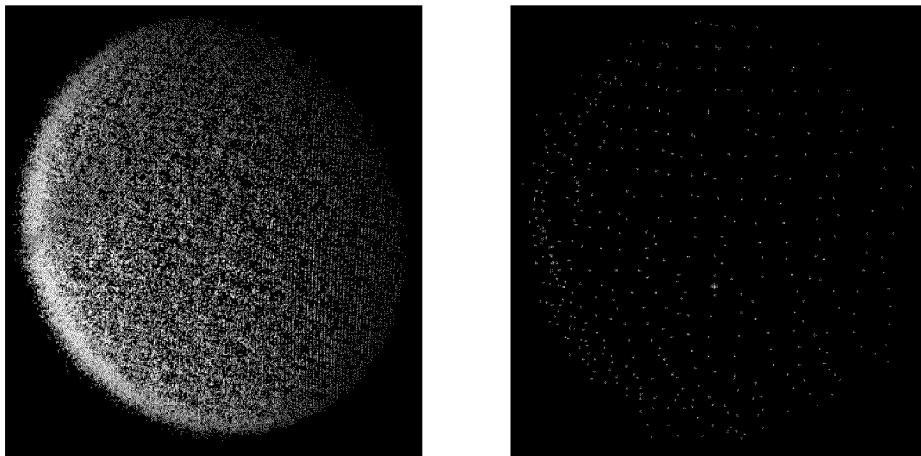


Figure 3.18: Points on a sphere with a diameter of 15 cm in a range of 2 m (left) and 19 m (right) acquired by the scanning mode 'superhigh'.

3.2.3 Long-Term Stability

The distances provided by the laser scanner can vary over a long time since internal heating effects lead to changes of the modulation frequency, cf. Section 3.2.4, or other internal and/or external influences, e.g. atmospheric influences, cause variations in the distance. Thus, the stability of the phase measurement system can be assessed.

For the investigation of the long-term stability, the laser scanner and targets with different reflectivity values attached on the theodolite DKM1 were installed on two observation pillars. The distance between the two pillars was approximately 3 m. Three targets with reflectivity values of 90 %, 60 % and 20 % were used. The observation period covered 3 h by a measurement interval between two distance measurements of 1 min.

The results of the derived distances as well as the precision are shown in Figure 3.19. The settings of the distance measurement match the settings chosen for the investigation of the distance measurement in the 'static mode'. The results can be interpreted as follows:

- Reflectivity values influence the distance detected by the laser scanner.
- Distances are not constant within the observation period and vary within the range of millimeters.
- Standard deviations show a constant precision within the observation period. The less the reflectivity, the worse the precision, according to SNR.

In summary, the long-term stability showed no systematic effects and no correlations due to thermal heating effects. The amplitude of the distance variation is about 2 mm for each reflectivity. Surprisingly, the offsets of the distances for the different reflectivity values are of several millimeters. However, the investigation of the 'static mode' concluded that a variation of several millimeters may be present, cf. Figure 3.12.

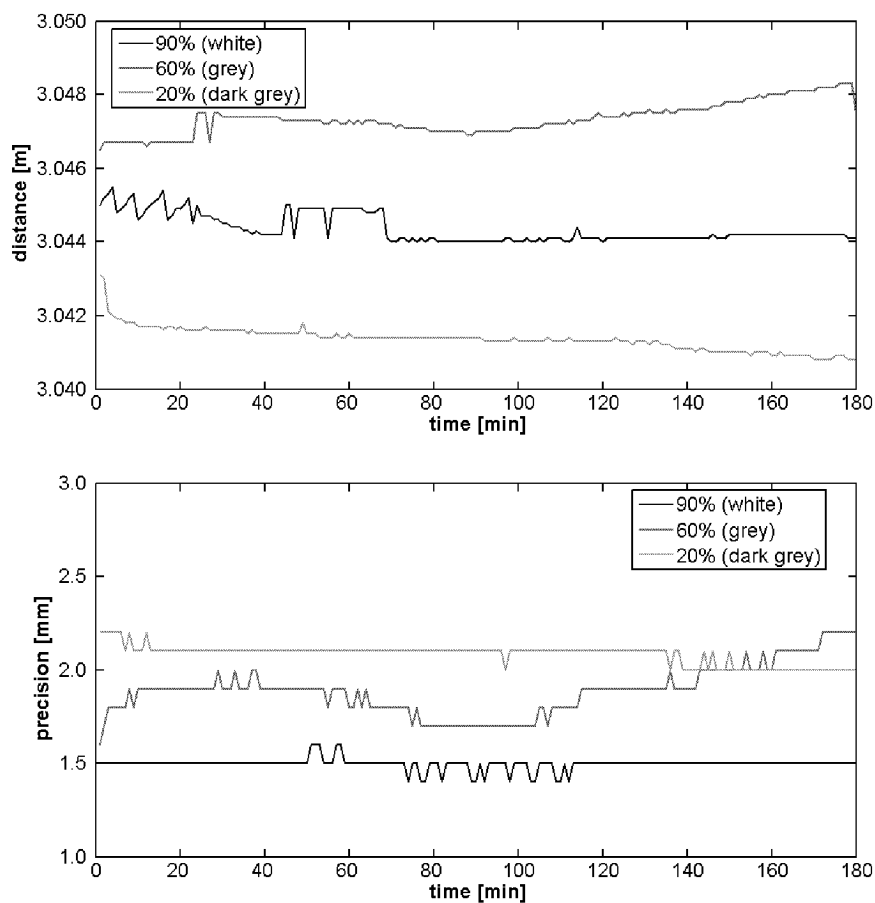


Figure 3.19: Development of the distance measurement system over a time period of 3h. The variations of the distances (top) and the variations of the precision (bottom) are shown.

3.2.4 Frequency Stability

The determination of distances is based on the modulation of carrier frequencies, cf. Section 3.2. A variation in the frequency directly influences the distance measurement. The variation can be of two different types: a long-term constant deviation of the real frequency to its nominal frequency and a short term variation.

The first one has to be proven by making periodic distance calibrations, called scale factor, and are caused by the oscillator. The second one can have different reasons that are caused by the environment such as temperature changes inside and/or outside the laser scanner.

Variations in frequency results in variations in the distance measurements. However, it is not possible to distinguish between variations in distances and variations in the frequency because several parameters interfere with each other and lead to distance variations, e.g. additive constant, scale factor, atmospheric conditions, properties of the target (such as colour, material, roughness), angle of incidence. Thus, the determination of frequency variations has to be done directly by using an electronic unit for frequency measurements, cf. Section 3.1.4.

The important frequency for the resolution of the distance measurement system is the modulated frequency of the fine channel component, i.e. high frequency signal 'hfs'. Thus, the investigation is focused on this modulation frequency. In the experimental setup, the laser beam is aligned towards the diode, the signal of the frequency is detected and the real frequency is derived, cf. Figure 3.6. The investigation was performed within an observation period of nearly three hours with a sampling interval of one minute. One assumes a time-dependent and temperature-dependent behaviour. Thus, the temperature inside the laser scanner is recorded additionally. The temperature of the environment is constant because the investigation was carried out in an air-conditioned laboratory.

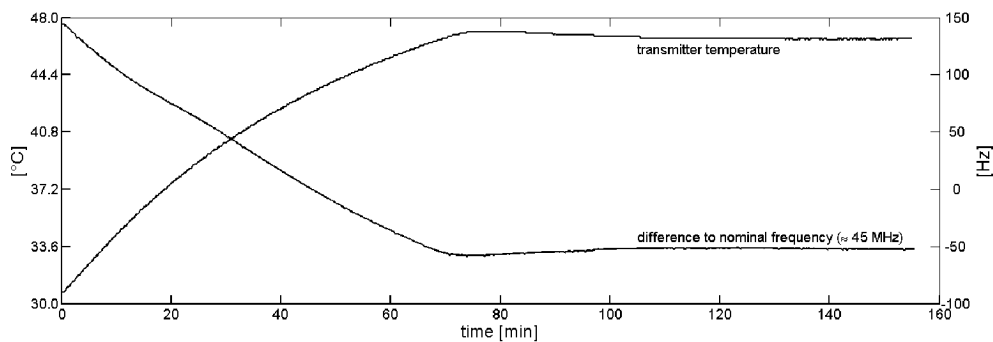


Figure 3.20: Development of the frequency of high frequency signal 'hfs' and the internal temperature of the laser scanner.

Figure 3.20 shows the time variations in both the modulation frequency 'hfs' and the internal temperature of the laser scanner, i.e. transmitter temperature. First, the deviations of the 'hfs' to the reference frequency can be seen. Second, the 'hfs' reaches a constant frequency after nearly two hours in operation and shows a deviation to the nominal frequency of nearly 50 Hz. Third, the behaviour of the internal temperature of the laser scanner correlates to the frequency behaviour: an increasing temperature leads to a decreasing deviation between real and nominal frequency, that means the real frequency is also increasing because the difference to the nominal frequency is calculated by subtracting the real frequency from the nominal frequency, and vice versa. The nominal frequency is defined by $f_{\text{hfs}} = 44.781250$ MHz.

Based on the given nominal frequency f_{hfs} and the real frequency f a scale factor m_f for the correction of a distance measurement caused by the difference of the real frequency to the nominal frequency can be derived with [Joeckel and Stober, 1991]

$$m_f = 1 + \frac{f_{\text{hfs}} - f}{f}. \quad (3.6)$$

Applying this formula to all acquired real frequencies of the modulation frequency 'hfs' one can achieve a maximum scale factor of 3.2 ppm. The constant frequency after two hours shows a value of -1.2 ppm. Considering the working range of the laser scanner of 50 m, the differences of the modulation frequency result

in a maximum distance error of less than 0.2 mm. Thus, the deviation of the modulation frequency of the fine channel component to its nominal frequency does not influence the distance measurement significantly and is negligible.

3.3 Angle Measurement System

The angle measurement system provides the missing two pieces of information in addition to the distance that are necessary in the derivation of 3D coordinates. The investigation of the angle measurement system regarding accuracy and precision have to be carried out by experimental setups that are not influenced by the other errors of the laser scanner. Since the angle measurements cannot be read directly, the required information regarding angle values have to be derived based on the supported measurement elements of Cartesian coordinates. The laser beam can be aligned manually towards a target and the angle values can be read. However, this alignment is difficult and does not provide sufficient precision. Furthermore, a real scanning procedure is more appropriate to assess the angle measurement system since the quality of the angle measurement system achieved during a scanning process is of interest. In the following, a single measurement refers to one scan of a sphere and a mean value is based on several single measurements, i.e. several scans of a sphere.

Generally, spheres were used for the investigation procedures and were scanned in different scanning modes. Based on the acquired point cloud, the center points of the spheres can be derived⁹. Based on the Cartesian coordinates of these center points, the spherical coordinates can be easily calculated. Thus, the horizontal angles and the vertical angles can be assessed. Furthermore, the distance measurement system has no influence on the angle measurement system because the horizontal angles and the vertical angles do not change if the distance is varying. Also other instrumental errors, e.g. error of collimation axis, error of horizontal axis, i.e. tilting axis, were eliminated by performing measurements in two faces analogous to a theodolite.

The **precision** of the angle measurement system is defined as the closeness of repeated angle measurements regarding the local scanner system or, how precisely the angles of the laser scanner fit to each other. The precision of the angle measurement system is assessed by repeated measurements to a sphere. The resulting spherical coordinates to the center point of this sphere are analyzed by means of the empirical standard deviation of a single measurement (s_s) and the empirical standard deviation of the mean value (s_m). In addition, the **accuracy** of the angle measurement system is defined as the deviations of acquired angle measurements with respect to nominal angle values derived by a reference system. Therefore, the angle measurements are described by the angle differences between the horizontal and vertical angles of two targets. For assessing the accuracy of the angle measurement system, two different experimental setups were chosen.

Test Field of Observation Pillars

The first method uses the test field of observation pillars, cf. Section 3.1.3. The symmetric configuration of the pillars takes advantage of covering a full circle from the point of view of the center pillar. The experimental setup was chosen so that the surrounding pillars were occupied by spheres and the laser scanner was set up on the middle one, cf. Figure 3.21. The spheres as well as the laser scanner were levelled. Thus, the horizontal positions are accurately guaranteed. The vertical height of each sphere is influenced by the positions of the screws on the tribrach. For having the same offset of each sphere in height caused by using tribrachs, the screws of all tribrachs were set to the same position. This can be easily done by mounting each tribrach (supported by a target) on the same pillar and surveying the height with a theodolite. An offset of the tribrach in height can be corrected by moving the screws of the tribrach and shifting the target

⁹Here, the diameters of the spheres were used as well-known constants to achieve the best accuracy ('fix' adjustment).

vertically. Thus, the vertical positions are guaranteed with a sufficient accuracy (< 0.5 mm).

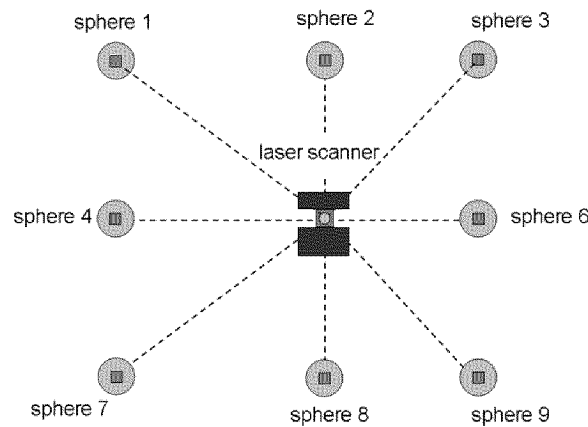


Figure 3.21: Experimental setup: test field of observation pillars for determining the accuracy of the angle measurement system. The laser scanner is set up on the center pillar and the spheres on the surrounding pillars (top view).

The spheres were scanned in all provided scanning modes varying from ‘superhigh’ to ‘preview’ in two faces. Cartesian coordinates of the center points were calculated and the spherical coordinates were derived. Spherical coordinates obtained by the measurement in two faces were averaged to eliminate typical instrumental errors, e.g. error of collimation axis, error of horizontal axis, i.e. tilting axis. Based on the resulting horizontal and vertical angles, the angle differences between two adjacent pillars can be computed, in horizontal and vertical directions. Overall, the laser scanner positioned on the center pillar is surrounded by eight other pillars. Selecting one pillar as a reference, seven angle differences between the selected one and the others can be derived. Thus, there are eight possibilities to choose from for the reference pillar. Overall, 7×8 angle differences in horizontal and in vertical direction can be used to calculate a mean value and the precision of the mean value to assess the accuracy of the angle measurement system.

Calibration Track Line

The second method uses the calibration track line, which has a well-known trajectory, cf. Section 3.1.1. The trolley including a sphere was positioned along the track line in specific positions and the sphere was scanned from the pillar in extension with the track line (pillar number 2000). Then, the center points of the spheres were derived according to the local scanner system. A coordinate transformation¹⁰ can be performed to compare the derived center points of each sphere with its nominal position with respect to the reference system of the calibration track line, cf. Figure 3.4. The resulting residuals can be interpreted as follows:

- *Residuals along the track line (x-direction):* accuracy of the distance measurement system
- *Residuals in transverse direction of the track line (y-direction):* accuracy of the angle measurement system of the horizontal direction
- *Residuals in vertical direction of the track line (z-direction):* accuracy of the angle measurement system of the vertical direction

The residuals, resulting from the transformation of coordinates, are expressed in metric values. The conversion of the metric values of the residuals, expressed in millimeter, to angles, expressed in degrees, is crucial

¹⁰The transformation can be done either as a complete 3D-transformation or as a separate 2D-transformation containing the xy -, the xz - and the yz -direction. The results of the residuals are identical, but the transformation parameters are different.

because of the short ranges between 1 m and 20 m due to the limited range to scan spheres, cf. Section 3.2.2. Disregarding the first three meters and averaging the angular values, a mean value and the precision of the mean value to assess the accuracy of the angle measurement system can also be provided in the horizontal and vertical directions. However, the linear alignment of the calibration track line is not well-suited for a 3D coordinate transformation, but provides an independent method for the investigation of the angle measurement system.

Thus, the mean values obtained by the two different experimental setups can be compared. The specifications of the manufacturer state that the accuracy for the angle measurement system of both the horizontal and the vertical encoders are within 0.02° (RMS).

3.3.1 Horizontal Encoder

The precision of the horizontal encoder of the angle measurement system is shown in Table 3.3. The precision of a single measurement (s_s) and the precision of the mean value (s_m) are also given. The precision of a single measurement shows good values for all scanning modes and can be assessed as sufficiently high. These values were derived by ten repeated measurements within the same experimental setup. The range to the sphere was approximately 3 m. The decreasing precision from the scanning mode 'superhigh' to 'middle' conforms with an increasing range to the sphere in the scanning mode 'superhigh', i.e. the precision decreases with increasing ranges. The quality and the quantity of the point cloud worsen with either the range or the scanning resolution.

Table 3.3: Precision for the horizontal encoder of the angle measurement system gained by repeated scanning of a sphere for the scanning modes 'superhigh', 'high' and 'middle'.

Scanning Mode	s_s [$^\circ$]	s_m [$^\circ$]
superhigh	0.001	0.0004
high	0.002	0.0007
middle	0.006	0.0020

The accuracy of the horizontal angle measurement system obtained by the method using the test field of observation pillars are summarized in Table 3.4. The mean value as well as precision of the mean values are based on all 7×8 combinations of the horizontal angle between two pillars. The table shows equivalent values of the accuracy for the scanning modes 'superhigh', 'high' and 'middle'. The precision shows that the results are reasonably.

Table 3.4: Accuracy for the horizontal encoder of the angle measurement system obtained by using the test field of observation pillars.

Scanning Mode	Mean Value [$^\circ$]	s_m [$^\circ$]
superhigh	0.011	0.002
high	0.011	0.002
middle	0.008	0.004

The residuals transversal to the calibration track line representing the y-axis for assessing the accuracy of the angle measurement system are shown in Figure 3.22. In the upper figure, the residuals resulting from the coordinate transformation of the local scanner system to the calibration track line system are plotted based on the scanning modes 'superhigh', 'high' and 'middle'. The sphere used has a diameter of 15 cm. The lower figure shows the absolute values of the residuals expressed in degrees. It can be seen that in all scanning modes nearly the same results can be achieved. The residuals are oscillating between $+2$ mm

and -2 mm, only in the scanning mode 'middle' do the residuals increase from ranges of more than 12 m. Considering the residuals in terms of degrees, it can be seen that the values do not exceed 0.01° with the exception of the first three meters, which is due to the unfavourable geometrical conditions for the translation from metric values to angular values in short distances.

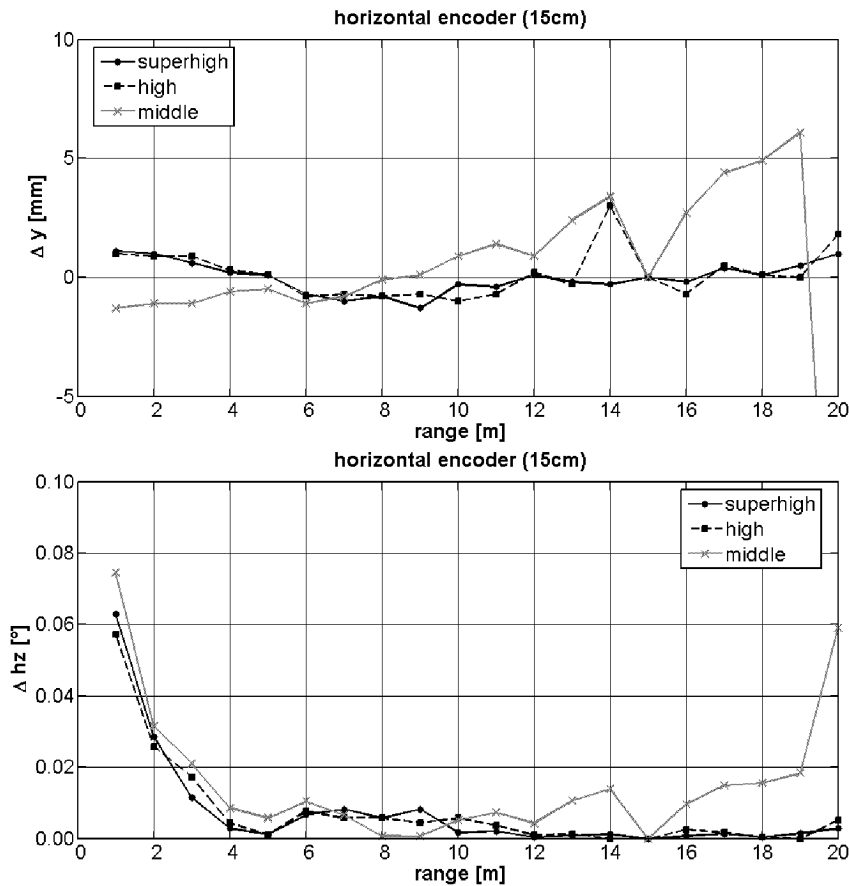


Figure 3.22: Residuals of the horizontal encoder based on the coordinate transformation from the local scanner system to the calibration track line system. Top: Residuals expressed in millimeters. Bottom: Absolute values of the residuals expressed in degrees.

Generally, it can be summarized that the accuracy for the horizontal encoder of the angle measurement system lies within $\pm 0.01^\circ$. The results obtained by the two different experimental setups fit each other and confirm the achieved accuracy independently. Considering the residuals expressed in millimeters, it can be stated that the accuracy of the horizontal angle measurement system is not as crucial as the distance measurement system. Furthermore, the specifications of the manufacturer are in agreement. The precision for the horizontal encoder is of a factor of ten better than the accuracy.

3.3.2 Vertical Encoder

The precision of the vertical encoder for the angle measurement system is shown in Table 3.5. The precision of a single measurement (s_s) and the precision of the mean value (s_m) are also given. The precision of a single measurement has acceptable values for all scanning modes and are sufficiently high. These values were derived from ten repeated measurements within the same experimental setup. The range to the sphere was approximately 3 m. The results are similar to the results derived for the precision for the horizontal encoder for the angle measurement system.

Table 3.5: Precision for the vertical encoder of the angle measurement system obtained by repeated scanning of a sphere for the scanning modes ‘superhigh’, ‘high’ and ‘middle’.

Scanning Mode	s_s [°]	s_m [°]
superhigh	0.001	0.0003
high	0.003	0.0011
middle	0.005	0.0017

The accuracies of the vertical angle measurement system gained by the method using the test field of observation pillars are summarized in Table 3.6. The mean value as well as the precisions are based on all 7×8 combinations for defining a vertical angle between two pillars. The table shows equivalent values for the accuracy of the scanning modes ‘superhigh’, ‘high’ and ‘middle’. The precision shows that the results are reasonable.

Table 3.6: Accuracy for the vertical encoder of the angle measurement system obtained by using the test field of observation pillars.

Scanning Mode	Mean Value [°]	s_m [°]
superhigh	0.008	0.004
high	0.010	0.002
middle	0.014	0.005

The residuals vertical to the calibration track line representing the z-axis for judging the accuracy of the angle measurement system are shown in Figure 3.23. In the upper figure the residuals resulting from the coordinate transformation of the local scanner system to the calibration track line system are plotted based on the scanning modes ‘superhigh’, ‘high’ and ‘middle’. The used sphere has a diameter of 15 cm. The lower figure shows the absolute values of the residuals expressed in degrees. It can be seen that in all scanning modes, nearly the same results can be achieved. The residuals are oscillating between +2 mm and –2 mm, only in the scanning mode ‘middle’ do the residuals increase from ranges of more than 12 m. Considering the residuals in terms of degrees, it can be seen that the values do not exceed 0.01° with the exception of the first two meters, which are due to the unfavourable geometrical conditions for the translation from metric values to angular values in short distances.

Generally, it can be summarized that the accuracy for the vertical encoder of the angle measurement system lies within $\pm 0.01^\circ$. The results obtained by the two different experimental setups fit each other and confirm the achieved accuracy independently. Considering the residuals expressed in millimeters, it can be stated that the accuracy of the vertical angle measurement system is not as crucial as the distance measurement system. Furthermore, the specifications of the manufacturer are in agreement. The precision for the vertical encoder is of a factor of ten better than the accuracy. Furthermore, the angular precision and the angular accuracy in the horizontal direction and in vertical direction are in the same order and fit each other.

3.3.3 Angular Resolution

The angle measurement system defines the vertical and horizontal resolution since the laser beam is deflected by the deflection unit in these two directions. The investigation of the angular resolution shall assess the manufacturer’s specifications.

The angular resolution is provided by using three different scanning modes: ‘superhigh’, ‘high’ and ‘middle’. A planar object aligned normal to the laser beam was scanned. For a specific distance a which is equal in the horizontal and vertical directions, the number of points in a horizontal and vertical profile

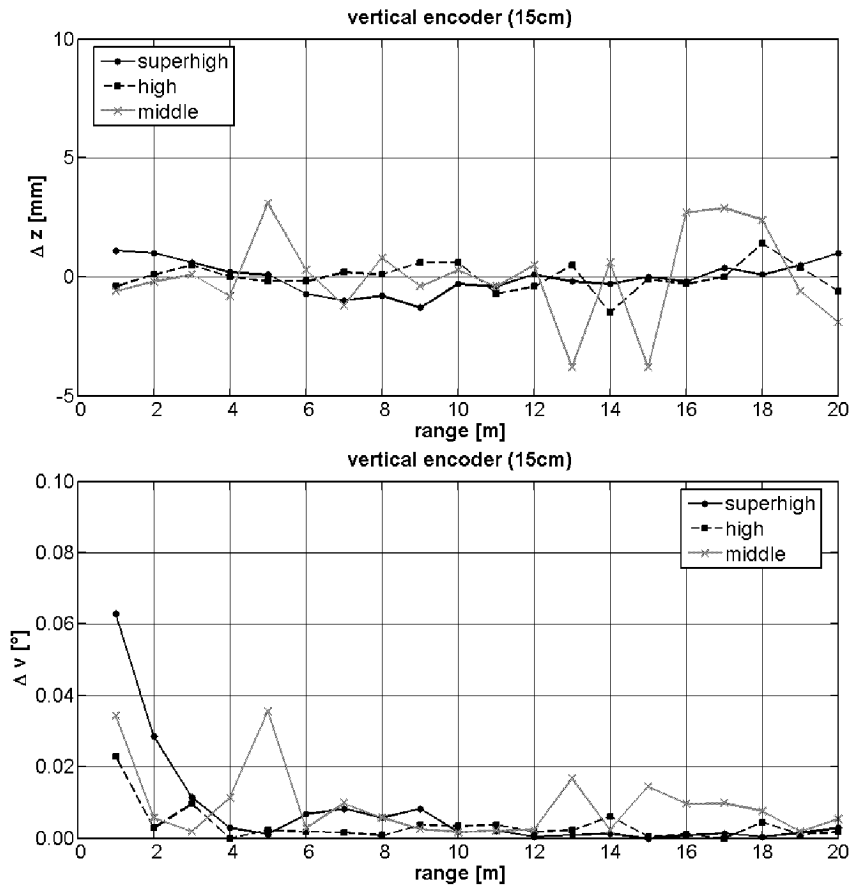


Figure 3.23: Residuals of the vertical encoder based on the coordinate transformation from the local scanner system to the calibration track line system. Top: Residuals expressed in millimeters. Bottom: Absolute values of the residuals expressed in degrees.

were counted. By knowing the range s to the plane, the angular resolution of the deflection system θ can be derived by

$$\theta = \arctan\left(\frac{a}{s}\right). \quad (3.7)$$

The distance s does not have to be known precisely because five centimeters do not influence the angular resolution significantly. In addition, the distance a has a larger influence. Thus, the distance a is not defined by the distance between two adjacent points. Rather, a mean distance is used by considering several points in a profile and the distance between the first point and the last point. Since the sub-sampling¹¹ directly influences the point spacing between two adjacent points, the sub-sampling has to be taken into account by deriving the angular resolution. Table 3.7 summarizes the results for the angular resolution obtained by the different scanning modes. It can be seen that they fit each other and that the result is an equal resolution of 0.017° in horizontal and vertical directions.

The manufacturer gives an angular resolution of 0.01° horizontally and 0.018° vertically. Considering the principle of specular reflection, a variation of the deflection mirror of α causes an angle variation of the laser beam of 2α . The horizontal angle increment is decreased to 0.018° to generate an equidistant raster of the point cloud.

¹¹Sub-sampling here means that only every i^{th} pixel (measured point) is stored and all other pixel are neglected. This is valid for both directions horizontally and vertically.

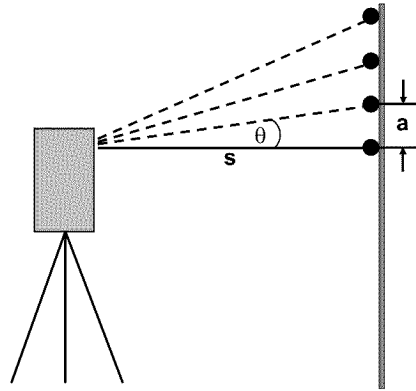


Figure 3.24: Determination of the angular resolution. The point spacing a in a distance s defines the angular resolution θ .

Table 3.7: Angular resolution of the deflection unit derived by three different scanning modes: 'middle', 'high' and 'superhigh'.

Deflection Direction	Parameter	Middle	High	Superhigh
horizontal	sub-sampling	4	2	1
	# points	6	13	7
	distance [mm]	40	45	12
	point spacing [mm]	6.7	3.5	1.7
	actual resolution [°]	0.068	0.035	0.017
	angular resolution [°]	0.017	0.018	0.017
vertical	sub-sampling	4	2	1
	# points	7	15	7
	distance [m]	43	50	11
	point spacing [mm]	6.1	3.3	1.6
	actual resolution [°]	0.062	0.034	0.016
	angular resolution [°]	0.016	0.017	0.016

The angular resolution is not only dependent on the deflection unit. The spot size defined by the beam divergence and the resulting footprint has also to be taken into account. The increment of the angular unit should not be smaller than the spot size since two adjacent footprints overlap each other. [Lichti and Jamtsho, 2006] introduced the effective instantaneous field of view (EIFOV) as a new parameter for defining the angular resolution of terrestrial laser scanners by considering both the angular resolution, i.e. sampling interval, and the spot size, i.e. laser beamwidth.

3.4 Instrumental Errors

This section discusses some of the major instrumental errors that can influence each single measurement. In contrast to the sections before, cf. distance measurement system and angle measurement system, the possible errors due to the mechanical realization of the laser scanner are investigated, e.g. the well-known instrumental errors of theodolites: eccentricities, wobble of rotation axes, error of collimation axis, and error of horizontal axis, i.e. tilting axis. This approach is valid since the working principle and design of the laser scanner corresponds to the working principle and design of theodolites and laser trackers.

3.4.1 Eccentricity of Scan Center

The ideal construction of a rotating instrument assumes that the real center of rotation corresponds to the ideal center of rotation. If there is a deviation due to mechanical imperfections, then an instrumental error is present. The laser scanner system to be calibrated has two different rotations: a primary rotation about an horizontal axis, i.e. tilting axis, and a secondary rotation about a vertical axis, i.e. rotation axis. In the following, an examination of the eccentricity of the laser scanner center is presented. In particular, two different aspects are discussed:

- the eccentricity of the vertical axis
- the eccentricity of the scan center

Influences caused by errors in the horizontal axis are discussed separately, cf. Section 3.4.4. All described investigations were carried out in such a way that errors caused by the horizontal axis do not influence the investigations. All objects to be scanned, e.g. spheres, were positioned horizontally and at the same height. Thus, errors resulting from the horizontal axis can either be eliminated or they have the same influence on all the object points. Possible errors caused by the distance measurement system, e.g. additive constant, scale factor, also have to be reduced from the measurements.

The objective is to verify that the laser scanner can be mounted on a tripod or on an observation pillar, like a total station. This means the laser scanner can be centered on a control point and the rotation center of the vertical axis corresponds to the center of this control point. Furthermore, the origin of the local scanner system has to conform with the rotation center. The setup of a laser scanner can be analogous to that of a total station. First, a tribrach is mounted on a tripod or on an observation pillar and is then levelled using a plate level, which is attached securely on the laser scanner. Second, an adapter plate is fixed onto the tribrach. Third, the laser scanner is installed on this adapter plate and is ready for use. The laser scanner and the rotation axes can be seen in Figure 3.25.

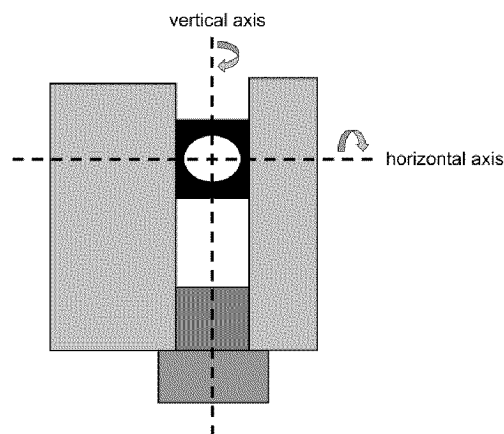


Figure 3.25: Principle of the laser scanner and the axes of rotation. The laser scanner has two axes of rotation: a primary fast rotation about the horizontal axis and a secondary slow rotation about the vertical axis.

Eccentricity of Vertical Axis

The investigation of the eccentricity of the vertical axis covers two aspects: the rotation has to be homogeneous, i.e. resulting in a circle, and the center point of this circle has to fit the nominal center of the control point on which the laser scanner was set up. This examination requires high precision regarding the surveying of a target that is mounted on top of the laser scanner and represents the rotation of the laser scanner.

Thus, the surveying has to be performed by the intersection from two viewpoints by using theodolites¹². The investigation was carried out in the test field of observation pillars. The base of the two viewpoints used is well-known because the coordinates of the observation pillars were surveyed with high accuracy and thus, well-known, cf. Section 3.1.3. The target mounted on top of the scanner was defined by a spike, representing a target, which is well-suited for angular measurements.

The laser scanner was rotated by discrete angles using the control software for the laser scanner¹³. The angle increment for the positions of the vertical axis was 45° . Thus, eight positions for the spike were surveyed. Based on these positions, two questions can be raised:

- Do the positions of the spike fit a circle?
- Does the center point of the circle correspond to the nominal position of the observation pillar?

The first question can be answered with an affirmative in that the positions of the spike do fit an adjusting circle, cf. Figure 3.26. Considering the residuals of the observations and the unknowns of the adjustment, including their accuracies, cf. Table 3.8 and Table 3.9, it can be concluded that the spike moved along a circle. This means that the rotation is homogenous and the laser scanner was well-levelled. A levelling error caused by non-exact levelling produces an error in such a way that the rotation about the vertical axis does not take place in a horizontal plane but rather in an inclined plane. Thus, the projection of the positions of the spikes would yield to an ellipse instead of a circle. Another error that is also conceivable is one that can influence the rotation behaviour: the wobble of the vertical axis, cf. Section 3.4.2. However, such an error has to be rather large before it influences the horizontal positions of the spike (an inclination of 4° causes an error of about 0.1 mm).

Table 3.8: *Residuals of observations.*

Data Point	Residuals v_x [mm]	Residuals v_y [mm]
1	0.01	-0.01
2	0.03	0.06
3	-0.01	-0.10
4	0.01	-0.06
5	-0.02	0.03
6	-0.01	0.02
7	0.00	0.06
8	-0.01	0.06

Table 3.9: *Unknowns of the adjustment including their precisions.*

		Value [m]	Precision [mm]
center point (real)	x	14.93038	0.02
	y	7.80710	0.03
radius	r	0.04286	0.23
center point (ideal)	x	14.93018	0.1
	y	7.80736	0.1

The second question can also be answered with an affirmative in that there was no significant offset in the real rotation center versus its ideal rotation center, cf. Table 3.9. The offsets in the x - and y - directions have

¹²The accuracy of distance measurements of total stations does not meet the required accuracy of tenths of a millimeter.

¹³The laser control software LRViewer and LRCServer by Zoller+Fröhlich allows the rotation of the laser scanner in a specific direction with a resolution of 0.01° .

values of 0.2 mm and 0.3 mm, respectively. Thus, this deviation between the real and ideal center points is nearly in the same order as the precision, i.e. standard deviation, of the ideal offset. In summary, the real rotation center fits the ideal rotation center.

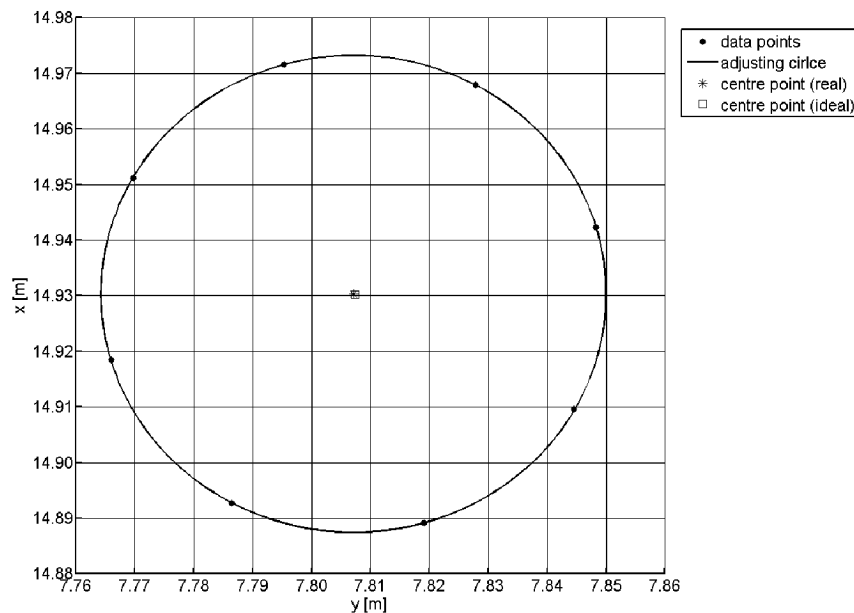


Figure 3.26: *Adjusting circle: The rotation center of the laser scanner fits to the ideal center and the data points fit to the adjusting circle.*

Eccentricity of Scan Center

The real physical center of an instrument has to coincide to its ideal center, otherwise offset parameters have to be taken into account. Disregarding this concept leads to an eccentricity of the real center, which causes a constant offset. Considering that the laser scanner captures the 3D environment, the eccentricity of the scan center has to be determined in three directions: x , y and z . Knowing the eccentricity eases the use of the laser scanner for repeated measurements because this sensor can be used analogous to a total station. Contrarily, if the eccentricity is not known or not determinable, the laser scanner has to be oriented completely in 3D during the measurement procedure. Normally, this is the common practice in laser scanning. However, there are some applications for which the knowledge of the eccentricity of the scan center is of advantage. In such applications, in-situ calibration is rarely possible and the eccentricity is of importance, e.g. deformation measurements, profile measurements of tunnels, scanning of environments defined by a lack of space. Thus, the knowledge of the eccentricity is not essential but helpful.

The eccentricity of the scan center can be defined by three parameters: a vertical offset in height and two horizontal offsets. The vertical offset is defined by the height difference between the internal scan center and the center of reference and the horizontal offsets are defined by the two horizontal differences between the internal scan center and the center of reference. The center of reference is represented by a well-known control point on which the laser scanner can be mounted.

The calibration of the eccentricity was performed by means of a 3D coordinate transformation (six parameter transformation without a scale factor). The laser scanner was set up on a control point defining the center of reference. Several surrounding control points represented by spheres were scanned. The center points of the spheres were calculated by an adjustment procedure using the 'fix' adjustment. Based on the derived center points of the spheres and the position of the laser scanner as the origin of the local scan-

ner system, a coordinate transformation can be applied using the coordinates of the control points. The residuals of the local scanner origin define the eccentricity of the scan center.

The results of several independent and different setups show that there is no significant eccentricity in the scan center. The residuals of the transformed local origin, defining the scan center, to the coordinate system of the control points are less than 1 mm for the horizontal position. Thus, the eccentricity is below the accuracy of the distance measurement system and the angle measurement system, respectively. Furthermore, a vertical offset was identified with a value of $0.222\text{ m} \pm 1\text{ mm}$ depending on the screws of the tribachs.

3.4.2 Wobble of Vertical axis

The wobble of an axis is an instrumental error, which is caused by variations in the axis during rotation. The ideal case is that the axis remains at a constant orientation during rotation, but in practice, motion of the axis leads to deviations from the ideal position. Causes for the wobble are either manufacturing imperfections resulting from mechanical deficiencies, e.g. defective mould of the bearing, or the mechanical components of the axis. The bearing can especially cause systematic effects and result in changes in the orientation of the axis, cf. [Matthias, 1961] and [Gerstbach, 1976].

Variations in the vertical axis are investigated by measuring the inclination of the vertical axis. Developing values for the orientation, i.e. the inclination of the vertical axis, allows conclusions to be drawn regarding the behaviour of the vertical axis. The raw data provided by the inclination sensor have to be pre-processed because these data include some systematic effects. First, possible systematic effects caused by the inclination sensor itself have to be identified [Löffler et al., 2002]: additive constant, linearity error¹⁴, long-term stability, temperature influences etc. Second, systematic effects caused by the rotation of the laser scanner are of importance: the influence of the levelling error, properties of the bearing, etc.

The inclination sensor used is the Nivel 20 of Leica Geosystems. The main characteristics of this sensor are [Leica Geosystems, 1988]:

- inclination resolution: 0.001 mrad (measuring range ± 2 mrad)
- linearity error: $\pm [0.005\text{ mrad} + 0.5\% \text{ of inclination value}]$

For acquiring the inclination data during rotation, the Nivel 20 is mounted on top of the laser scanner, nearly centrally in the vertical axis. The laser scanner has to be levelled so that the inclination sensor is within the measuring range during the rotation. A levelling error is present because absolute precise levelling cannot be performed due to imperfectness in the levelling procedure. However, the levelling error produced can be eliminated mathematically. The laser scanner is then controlled via the operating software LRCServer or LRViewer¹⁵. Within this software, the laser scanner can be rotated to discrete horizontal directions based on the local scanner orientation. The inclination of the actual vertical axis, in two perpendicular directions x and y , can be read by the inclination sensor, as controlled by NivelPlane¹⁶.

The goal of the wobble analysis of the vertical axis is to analyze whether there are systematic effects that can describe the wobble mathematically or whether there are no systematic effects and consequently, the vertical axis has no wobble. The assumption is that the wobble results in harmonic oscillations, which can be approximated by sine terms. Therefore, a Fourier analysis is applied on the inclination data to derive the frequency, or period, the amplitude, and the phase angle of a possible significant frequency causing the wobble of the vertical axis. The sampling theorem has to be taken into account when the Fourier analysis

¹⁴An inclination displayed by the inclination sensor should be proportional to the real inclination. The deviation between displayed and real inclination is defined as a linearity error of the sensor.

¹⁵LRCServer and LRViewer are software for operating and controlling the laser scanner, both provided by Zoller+Fröhlich GmbH.

¹⁶NivelPlane is a software tool for controlling the Nivel20 provided by Leica Geosystems

is applied to a data series [Taubenheim, 1969]. The Nyquist frequency f_{nyq} defines the maximum frequency based on the sampling interval Δt , which can be detected by

$$f_{nyq} = \frac{1}{2\Delta t}. \quad (3.8)$$

This means the real signal can only be detected if at least two samples fall within a full period of the wavelength. All frequencies higher than the Nyquist frequency cannot be detected and lead to aliasing effects thereby, defining the aliasing frequencies that superpose the frequency f [Taubenheim, 1969]:

$$f, 2f_{nyq} \pm f, 4f_{nyq} \pm f, \dots \quad (3.9)$$

An example of aliasing is given in Figure 3.27. It can be seen that based on the samples more than one sine curve fits to the data. All frequencies higher than the Nyquist frequency remain undetected and lead to aliasing effects. More information concerning Fourier analysis, Nyquist frequency, aliasing, etc. can be found in [Taubenheim, 1969] and [Welsch et al., 2000].

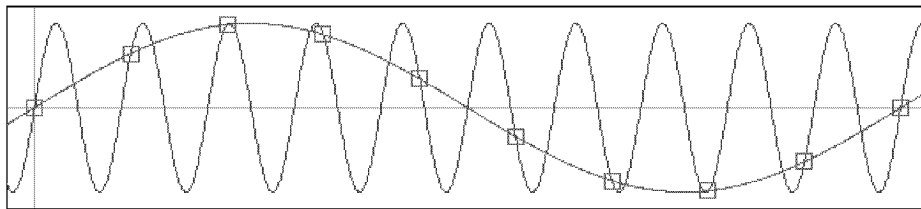


Figure 3.27: *Aliasing effects based on sampling: More than one sine curve fits to the samplings.*

The comprehensive investigations of the vertical axis wobble include several different experimental setups:

- (1) The laser scanner was mounted on a tribrach and then installed on a tripod and on an observation pillar.
- (2) The laser scanner was mounted on a granite table directly without using a tribrach.

During the investigation a counter weight was attached on one side of the laser scanner to balance the mass of the laser scanner (approx. 5 kg). The advantage is better symmetry in mass, but the disadvantage is that the counter weight increases the mass of the laser scanner considerably. The assumption is the balance weight influences the wobble of the vertical axis in a positive way. All different data series have two things in common: the sampling interval Δt varies between 5° to 30° and the sampling range varies between three to four full rotations according to 1080° and 1440° . Thus, a reasonable acquisition of data series is guaranteed assuming that the wobble causes harmonic oscillations with periods of 720° or shorter. The mathematical description of a possible wobble of the vertical axis requires both repeatability and reproducibility of the parameters characterizing the wobble: amplitude, frequency and phase angle. Comparing data series acquired by the same setup, one also finds that the levelling errors correspond with each other.

Analysis of Data Series

The acquisition of the inclination values of the vertical axis using the inclination sensor Nivel 20 includes two systematic effects, which have to be eliminated beforehand through application the Fourier analysis. These systematic effects are a balance error, on the part of the inclination sensor, and a levelling error, on the part of the laser scanner. The balance error can be applied to the data easily after a calibration procedure of the inclination sensor, e.g. two-face-measurements. This error, always present and produced

by an imperfect levelling procedure, can be eliminated in two ways. First, the levelling error results in a sine curve during a full rotation about 360° . This sine curve has to be calculated and the inclination data have to be reduced according to this sine curve. Second, the levelling error is derived by averaging the corresponding inclination data in the two faces. This means the data at position x and position $x + 180^\circ$ are averaged and result in a new inclination value that represents the levelling error. The absolute length of the original data is reduced by 180° . Both methods yield new inclination values that should be zero via the first method or a constant value, which defines the absolute levelling error, via the second method. However, if the data are different to these ideal cases, other errors in the vertical axis influencing the inclination are present, such as wobble of the vertical axis.

Before discussing the wobble of the vertical axis with one data series as an example, a summary of several different and independent data series will be examined with respect to the repeatability of the levelling error acquired by the inclination sensor. Therefore, the sine curve representing the levelling errors of the setups are calculated by using the Curve Fitting Tool Box provided by Matlab[®]. The results of three independent data series including three to four repeated measurements within each data series are discussed. The derived levelling error is based on the mathematical model of a sine oscillation [Matthias, 1961] and can be expressed mathematically [Bronstein and Semendjajew, 1999] by

$$f(x) = a \cdot \sin(f \cdot x + \varphi). \quad (3.10)$$

Table 3.10: Results of the calculation of the levelling error based on the data of the inclination sensor in the x -direction and in the y -direction for different setups (A, B, C) and repeated data series (1, 2, 3) within each setup.

Setup	Data Series	Amplitude a [mrad]		Frequency f		Phase Angle φ [$^\circ$]	
		x	y	x	y	x	y
A	1	0.401	0.432	1.029	1.025	305	218
	2	0.414	0.457	1.021	1.014	312	227
	3	0.414	0.444	1.012	1.014	317	229
B	1	0.476	0.490	1.028	1.022	123	37
	2	0.469	0.496	1.015	1.012	137	49
	3	0.462	0.506	1.010	1.007	140	53
C	1	0.271	0.209	0.989	1.005	344	256
	2	0.282	0.219	0.980	0.991	349	266
	3	0.286	0.212	0.978	0.990	352	267

Table 3.10 gives an overview of the calculated levelling errors based on the data of the inclination sensor in the x -direction and in the y -direction. The setups are independent from each other and the inclination data were acquired with different setups of the laser scanner, i.e. the laser scanner was set up with and without a tribach on an observation pillar and a granite table. The homogeneity in the data series within each setup can be seen and the levelling error appears to be repeatable because

- (1) the amplitudes a are nearly constant in the x -direction and y -direction within each setup,
- (2) the phase angles φ are nearly constant in the x -direction and y -direction within each setup,
- (3) the frequency of the levelling error corresponds with each other and is nearly 1.000, which means a period of 2π , and
- (4) the angle differences of the phase angles φ match up to 90° between the x -direction and the y -direction, according to the Cartesian coordinate system of the inclination sensor.

The inclination sensor produces reasonable data and the levelling error can be derived reliably. However, the question is whether a wobble of the vertical axis is present and whether this error is both repeatable and reproducible. Therefore, the analysis of one data series is described as an example. In this example, the laser scanner was mounted directly on a granite table without using a tribrach, cf. Figure 3.28. This setup represents an ideal setup because the granite table shows no deformations or vibrations during the rotation as tripods or tribrachs normally do.

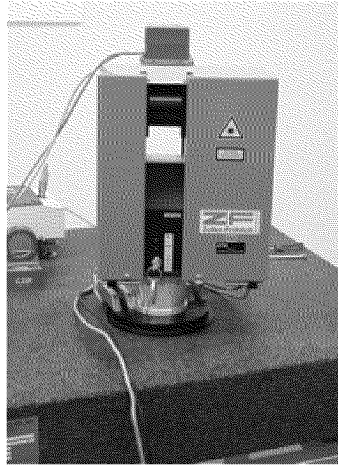


Figure 3.28: Laser scanner mounted on a granite table directly without using a tribrach. On top of the laser scanner the inclination sensor *Leica Nivel 20* can be seen.

Figure 3.29 shows the inclination data acquired by the inclination sensor *Nivel 20*. The levelling error is already eliminated from the inclination data and the left error shows a harmonic oscillation caused by the wobble of the vertical axis. The data for the x -direction and the y -direction show similar behaviour. First, it seems that the present harmonic oscillation is repeatable because the three data series for the x -direction and the y -direction fit each other. Second, the amplitudes of the harmonic oscillations are identical considering the x -direction and the y -direction. Third, the data series acquired in the x -direction of the inclination sensor are closer to each other than the data series acquired in the y -direction of the inclination sensor. Fourth, the amplitude of the first oscillation does not fit the amplitude of the other oscillations both in the x -direction and in the y -direction. Nevertheless, the acquired data series suggest that there is a significant frequency in the harmonic oscillation, which can be identified by a Fourier analysis.

Table 3.11: Results from the Fourier analysis of the vertical axis wobble. The values for the dominant frequency are summarized for both directions of the inclination sensor, x and y .

Data Series	Period [°]		Amplitude a [mrad]		Phase Angle φ [°]	
	x	y	x	y	x	y
1	180	180	0.133	0.115	176.2	60.5
2	180	180	0.119	0.113	178.7	61.2
3	180	180	0.121	0.117	182.1	61.2

The Fourier analysis, cf. Figure 3.30, shows a dominant frequency, which is identical in each data series and for both directions x and y of the inclination sensor. A more precise overview is given in Table 3.11, where the parameters of interest, i.e. frequency (period), amplitude and phase angle of the three data series, are summarized. It can be seen that also the parameters amplitude and phase angle fit relatively well with each other considering the x -direction and the y -direction, separately. The amplitude of the wobble acquired in the x -direction also corresponds to the amplitude of the wobble acquired in the y -direction. Unfortunately, the phase angle gives an indifferent impression: the phase angle derived by the x -direction should match to

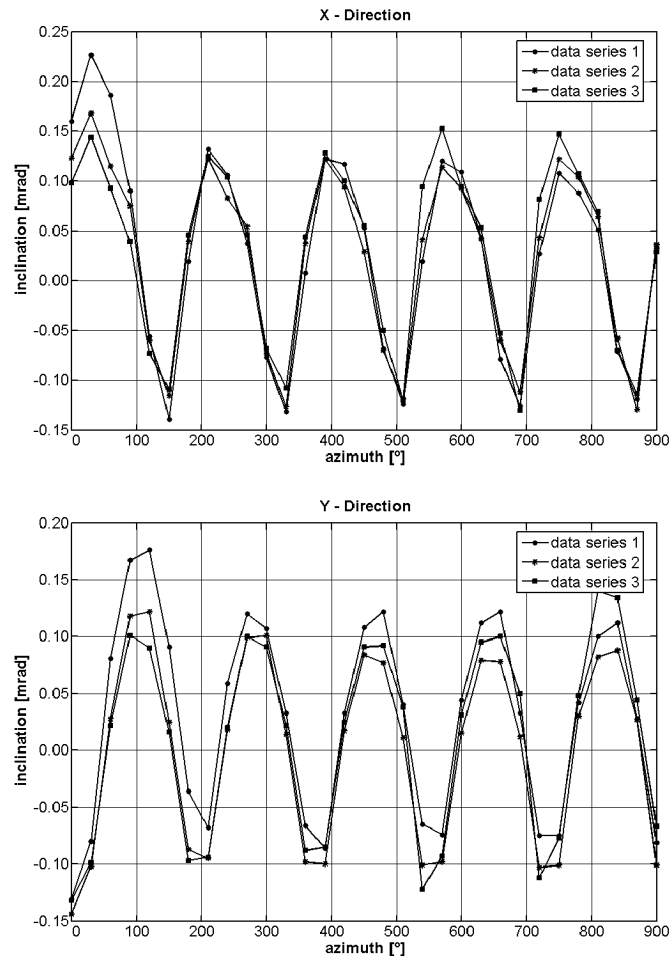


Figure 3.29: Inclination values of three data series acquired by identical setups and reduced by the levelling error; *x*-direction (top) and *y*-direction (bottom).

the phase angle derived by the *y*-direction, but there is an angle difference of approximately 120° between the *x*-direction and the *y*-direction instead of 90° . In addition, [Gerstbach, 1976] investigated the theodolite Kern DKM2-A and found a phase shift in the wobble of the vertical axis between the *x*-direction and the *y*-direction of 30° .

The results show a significant wobble of the vertical axis exists and the wobble is repeatable. The next question raised is if these results can be reproduced by independent setups. This means the wobble of the vertical axis should also be reproducible concerning the frequency, or period, the amplitude and the phase angle, including the difference of the phase angles between the *x*-direction and the *y*-direction.

Results

The wobble of the vertical axis was investigated with several different and independent setups. All data series were analyzed in the way shown so that the results concerning the harmonic oscillations described by the parameters frequency, or period, amplitude and phase angle can be compared. The results are the following:

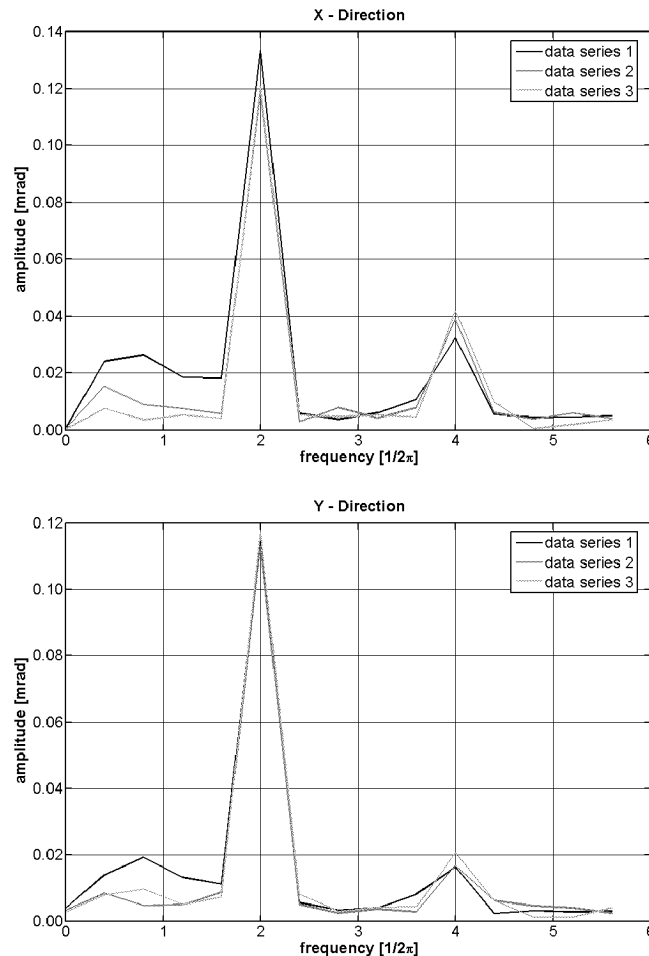


Figure 3.30: Amplitude spectrum derived by Fourier analysis for the data series acquired by identical setup eliminated by the levelling error for; x -direction (top) and y -direction (bottom).

- The dominant frequency has a period of 180° .
- The amplitude of the dominant frequency within the same data series is not always identical, as acquired in the x -direction and y -direction. There is a difference of up to 0.1 mrad.
- The amplitude of the dominant frequency is in the range of 0.1 mrad to 0.2 mrad.
- The phase angle is not constant and depends on the setup. Apparently, the wobble is influenced by external properties, e.g. imperfections of the bearing.
- The difference of the phase angle of the dominant frequency within the same data series between the x -direction and the y -direction is not systematical and varies from setup to setup.
- The use of the counter weight splits the amplitude of the dominant frequency roughly in two.

Thus, the results show that a wobble of the vertical axis can be seen. One dominant frequency is detectable and repeatable, but unfortunately, not reproducible in a way that this wobble can be reliably modeled mathematically for independent and different setups. The difficulties lie in the variation of the amplitude and in the variation of the phase angle. Generally, it can be stated that a wobble of the vertical axis exists with an amplitude of 0.1 mrad to 0.2 mrad, which means an influence of 1 mm to 2 mm at 10 m. However, the setup may influence the wobble.

For comparison, another laser scanner¹⁷ was investigated in the same way. The data acquired by the inclination data in the x -direction and y -direction as well as the sine curve defining the levelling error are shown in the upper part of Figure 3.31. The parameters for the levelling error are identical concerning the frequency and the amplitude, and the difference of the phase angle between the x -direction and the y -direction is 90° . The remaining residuals between the acquired inclination data and the sine curve defining the wobble of the vertical axis can be seen in the lower part of Figure 3.31. These residuals show no systematic trends and are small (< 0.03 mrad). Thus, this vertical axis has an ideal rotation and is free of a wobble.

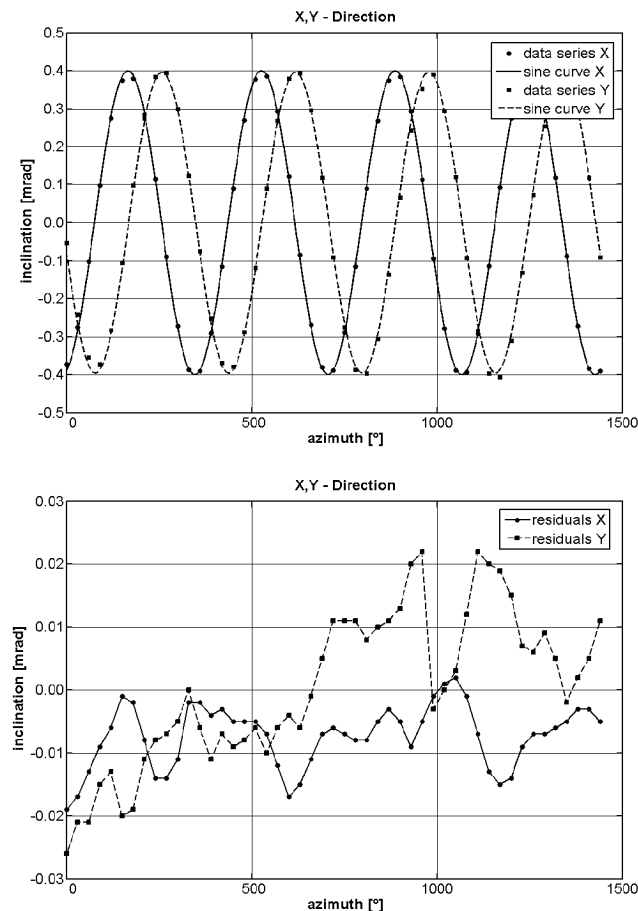


Figure 3.31: Inclination values of a data series including the sine curve of the levelling error for the x -direction and the y -direction (top). The residuals of the inclination data to the sine curve for the x -direction and the y -direction (bottom).

In addition, a theodolite has a much smaller wobble of the vertical axis. According to [Matthias, 1961], the investigation of a theodolite results in a maximum error of 0.005 mrad that is caused by the vertical axis wobble. Finally, it should be mentioned that not only is the vertical axis affected by the wobble, but the horizontal axis can also be influenced.

3.4.3 Error of Collimation Axis

The ideal construction of the collimation axis of a theodolite should be normal to the horizontal axis, i.e. tilting axis. Furthermore, the collimation axis should intersect the horizontal axis at the (virtual) intersection point between the vertical axis and the horizontal axis. The realisation of this ideal condition leads to errors

¹⁷Laser scanner HDS 3000 of HDS Leica Geosystems

in the collimation axis. In detail, it can be distinguished between two different errors [Deumlich and Staiger, 2002]:

- collimation error and
- eccentricity of the collimation axis.

The investigated laser scanner has axes according to a theodolite, a collimation axis, defined by the laser beam, a horizontal axis and a vertical axis, cf. Figure 3.25. Thus, the influence of the two errors of the collimation axis can be investigated by performing measurements in two faces. For minimizing and separating further instrumental errors, e.g. errors of the horizontal axis, the measurements were carried out on targets aligned in a horizontal line of sight, as defined by a zenith angle of $\approx 90^\circ$. The targets were spheres and positioned along the calibration track line. The range for positioning the spheres is limited to 20 m according to the quality and the quantity of the point cloud by scanning the spheres, cf. Section 3.2.2.

The investigation procedure includes two spheres with two different diameters of 12 cm and 15 cm, which were scanned in two faces¹⁸ and twice by independent setups. The center points of the spheres were calculated by applying the 'fix' adjustment. Since the results from computing the center points are in Cartesian coordinates, the spherical coordinates are derived by

$$\begin{aligned}hz &= \arctan\left(\frac{y}{x}\right) \\v &= \arccos\left(\frac{z}{s}\right) \\s &= \sqrt{x^2 + y^2 + z^2}\end{aligned}\tag{3.11}$$

If the collimation axis shows errors, then the spherical coordinates, based on surveying in two faces, are different. This is especially true for the horizontal angle hz and the vertical angle v . The deviations in the angles based on measurements in two faces are caused by the collimation error and the eccentricity of the collimation axis.

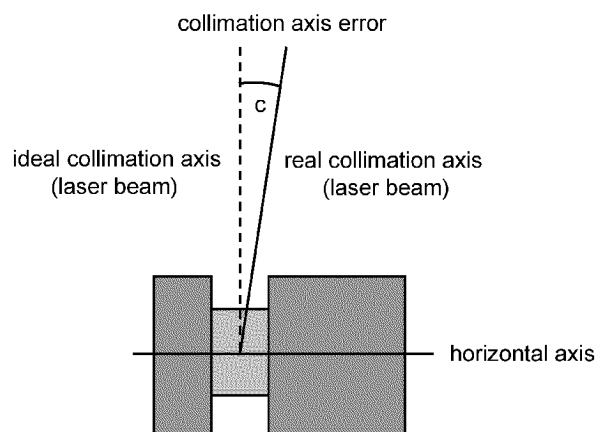


Figure 3.32: Collimation error applied to the laser scanner (top view). The real collimation axis, visualized by the laser beam, shows a deviation from the ideal collimation axis (angle c) which hits the horizontal axis at a normal.

A collimation error is present if the collimation axis is not normal to the horizontal axis. Figure 3.32 shows the influence of the collimation error c on the horizontal direction. In addition, if the collimation error has corresponding deviation in the vertical direction, i.e. the collimation axis is not normal to the vertical

¹⁸Due to the deflection principle, the rotating mirror of the laser scanner can be seen as the telescope of a theodolite

axis, then this is not a collimation axis error but an index error for the vertical encoder. This means the positioning of the laser beam shows an encoder reading that is falsified by the index error. These errors, existing in both the horizontal direction and in the vertical direction, can be determined by measurements in two faces. Performing measurements only in one face requires that the encoder readings have to be corrected by the collimation error.

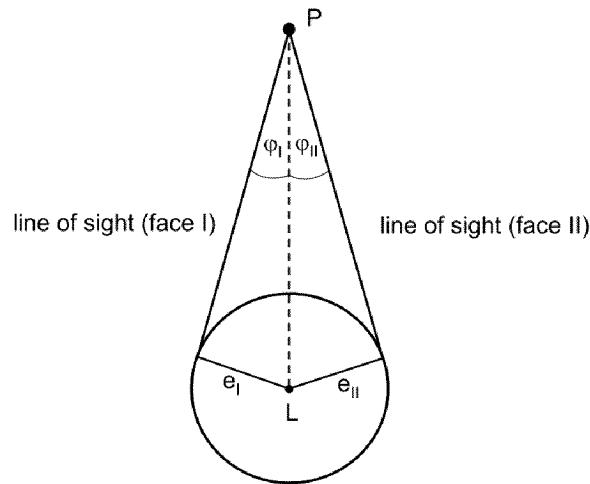


Figure 3.33: Eccentricity e of the collimation axis according to [Deumlich and Staiger, 2002]. The line of sight is not centrally during the rotation and shows an offset described by the tangent on a circle. The diameter of this circle corresponds to the eccentricity and the resulting influence is defined by the angle φ .

An offset of the collimation axis can generally be defined by a line of sight that is not centrally during rotation. The collimation axis can be rotated in a horizontal direction and in a vertical direction. In the case of a horizontal rotation, the eccentricity of the collimation axis means the line of sight does not intersect the vertical axis. Instead, the line of sight is a tangent on a circle during the rotation whereas the center point of the circle defines the ideal position of the line of sight hitting the vertical axis. The radius of this circle corresponds to the eccentricity of the collimation axis. Figure 3.33 outlines the eccentricity e and the resulting error in terms of the influence φ on the desired angle, according to [Deumlich and Staiger, 2002]. Analogously, the same considerations concerning the eccentricity in the case of a vertical rotation of the collimation axis can be applied. In this case, the eccentricity means the line of sight does not intersect the horizontal axis. The influence on the desired angle caused by the eccentricity decreases with the range. The farther the target point P is the smaller is the influence φ of the eccentricity e . Table 3.12 shows the varying influence for different eccentricity values.

Table 3.12: Influence of the eccentricity of the collimation axis for different eccentricities and ranges.

	$e = 0.1 \text{ mm}$	$e = 0.5 \text{ mm}$	$e = 1 \text{ mm}$	$e = 2 \text{ mm}$	$e = 5 \text{ mm}$
Range [m]	$\varphi [^\circ]$	$\varphi [^\circ]$	$\varphi [^\circ]$	$\varphi [^\circ]$	$\varphi [^\circ]$
1	0.0057	0.0286	0.0573	0.1146	0.2865
5	0.0011	0.0057	0.0115	0.0229	0.0573
10	0.0006	0.0029	0.0057	0.0115	0.0286
20	0.0003	0.0014	0.0029	0.0057	0.0286
50	0.0001	0.0006	0.0011	0.0023	0.0057

The error budget consisting of the collimation error and the eccentricity of the collimation axis can be separated into the horizontal component and into the vertical component.

Horizontal Component

First, the component in the horizontal direction is discussed. The results gained by the two independent setups are shown in Figure 3.34. The upper figure indicates the deviations of the horizontal encoder for the sphere with a diameter of 12 cm and the lower figure shows the corresponding results for the sphere with a diameter of 15 cm. The data points are approximated by a hyperbola based on a least square adjustment [Bronstein and Semendjajew, 1999]:

$$y = \frac{a}{x} + b \tag{3.12}$$

since the hyperbola approximates the data points sufficiently. The parameter a defines for the gradient of the curve and the parameter b defines the twofold collimation error. Referring to the aforementioned considerations, the eccentricity has to be taken into account for short ranges. The limit of the hyperbola describes the collimation error because the influence of the eccentricity is rapidly increasing with the range, cf. Table 3.12. The homogeneity of the results of the parameters for the adjusting hyperbola are shown in Table 3.13.

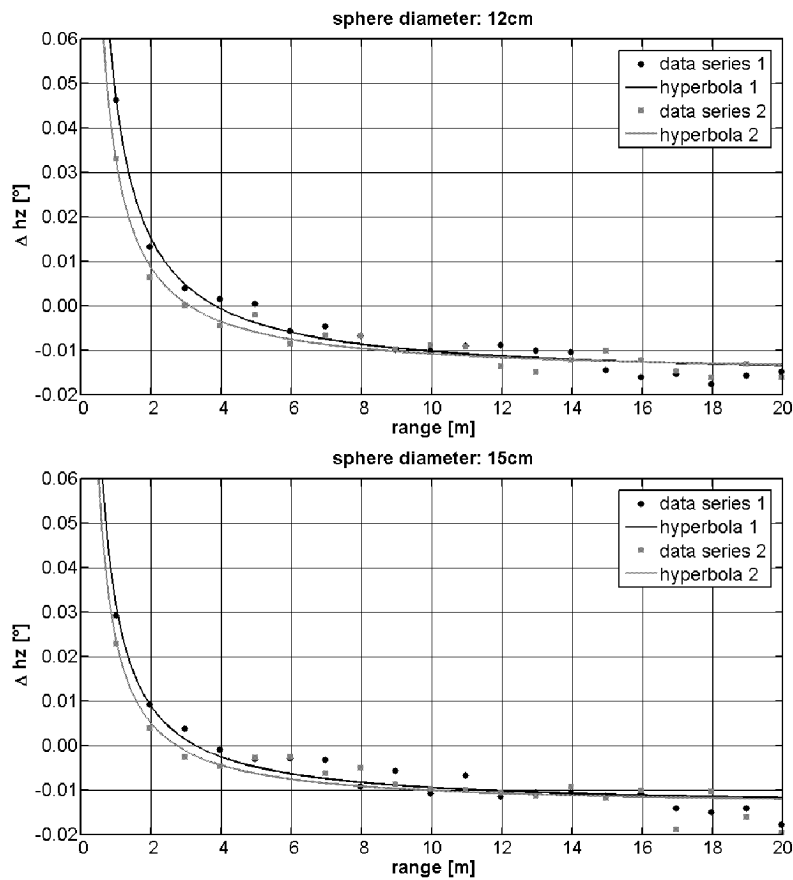


Figure 3.34: Influence of the errors of the collimation axis in horizontal direction. In the figures, the differences of the horizontal directions in two faces derived by spheres with diameters of 12 cm (top) and 15 cm (bottom) are shown.

The significance of the collimation error can be assessed by applying a t – test. The result is that the collimation error differs significantly from zero (two-side alternative hypothesis and a significance level of $\alpha = 5^\circ$). Thus, the collimation error can be reduced to a value of $e = -0.0075^\circ$. The eccentricity can be calculated by, cf. Figure 3.33:

$$e = s \cdot \sin(\varphi) \tag{3.13}$$

Table 3.13: Results of the adjusting hyperbola concerning the error of the collimation axis in horizontal direction. Parameter a defines for the gradient and parameter b defines the limit.

Data Series	a [°/m]	b [°]	σ_a [°/m]	σ_b [°]
sphere 12 cm (1)	0.064	-0.016	0.0025	0.0007
sphere 12 cm (2)	0.049	-0.016	0.0022	0.0006
sphere 15 cm (1)	0.046	-0.014	0.0007	0.0002
sphere 15 cm (2)	0.038	-0.014	0.0034	0.0010

with the range s and the difference φ of the horizontal directions in two faces corrected by the twofold collimation error. The resulting values for the eccentricity are summarized in Figure 3.35. The eccentricity e can be described by a mean value of 0.9 mm and a precision of 0.1 mm. The mean value is based on data up to 15 m because the influence of the eccentricity decreases and then reaches the same degree of precision as the precision of the angle measurement system, cf. Table 3.12.

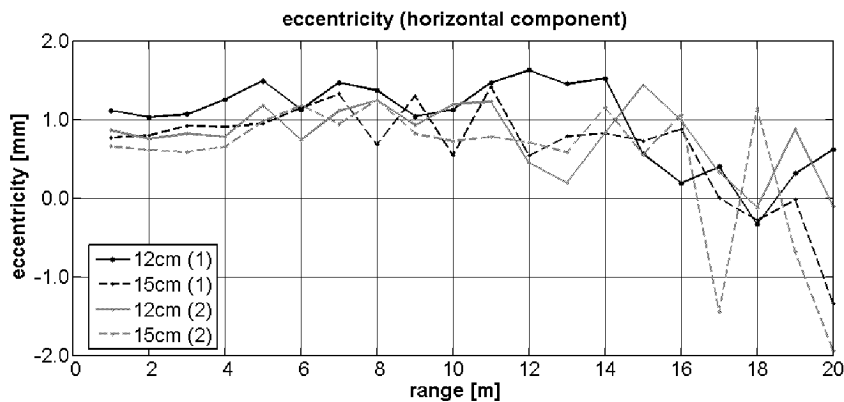


Figure 3.35: Eccentricity of the collimation axis in horizontal direction. The eccentricity of the collimation axis in the horizontal direction is derived by using spheres with the diameters of 12 cm and 15 cm based on two independent setups (1) and (2).

In summary, the error budget of the collimation axis, consisting of the collimation error and the eccentricity, was derived. Considering the influence of both errors shown in Figure 3.34, it can be seen that the adjusting hyperbolae intersect the abscissa. This means at the intersection point, about 3 m to 4 m), the error of the collimation axis has no influence on the horizontal direction. The interpretation is the collimation error and the eccentricity have opposite signs and they compensate each other. However, the most important aspect is that the influence of the error of the collimation axis is not constant for close ranges. The correction of the horizontal angle data has to be completed separately according to the range and its error budget.

Vertical Component

Second, the component in vertical direction is discussed. The results obtained by the two independent setups are shown in Figure 3.36. It can be seen that the results of each setup obtained by the two spheres with different diameters match each other. However, the results of the two independent setups do not fit each other. With the exception of the first two meters, no systematic effects, depending on the range, can be seen. The lines approximately describe a constant line. Thus, a significant influence of an eccentricity of the collimation axis in the vertical direction cannot be seen. The constant line defines a collimation error in the vertical direction, which can be interpreted as an index error in the vertical encoder. Further assumptions of the factors that influence the orientation of the laser beam concern an offset between the outgoing laser beam and the encoder readings, variations on the rotation time and wobble effects of the horizontal axis.

Nevertheless, the index error appears to be constant within each setup and is therefore, repeatable. However, in an independent setup - associated with a restart of the laser scanner - the influence of the error of the collimation axis is different and is therefore, not reproducible.

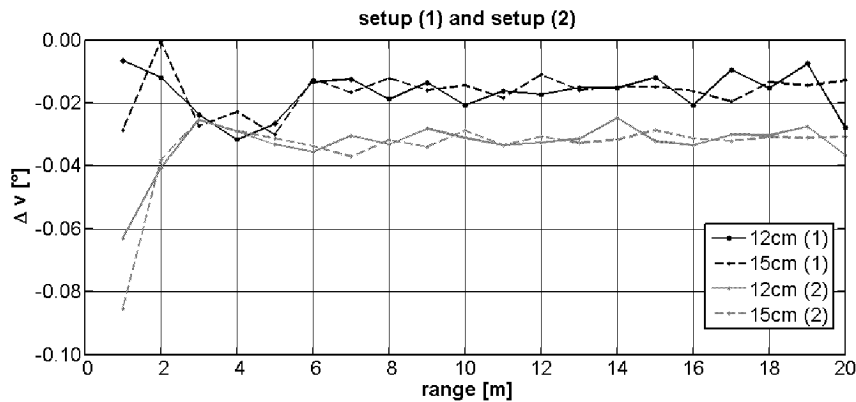


Figure 3.36: Influence of the errors of the collimation axis in vertical direction. The differences of the vertical directions in two faces derived by using spheres with diameters of 12 cm and 15 cm are shown for two independent setups (1) and (2).

3.4.4 Error of Horizontal Axis

The error of the horizontal axis has to be discussed in a similar manner to the error of the collimation axis. The error budget consists of an eccentricity in the horizontal axis and a horizontal axis error. The horizontal axis error is defined as the horizontal axis not being normal to the vertical axis. The steeper the line of sight the greater is the influence of the horizontal axis error in the horizontal direction. The determination of the error of the horizontal axis i is described in the literature. The formula for the calculation can be expressed by [Deumlich and Staiger, 2002]:

$$i \approx \left(\frac{\Delta h_z}{2} - \frac{c}{\sin(v)} \right) \cdot \tan(v). \quad (3.14)$$

Therefore, the collimation error c , the difference of the horizontal directions Δh_z , derived by measurements in two faces, and the vertical angle, corrected by the index error, have to be known. The formula described is an approximation that is sufficient with the exception of very steep lines of sight ($< 1^\circ$). A comprehensive discussion of the axis errors of theodolites including a derivation of exact formulas, especially for the tilting axis error, can be found in [Stahlberg, 1997].

The experimental setups for the determination of the error of the horizontal axis were performed by scanning spheres in two faces. The spheres were distributed in a vertical plane to generate varying lines of sight regarding the vertical direction. The slope distances differ between 1.5 m and 5 m. The lines of sight cover a field of view between 15° and 164° in the vertical direction. The calculations were carried out using Equation (3.14). Since within close ranges, up to 15 m, the influence of the error of the collimation axis is not constant, cf. Section 3.4.3, the values for the parameter c are varying. The corresponding influence of the error of the collimation axis then has to be applied.

The results for two different experimental setups in Table 3.14 show an error in the horizontal axis of up to an absolute value of 0.08° , but the values differ substantially and the signs change. Building an average of the values, an error of approximately 0.045° is derived.

Since the setups for the investigation procedure were not optimal, the results have to be interpreted in a critical manner. Short ranges did not allow for the assessment of the error budget of the horizontal axis, es-

Table 3.14: Error of the horizontal axis derived by measurements in two faces to targets installed at different vertical angles.

Setup	Point Number	Vertical Angle ν [°]	Error of Horizontal Axis i [°]
1	1	15	-0.083
	2	64	-0.064
	3	86	-0.048
	4	112	0.051
	5	140	0.001
	6	164	0.005
2	1	54	0.034
	2	72	0.004
	3	81	-0.052
	4	114	0.086
	5	145	0.067

pecially regarding the eccentricity. A conceivable eccentricity may influence the interpretation significantly. The experimental setup has to be improved so that with different constant vertical directions and growing ranges, the investigation has to be repeated. The setup for the examination of the collimation axis may provide some indications, with the difference that the lines of sight do not run horizontally but vertically.

3.5 Non-Instrumental Errors

Laser scanning technology is based on performing measurements on various kinds of objects. Since the use of prisms is not necessary, nor recommended, the distances to be measured are affected by several parameters, such as the intensity of the reflected laser beam, the angle of incidence, surface properties, e.g. colour and roughness, multipath, speckle effects, etc. In the following, some of these parameters are discussed and investigated.

3.5.1 Intensity of Laser Beam

The intensity of the reflected laser beam is of importance since the amplitude of the received signal is correlated with the quality of the detecting range. The better the signal-to-noise ratio, the better the determination of the distance. The intensity (I) is influenced by three parameters:

- the range d ($I \sim \frac{1}{d^2}$),
- the reflectivity of the object, and
- the angle of incidence.

Figure 3.37 shows the development of the intensity relative to a maximum. The upper figure indicates the relation between the range and the intensity for different reflectivity values. The longer the range and the lower the reflectivity of the object, the less the intensity. The lower figure presents the intensity of a target with a reflectivity of 90% and shows that the intensity also decreases systematically. For example, the intensity line of the target with a reflectivity of 20% corresponds to the intensity line to a target with a reflectivity of 90% and an angle of incidence of 30°. The intensity worsens with respect to low reflectivity values and low angles of incidence.

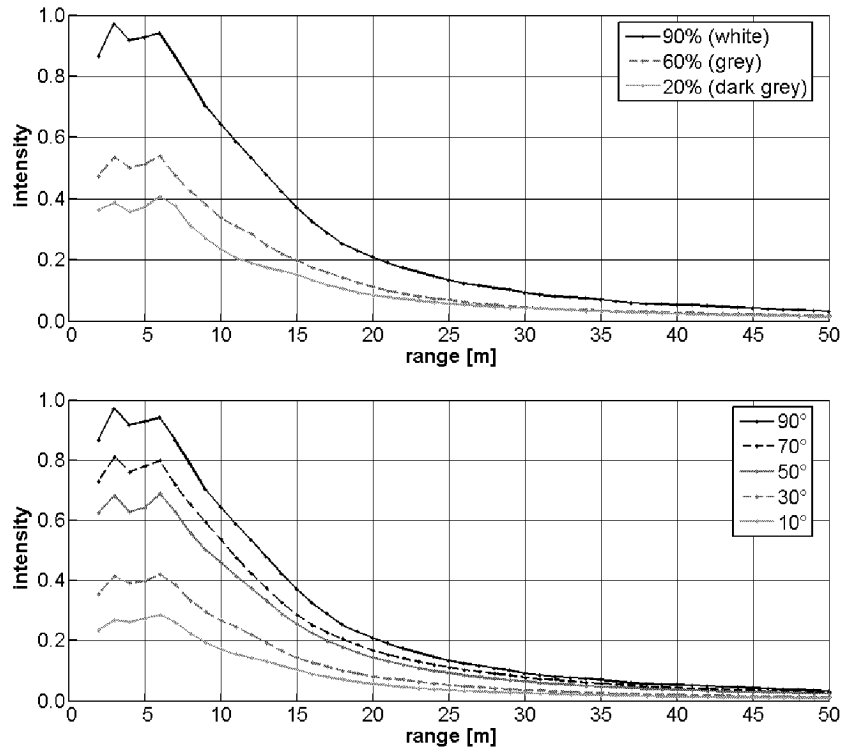


Figure 3.37: Intensity of reflected laser beam. Influence of the reflectivity (top) and influence of the angle of incidence (bottom).

The relative intensity values in Figure 3.37 do not match the given reflectivity values of the targets. Up to 5 m, the white target shows a relative intensity of $\approx 93\%$, the grey target shows a relative intensity of $\approx 52\%$ and the dark grey target shows a relative intensity of $\approx 38\%$. Thus, the given reflectivity values indicate system-related reflectivity values more than absolute reflectivity values.

Concerning the intensity of laser light, the speckle effect also has to be considered. Speckles are based on variations of the intensity of coherent laser light produced by the interference of the diffuse scattered light on rough surfaces with the incident light. This means the intensity of the reflected laser light can vary depending on the intensity of rough surfaces and can be affected by speckle effects.

3.5.2 Angle of Incidence

The angle of incidence is defined as the angle between the incident laser beam and the tangent on the surface from which the laser beam is reflected. Generally, the angle of incidence can be measured in two directions, horizontally and vertically. An angle of incidence of 90° describes a laser beam hitting the surface of the object at a normal.

The angle of incidence influences the distances to be measured in two different ways. On one hand, the center of reference for the distance is shifted because the footprint of the laser beam varies from a circular form to an elliptical form. On the other hand, the footprint of the laser spot increases and covers a larger area. The reference point for measuring the distance is shifted and not well-defined because of the distortion of the footprint. Thus, the distance has a systematic offset leading to a false range between object and laser scanner. Furthermore, the noise of the distances increases with a decreasing angle of incidence because the intensity of the reflected laser beam decreases and the footprint of the laser beam enlarges.

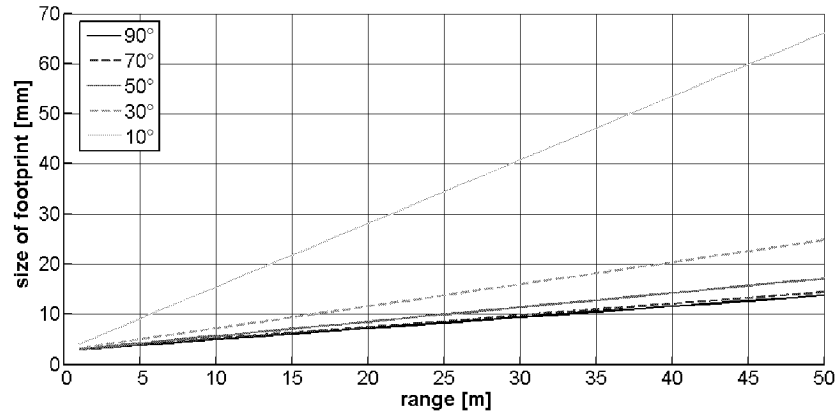


Figure 3.38: Influence of the angle of incidence on the size of the footprint of the laser beam. The size of the footprint significantly increases with a decreasing angle of incidence.

The investigated laser scanner has a beam divergence of 0.22 mrad and defines the aperture angle of the mechanical system that generates the laser beam. Considering a spot size of the laser beam of 3 mm at a distance of 1 m¹⁹, the projection of the laser beam on a slope surface depending on both the angle of incidence and the range, cf. Figure 3.38, can be developed. The smaller the angle of incidence, the larger the size of the footprint. Considering angles of incidence of less than 30°, the size of the spot is multiplied by a factor of 1.5 up to a factor of 4 in contrast to a laser beam hitting the surface at a normal.

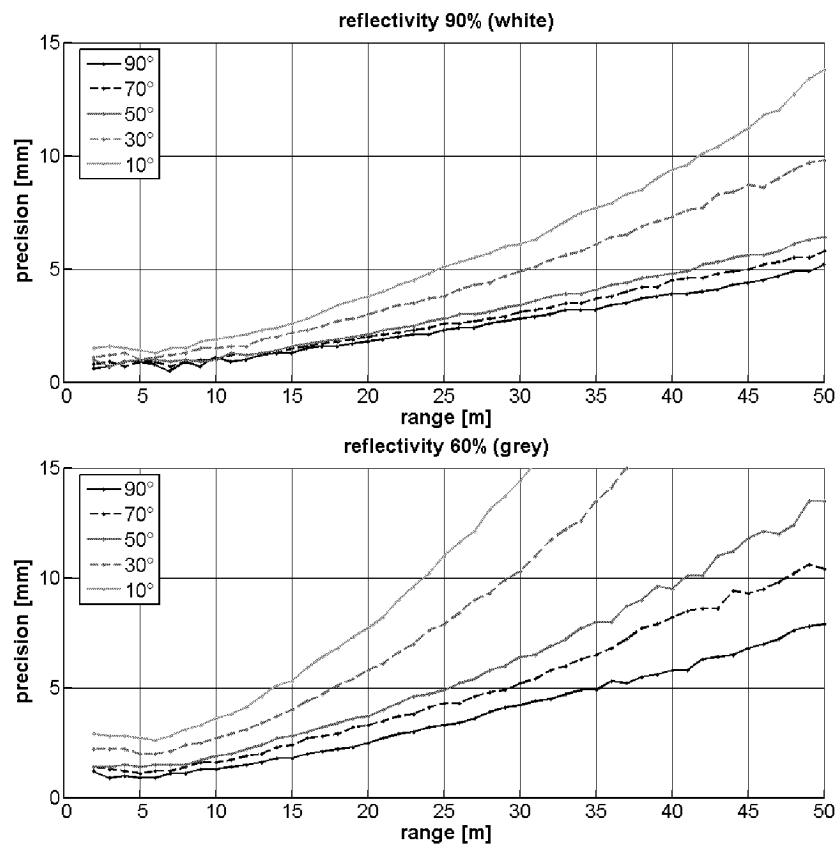


Figure 3.39: Influence of the angle of incidence to the distance precision regarding targets with a reflectivity of 90% (top) and with a reflectivity of 60% (bottom).

¹⁹specification of the manufacturer

The influence of the angle of incidence can be defined by the precision and the accuracy. In Figure 3.39, the precision of different angles of incidence to targets with reflectivity values of 90 % and 60 % are given. It can be clearly seen that the precision worsens with both a lower reflectivity and a smaller angle of incidence. This means that the data are more biased.

Concerning the systematic offset of the distance caused by the shifted projection center of the footprint and the larger footprint, the accuracy for different angles of incidence and different reflectivity values are given in Figure 3.40. It can be seen that depending on the angle of incidence, the systematic deviations and the oscillations of the curves increase. Thus, the results are not trustworthy distance measurements. These findings correspond to the precision, cf. Figure 3.39, of strongly biased data.

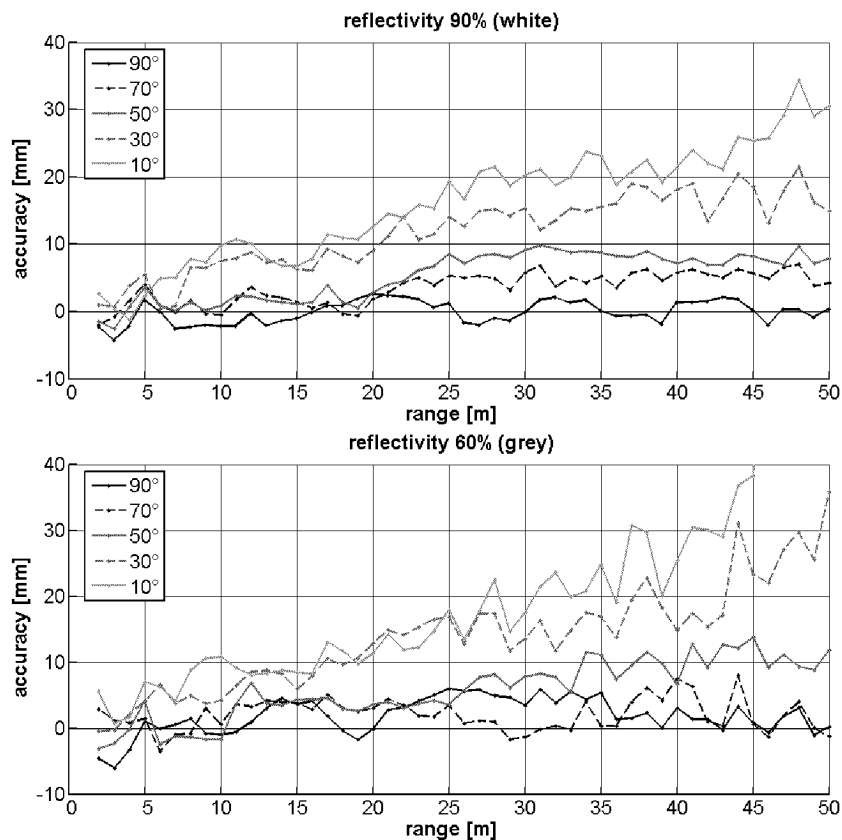


Figure 3.40: Influence of the angle of incidence to the distance accuracy regarding targets with a reflectivity of 90% (top) and with a reflectivity of 60% (bottom).

The simulation of the precision of the distance measurement applied to a plane in a range of 10 m shows the influence of the angle of incidence. The object is not only inclined in one direction, i.e. horizontally, but also in a second, i.e. vertically. Most of the objects to be scanned show inclinations in two directions. Figure 3.41 gives an impression of the decreasing precision and the increasing noise of the range data. The precision is the worst in the corners since the angles of incidence in the horizontal direction and in the vertical direction are the smallest.

3.5.3 Surface Properties of Materials

The results of the distance measurement regarding precision and accuracy depend not only on the parameters range, reflectivity of the object and angle of incidence, but also on the characteristics of the surface material. Considering semitransparent materials, e.g. styrofoam, wood, marble, the incident ray is not only reflected on the surface of the materials, but also intrudes the first layer of the material until the ray hits a

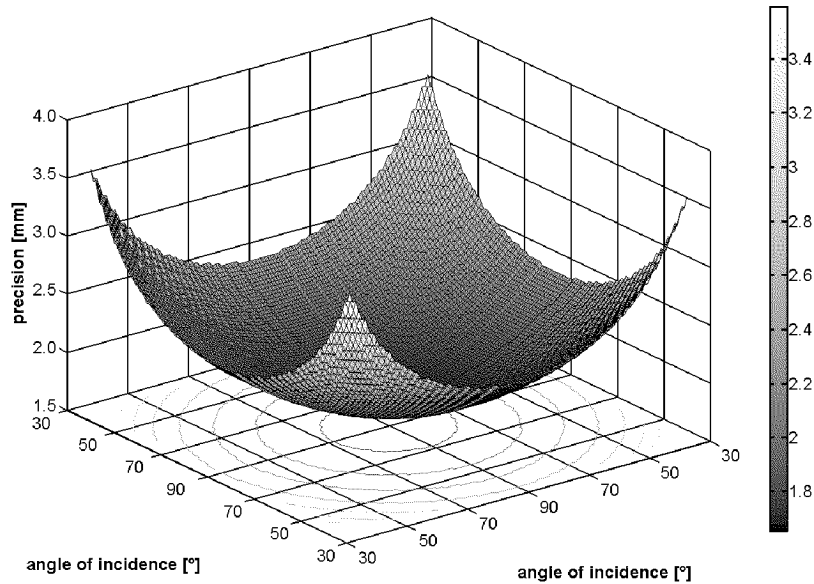


Figure 3.41: Influence of the angle of incidence on the precision of the distance measurement to a planar object.

particle. This particle causes a reflection of the ray inside the material, cf. Figure 3.42. Thus, the measured distance is always longer than the desired distance to the surface of the object.

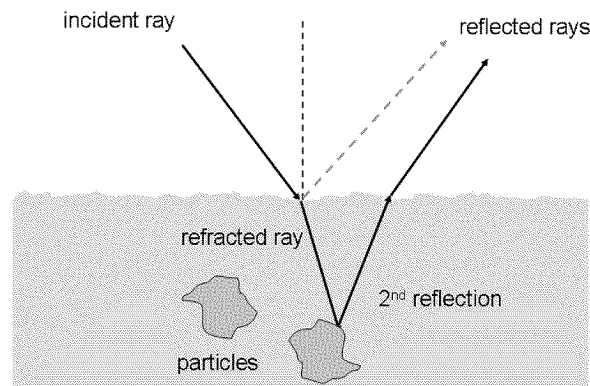


Figure 3.42: Surface backscattering and refractive effects in inhomogeneous semitransparent materials, e.g. styrofoam, wood, marble [Ingensand, 2006].

The effect of refraction and intrusion of the laser beam in materials is verified by comparing the distances detected by the laser scanner and the nominal distances provided by the interferometer on the calibration track line. The experimental setup is analogous to the investigation of the 'static mode' of the distance measurement system, cf. Section 3.2.1. The resulting residuals between nominal and measured distances can be interpreted regarding systematic effects caused by the intrusion of the laser beam. The following materials were investigated: styrofoam (thickness of 2 cm and 5 cm), wood and metal.

The results are given in Figure 3.43 and Figure 3.44. Figure 3.43 shows the accuracy for styrofoam and wood in comparison to a white paper used as a reference target. The findings are clear: the laser beam intrudes the styrofoam and wood. The depth of the intrusion depends on the granulation and the roughness. For the materials used, the intrusion depth shows a value of nearly 15 mm for styrofoam and nearly 5 mm for wood.

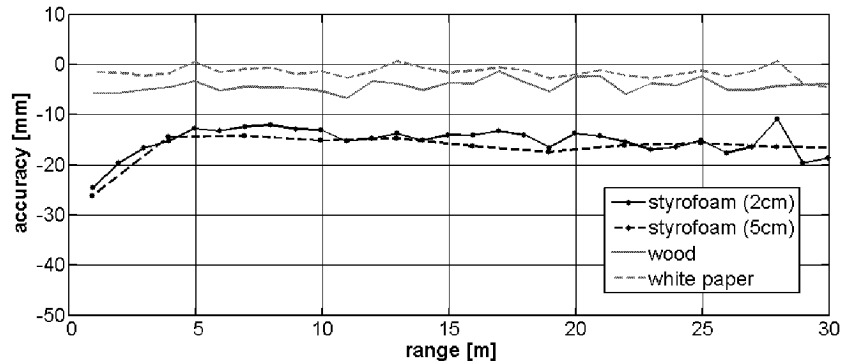


Figure 3.43: Distance accuracy of some materials (styrofoam, wood, white paper).

In Figure 3.44, another systematic effect based on the reflected intensity of the laser beam can be seen. Since in most laser scanners the signal-to-noise ratio is not regulated and not optimised the receiving avalanche diode is over-steered and generates systematic effects, which result in distance errors. This effect becomes clear considering the distance accuracy of metal. The upper part of Figure 3.44 shows systematic deviations within the first 25 m of several meters. Only beyond 35 m does the intensity of the reflected laser beam allow the avalanche diode to work properly and the distances become reasonable. However, a systematic offset of nearly 5 mm is left.

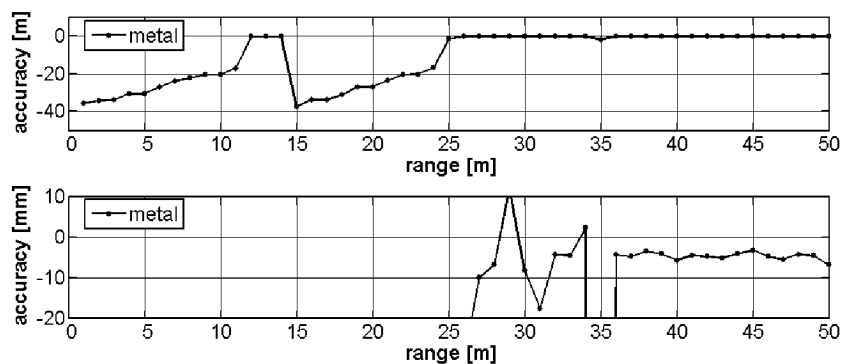


Figure 3.44: Distance accuracy of metal. Only beyond 35 m does the distance accuracy becomes reasonable.

The discussed selection of only three different materials (styrofoam, wood, metal) demonstrates that the influence of the surface properties of different materials is important. For achieving a high accuracy, the properties of the material to be scanned have to be verified. Especially, regarding the influence of the surface reflectance, there are several investigations and publications for the specific laser scanner system, e.g. [Lichti and Harvey, 2002b], [Clark and Robson, 2004], and [Reshetyuk, 2006a]. Each laser scanner and its wavelength of the laser beam has a different behavior for different materials and makes it difficult to generalise the findings. There are some materials that may cause systematic effects, such as glass, metal, and other high-reflective surfaces.

3.6 Precision and Accuracy of Terrestrial Laser Scanner Data

The investigation and calibration of each single component of a terrestrial laser scanner are necessary and important. The interesting question, which also has to be answered, is how precise and how accurate are the results of one acquired single point and the results of the modeled objects. In the following, these questions shall be answered.

3.6.1 Single Point Precision

The precision of one single point is derived by two methods. The first one is based on the identified precision for the distance component (s_s) and the encoder components for the horizontal direction (s_{hz}) and the vertical direction (s_v). A theoretical error budget for one single point (s_p) can be calculated by:

$$s_p = \sqrt{s_x^2 + s_y^2 + s_z^2} \quad (3.15)$$

with

$$\begin{aligned} s_x &= 3 \cdot s_s \\ s_y &= s \cdot \tan(3 \cdot s_{hz}) \\ s_z &= s \cdot \tan(3 \cdot s_v) \end{aligned} \quad (3.16)$$

For the precision of the x -component, the trifold precision, i.e. standard deviation, is used since it refers to 99.9% of measurements. For the y -component and the z -component, the distance s has to be taken into account as well as the trifold precision of the angle measurement system. The second method uses the acquired point cloud to derive a single point precision. Spheres were scanned and the center points were calculated by applying the adjustment algorithm, cf. Section 3.1.5. The resulting mean error of the unit weight (s_0) defines the precision of one single coordinate. Thus, the precision of one single point containing three coordinates can be determined by:

$$s_p = \sqrt{3} \cdot s_0. \quad (3.17)$$

The spheres were positioned along the calibration track line in varying ranges so that the development of the precision of one single point can be derived. Figure 3.45 shows the results obtained by the two different methods. Since the second method can only be applied up to ranges of approximately 20 m, the upper figure is also limited up to this range. Reasons for the limited range are the quality and the quantity of the acquired point cloud decrease rapidly with the range, cf. Section 3.2.2. The precision obtained by the second method is verified using two spheres with different diameters, i.e. 12 cm and 15 cm. The values lie about 5 mm and fit with each other. In addition, the theoretical precision based on the first method increases with the range. The lower figure shows the development of the precision. The noise of one single point reaches values in the order of some centimeters in ranges of more than 30 m.

In summary, it can be concluded that the two methods fit each other and show a precision for one single point of less than 1 cm up to a range of 20 m. The development of the theoretical precision gives an impression of the resulting precision in ranges of more than 30 m, which increases up to 2 cm. The difference in the two methods is that the derived theoretical precision is based on an angle of incidence of 90° , which means the laser beam hits the object normal. A variation of the angle of incidence leads to lower distance precision and also results in lower single point precision, cf. Section 3.5.2. On the contrary, the method using the spheres takes the varying angle of incidence into account. Furthermore, the investigation can be continued for different reflectivity values. The spheres used are white in colour, approximating a reflectivity of 90%. Also, the distance accuracy required for the first method refers to a reflectivity of 90%.

3.6.2 Accuracy of Modeled Objects (Spheres)

The accuracy of modeled objects is shown exemplarily by considering the calculated center point of spheres. The spheres with two different diameters, i.e. 12 cm and 15 cm, were positioned along the calibration track line and were scanned with three different scan resolutions. Based on the acquired data, the center point

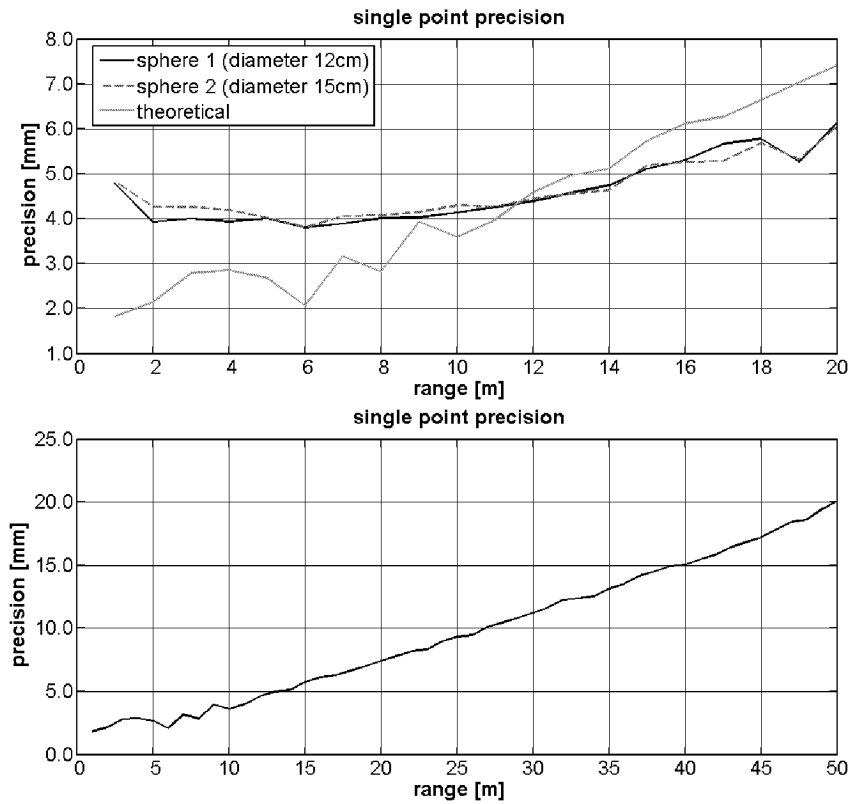


Figure 3.45: 3D single point precision: precision using spheres (top) and the precision of the distance measurement system and the angle measurement system (bottom).

of each sphere was calculated using the adjustment tool. Since the diameter of the spheres are well-known, the center points can be derived using both the 'free' adjustment and the 'fix' adjustment. The coordinates of the center points refer to the local scanner system. These local coordinates can be transformed into the coordinate system of the calibration track line using the positions of the spheres as control points. The resulting residuals in all three coordinate directions can be summarized as a 3D accuracy for the center points of the modeled spheres.

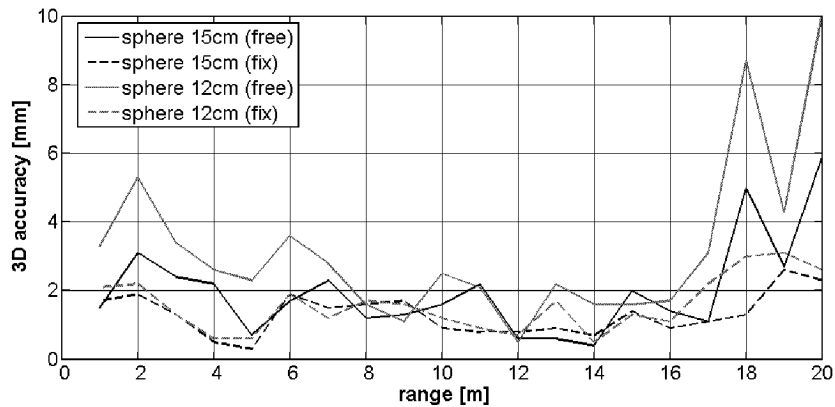


Figure 3.46: 3D accuracy of modeled spheres. Two different diameters were used, which are unknowns or well-known constants in the adjustment model (free and fix, respectively).

Figure 3.46 shows the 3D accuracy of the center points of the spheres. The data were acquired with the highest scan resolution. Generally, the accuracy of the center points based on the 'fix' adjustment is better

than the calculated center points based on the 'free' adjustment and is within 2 mm. Referring to the investigation of the distance measurement system in the 'scanning mode', an additive constant of 3 mm to 4 mm in the 'free' adjustment was identified. By applying the coordinate transformation, this systematic offset is taken into account and the center points are shifted by this additive constant. Thus, the 3D accuracy of the center points is better than the distance accuracy, cf. Figure 3.16 and Figure 3.46.

The 3D accuracy of the center points can be also derived by interpreting the distance accuracy along the calibration track line as accuracy in x-direction, the accuracy of the horizontal encoder transversal to the calibration track line as accuracy in y-direction and the accuracy of the vertical encoder as accuracy in the vertical direction of the calibration track line. The results are identical to the coordinate transformation except that the additive constant has to be subtracted manually with respect to the 'free' adjustment.

The use of the other 'scanning modes' does not change the achievable 3D accuracy. Only the range from which the accuracy is getting worse decreases, cf. the corresponding results gained by the investigation of the distance measurement system in the 'scanning mode', Section 3.2.2.

Static Laser Scanning

This chapter discusses the post-processing of 3D point clouds as applied to static laser scanning. Static laser scanning implies that the objects to be scanned and the laser scanner do not move relative to each other during the data acquisition process. Post-processing of 3D point clouds requires software packages to derive the final products, e.g. 3D models. Since the implemented algorithms in these software packages are not fully automated, the operator has to assist the software. Thus, the process of deriving the final product based on the 3D point cloud is time-consuming. The time ratio between post-processing of laser scanning point clouds and data acquisition can be up to 10 : 1 or more. The following sections cover some aspects of data processing, registration, and modeling and visualization.

4.1 Data Processing

Laser scanning is one of the fastest data acquisition techniques in geodesy and generates a huge number of points, which describe the environment, in a short time. However, data acquisition produces blunders and noise within the point clouds. Noise can be distinguished in white noise and coloured noise. Here, noise is assumed to be white noise and Gaussian noise. The following sections give an overview of the conceivable errors and error sources. They result in noisy data and have to be processed by applying special filtering and noise reduction techniques.

4.1.1 Blunder Detection

The laser scanner system acquires data within a distance and an intensity interval. Sometimes, only data within a specific range regarding distance and intensity values are required. The points which fulfil these requirements can easily be separated from the points that do not fulfil the requirements by introducing minimum and maximum limits for both range and intensity data, a threshold:

$$range_{\min} \leq range \leq range_{\max} \quad (4.1)$$

$$intensity_{\min} \leq intensity \leq intensity_{\max} \quad (4.2)$$

The borders of this simplified bandpass filter depend on the working range of the laser scanner and the application. Applying a threshold to the intensity values may not only reduce the number of points considerably but also eliminate blunders.

4.1.2 Mixed Pixel

Due to beam divergence, the laser beam is spread out during propagation. Depending on the range and the beam divergence, the laser beam creates a characteristic footprint when hitting objects. The situation to be scanned and the deflection of the laser beam may cause the footprint to hit a surface that does not belong to only one object but to two or more objects situated at different distances. The reflected energy cannot be identified with one of these objects since the range is measured by integrating over the entire footprint, as characterized by the projected spot. This phenomenon is referred to as mixed pixels, which can be anywhere along the line of sight [Hebert and Krotkov, 1992]. The detected ranges from such mixed pixels are somewhere in between, behind or in front of the surfaces.

The interpretation for the existence of such mixed pixels is described by [Hebert and Krotkov, 1992]. If one surface occludes a second surface, the laser beam is reflected by both objects. The geometrical location of the resulting mixed pixel is obtained according to a description of the range and the intensity as a complex number with the vector components

$$v = I + \phi i \quad (4.3)$$

where I is the intensity or magnitude, which depends on several parameters, e.g. the reflectivity of the material, the range, and the angle of incidence, and ϕ is the phase, which is proportional to the range. The resulting elements of a mixed pixel caused by two reflections v_1 and v_2 is calculated by

$$v = v_1 + v_2 = I_1 + I_2 + (\phi_1 + \phi_2)i. \quad (4.4)$$

The addition of two vectors results in a new vector, with a phase ϕ that can be anywhere, depending on the ratio of the lengths and depending on the phase angles. Considering the difference in the phase angles $\Delta\phi$ of the two objects, a distinction can be made between

$$(1) \Delta\phi = \phi_2 - \phi_1 \leq \pi$$

$$(2) \Delta\phi = \phi_2 - \phi_1 > \pi$$

The first one results in a mixed pixel with a phase, i.e. the range, between the phase of the individual components. The second one produces a mixed pixel with a phase that is either greater than or less than the phase of both individual components, depending on the ratio of the intensity values. Figure 4.1 visualizes the effects of mixed pixels with respect to phase angles and intensity values. The left part shows case (1) and the right one shows case (2). For (2) a case differentiation is necessary to decide whether the mixed pixel is closer or farther than the object. The right figure shows the mixed pixel, which is closer than the object.

The elimination of mixed pixels is proposed to be carried out by applying a median filter to the range image [Hebert and Krotkov, 1992]. Most of the pixels should be detected since they appear only along the direction of edges. The mixed pixels are often isolated pixels in 3D space and thus, can be removed easier in 3D space than in 2D images, e.g. range images. The elimination of mixed pixels is only successful if these pixels are far from objects. In contrast, if mixed pixels occur cumulatively near the vicinity of objects, they can rarely be removed automatically. However, in combination with images, the identification and elimination of such mixed pixels can be improved.

The appearance of mixed pixels can be avoided with a small beam divergence. The smaller the beam divergence, the less the probability that more than one object will be hit by the laser beam. Furthermore, the problem of mixed pixels is related to laser measurement systems using AMCW technique and cannot be

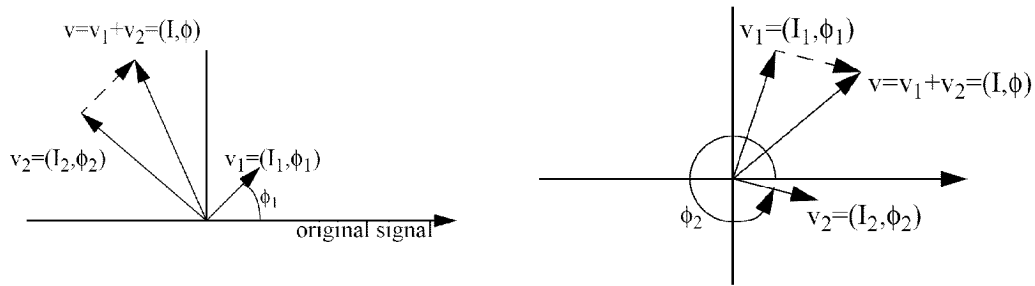


Figure 4.1: Geometrical interpretation of mixed pixels for two surfaces. The left figure shows a phase difference of less than π , the right figure shows a phase difference of greater than π , adapted from [Hancock, 1999].

completely avoided but can be minimized. In case of the direct time-of-flight principles, the measurement system can separate the incoming signals in first and last pulses. Thus, the problem of mixed pixels should not be of interest if a first pulse and a last pulse is detectable.

Figure 4.2 shows the presence of mixed pixels, which are either between two objects or farther or closer than the objects. In the figure, a sphere is placed in front of a wall. The mixed pixels are both in front of the sphere and between the sphere and the wall.

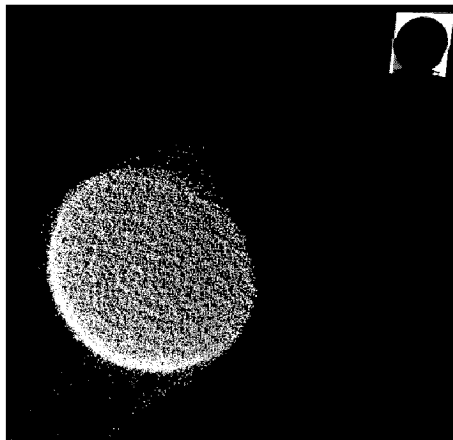


Figure 4.2: Mixed pixels occurred near objects: A sphere is positioned in front of a wall. The mixed pixels seen at the edges of the sphere are either in front of the sphere or between the sphere and the wall.

4.1.3 Range/Intensity Crosstalk

The distance measurement system does not operate independently from the received intensity value. The intensity value of the reflected laser beam influences not only the noise of the range but also the absolute distance value. Objects, which differ in reflectivity, measured at the same range, should have identical detected ranges. Unfortunately, reflectivity causes different values for the distance to the objects since the intensity of the laser beam varies. Thus, the less the intensity, the more biased the range data. This is called crosstalk between range and intensity. This can be distinguished between electronic crosstalk, caused by the implementation of detection electronics, and optical crosstalk, caused by the sensor optics due to internal reflections.

The receiver electronic is limited to function only within a specific intensity range. Measurements derived from intensity values outside the intensity range are noisy or erroneous, cf. Figure 3.44. Ideally, the operating range should be adjusted dynamically according to the intensity, as it is done in modern total stations.

Optical crosstalk depends on several parameters, e.g. orientation of the deflecting unit and intensity values. Thus, compensation for internal reflections is nearly impossible.

The results of the range/intensity crosstalk is considered in Chapter 3 within the calibration procedure of the laser scanner. The precision as well as the accuracy of distances acquired to objects with varying reflectivity are also discussed. However, crosstalk should also be considered at regions characterized by a change in range and in reflectivity.

Another affect, called temporal mixing [Hancock, 1999], can also be categorized as crosstalk. Temporal mixing can be noticed at transitions between darker and brighter surfaces. The transition between these two different reflectivity values leads to a jump in the returned signal amplitude of the laser beam. The jump can cause large errors in phase estimation, which correlates with the range.

4.1.4 Multipath

Multipath effects are well-known, e.g. in GPS technology. Multipath is defined as the effect that signals are reflected by more objects than desired. For example, with GPS, the signals do not travel directly from satellites to receivers. They are reflected on nearby and high-reflective objects. In laser scanning technology, multipath is characterised as the laser beam being reflected two times or more. The signal is not received directly after hitting the first object, rather, the signal is reflected by several objects and therefore, is not travelling the shortest path between the laser scanner and the object.

The probability of multipath is prevalent in scanning high reflective materials, scanning at close ranges and scanning corners [Runne et al., 2001]. Errors produced by multipath can be of any magnitude to unambiguity, i.e. the maximum range. Multipath results mostly in isolated pixels since the distance is highly different to the pixels in the neighbourhood. Multipath returns are mirror-inverted, which can be seen especially by scanning windows. The detection of points affected by multipath becomes difficult if they are surrounded by other points and if they are not clearly detectable as isolated pixels, e.g. in corners and at nearby objects.

In Figure 4.3 the effect of multipath is shown. The laser scanner was set up in a room which has a window from the ceiling to the floor at the right side and a mirror and window in the upper left corner. The laser beam is reflected twice due to multipath and the distance measurement results in pixels which are mirror-inverted. The inside of the room is projected to the outside of the room.

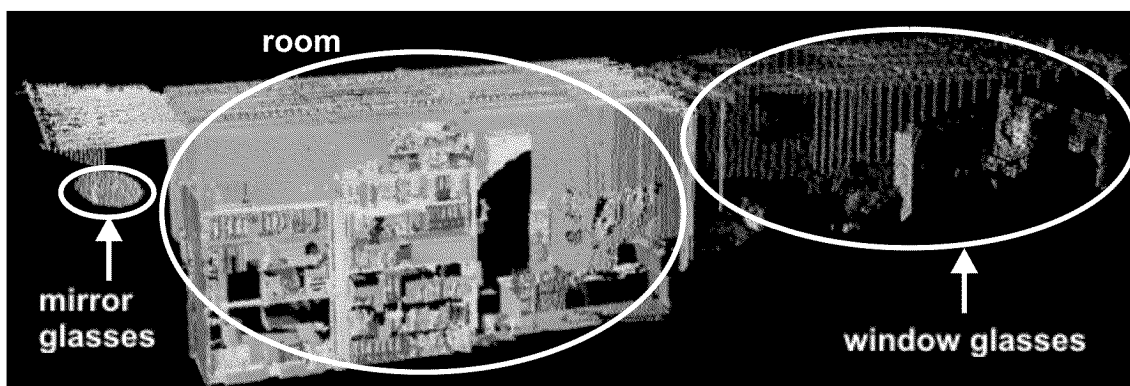


Figure 4.3: Effect of multipath. The scanned room is clearly visible in the middle of the figure. In the left part and in the right part erroneous pixels are caused by mirrors and windows.

4.1.5 Noise Reduction

Noise in laser scanning point clouds is mostly caused by the distance measurement system. The range, the colour of the surface and the angle of incidence influence the intensity of the reflected laser beam. The less the intensity, the more biased the data, cf. Chapter 3. Considering the noise, which is aligned along the distance measurement direction, processing of the noisy data can be carried out by filtering the data along the measuring direction.

It was found that the approximation of a pyramidal frustum, with its principal axis representing the measuring direction as defined by the center of the laser scanner towards the object points, is a promising filtering model. The length of the principal axis, which defines the height of the pyramidal frustum, considers the noise of the data. The noisier the data, the longer the principal axis. The bottom base and the top base define the filtering interval according to the scanning resolution of the laser scanner in the horizontal and vertical directions. The larger the base of the pyramidal frustum, the larger the resulting point spacing of the noise-reduced point cloud. Naturally, the base dimensions should not be smaller than the scanning resolution of the acquired point cloud.

As an example, a biased data set can be seen in Figure 4.4. The noise of the data is mostly caused by a small angle of incidence and a dark surface colour. The data shown describe the cross section of a one lane road section. The noise is found mostly at the dark skidmark. The indicated pyramidal frustum is oriented along the measuring direction. The height of the pyramidal frustum is chosen to define the amplitude or thickness of the noise. The rays defining the measuring direction intersect in the center of the laser scanner.

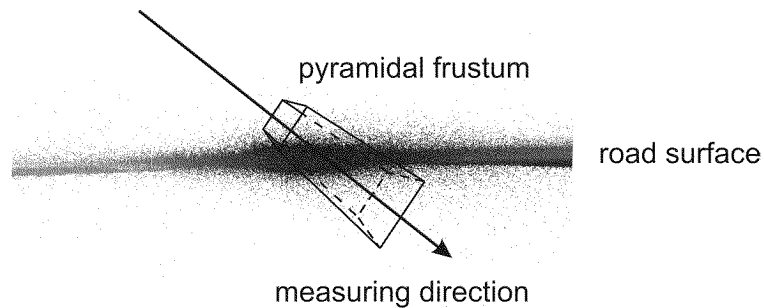


Figure 4.4: Noise in laser scanning data oriented along the measuring direction according to the filtering approach.

The noise reduction is made by averaging all points inside the pyramidal frustum. The averaging acts as a low pass filtering suppressing high-frequency noise from the signal. The signal is assumed to be the mean value, i.e. Gaussian noise. If the points are described by spherical coordinates¹, which refer to the local scanner origin (center of laser scanner), the mean value can be calculated by:

$$h = \frac{1}{n} \sum_{i=1}^n h_i, \quad v = \frac{1}{n} \sum_{i=1}^n v_i, \quad s = \frac{1}{n} \sum_{i=1}^n s_i, \quad (4.5)$$

where n is the number of points inside the pyramidal frustum. The selection of points to be located inside the pyramidal frustum is carried out based on the differences of the spherical coordinates of each point of the point cloud. One point of the point cloud is picked and the spherical coordinates are compared. The base of the pyramidal frustum is defined by a maximum acceptable angle difference, which has to be smaller than the scanning resolution of the point cloud. The maximum acceptable angle difference is equal in the horizontal and vertical directions since the scanning resolution of the laser scanner as well as the precision and the accuracy of the angle measurement system are also equal in both directions. If a different

¹Spherical coordinates are defined by two angle values h and v in the horizontal and vertical directions as well as by a distance value s .

maximum angle difference for the horizontal direction and the vertical direction is chosen, only the base of the pyramidal frustum changes from a square to a rectangle. The maximum difference in distances defines the height of the pyramidal frustum according to the thickness of the noise. Mathematically, the points are selected by

$$|h - h_i| \leq \Delta h, \quad |v - v_i| \leq \Delta v, \quad |s - s_i| \leq \Delta s, \quad (4.6)$$

where the pick point is described by the spherical coordinates h, v, s and all other points of the point cloud are described by h_i, v_i, s_i . The parameters $\Delta h, \Delta v, \Delta s$ define the dimensions of the pyramidal frustum. If one point is identified inside the pyramidal frustum, this point is flagged accordingly. The flag identifies the point belonging to a pyramidal frustum.

The result of the noise reduction is a smoothed and reduced point cloud. The sampling interval is increased according to the base of the pyramidal frustum. The number of points is decreased depending on the noise in the data and the chosen diameter. Intensity values are averaged according to Equation (4.5). The filtering algorithm requires spherical coordinates since Cartesian coordinates do not consider the noise aligned along the measuring direction. The base of the pyramidal frustum to be selected depends strongly on the measurement setup, especially the scanning resolution. Furthermore, the surface properties, e.g. colour and roughness, the range and the angle of incidence influence the noise and therefore, the dimensions of the pyramidal frustum.

The filter discussed combines both angle limits and distance limits. Other forms of filters are based either on distances or on angles. Points fulfilling the constraints showing similar distances or similar angles according to Equation (4.6) are averaged and replaced by a mean value. An indirect filtering and smoothing of point clouds is achieved by meshing and triangulation algorithms in commercial software packages, cf. Section 4.3.2.

4.2 Registration

Since most objects cannot be scanned from one single viewpoint, due to obstacles and line-of-sight obstructions, the laser scanner has to be positioned at different locations to scan the object or scene completely. From each viewpoint the acquired data of the laser scanner refer to the local scanner coordinate system. The goal is to find a transformation that optimally positions two or more data sets with respect to one reference data set, which is called registration. The transformation between two different coordinate systems \vec{x}_g and \vec{x}_l can be described mathematically by a rigid body transformation [Luhmann, 2003]:

$$\vec{x}_g = R \cdot \vec{x}_l + \vec{t} \quad (4.7)$$

where R defines the rotation matrix and \vec{t} describes the translation components. Furthermore, a scale factor, or a scale matrix by different scaling of the axes, can be introduced. Generally, the rotation matrix is an orthogonal matrix, which has to fulfil the three constraints [Bronstein and Semendjajew, 1999]

$$\begin{aligned} R^T &= R^{-1} \\ R \cdot R^T &= R^T \cdot R = I \\ \det R &= \pm 1 \end{aligned} \quad (4.8)$$

The rotation matrix can be defined in several ways. Two common ways are to describe the rotations by

- Euler angles and
- quaternions.

The use of Euler angles can be interpreted as a rotation about the coordinate axes by specific angles. The order of the rotations is important and not arbitrary. In some branches, e.g. physics and group theory, one distinguishes between x -convention, i.e. order of rotation about the axes are z, x, z , and the y -convention, i.e. order of rotation about the axes are z, y, z . A more general description is the rotation about all three coordinate axes in the order of x, y, z with [Jekeli, 2001]:

$$\begin{aligned} R(\alpha, \beta, \gamma) &= R_z(\gamma) \cdot R_y(\beta) \cdot R_x(\alpha) \\ &= \begin{bmatrix} \cos(\gamma) & \sin(\gamma) & 0 \\ -\sin(\gamma) & \cos(\gamma) & 0 \\ 0 & 0 & 1 \end{bmatrix} \begin{bmatrix} \cos(\beta) & 0 & -\sin(\beta) \\ 0 & 1 & 0 \\ \sin(\beta) & 0 & \cos(\beta) \end{bmatrix} \begin{bmatrix} 1 & 0 & 0 \\ 0 & \cos(\alpha) & \sin(\alpha) \\ 0 & -\sin(\alpha) & \cos(\alpha) \end{bmatrix} \end{aligned} \quad (4.9)$$

The advantage of Euler angles is that they can be interpreted geometrically and are easy to understand. However, there are also some disadvantages. The resulting rotation matrix can become singular. Thus, one rotation can be expressed by several Euler angles, which is called ‘Gimbal Lock’, due to the loss of one degree of freedom. Furthermore, the rotation matrix contains trigonometric functions. The equations have to be linearized if they are used for adjustment.

The rotation matrix can also be described by four parameters, called quaternions, which can be considered as a generalization of complex numbers [Jekeli, 2001]. Instead of representing a vector in two dimensions, in the case of complex numbers, a quaternion is a number representing a vector in four dimensions. It consists of a real part and an imaginary part [Jekeli, 2001]:

$$\vec{q} = q_0 + iq_x + jq_y + kq_z = \left[q_0, \begin{pmatrix} q_x \\ q_y \\ q_z \end{pmatrix} \right]. \quad (4.10)$$

The rules for algebraic operations can be found in various literature, cf. [Jekeli, 2001], [Dam et al., 1998] and [Mikhail et al., 2001], and are similar to the rules for complex numbers. Geometrically, the quaternion describes a rotation about a vector, which intersects the origin of the coordinate frame. The orthogonal rotation matrix resulting from a rotation of one unit quaternion, which is a quaternion of absolute value 1, can be described by

$$R(q) = \begin{bmatrix} q_0^2 + q_x^2 - q_y^2 - q_z^2 & 2 \cdot (q_x q_y - q_z q_0) & 2 \cdot (q_x q_z - q_y q_0) \\ 2 \cdot (q_x q_y + q_z q_0) & q_0^2 - q_x^2 + q_y^2 - q_z^2 & 2 \cdot (q_y q_z - q_x q_0) \\ 2 \cdot (q_x q_z + q_y q_0) & 2 \cdot (q_y q_z + q_x q_0) & q_0^2 - q_x^2 - q_y^2 - q_z^2 \end{bmatrix} \quad (4.11)$$

The use of quaternions instead of Euler angles is of advantage. The rotation can be described by four parameters. The resulting degree of freedom of only one can be eliminated by introducing the condition that the quaternion has to be a unit quaternion. The concatenation yields an efficient algorithm due to the reduced number of numerical operations. Furthermore, the algorithm does not need initial values for the unknowns because of the bilinear equations [Rietdorf, 2005].

In either case, the registration algorithm is described by at least six parameters, three for the translation and three for the rotation. This description is feasible since the two coordinate frames to be registered are similar

and generally fulfill the constraints of orthogonality. Furthermore, a scale factor can be introduced, which increases the number of unknowns up to seven. The minimum number of corresponding points defining the transformation between the two coordinate frames is three. Generally, these corresponding points can be either defined by targets, which have to be modeled using the point cloud, or by using the point cloud directly.

A distinction can be made between a registration based on artificial or natural targets and a registration based on overlapping point clouds. Both methods are introduced and discussed regarding advantages and disadvantages. Depending on the method, the registration describes only a transformation between local coordinate frames or defines a transformation between several local coordinate frames and one global reference frame. The transformation into a global reference frame requires control points with known coordinates.

4.2.1 Target-Based Registration

Registration using targets requires considerations regarding two different aspects: the type of targets and the spatial distribution of targets. Targets can be both artificial and natural. In either case, the target information has to be derived based on the acquired point cloud, e.g. center point, radius, normal vector. Geometrical primitives seem to be well-suited for supporting this information, such as planar objects, i.e. planes, spheres, cylinders. Generally, the best results can be obtained by specific artificial targets. Most laser scanner manufacturers also provide targets, which define such tie points or control points². Often, these tie points can be surveyed by total stations or by GPS. This is helpful since the local coordinate frame defined by the laser scanner can be included into other local or global reference frames. Another aspect is the surveying of such targets reduces the constraint that neighbouring point clouds have to be connected by at least three tie points or objects.

Artificial targets have to be designed according to the specifications of the laser scanner. The target should be dimensioned such that a sufficient number of points hit the surface. The material and the colour have to have the appropriate wavelength and reflectance properties. The use of different reflectivity values may ease the calculation of the geometrical center of the target, e.g. retro-reflective targets. Figure 4.5 shows three different targets used for laser scanning. The left one is a circular planar retro-reflective target with a white inner circle and a blue outer circle, designed by HDS Leica Geosystems. In the middle, a planar black-white coded target of Zoller+Fröhlich can be seen. The right part contains a wooden and white-painted sphere mounted on a tribrach constructed by ETH Zurich. All three targets have dimensions and masses appropriate for field work. The balance between size and mass of the target on one side and the ease of transportation on the other side are of importance.

Instead of artificial targets, natural targets can also be used. Often, planar objects can be found in the environment, e.g. walls of buildings. Sometimes, also cylinders or spheres are available. They are good choices to be included in the registration process, especially if they are located in regions in which artificial targets can be rarely positioned and/or are inaccessible. The accuracy provided by natural targets are not as high as that provided by artificial targets. However, the use of such targets is recommended to stabilize the registration. Based on registration results, targets can be assessed and deactivated when they do not satisfy accuracy requirements.

The algorithms for calculating the mathematical point of reference for each target is either implemented in the software tools provided by the manufacturers or available in numerous software tools for processing laser scanning point clouds. The accuracy achievable for the point of reference is dependent on several aspects, e.g. geometry and orientation of the target, noise within the point cloud, but can be increased up to a few millimeters.

²A control point is a tie point that was surveyed and can be defined by global coordinates.

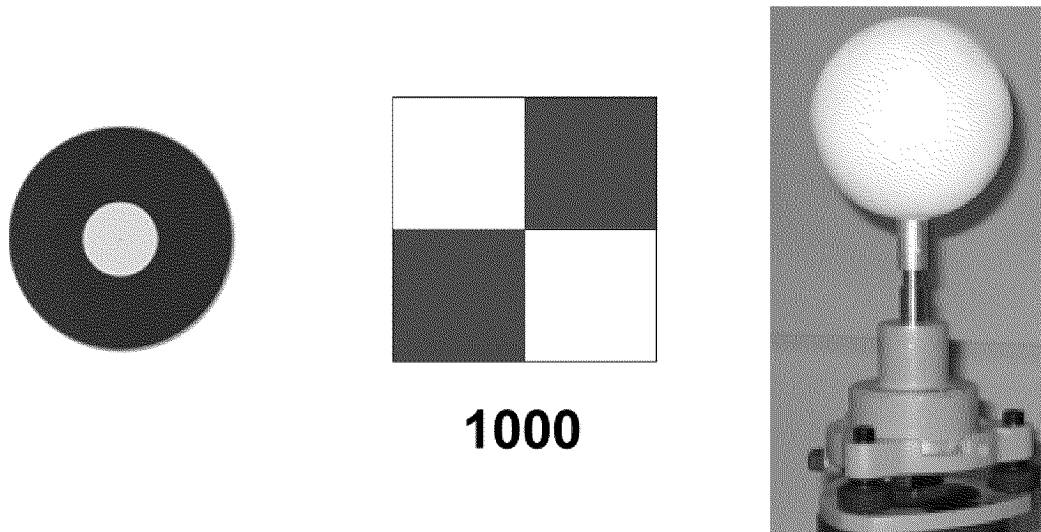


Figure 4.5: *Types of artificial targets used for laser scanning: HDS Leica Geosystem circular planar target (left), ZF coded planar target (middle), ETH Zurich sphere target (right).*

The distribution of targets is often disregarded during laser scanning field work. The instruments are investigated and calibrated intensively to improve the accuracy of laser scanners. But in return, the accuracy is decreased through carelessness in the field caused by awkward and poor target distributions. The results based on the distribution worsens the accuracy significantly. In photogrammetry, and analogous in terrestrial laser scanning, control points have to be chosen in such a way that they

- cover the full object volume to avoid extrapolation,
- do not hide important parts of the object, and
- are of a reasonable number.

Investigations showed that for an indoor project with a dimension of $10 \times 10 \times 3 \text{ m}^3$ the influence of poor distributions of control points can reach several centimeters. A reasonable number of targets of about 4 to 6 for two different scan positions is recommended. The use of more targets does not increase the accuracy significantly unless there is a probability of unsuitable targets that should not be used for the registration process.

The coverage of the full object volume is essential since extrapolation should be avoided and may result in increasing errors. High or linear objects, such as towers and buildings, require an appropriate distribution of the targets in height as well. Unfortunately, in most cases the attachment of artificial targets is impossible. Thus, other registration techniques should be used, e.g. natural targets or point cloud registration, and should be combined with each other.

4.2.2 Point Cloud Registration

The point cloud registration offers the possibility to transform one or more data sets to another without using targets. The only constraint is the two data sets show areas of overlapping point clouds. This means both data sets have to contain point clouds that describe the same objects. The advantages of this procedure is that no artificial or natural targets are required and a high redundancy is achieved. The disadvantages are due to the principle of laser scanning:

- There is no object point that can be acquired exactly and identically a second time from a different scanner position.
- Blunders and noise of the point clouds have to be completely eliminated beforehand since they directly influence the registration algorithm.
- The registration only refers to a local coordinate frame defined by one scanner position.

The point cloud registration tries to find corresponding points within the point clouds despite each single point not being acquired a second time. First, the scanning principle does not support the alignment of the laser beam exactly in the same direction a second time, due to the rough angle increment. Second, the change of the viewpoint implies a change in the alignment of the laser beam, which results in a different position of the footprint of the laser beam and a different angle of incidence. The quality of the point cloud is influenced by several parameters, e.g. range, surface properties and angle of incidence, which cause noise and blunders. Since the point cloud registration directly uses the acquired data, the results are directly dependent on the quality of the point cloud. It is recommended to pre-process data with appropriate noise reduction and filter techniques. Since the point cloud registration algorithm works only with the acquired point cloud, the reference frame is defined by one local reference frame. If the point cloud has to be included in a global reference frame, additional control points with global coordinates are required.

In recent years, several algorithms have been developed and are currently the topic of research projects. The most popular algorithm is the iterative-closest-points algorithm (ICP) developed by [Besl and McKay, 1992], [Chen and Medioni, 1991], and [Zhang, 1994]. This algorithm starts with two point clouds and an estimate of aligning the rigid body transform. It then iteratively refines the transformation by alternating the steps of choosing corresponding points across the point clouds, and finding the best rotation and translation that minimizes an error metric based on the distance between corresponding points. The ICP algorithm is varied and improved many times [Bergevin et al., 1996], [Masuda and Yokoya, 1996]. A detailed overview at ICP algorithms can be found in [Gühring, 2002] and [Grün and Akca, 2005], who also introduced a new algorithm, the least squares 3D surface matching.

4.3 Modeling and Visualization

Modeling is the step followed by registration. The objects described by a point cloud have to be processed in such a way that geometrical information can be derived. The point cloud is well-suited for online-visualization. All conceivable information are hidden within the point cloud. Although, point clouds can be the final products of laser scanning, information derived from the point cloud are often what is required. Such information are frequently of geometrical nature, but classifications analogous to airborne laser scanning and remote sensing are also conceivable to distinguish between different objects on the surface, e.g. wet areas, roads, vegetation.

The processing of the point cloud depends on the project and the application. Based on these aspects the most suitable software has to be selected. Commercial software packages can be distinguished between software directly using the large number of points of the acquired point cloud and software operating only with a selected number of points.

Working group V/3 from the International Society of Photogrammetry and Remote Sensing (ISPRS) has published the most popular software based on a questionnaire in 2005. Table 4.1 summarizes the most popular software. The goal of using this software is of further interest, e.g. for registration, modeling, editing, visualization, data inspection, format conversion. More information can be found from the ISPRS working group V/3.

Table 4.1: Software for processing laser scanning data. The results are based on a questionnaire carried out by the ISPRS working group V/3.

Software	Manufacturer	Use [%]
Cyclone	HDS Leica Geosystems	28
Geomagic	Raindrop	17
RiScanPRO	Riegl	11
CloudWorx	HDS Leica Geosystems	9
Polyworks	InnovMetric	8
rest	various	27

4.3.1 Geometrical Primitives

The modeling of geometrical primitives is extensively automated. The parameters for geometrical objects are computed by a least square adjustment using Gauss-Markov or Gauss-Helmert. The following objects are considered as geometrical primitives and can be mostly computed semi-automatically or fully automatically:

- patch or plane : $\vec{p}_i \vec{n} - d = 0$
- sphere : $|\vec{p}_i - \vec{m}| - r = 0$
- cylinder : $\vec{a}(\vec{p}_i - \vec{m}) - r = 0$

The vector \vec{n} describes the unit normal, \vec{p} defines each point of the point cloud, \vec{m} is the center point of the sphere or the cylinder, and \vec{a} characterizes the orientation of the principal axis of the cylinder. The parameters r and d define the radius and the diameter, respectively. A more detailed description for calculating geometrical primitives can be found in [Hovenbitzer, 2003].

4.3.2 Triangulation

Triangulation or mesh generation can be described as the process of finding geometrical objects in a given data set, i.e. triangles in 2D and tetrahedra in 3D. Typically, this process is based on Delauny triangulation or marching cubes [Hoppe et al., 1992] and [Carr et al., 2001]. Some possible constraints for building triangles or tetrahedra are defined by [Hoscheck and Lasser, 1992]

- criterion of the shortest diagonal,
- criterions of the minimum/maximum angle and maximum/minimum angle, respectively, and
- criterion of the circumscribed circle.

The last criterion leads to the Delauny triangulation, which postulates that the circumscribed circle of each triangle must not contain a fourth point of the data set [deBerg et al., 2002]. The Delauny triangulation computes uniform triangles and avoids both long and short triangles as well as overlapping triangles. More information can be found in a number of publications, e.g. [deBerg et al., 2002], [Carr et al., 2001] [Hoppe et al., 1992], [Hoscheck and Lasser, 1992], [Rietdorf, 2005].

4.3.3 NURBS

NURBS is an acronym for non-uniform rational B-splines. The first publications of NURBS refer to [Riesenfeld, 1973] and [Versprille, 1975]. A NURBS can be described either by a curve or by a surface. Detailed mathematical descriptions can be found in [Piegl, 1991].

For laser scanning, the use of NURBS is becoming important since the surveyed objects described by the point cloud cannot only be modeled with geometrical primitives but also with free-form shapes. NURBS is an efficient tool for approximating free-form curves and surfaces. According to [Piegl, 1991], some of the advantages of NURBS are they

- offer a common mathematical form for standard analytic shapes and free-form curves and surfaces,
- provide the flexibility to design a large variety of shapes,
- have clear geometrical interpretations,
- have a powerful geometrical tool kit,
- are invariant regarding scale, rotation, translation, and
- are genuine generalizations of non-rational B-spline forms as well as rational and nonrational Bézier curves and surfaces.

Some drawbacks of NURBS are they require extra storage to define traditional curves and surfaces and they can result in very poor parameterization due to improper use of required parameters.

Designing NURBS can be carried out in two ways, interpolation and data filtering. Interpolating means geometrical functions are fitted into a given set of control points to derive a new set of data. Interpolating can produce erroneous results due to the existence of noise or blunders. A better solution is an approximation of the given set of data by fitting geometrical functions close to the given data set and by passing only a few of them. The most popular approximation is least-squares fitting. The result of least squares fitting is a smoothed and less-biased description of the data set.

NURBS has become widely accepted and popular, especially in computer-aided design (CAD), computer-aided manufacturing (CAM), and computer-aided engineering (CAE), and the graphics community.

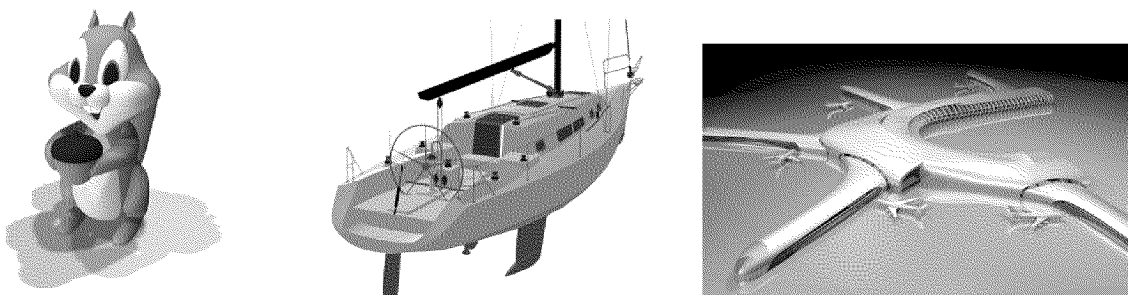


Figure 4.6: Examples for NURBS modeling and rendering, from left to right: squirrel, sailing yacht, airport [Rhinoceros[®], 2006].

4.3.4 CAD

Computer-aided Design (CAD) is a computer-based tool to design and develop 2D drawings or 3D models. CAD is used in many fields, such as architecture, building engineering and mechanical CAD, e.g. automotive, aerospace, ship building. Within the product lifecycle management process, CAD is the main geometry authoring tool, cf. Figure 4.7.

There are various different software packages available on the market, e.g. AutoCAD, Microstation, SolidWorks. Depending on the application area, the most suitable software has to be chosen. Compared to 3D point cloud software, the drawback of CAD software is only a limited number of points that can be imported into the CAD software. Either the point cloud has to be processed and reduced beforehand or additional tools have to be used, such as CloudWorx, which allows one to work in the AutoCAD environment but also allows access to the whole point cloud.

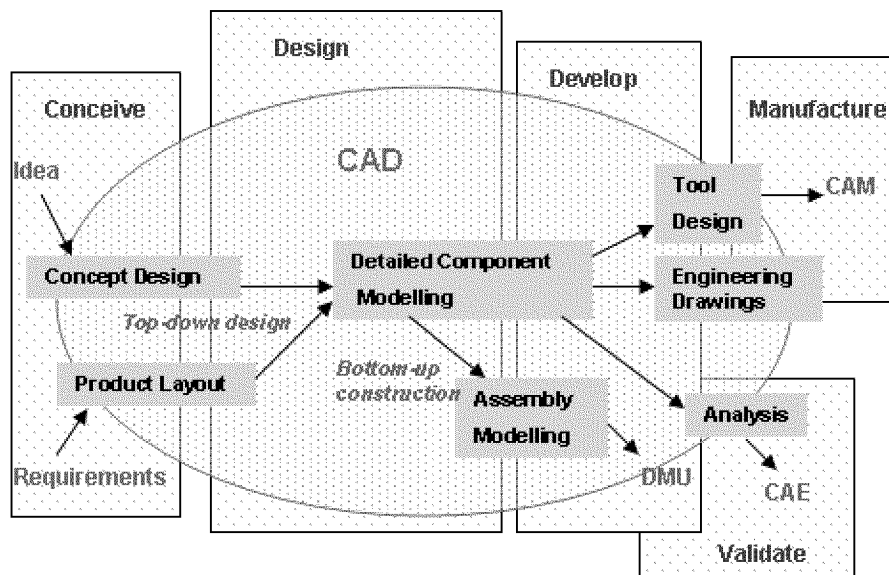


Figure 4.7: CAD and the many fields of applications, adapted from [Wikipedia, 2006].

4.3.5 Rendering and Texture Mapping

Since CAD models or NURBS models do not show a realistic image of the object, the derived model can be processed by rendering or texture mapping. Rendering is the process of improving the appearance of the object by introducing light sources or other visual effects. Texture mapping means that digital images, either images of the real object or patterns, are mapped onto the model in perspective view. Such processes are often necessary to provide impressive and realistic models for marketing and visualization purposes. Some examples are shown in Figure 4.6. For such purposes, visualization graphics libraries are required. The most-used libraries are OpenGL, VRML, Java3D and Direct3D [Hovenbitzer, 2003].

Kinematic Laser Scanning

The high data acquisition rate of laser scanners facilitates the use of such instruments in a kinematic mode. The advantages of performing kinematic measurements are manifold, e.g. reducing surveying time at construction sites and improving the performance of surveying. In the application of railways and roads, kinematic laser scanning is especially beneficial for the detection of linear structures, such as rails, catenary, and sign-posts.

For several years, laser scanners have been included in so-called mobile mapping systems for surveying roads and road installations, e.g. conditions of the roads, traffic lights, traffic signs, sign-posts. However, roads are not the only objects of interest. In recent years, the monitoring of tunnels during and after excavation has become more of interest. Traditional techniques for deformation surveying are no longer the only conceivable possibilities. Laser scanners guarantee high point density and high sampling frequency. Furthermore, laser scanning is based on an active laser light and prismless distance measurements. An accuracy in the order of millimeters is achievable if influential parameters are considered and if the laser scanner was calibrated beforehand. High point density seems to be the most important advantage because deformation monitoring is not only limited to some discrete points but also to whole objects.

This chapter deals with the essential aspects concerning the use of a terrestrial laser scanner in kinematic applications. Before introducing the problem and the key elements of kinematic measurements, the meaning of 'kinematics' should be clarified. One definition of kinematics is given in [American Heritage Dictionary, 2004]

Kinematics is the branch of mechanics that studies the motion of a body or a system of bodies without consideration given to its mass or the forces acting on it.

From the point of surveying, a 'kinematic' application means that during a measurement process there is a relative motion between the surveying instrument and the object to be surveyed. Thereby, either the object is in motion, e.g. deformation process, or the surveying instrument is in motion, e.g. mounted on a vehicle. Here, the focus is on the latter. Several aspects have to be considered, such as:

- generation of time tags for data acquisition of all involved instruments
- synchronisation of all different types of involved instruments
- calculation of position and orientation of the surveying instrument with respect to a global coordinate system

In this thesis, the terrestrial laser scanner Imager 5003 of Zoller+Fröhlich is the surveying instrument in motion. The 'scanning' mode was characterized by a deflection mirror that rotates about two perpendicular axes. On the contrary, in the 'profiler' mode used for kinematic application, there is only rotation of the

mirror about one axis. The missing third dimension is generated by the motion of the scanner by means of a test trolley.

The following sections discuss the key elements that are necessary to perform kinematic applications. First, the test trolley, the calibration track line and the characteristics and particularities of the test laboratory are described. Second, the laser scanner is investigated regarding the determination of a rotation time that may define a time tag. The third part involves the total station, which determines the position of the moving test trolley on the calibration track line. The focus is on the processing of the acquired data with the purpose of using this data for kinematic applications. Last, some aspects regarding the synchronization of the data, which were acquired by the two instruments, the laser scanner and the total station, are discussed.

Although the data acquisition and registration processes differ for static laser scanning applications and kinematic laser scanning applications, data processing and modeling and visualization aspects are similar. Thus, the remarks of Chapter 4 regarding these aspects are also applicable for kinematic laser scanning.

5.1 Test Trolley on Calibration Track Line

The laser scanner is mounted on the test trolley, which moves along the calibration track line. The laser scanner operates in the profiler mode. This means the laser beam only rotates in a 2D plane. The resulting coordinates, regarding the relative local scanner system, are only 2D coordinates. The absolute position, as well as the missing third dimension for 3D coordinates, have to be acquired by additional sensors. The third dimension is generated by an automated total station, which is tracking the moving test trolley. The use of a total station also allows for the inclusion of the 3D coordinates in an absolute reference system.

Surveying in kinematic applications requires not only the position of the moving trolley in 3D coordinates, but also additional information on the orientation of the test trolley. The latter is essential since varying orientations of the trolley lead to variations in the local reference system. The orientation can be described by three attitude angles, which define the orientation of the local system with respect to the absolute system.

In summary, the information required to generate 3D point clouds, which are acquired by the moving laser scanner, in an absolute coordinate system are:

- position vectors of the point cloud in the local scanner system \vec{x}_l
- rotation matrices described by three attitude angles that define the orientation of the local scanner system with respect to the absolute coordinate system
- position vectors of the moving local scanner system with respect to the absolute coordinate system \vec{x}_a .

Mathematically, the position vectors for the point cloud with respect to the absolute reference system can be calculated by

$$\vec{p} = \vec{x}_a + R \cdot \vec{x}_l. \quad (5.1)$$

The rotation matrix R influences the position vectors \vec{p} such that with growing distances from the laser scanner, an erroneous rotation increases errors in the position of the points. This is known as the lever arm effect. The shorter the object range, the less the position error. In addition, the translation vector \vec{x}_a only causes a constant shift of all the points. Thus, an erroneous translation vector has the same influence on each point.

The setup for kinematic laser scanning is shown in Figure 5.1. The laser scanner is mounted on the test trolley and is equipped with a prism on top of the laser scanner. The trolley moves along the track line and

the automated total station tracks the prism. The laser scanner generates 2D profiles of the environment. The following sections describe the setup for the kinematic application performed on the calibration track line. The setup is optimized and applied to the present situation, but the considerations are in a general way and can also be adapted to other setups.

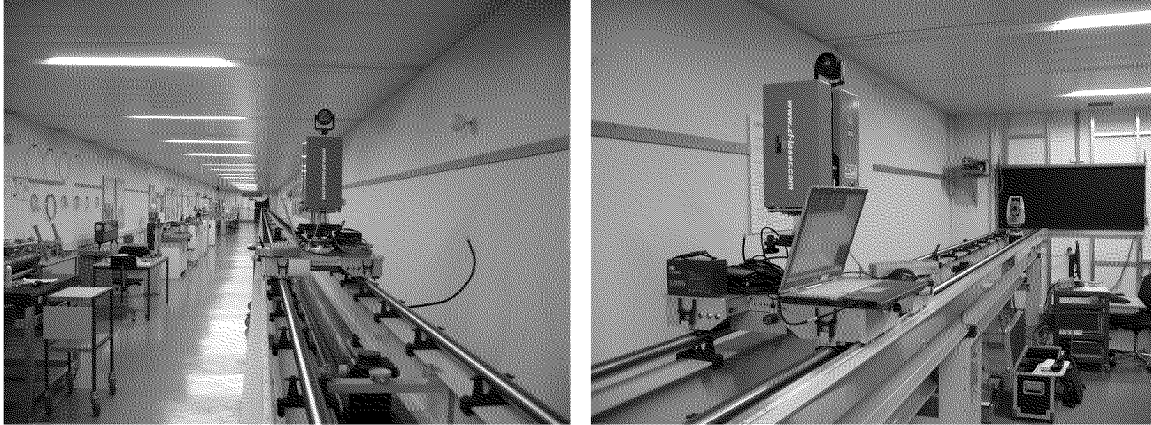


Figure 5.1: Laser scanner mounted on the test trolley of the calibration track line. The test trolley is moving along the calibration track line. The laser scanner is operated in the profile mode and is tracked by an automated total station.

5.1.1 Relative Position and Orientation

The laser scanner defines the relative coordinate system, which moves along the calibration track line. The data acquired by the laser scanner refer to the local scanner system. Since the profile mode is used, the laser beam is deflected only in a 2D plane and the resulting coordinates for each point of the generated point cloud show two varying coordinates describing a 2D plane while the information required for the third dimension is not collected.

The relative position is defined by a centering device installed on the test trolley. This centering device allows for the positioning of geodetic instruments to a high degree of accuracy, i.e. tenths of a millimeter. An instrument can be attached directly on the centering device or indirectly by using traditional surveying accessories like adapters and tribrachs. Thus, the position of the laser scanner on the test trolley is defined and the accuracy for independent and repeated measurements is guaranteed.

The relative orientation of the laser scanner can be divided into two aspects. The first aspect refers to the levelling procedure and the second aspect refers to the azimuthal direction of the laser scanner. In the levelling procedure, the instrument is levelled horizontally by using screws and a level attached on the laser scanner. The azimuthal orientation defines the orientation of the profiles that are acquired by the laser scanner. The azimuthal orientation can be done by using the calibration track line and the observation pillars. Specifically, the observation pillar, which is located in extension from the track line (pillar number 2000, cf. Figure 3.4), is used. This observation pillar is positioned nearly along the axis of the track line. Each azimuthal orientation can be achieved by determining the orientation, e.g. scanning a sphere mounted on the pillar and deriving the azimuthal direction, and adding an angle to determine the orientation for the profiles. The laser scanner can be rotated to the specific azimuthal direction and therefore, is oriented. The azimuthal orientation is chosen in such a way that the profiles of the laser scanner are normal to the moving direction of the test trolley along the calibration track line. This means that to the azimuthal direction to the center point of the sphere placed on the pillar in extension from the track line an angle of 90° has to be added, cf. Figure 5.2. The levelling procedure and the azimuthal orientation are essential parts of the relative orientation.

The accuracy of the orientation depends on the accuracy of the determination of the azimuthal direction to the sphere and the precision of the horizontal encoder system. If the scanning profiles are not normal to the moving direction, the misalignment can be corrected mathematically by using control points since the profiles are shifted by a constant angle. This lever arm effect was discussed earlier.

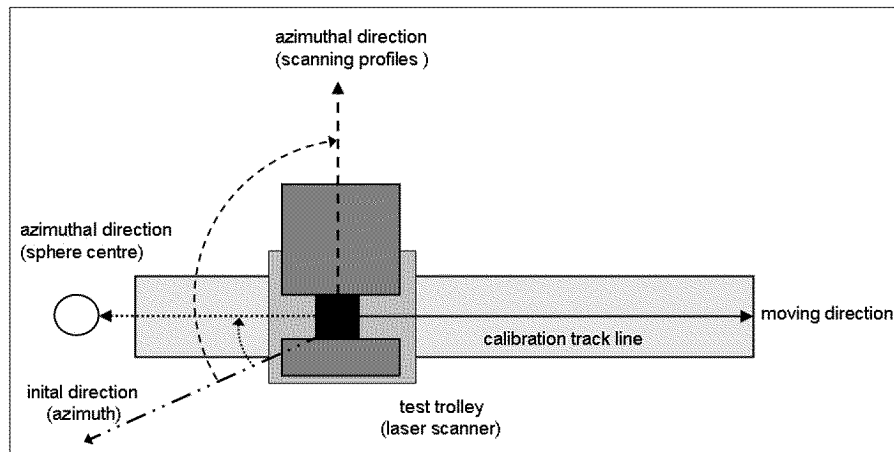


Figure 5.2: Azimuthal orientation of the laser scanner. The azimuthal direction to the sphere can be derived and the azimuthal direction for the profiles can be determined by adding a specific angle (here: 90°).

5.1.2 Absolute Position and Orientation

The absolute position and orientation of an object is defined by three coordinates and three attitude angles. To measure the six degrees of freedom, different sensors and instruments can be used, e.g. accelerator sensors, inclination sensors, tracking total station, global positioning system. Inertial navigation systems (INS) directly provide the desired six parameters. The sensors and instruments that should be used and are appropriate for the specific application depend on the desired accuracy and the environment. If the object is in motion, these six parameters are time-dependent and define the 3D-trajectory.

The kinematic application performed on the calibration track line allows for some simplifications. The test trolley moving along the track line is forced to run on a fixed track. The trolley cannot run in other directions. The trajectory of the calibration track line is well-known and already discussed in Section 3.1.1. This trajectory can be described by variations in the straightness of the alignment, by variations in the vertical alignment and by variations in the cant. The verification of the deviations of the different linearities shows only small variations. The measurement of the three attitude angles (ω , ϕ , κ) is not necessary since the trajectory is well-defined. For simplifications, it is also possible to approximate the trajectory as a constant line, which runs horizontally. The error budget of this approximation is in the same order of magnitude as the accuracy of the point cloud acquired by the laser scanner.

The absolute position of the test trolley moving along the track line is measured by an automated total station. The laser scanner is equipped with a prism holder to attach a prism, which is tracked by the total station. Since in kinematic applications the synchronization between the distance and the angle measurement system of tracking total stations is of importance [Stempfhuber, 2004], a setup for the kinematic application is chosen so that the error resulting from a conceivable erroneous synchronization is minimized. The total station is positioned in extension from the track line (pillar number 2000, cf. Figure 3.4). The test trolley moves away or towards the total station, resulting mostly in varying distances rather than varying angle directions. The setup can be seen in Figure 5.1.

Since the prism is not installed in the origin of the local scanner system, the translation vector between the prism and the origin of the local scanner system has to be verified. The translation vector consists of three components in x -, y - and z -direction. The installation of the prism was chosen so that the prism is on an axis that is parallel to the moving direction and normal to the scanning profiles, cf. Figure 5.3.

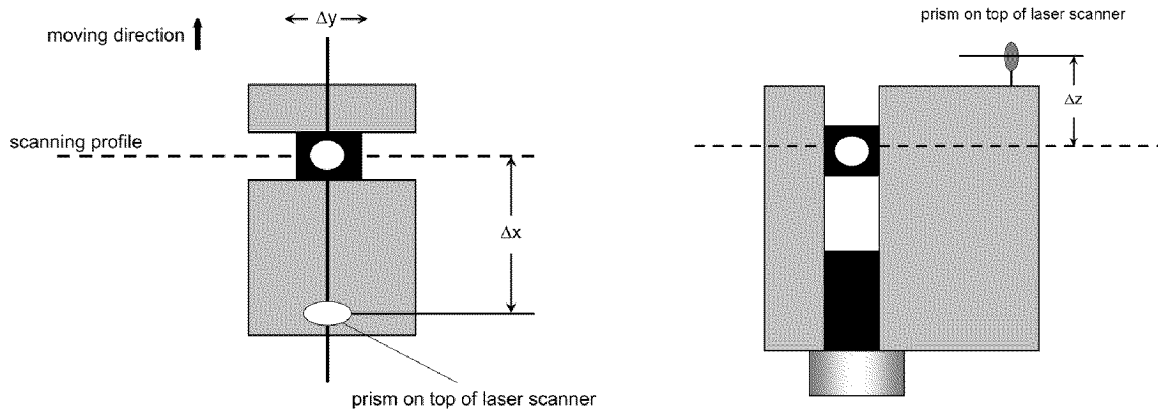


Figure 5.3: Installation of a prism on top of the laser scanner. The offsets to be calibrated can be seen in the horizontal projection (left) and in the vertical projection (right).

The translation vector can be described by

- a translation normal to the scanning profiles: Δx ,
- a translation normal to the moving direction: Δy , and
- a translation vertical to the moving direction (Δz).

The component Δy should be minimized, in the ideal case becomes $\Delta y = 0$. The determination of the position of the prism holder regarding the offset Δy is carried out as follows. The laser scanner is mounted on an observation pillar and a sphere is mounted on another observation pillar. The azimuthal direction to the center of the sphere is derived by scanning the sphere and calculating the center point. Based on the coordinates of the center point, the azimuthal direction is given and the laser scanner can be positioned in such a way that the scanning profile is perpendicular to the azimuthal direction of the center point of the sphere by rotating the laser scanner $\pm 90^\circ$. The precision in orienting the laser scanner to a specific azimuthal direction is verified beforehand by using a total station and surveying a target attached on the laser scanner. The precision shows a value of less than 0.0015° . The scanned sphere on the observation pillar is then replaced by a total station. The prism on top of the laser scanner is surveyed and the horizontal directions are read. In the ideal case, the horizontal directions to the prism have to be equal if the laser scanner is rotated $+90^\circ$ and -90° , regarding the computed azimuthal direction to the observation pillar. In reality, there is a deviation of 0.015° between the two horizontal directions. Considering a distance of approximately 5.24 m between laser scanner and total station, the deviation can be expressed by a metric value of 1.4 mm. Half of this value defines the offset Δy between the prism center and the normal line to the scanning profile that intersects the origin of the local scanner system. Considering the accuracy of the laser scanner, the offset of 0.7 mm is negligible.

The component Δx is derived by total station surveying and using the test field of observation pillars, cf. Section 3.1.3. The laser scanner is attached on a pillar and from the other pillars, a test field consisting of three prisms and the prism mounted on top of the laser scanner is surveyed. The local nets of the surveying can be transformed to the coordinate system of the observation pillars by using control points. As a result, the prism of the laser scanner has coordinates with respect to the reference system. Since the laser scanner

has a negligibly small eccentricity of the scan center, cf. Section 3.4.1, and since the prism attached to the top of the laser scanner has a negligibly small offset of Δy , the coordinates of the pillar on which the laser scanner is set up and the coordinates of the prism can be compared. Therefore, the coordinate differences in x - and y -direction define the component Δx of the translation vector between the origin of the laser scanner system and the prism attached to the laser scanner. The resulting value of the component Δx has an offset of 0.158 m. The accuracy is sufficient with a value of less than one millimeter.

The component Δz can be obtained by using the same procedure applied for deriving the component Δx . The only difference is the resulting coordinate difference between the z -values of the prism and the observation pillar on which the laser scanner is mounted also contains the height of the origin of the laser scanner system. Thus, the height of the instrument has to be considered and subtracted. The resulting value of the component Δz is an offset of 0.159 m. The accuracy is sufficiently high with a value of less than one millimeter.

Table 5.1 summarizes the translation vector between the prism on top of the laser scanner and the origin of the local scanner system.

Table 5.1: 3D translation vector between the prism atop the laser scanner and the origin of the local scanner system.

Δx [m]	Δy [m]	Δz [m]
0.158	0.000	0.159

5.2 Rotation Time of Rotating Mirror of Laser Scanner

The laser scanner is operated in the profile mode. For each point measured by the laser scanner, a time reference is required to synchronize the laser scanner data with data from additional instruments. The mirror of the laser scanner rotates quickly about its horizontal axis and the data acquisition rate is fast. Therefore, the generation of a time tag for each single laser point is not recommended. It seems more reasonable to validate if the rotation of the mirror is constant and is, therefore, appropriate for the use as time base. If there is a constant periodic time for one full rotation about 360° , the rotation time T can be derived by

$$T = \frac{2\pi}{\omega}. \quad (5.2)$$

The rotation time T then serves as time information. By knowing this rotation time and the number of measured points for one vertical profile, a time tag can be calculated for each single point measured by the laser scanner. If a common time base is available, data from different instruments can be synchronized. For example, one typical time tag is the PPS signal provided by GPS signals with an accuracy of approximately 1 ms. The following sections deal with the determination of the rotation time T . The aim is to specify the rotation time with a precision of

$$\sigma_T \sim 1 \mu s. \quad (5.3)$$

Two different and independent ways are presented to determine the rotation time T with high precision. The first method derives directly the rotation time T by means of two photo diodes, which detect the rotating laser beam. Additionally, a center angle α has to be determined. Based on the measured time delay between the two photo diodes, which were hit by the rotating laser beam, and the corresponding center angle, the rotation time T can be calculated. In contrast, the second method deals with the runtime and

with the total number of rotations of the mirror during a measurement and derives the rotation time T indirectly.

5.2.1 Direct Method

In the direct method, the principle of deriving the rotation time is based on measuring a specific time delay Δt . This time delay is defined by two adjacent photo diodes, which detect the rotating laser beam of the scanner. By knowing both the time delay Δt and the corresponding center angle α , defined between the center point of the rotation mirror and the two diodes, the rotation time T can then be calculated. The implemented diodes¹ are especially suitable for wavelengths between 460 nm and 1060 nm. The carrier wave of the laser scanner shows a wavelength of ≈ 700 nm and therefore, fits into the sensitivity interval. The maximum sensitivity is at 850 nm. Since the high frequency signal 'hfs' and the low frequency signal 'lfs' have wavelengths of $\lambda_{hfs} \approx 6.7$ m, $\lambda_{lfs} \approx 54$ m (close) and $\lambda_{lfs} \approx 108$ m (far), respectively, cf. Section 3.2, they fit not into the sensitivity interval of the diodes. Thus, the modulation frequencies cannot disturb the determination of the rotation time T using these diodes.

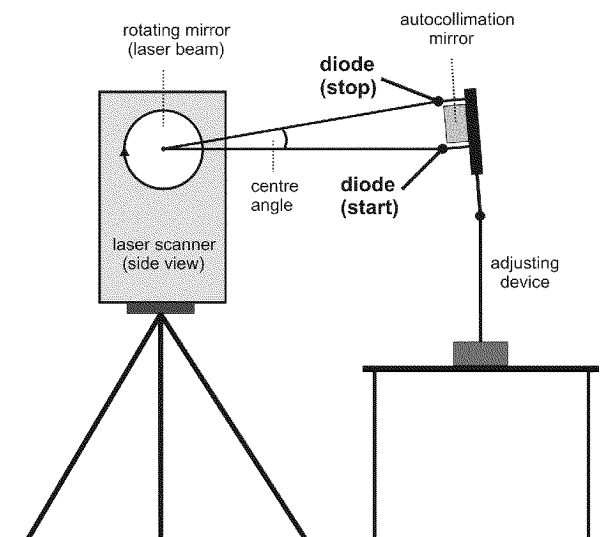


Figure 5.4: Experimental setup for deriving the rotation time T directly. Two photo diodes have to be aligned by means of autocollimation. The rotation time T can be calculated by knowing the time delay detected by the photo diodes and the center angle α .

An illustration of the principle is shown in Figure 5.4. At a certain distance, two diodes mounted on a plate were set up. One diode starts and the other diode stops the time measurement. A closer look to Figure 5.4 shows that the start-diode is below the stop-diode. This means that the derived time Δt does not correspond to the center angle α but rather to the opposite adjacent angle $\bar{\alpha}$ since in this setup the orientation of the rotation of the laser beam is clockwise. Consequently, the rotation time T results from

$$T = \frac{2\pi}{\bar{\alpha}} \cdot \Delta t = \frac{2\pi}{2\pi - \alpha} \cdot \Delta t. \quad (5.4)$$

Before explaining more in detail the experimental setup, the principle of deriving the time delay Δt and the center angle α , some notes are necessary regarding the use of two photo diodes. The ideal case is to mount only one photo diode on a plate and to detect the rotating laser beam hitting this diode. After initializing, the first detection of the rotating laser beam defines the start time and the second detection of the rotating laser beam defines the stop time. The theory seems to be simple, but in practice, it is more difficult. The laser

¹Mini-silicon NPN phototransistor SFH 305 of Siemens, Germany

beam is not punctiform, but has a more complex structure during propagation in the air, cf. Section 2.1.2. If the laser beam hits an object, a footprint of the laser beam is generated. Therefore, the 'real' footprint is much larger than the 'visible' footprint. Furthermore, the sensitivity of the diodes is important. Only a small part of the laser beam needs to hit the photo diode to start the process. If another part of the laser beam hits the photo diode directly a second time, the stopping process is performed. Neither does the laser beam rotate 2π nor can a reproducible and reasonable rotation time T be derived. To avoid these problems, either a more complex electronic circuit has to be developed or two photo diodes with a distance between them have to be implemented. The latter was used in this study.

The use of two photo diodes implicates some specialties with respect to the experimental setup. Additionally, the center angle α has to be determined. Referring to the postulation regarding the precision of the rotation time T , the required precision for the center angle α can be estimated. To achieve the best possible precision for the center angle α , the principle of autocollimation was used. In Figure 5.4, the two photo diodes, as well as the autocollimation mirror mounted on a plate, can be seen. This plate can be aligned by an adjusting device.

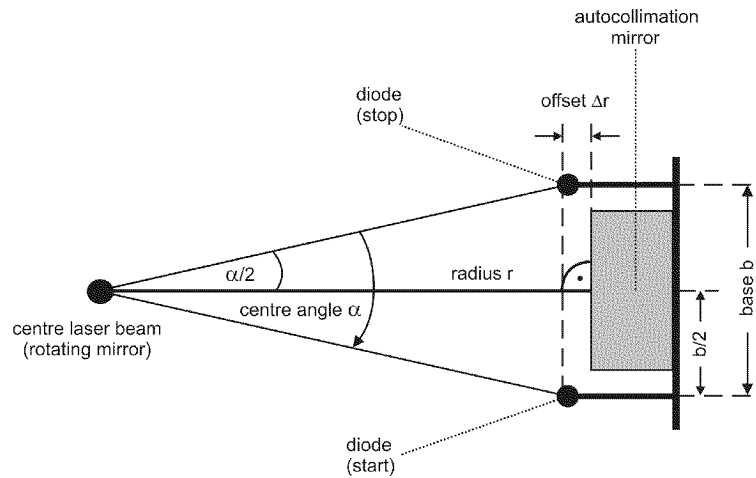


Figure 5.5: Mathematical relations for deriving the center angle α : the radius r , the base b and the offset Δr has to be known.

In Figure 5.5, the mathematical relation between the desired center angle α , the plate including the photo diodes, and the autocollimation mirror can be seen. The center angle α can be calculated by

$$\alpha = 2 \cdot \arctan \left(\frac{b}{2(r - \Delta r)} \right), \quad (5.5)$$

where r is the radius, i.e. distance between center of rotating mirror and autocollimation mirror, Δr is the offset between the photo diodes and the autocollimation mirror and b is the base i.e. the distance between the two diodes. The offset Δr was measured with a slide gauge several times. As result, the offset Δr is less than 0.5 mm with a precision of about 0.1 mm. Considering Equation (5.5), the influence of Δr is negligible, if the radius r is larger than 0.5 m. The reason is that, assuming the slowest angular frequency of 12.5 rps², the influence on the rotation time T is less than the time precision of $1\mu\text{s}$ claimed. Thus, Equation (5.5) simplifies to

$$\alpha = 2 \cdot \arctan \left(\frac{b}{2r} \right). \quad (5.6)$$

²Rps: rotations per second. According to the specifications of the manufacturer, there are three different rotating velocities: $\omega_{12.5} \approx 12.5 \text{ rps}$ ($T \approx 0.08 \text{ s}$), $\omega_{25} \approx 25 \text{ rps}$ ($T \approx 0.04 \text{ s}$) and $\omega_{33} \approx 33 \text{ rps}$ ($T \approx 0.03 \text{ s}$)

The questions raised now are: (1) How precisely does the center angle α have to be determined or what is the influence of the parameters base b and radius r . And (2) how accurate is the autocollimation.

(1) Precision of center angle α

Applying the propagation of errors and forming the total differential equation for Equation (5.6), the error for the center angle α can be estimated. Alternatively, the influence of the two parameters base b and radius r can be identified:

$$\sigma_{\alpha}^2 = \left(\frac{\partial\alpha}{\partial r}\right)^2 \sigma_r^2 + \left(\frac{\partial\alpha}{\partial b}\right)^2 \sigma_b^2. \quad (5.7)$$

Referring to the postulated requirement that the rotation time T should have a precision of less than $1\mu\text{s}$ at the beginning of this section, the maximal error for the center angle α can be derived. In other words: the time error σ_T for rotation time T caused by the precision of the center angle σ_{α} has to fulfill Equation (5.3). The maximal influence of this time error σ_T occurs at the slowest rotation speed $\omega_{12.5\text{rps}}$. In general, the required precision of the center angle σ_{α} can be derived from

$$\sigma_{\alpha} = \frac{\sigma_T}{\omega_{\text{rps}}} 2\pi. \quad (5.8)$$

Inserting all three possible rotation times provided by the manufacturer, the desired precision for the center angle α can be estimated. Table 5.2 shows the results of different time precisions σ_T and rotation times T . The shorter the rotation time, the more crucial the time resolution σ_T and the influence on the precision of the center angle σ_{α} .

Table 5.2: Influence of different time resolutions σ_T on the precision of the center angle σ_{α} . It is distinguished between the different angular frequencies ω_i . The higher the angular frequency, the more crucial the time resolution σ_T and influence on the precision of the center angle σ_{α} .

σ_T [μs]	σ_{α} [$^{\circ}$]		
	$\omega_{12.5}$	ω_{25}	ω_{33}
1	0.004	0.009	0.012
2	0.009	0.018	0.024
5	0.023	0.045	0.060
10	0.045	0.090	0.120

Now, the precision required for σ_{α} can be assessed. Considering Equation (5.7) once again, the base b becomes the key factor. The following Table 5.3 shows the influence of the precision of the base σ_b and the radius σ_r on the precision of the center angle σ_{α} . The base b was measured several times with a slide gauge. The base has a value of 24.8 mm with a precision of less than 0.1 mm. Thus, all derived values for σ_{α} are based on this specific base.

Table 5.3: Precision of center angle σ_{α} by using autocollimation. The precision of the radius σ_r has a minor influence compared to the precision of the base σ_b . The longer the radius r , the better the precision of the center angle σ_{α} .

	$r = 1 \text{ m}$			$r = 2 \text{ m}$			$r = 5 \text{ m}$		
	σ_b [mm]	σ_r [mm]	σ_{α} [$^{\circ}$]	σ_b [mm]	σ_r [mm]	σ_{α} [$^{\circ}$]	σ_b [mm]	σ_r [mm]	σ_{α} [$^{\circ}$]
σ_b [mm]	1	1	0.5	1	1	0.5	1	1	0.5
σ_r [mm]	1	5	5	1	5	5	1	5	5
σ_{α} [$^{\circ}$]	0.029	0.029	0.015	0.014	0.014	0.007	0.006	0.006	0.003

Table 5.3 shows two aspects. First, the precision of the radius σ_r does not influence the precision of the center angle σ_α . Second, both an increasing radius and an increase in the precision in the base σ_b lead to an increasing precision of the center angle σ_α . Furthermore, at least a value for $\sigma_b \approx 0.5 \text{ mm}$ as well as a distance of 2 m to 5 m are required to meet the criterion of a time precision for $\sigma_T \approx 1 \mu\text{s}$.

(2) Accuracy of autocollimation

The principle of autocollimation, for a parallel path of rays, is to reflect a ray in itself by means of a mirror, which is perpendicularly oriented to the ray. Here, the rays of the laser light are considered as being parallel. If the mirror is not perpendicular to the ray but rather has a small deviation δ an error occurs because the incoming ray and the reflecting ray are not parallel, i.e. identical. The resulting difference Δd between the emitted and reflected ray can be measured on a scale against the radius r by

$$\tan(2\delta) = \frac{\Delta d}{r} \quad (5.9)$$

Based on Equation (5.9) the influence of δ on the difference Δd can be estimated. Table 5.4 shows the achievable accuracy of autocollimation. The longer the radius r , the larger the difference Δd . This means accuracy increases with a growing radius. Furthermore, it can be concluded that an accuracy for the center angle α from tenths up to hundreds of a degree can be easily achieved.

Table 5.4: Resolution of autocollimation in dependence of different radii. The longer the radius r , the larger the deviation Δd that is caused by different deflection angles δ .

δ [°]	$r = 1\text{m}$			$r = 2\text{m}$			$r = 5\text{m}$		
	1	0.1	0.01	1	0.1	0.01	1	0.1	0.01
Δd [mm]	4.4	0.4	0.05	8.7	0.9	0.1	21.3	2.2	0.2

The last consideration concerns the influence of δ on the center angle α . How does the deviation δ affect the center angle α ? Figure 5.6 shows the ‘desired’ center angle α , the deviation δ and the resulting ‘falsified’ center angle β , defined as sum of β_1 and β_2 .

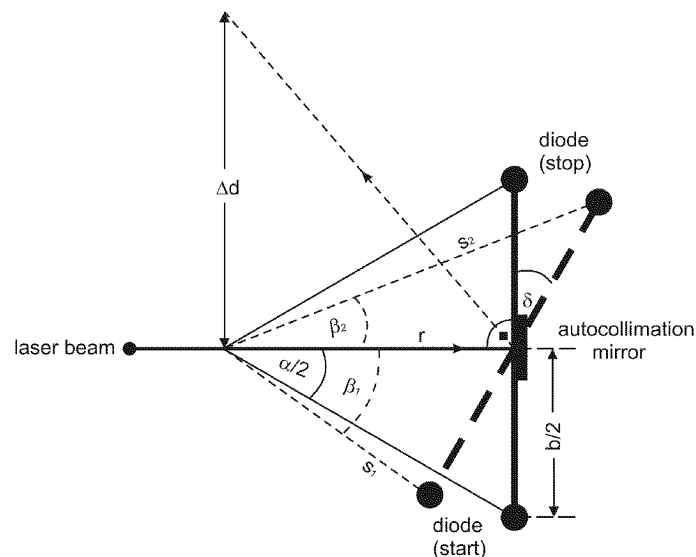


Figure 5.6: Influence of a deflection angle δ of the autocollimation mirror. The resulting center angle is $\beta = \beta_1 + \beta_2$ instead of α . The offset between emitting and reflecting laser beam is described by Δd .

Table 5.5 shows the influence of δ on the center angle α . The important value is the difference $\Delta\alpha$ between the 'desired' center angle α and the 'falsified' center angle β . Equating the resulting difference $\Delta\alpha$ to the precision of the center angle σ_α and referring to Table 5.2, it can be seen that, except for the implausible deviation δ of 10° , all resulting differences $\Delta\alpha$ causes an error in the rotation time T of less than $1\ \mu\text{s}$.

Table 5.5: Difference $\Delta\alpha$ between 'desired' center angle α and 'falsified' center angle β caused by a deflection angle δ using autocollimation. The longer the radius r and the smaller the deviation δ , the smaller the resulting difference $\Delta\alpha$.

δ [°]	$r = 1\text{m}$			$r = 2\text{m}$			$r = 5\text{m}$		
	10	5	1	10	5	1	10	5	1
α [°]	1.4185	0.7093	0.2837	1.4185	0.7093	0.2837	1.4185	0.7093	0.2837
β [°]	1.3970	0.6985	0.2794	1.4131	0.7066	0.2826	1.4183	0.7092	0.2837
$\Delta\alpha$ [°]	0.0215	0.0108	0.0043	0.0054	0.0027	0.0011	0.0002	0.0001	0.0000

The result of this discussion is that the autocollimation is well-adapted. The autocollimation can be carried out with high accuracy. Here, the accuracy of autocollimation is further influenced by the precision of the orientation of the mirror mounted on the plate, cf. Figure 5.5. Furthermore, a sufficient precision for the center angle α can be achieved so that a time resolution, i.e. precision, for the rotation time T of $1\ \mu\text{s}$ is possible.

As described above, the most crucial parameter for the center angle α is the precision of the base σ_b . In addition to the precision of the base, the position of the reflection point on the autocollimation mirror also has to be in the middle, between the two photo diodes. To determine this center point with high accuracy, the autocollimation mirror is covered with an adhesive tape. Only a small gap with a width of approximately 1 mm is left in the middle. This setup allows for both sufficient central positions of the reflection point required for autocollimation and a reflected laser beam necessary to perform the autocollimation. Furthermore, a scale is installed on the rotating mirror of the laser scanner. This scale includes a hole through which the laser beam is emitted. The reflected laser beam hits the scale, and based on the position on the scale, the autocollimation mirror can be aligned perpendicular to the laser beam by means of the adjusting device. The autocollimation mirror is perpendicular to the laser beam if the reflected laser beam is overlaid with the emitted laser beam. In Figure 5.7, on the left side the plate including the two photo diodes, the autocollimation mirror covered with the adhesive tape as well as the left gap, defining the position for the autocollimation, can be seen. On the right side, the scale fixed on the rotating mirror is shown.

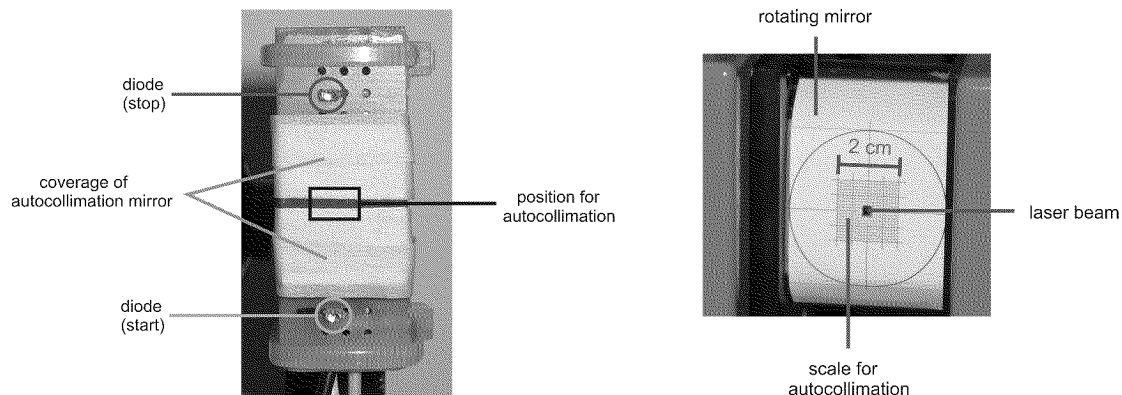


Figure 5.7: Left: Arrangement of the two photo diodes and the coverage of the autocollimation mirror. Right: Scale attached on the deflecting mirror of the laser scanner for measuring the offset between the emitting and reflecting laser beams.

After discussing the influencing parameters in detail, some notes regarding the principle of measuring the time delay Δt are necessary. For this, a special electronic device was developed, which is controlled via parallel port (LPT). After initializing the electronic circuit, the time passed between the detection of the laser beam on the start diode and on the stop diode is stored. Therefore, the clock generator is based on oscillators with different frequencies, i.e. 2 MHz, 4 MHz, 8 MHz, and 16 MHz. The derived time can be read from the electronic circuit and again a new measurement can be initialized. This procedure is repeated within a loop. The total number of time measurements as well as the time gap between each measurement can be defined manually. The stability of the oscillators is given by 50 ppm. Since 1 Hz equals $1 \mu\text{s}$, an instability in the frequency of 50 ppm leads to time variations of a single time measurement between $25 \mu\text{s}$ for the oscillator frequency of 2 MHz up to $3 \mu\text{s}$ for the oscillator frequency of 16 MHz. Performing repeated time measurements, the precision of the mean value can be increased significantly up to the desired precision for the rotation time T of $1 \mu\text{s}$. Further details regarding the electronic circuit are described in Appendix D.

Results

In general, two independent setups, including several data series, were performed. For each setup, the autocollimation had to be carried out and the center angle α had to be derived. First, three data series are presented. All data series include 1000 measurements with a time interval of 1 s. The frequency of the oscillator used was 2 MHz. In Figure 5.8, the detected time delay Δt corresponding to the three different rotation velocities, i.e. 12.5 rps, 25 rps, and 33 rps, are plotted. As seen, the raw data contains some blunders. The noise can be reduced by applying a median filter. The result is a smoothed data series from which the rotation time T can easily be derived. In the data series, another fact is also visible. The noise present at 12.5 rps is much higher than the noise present in 25 rps and 33 rps. The reason is in mass inertia. Mass inertia leads to higher noise if the rotation is slower. On the contrary, the noise decreases if the rotation is faster. To exclude systematic effects, the Fourier analysis is applied on the data series. The results were no significant frequencies were present and all amplitudes were within $2 \mu\text{s}$. Naturally, all blunders have to be eliminated before.

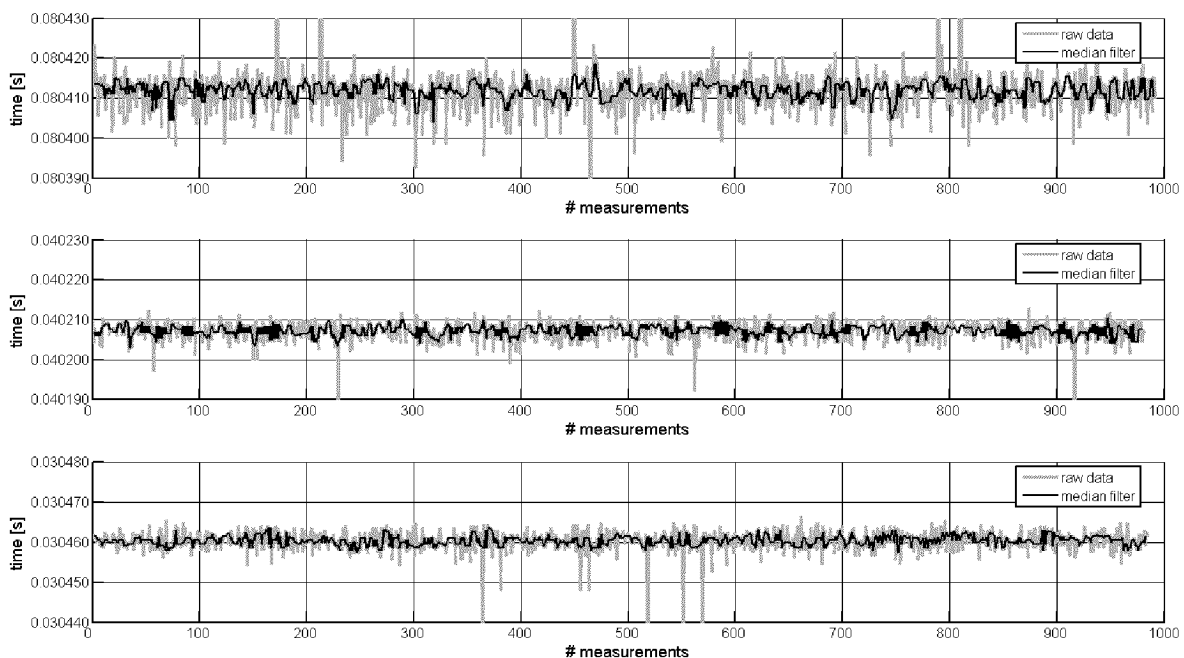


Figure 5.8: Measured time delay Δt for 12.5 rps, 25 rps and 33 rps: 1000 Measurements with a sampling interval of approximately 1 s. The oscillator used has a frequency of 2 MHz.

Second, a data set is used to verify the precision of the electronic circuit. As an example, the angular velocity of 25rps is chosen. Table 5.6 shows the reproducibility with different oscillator frequencies. The mean value for the time delay Δt , the precision of the mean value σ_m and the precision of one single measurement σ_s are calculated.

Table 5.6: Results of the derived mean value based on 1000 measurements for the time delay Δt according to the angular velocity of 25rps. Homogeneous results achieved by different oscillator frequencies can be seen.

Oscillator [MHz]	Δt [s]	σ_m [μ s]	σ_s [μ s]
2	0.0402071	0.1	2.4
4	0.0402073	0.1	2.4
8	0.0402072	0.1	2.6
16	0.0402070	0.1	2.6

Third, all results achieved by two different and independent setups are summarized in Table 5.7, which contains the mean values of the time delay Δt , the calculated center angle α , and the calculated rotation time T . The two setups differ at different values for r . The radius r for setup 1 is 1.430 m, and the radius for setup 2 is 2.900 m. The radius can be easily measured with the laser scanner in the so-called ‘static mode’. The corresponding precision of the radius can be specified as sufficiently high with a value of $\sigma_r \approx 2$ mm.

Table 5.7: Results of the measured time delay Δt , derived center angle α and the calculated rotation time T . Consistent results for both setups with deviations of maximum 2 μ s can be seen.

RPS	Setup	Time Delay Δt [s]	Center Angle α [°]	Rotation Time T [s]
12.5	1	0.080526	0.4892	0.080635
	2	0.080412	0.9920	0.080634
25	1	0.040262	0.4892	0.040317
	2	0.040207	0.9920	0.040318
33	1	0.030502	0.4892	0.030543
	2	0.030460	0.9920	0.030545

In Table 5.7, it can be seen that with both setups, equivalent results were achieved. Hence, the desired time resolution σ_T for the rotation time T of 1 μ s was nearly realized. Two problems remain: the oscillators can have a time offset and a scale factor, i.e. frequency drift. The presence of a scale factor can be excluded because of the use of different oscillators. Furthermore, by referring to the data plotted in Figure 5.8, no drifts can be seen. On the contrary, an additive constant in terms of a time offset due to transmission delays is conceivable. The rotation time T is then too short and yields systematic errors, which can be corrected mathematically.

5.2.2 Indirect Method

The indirect method deals with a long-term investigation of the rotation. The rotation time T can be calculated indirectly if both the total time t of the rotations and the total number n of rotations are known:

$$T = \frac{t}{n} \quad (5.10)$$

The total time t is measured by a computer that allows for retrieving the frequency of the high-resolution performance counter. By reading the current counter and scaling with the frequency of the counter, a time precision of several milliseconds or better can be achieved. The actual operating system time of the

computer is derived as follows. A first time tag is stored, when the rotation is started. And a second time tag is stored, when the rotation is stopped. The difference of these two time points defines the total time t . However, there is an uncertainty in this total time. A delay is obviously present, especially between starting the rotation, defined by clicking a button 'start', and reaching the specified angular velocity, defined by counting the number of vertical profiles. This time delay δt is a specific constant for each angular velocity and can, therefore, be modeled mathematically. The modified relation is:

$$T = \frac{t - \delta t}{n} \quad (5.11)$$

Considering Equation (5.11), an adjustment problem can be formulated. The observation is the total time t and the unknowns are the rotation time T as well as the time delay δt . Based on the treatment of the number of rotations n , a different adjustment problem is achieved: either (1) Gauss-Markov, i.e. n represents a constant, or (2) Gauss-Helmert, i.e. n represents an observation. The resulting functional models are:

$$f(t, \omega, \delta t) : \quad t = n \cdot T + \delta t \quad (5.12)$$

$$f(t, n, \omega, \delta t) : \quad (t - \delta t) - (n \cdot T) = 0 \quad (5.13)$$

Both adjustment problems yield the same results. The advantage of Gauss-Markov is that no initial value for the unknown is required. In addition, Gauss-Helmert needs initial values. To determine the unknown rotation time T , several measurements were carried out. They cover a total time of one minute, ten minutes and one hour. Table 5.8 gives an overview of both the measurements and the results of the adjustments.

Table 5.8: Results of both types of adjustment for deriving the rotation time T and the time offset δt indirectly. A precision for the rotation time T of $\sigma_T \approx 1 \mu\text{s}$ can be seen.

	12.5 rps		25 rps		33 rps	
	n	t [s]	n	t [s]	n	t [s]
1min	730	59.012	1422	59.710	1909	58.343
	728	58.819	1426	59.854	1909	58.278
	728	58.874	1426	59.694	1909	58.311
	726	58.673	1426	59.837	1911	58.391
	727	58.722	1426	59.759	1913	58.423
10min	7433	599.433	14872	599.672	19619	599.368
	7435	599.552	14866	599.369	19616	599.181
	7435	599.541	14879	599.934	19617	599.180
	7433	599.361	14868	599.523	19617	599.212
	7439	599.912	14947	602.704	19613	599.068
60min	44688	3603.738	89382	3603.859	117975	3603.510
	44693	3604.002	89391	3604.370	117973	3603.447
	44691	3603.802	89382	3604.538	117971	3603.526
	44691	3603.980	89408	3605.488	119940	3663.517
	44691	3603.898	89382	3603.914	117973	3603.478
T [s]	0.080638		0.040323		0.030545	
σ_T [μs]	1.0		1.2		0.2	
δt [s]	2.20		2.28		2.49	
$\sigma_{\delta t}$ [s]	0.02		0.06		0.02	

5.2.3 Discussion and Comparison

The rotation time T of the rotating mirror were derived by two independent methods. The direct method requires a more careful consideration of different influencing parameters caused by the use of two photo diodes. The autocollimation thereby defines the main problem, which is to achieve the claimed precision for the rotation time T . Comprehensive considerations regarding different parameters for carrying out the autocollimation yield acceptable results. On the contrary, the indirect method only deals with the number of full rotations and the total time. By using the tools of adjustment the rotation time T as well as the specific time delay δt for the three supported angular velocities can be derived indirectly. These time delays are of further interest in performing kinematic applications.

Table 5.9 summarizes the results and derives a mean value for the rotation time T . It can be seen that a maximal difference of $5 \mu\text{s}$ was achieved between the two methods. The claimed precision was not achieved completely, but the results are close.

Table 5.9: Comparison of the results of both methods deriving the rotation time T . Homogeneous results with a maximum difference of $5 \mu\text{s}$ between the direct method and the indirect method can be seen.

RPS	Direct Method T_1 [s]	Indirect Method T_2 [s]	Mean T [s]
12.5	0.080635	0.080639	0.080637
25	0.040318	0.040323	0.040320
33	0.030544	0.030544	0.030544

Finally, a short discussion shall be presented to clarify the meaning of (1) a precision and (2) a systematic error of $1 \mu\text{s}$ for the rotation time T . If the rotation time has a precision of $1 \mu\text{s}$, then the 'true' value is oscillating around the derived value of $1 \mu\text{s}$. In addition, a systematic deviation of the derived value from the 'true' value means that with a growing measuring time, the error caused by the systematic deviation of $1 \mu\text{s}$ is increasing. Supposing a velocity of $v \approx 0.2 \frac{\text{m}}{\text{s}}$ of a test trolley on which the laser scanner is mounted, the observation time can be estimated at which an error in the position of the test trolley of 1 mm is achieved. In this example, each rotation generates an error of $\Delta s = v \cdot \Delta t = 0.2 \frac{\text{m}}{\text{s}} \cdot 0.000001 \text{ s} = 0.0002 \text{ mm}$. This means 5000 rotations yield the supposed position error of 1 mm . Considering the different rotation times T the observation time covers a time period of 2.5 min up to 6.7 min. In terms of a file size for a laser scan of 2.5 min, depending on the scan resolution, several hundreds of Megabytes up to some Gigabytes are obtained.

In summary, three rotation times T are derived with high precision. Based on the desired spacing between two adjacent vertical profiles an appropriate velocity of the test trolley has to be chosen. Additionally, the spacing can also be influenced by selecting another rotation time T . On the contrary, the scan resolution within each vertical profile is only correlated to the sampling interval and cannot be changed by the velocity of the test trolley or by the rotation time. Considering a mean velocity of $0.2 \frac{\text{m}}{\text{s}}$, two adjacent vertical profiles have a spacing of

- 1.6 cm (for $\omega \approx 0.08 \text{ s}$),
- 0.8 cm (for $\omega \approx 0.04 \text{ s}$), and
- 0.6 cm (for $\omega \approx 0.03 \text{ s}$).

In general, there are three different parameters to achieve the most appropriate point density for kinematic laser scanning: the rotation time, the velocity of the test trolley and the scan resolution within each vertical profile.

5.3 Position-Fixing Using Total Station

The use of a total station for kinematic applications requires some considerations that differ from those for static applications. The main restriction is based on the spatial resolution of the measurements. The spatial resolution depends on both the velocity of the moving trolley and the sampling frequency of the total station. Typical sampling frequencies are from 5 Hz to 10 Hz. The velocity of the moving trolley depends on the application.

The operating range for total stations is defined by the line of sight and the environment. Thus, typical ranges for kinematic applications do not exceed 200 m [Glaus, 2005]. The operation of the total station is mostly performed via a personal computer, which controls the total station. The data transfer between computer and total station is carried out via radio communication. After setting up the total station, the prism is automatically searched for within a user-defined window. For a precise positioning of the telescope, the automated target recognition (ATR) has to be activated. This fine search uses digital image processing or further scan techniques [Ingensand and Böckem, 1997]. If the positioning is successful, the prism is locked in and the tracking mode can be started. If the target is lost due to the loss of signals, the prism has to be searched for again. Most total stations provide search procedures and extrapolation algorithms to locate the lost target reliably.

The data read-out of the total station contains the angle measurements and the distance measurement. Therefore, the angle measurement can be corrected by applying instrumental errors due to measurements in only one face. For yielding fast encoder readings, the two-axis compensator has to be switched off or has to be used in a planar model [Leica Geosystems, 2004]. Furthermore, distance measurements, ATR and the compensator readout depend on exterior influences that can result in lags [Hennes, 1999]. The determination of the distance takes more time than the readings of the direction encoders and thus, defines the sampling frequency of the total station. Depending on the chosen distance measurement mode, e.g. single, standard or fast, the range provided by the total station is more or less accurate. The more accurate the distance the more time is required for the determination of the distance. Readings of the angle measurements and the distance measurement are not carried out at the same time. They are asynchronous and result in a time delay. This time delay has the largest influence, if the moving trolley passes the total station, and the smallest influence, if the moving trolley drives away from or towards the total station. A comprehensive investigation regarding tracking total stations and the synchronization of the angle and the distance measurement system can be found in [Stempfhuber, 2004].

Global Navigation Satellite Systems (GPS, GLONASS) can alternatively be used for kinematic applications or can complement tracking total stations. Gaps produced either by GPS or by total station can be filled. The combination of both GPS and total station leads to an improved accuracy of the trajectory.

The raw data acquired by the total station have to be processed regarding several aspects. These steps of processing contain the detection of blunders and smoothing of raw data, the derivation of equidistant measurements, the filling of data gaps, i.e. interpolation, and trajectory smoothing. In the following, the different steps of processing are discussed. Figure 5.9 shows the work flow for processing the total station data acquired in kinematic applications.

5.3.1 Blunder Detection and Smoothing

A signal $x_i(t)$ can be considered as being superimposed by additive Gaussian noise $n_i(t)$ and impulsive noise $i_i(t)$

$$x_i(t) = s_i(t) + n_i(t) + i_i(t). \quad (5.14)$$

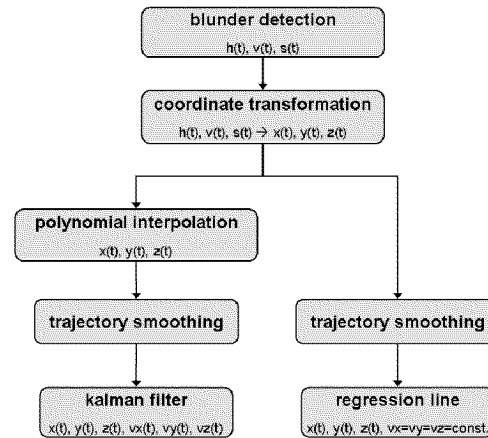


Figure 5.9: Work flow for total station data.

The median filter is a non-linear signal enhancement technique for the smoothing of the signal, the suppression of the impulsive noise, and preservation of edges [Tukey, 1977]. In the one-dimensional case, it consists of sliding a window of an odd number of elements along the signal, and replacing the actual sample by the median.

The impulsive noise is assumed to take a relatively large value compared to the signal and thus, results in a distinctive spike. The median filter acts as a low-pass filter and flattens the signal by eliminating spikes. Several variations of the median filter lead to modified filters, e.g. weighted median filter, MAD Filter [Sachs, 1984].

The median filter was already applied to the data describing the rotation time of the rotating mirror, cf. Section 5.2.2. Depending on the window size of the filter, most of the spikes representing blunders can be eliminated. The median filter is applied on the data of the total station, especially on the data of the distance measurement system. After median filtering, the spherical coordinates in terms of the horizontal direction (h), vertical direction (v) and distance (s) are transformed to Cartesian coordinates representing x , y and z .

5.3.2 Polynomial Interpolation

The data acquired by the total station have a time gap between the measurements corresponding to the sampling frequency of the total station. The limitations for the sampling frequency is given by the distance measurement system. The total station used, Leica TPS1201, shows a time gap Δt for a measurement in the tracking mode of $\Delta t < 0.15$ s. Since the time gap is not constant during data acquisition, the received data are not equidistant and show varying time gaps, cf. Figure 5.10. The manufacturer's specifications were generally met. However, there are several measurements that have a larger time gap. They may be caused by fine distance measurements with higher accuracy, which require more time.

Mathematically, polynomial interpolation is the interpolation of a given data set by a polynomial. The polynomial found intersects these points. An interpolation polynomial is defined by [Bronstein and Semendjajew, 1999]

$$y = \sum_{i=0}^n a_i x^n. \quad (5.15)$$

Depending on the number of interpolation points, the coefficients of Equation (5.15) satisfy a linear equation system [Press et al., 2002], described by the Vandermonde matrix. A Vandermonde system can be ill-conditioned and special techniques for solving such systems have to be considered. If the coefficients of

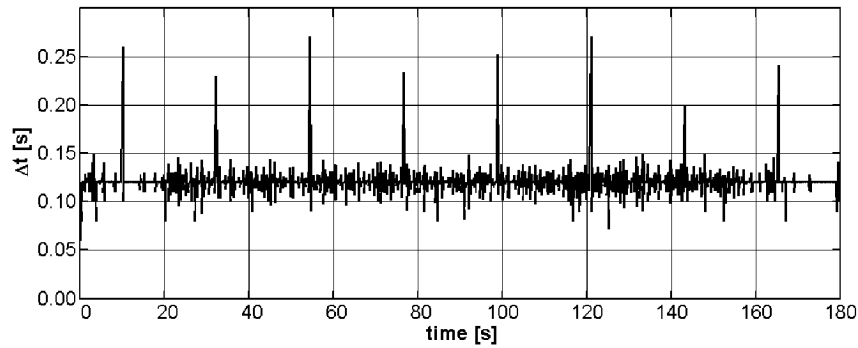


Figure 5.10: Sampling interval of the total station by using the tracking mode via the GeoCOM interface (Leica TPS 1201).

the polynomial is not of further interest, other techniques can be applied for finding interpolated values directly. In terms of a linear system of equation the Equation (5.15) can be expressed by

$$\begin{bmatrix} 1 & x_0 & x_0^2 & \cdots & x_0^n \\ 1 & x_1 & x_1^2 & \cdots & x_1^n \\ \vdots & \vdots & \vdots & \vdots & \vdots \\ 1 & x_p & x_p^2 & \cdots & x_p^n \end{bmatrix} \cdot \begin{bmatrix} a_0 \\ a_1 \\ \vdots \\ a_n \end{bmatrix} = \begin{bmatrix} y_0 \\ y_1 \\ \vdots \\ y_p \end{bmatrix} \quad (5.16)$$

where n is the order of the polynomial and p is the number of interpolation points. Therefore, the highest order of the polynomial is defined by the number of interpolation points:

$$n \leq p - 1. \quad (5.17)$$

The choice of the appropriate order of the polynomial approximating the process defined by the interpolation points depends on the mathematical model. Otherwise, if the chosen order is higher than the real process, the significance of the coefficients can be verified by standard hypothesis testing techniques. The higher the order of the polynomial, the higher the probability of oscillations to the polynomial's ends [Welsch et al., 2000]. Furthermore, one has to determine whether a global polynomial or only a local polynomial is of interest. A global polynomial is appropriate to approximate a trend over the whole data set. On the contrary, a local polynomial takes short-term variations better into account, but the continuity between two local polynomials is not guaranteed.

The polynomial interpolation generates a new set of data based on the acquired data and the selected order of the polynomial. This new data set shows equidistant data. Influences of oscillations of the local polynomial are minimized since the point to be interpolated is defined by the center point of the number of interpolation points. The window for the polynomial is shifted for one interpolation point if the point of interpolation is not the median of the interpolation points, cf. Figure 5.11. The trajectory of a moving platform, like the test trolley on the calibration track line, can be described sufficiently by a third order polynomial since a constant, a linear and an accelerated part are considered by using four coefficients. Other possible forms of approximation functions for deriving equidistant measurements and filling gaps are splines, e.g. cubic splines, rational splines or adjusting splines, rational functions and harmonic functions.

5.3.3 Regression Line

The regression line also provides a suitable tool for processing total station data. If the test trolley on the calibration track line is moving with a near constant velocity, the data acquired by the total station can be

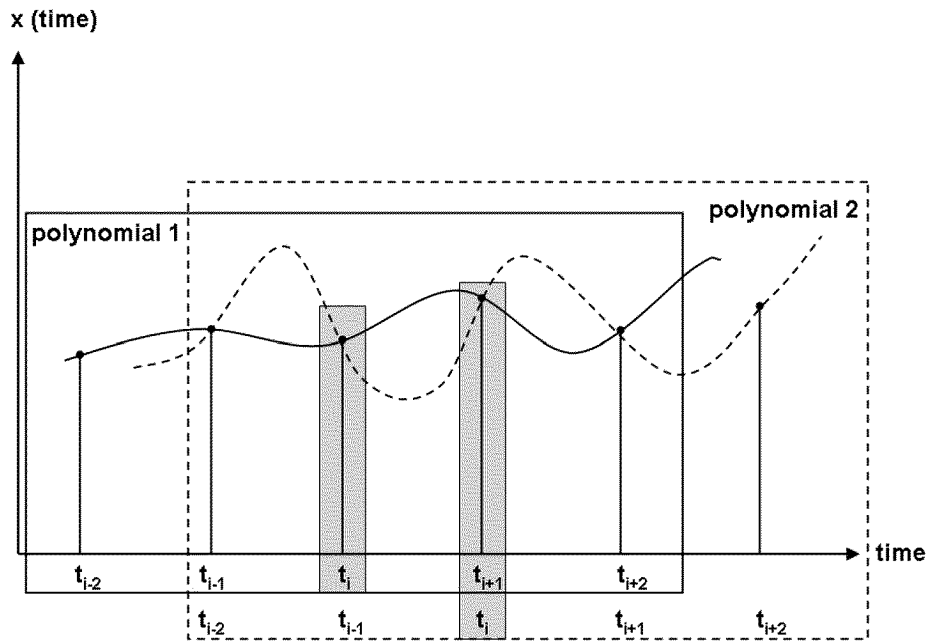


Figure 5.11: Polynomial interpolation and interpolation points.

approximated by a regression line. The mathematical model for a regression line is described by [Bronstein and Semendjajew, 1999]

$$y_i = a \cdot x_i + b \tag{5.18}$$

where a is the slope and b is the intercept of the ordinate. Considering a data set, the regression line can be calculated by applying the Gauss-Markov-Model. Since the equation is linear in the unknowns, no initial values are required for a and b :

$$\begin{bmatrix} x_1 & 1 \\ x_2 & 1 \\ \vdots & \vdots \\ x_n & 1 \end{bmatrix} \cdot \begin{bmatrix} a \\ b \end{bmatrix} = \begin{bmatrix} y_1 \\ y_2 \\ \vdots \\ y_n \end{bmatrix} \tag{5.19}$$

A regression line is also suitable for detecting blunders. Data snooping can be included in the adjustment of the regression line since the median filter does not find consecutive blunders due to the window size. The criterion for blunders can either be normalized residuals or absolute distance offsets. The advantage of using an absolute distance error can be seen in a mathematical interpretation, which ease the search for outliers. The adjustment of the regression line is iterated until all blunders are disabled.

5.3.4 Kalman Filtering

The Kalman filter has become very popular since its invention by [Kalman, 1960]. The Kalman filter is a recursive filter and a favorite method for combining data acquired by sensors or instruments for achieving an optimal estimation of the state vector of a motion and its stochastic behaviour. Thus, the state vector and its covariance matrix become time-dependent and are a function of time. Therefore, optimal estimation means that within the estimation, the error variances are minimized and all available deterministic and stochastic information are included.

The mathematical procedure of the Kalman filter is to update the state of a system at time t_k to the time t_{k+1} using observations at the same time and prior information captured in the state vector at time t_{k-1} . The state vectors at subsequent time t_{k+1} are obtained recursively. Thus, the Kalman Filter combines observations and the system dynamic. The state vector at a subsequent time t_{k+1} can be computed if the state vector at time t_k is given including a description of the system and control functions from that time in subsequent time. Such a dynamic system can be described in the state-space notation by [Gelb, 1974]

$$x_k = F_{k-1} \cdot x_{k-1} + G_{k-1} \cdot w_{k-1} + L_{k-1} \cdot u_{k-1}. \quad (5.20)$$

where x is the system state vector, w a stochastic vector and u a deterministic vector. F , G and L are matrices defining the system behaviour due to dynamic, stochastic and deterministic parts. Neglecting deterministic forces in Equation (5.20) the dynamic model can be expressed by [Hofmann-Wellenhof et al., 2003]

$$x_k = \Phi_{k-1} \cdot x_{k-1} + \Gamma_k \cdot w_{k-1}. \quad (5.21)$$

where Φ_{k-1} is the transition matrix for the system state and Γ_{k-1} is the disturbance input matrix for the system state affected by noise parameters between epoch t_{k-1} and t_k . Vector w_k is denoted as system noise, which is assumed following a Gaussian distribution with zero mean, uncorrelated white noise and a covariance matrix Q_{k-1} describing the uncertainties of modeling the behaviour of the dynamic system:

$$w_k \sim N(0, Q_k). \quad (5.22)$$

The state-space notation described by Equation (5.20) is the first fundamental equation that is required for the Kalman filtering. The second fundamental equation is defined by observations that survey the actual state of the system³

$$z_k = H_k \cdot x_k + v_k. \quad (5.23)$$

where z_k is the observation vector and H_k describes the linear relation between the observations and the system state variables. The vector v_k follows a Gaussian distribution with zero mean and white noise including a covariance matrix R_k describing the uncertainties of measurements:

$$v_k \sim N(0, R_k). \quad (5.24)$$

In the strict sense, the discussed formulae are only valid for dynamic processes that are discrete-time controlled and can be expressed by linear equations. The filter then is called a *discrete Kalman filter*. The expansion to a more general form of the dynamic process of a system state leads to non-linear equations of the system state and the observations. The given matrices, i.e. transition matrix Φ_k , the disturbance input matrix Γ_k and the measurement matrix H_k , have to be replaced by Jacobian matrices since the non-linear relations are developed in Taylor series around an initial state vector close to the real vector. The truncation of higher order terms in the Taylor series results in propagation errors and biased estimations. These linearizations lead to the *extended Kalman filter* [Jazwinski, 1970].

The Kalman filter can be divided into two steps since the filter estimates the system state at a time and then, obtains feedback in the form of measurements. These two steps are called time update and measurement update. The time update equations project forward in time the current state and the error covariance to obtain a priori estimation for the next time step. The measurement update equations incorporate new

³It is not required to survey the actual state of the system at every epoch in each parameter. The state-space equation may compensate missing parameters and missing epochs.

measurements into the a priori estimation to obtain an improved a posteriori estimation. It can be said that the time update acts as predictor equations and the measurement update acts as corrector equations.

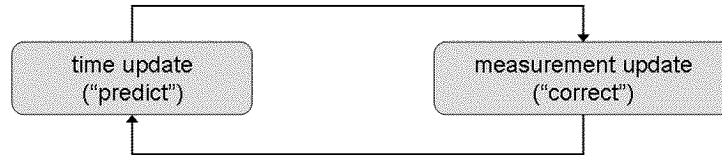


Figure 5.12: The Kalman Filter cycle consisting of a time update and a measurement update according to [Welch and Bishop, 2004].

In the following notations, the superscript minus ($^-$) states for a priori estimations at step k given knowledge of the process prior to step k . Otherwise, they are a posteriori state estimations at step k given measurement z_k . Since there is a discrepancy between a predicted measurement and the actual measurement, a difference is present, which is called filter innovation. The gain matrix K weights the innovation to obtain the update state estimation including the measurements:

$$\dot{i}_k = z_k - H_k \cdot x_k^- \quad (5.25)$$

$$x_k = x_k^- + K_k \cdot \dot{i}_k \quad (5.26)$$

A summary of the Kalman filter cycle including the equations are given in Table 5.10, adapted from [Welch and Bishop, 2004]. The filter has to be initialized by initial values for x_0 and P_0 .

Table 5.10: Kalman filter equations for the time update and the measurement update, adapted from [Welch and Bishop, 2004].

Time Update	Measurement Update
1) Project the state ahead $x_k^- = \Phi_{k-1} x_{k-1} + \Gamma_{k-1} x_{k-1}$	(1) Compute the Kalman gain $K_k = P_k^- H_k^T (H_k P_k^- H_k^T + R_k)^{-1}$
(2) Project the error covariance ahead $P_k^- = \Phi_{k-1} P_{k-1} \Phi_{k-1}^T + \Gamma_{k-1} Q_{k-1} \Gamma_{k-1}^T$	(2) Update estimate with measurements z_k $x_k = x_k^- + K_k (z_k - H_k x_k^-)$
	(3) Update the error covariance $P_k = (I - K_k H_k) P_k^- (I - K_k H_k)^T + K_k R_k K_k^T$

The Kalman filter described uses all collected data and information prior to the present epoch. If the system state is not of interest in real-time and the Kalman filter is applied in post-processing, the system state can be smoothed by using information of epochs after the present epoch. Therefore, the filter runs not

only in a forward direction but also in a backward direction. The combination of forward and backward filtering leads to optimal smoothing. The smoothing algorithms are classified in three groups [Jekeli, 2001]. Fixed-point smoothing estimates only the system state at a fixed epoch. Fixed-lag smoothing is applied on estimating the system state for a fixed, i.e. constant, time delay in the past. Fixed-interval smoothing uses all information, i.e. observations, of the interval for an estimation of the system state at each epoch.

Since the Kalman filter is applied in the post-processing, fixed-interval smoothing can be applied. Several versions of the smoothing algorithms were developed. One of them is the filter according to [Fraser, 1967], which uses a combination of forward-in-time and backward-in-time filter. The forward-in-time filter corresponds to the above discussed Kalman filter, whereas the backward-in-time filter starts from the last epoch and runs to the first epoch by using the same Kalman filter equations with careful implementation of time indices. The optimal estimation is obtained by building the weighted average of the forward and backward filter. Further information regarding Kalman filter and smoothing algorithms can be found in [Gelb, 1974] and [Jekeli, 2001].

Analogous to adjustment techniques, blunder detections can be carried out according to [Baarda, 1968] and [Pope, 1975]). The innovation i is appropriate as a parameter for a so-called local test that follows a normal distribution. Unfortunately, local tests are not sensitive enough to properly detect all possible errors. Additionally, global tests, which use the information of several foregoing epochs instead of only one foregoing epoch, should be applied. One global test is introduced by [Teunissen and Salzmann, 1988].

Before Kalman introduced his filter in the 1960s, the Wiener filter technique was widely used. The Wiener filtering is a method that recovers the original signal as close as possible from the received signal based on equation (5.14) by minimizing the mean-square error. It is designed to operate directly for each estimate on all of the data. The Kalman filter, instead, recursively conditions the current estimate on all of the past measurements.

5.4 Synchronisation

The data acquired by the laser scanner and the total station have to be synchronized. For the laser scanner, a rotation time was derived, cf. Section 5.2, which defines a relative time tag for each measurement. Since the laser scanner and the total station are controlled by one and the same computer, the common time base is provided by the frequency of the high-resolution performance counter of the computer used. The frequency cannot change while the system is running. Each received data sent from the total station is linked by a time tag derived by the performance counter of the computer. The data received by the laser scanner are not linked with the time tag since the rotation time of the rotating mirror provides a high-resolution counter. Only for the operation of starting the scanning process is a time tag generated. Thus, the relative time tag of the rotation time can be linked with the absolute time tag.

The time point of starting the operation of the scanning mode of the laser scanner does not fit the time point of the first measured point of the first profile. The reason is there is a first (short) time delay between sending the command of starting the profile mode from the computer to the laser scanner. Then, a second (long) time delay is given by starting the profile mode and acquiring the first data point. The rotating mirror has to be accelerated to the angular velocity, and if the angular velocity is reached, the data are acquired. This time delay from sending the command of starting the profile mode up to measuring the first point can be described by a constant time-offset that can be calibrated, cf. Section 5.2.2.

The synchronisation of multi-sensor systems is an important aspect. The use of several sensors requires real-time operating systems and knowledge of programming languages. Software packages, e.g. DasyLab[®], ADWin[®], or LabView[®], contain tools and libraries that facilitate the user in developing and programming [Gläser and Schollmeyer, 2004].

Applications of Terrestrial Laser Scanning

This chapter demonstrates the variability and the potential of terrestrial laser scanning for different applications. Engineering geodesy covers an important application area and in most cases, requires a high accuracy within the order of millimeters. Therefore, the used instruments have to be calibrated for fulfilling the requirements of a high accuracy. The following applications show the performance of a calibrated laser scanner.

The first application deals with a road surface analysis to derive catchment areas and mass balances. The goal is to determine the polluted road runoff and to estimate the consequences for the vegetation adjacent to the road. The second example deals with underground applications in the field of engineering geology. Displacement monitoring plays an important role in the understanding of stability problems. Therefore, deformation monitoring of discrete points and the rock surface are carried out to assess the potential of laser scanning. The third example deals with a kinematic application for surveying a test tunnel during motion. The goal is to also use laser scanning in a kinematic way and to achieve high absolute accuracy with respect to a global reference frame.

6.1 Static Application: Road Surface Analysis

6.1.1 Introduction

Nowadays, there are ongoing discussions in Switzerland about treatment of polluted runoff from roads with high traffic density. One treatment possibility is the infiltration of road runoff in vegetated road shoulders. In order to determine their loading and removal effectiveness for heavy metals, e.g. lead, zinc, cadmium, copper or organic substances, a pilot plant was installed in the shoulder of a road with a traffic density of more than 17,000 vehicles per day. The purpose of the pilot plant was, among others, to collect the runoff from a road section to calculate the percentage of runoff draining directly into the vegetated swale and not being dispersed diffusely with spray. Based on this information, mass balances can be carried out to access the accumulation rates of pollutants in the vegetated road shoulder and to calculate the removal efficiency of the vegetated swale.

The calculation of the part of runoff that drains directly can only be carried out if the size of the catchment area is known. Based on the rainfall height, the theoretical maximum runoff can then be calculated and compared with the measured volume in the pilot plant. As the pollutant load is related on average to the runoff volume, the distribution of the pollutants between runoff infiltrating into the vegetated road shoulder and diffuse spray dispersion can be derived. A classical approach to estimate the size of catchment areas is to conduct large scale experiments using coloured tracers sprayed over the whole road surface area

near the pilot plant. For the present situation, this is not a possibility because the road cannot be blocked for hours due to the heavy traffic density. Another possibility was to use a mathematical surface model, based on topological data, to calculate the catchment area. Therefore, the topological data, i.e. 3D coordinates, have to be acquired by surveying.

Terrestrial laser scanning is well-suited for acquiring 3D data including intensity values. This surveying technique offers the best performance regarding both the data acquisition rate and the point density compared to classical surveying methods, e.g. tacheometry, GPS and levelling. The performance played a key role since the road section was only blocked for a short time, i.e. a few minutes, due to the high traffic density. Furthermore, the area to be surveyed and the required accuracy of one centimeter can be achieved with the laser scanner.



Figure 6.1: Road section to be investigated. Control points, visualized by spheres and mounted on tripods, can be seen.

6.1.2 Method

The road to be scanned is located near the town Burgdorf, Switzerland. For this project, only a small section of the road, approximately $15 \times 5 \text{ m}^2$, was investigated. Care and attention was placed on reflection aspects, especially the angle of incidence and the colour of the road surface. The angle of incidence of the laser beam decreases with respect to the road surface with increasing distances. The dark surface of the road was an aggravating factor since the colours only varied from grey to black. To avoid insufficient results regarding noise and a poor accuracy, the range for scanning the road was limited to several meters, i.e. less than 10 m. Therefore, two opposite viewpoints on both sides of the road were chosen for laser scanning, thereby meeting the requirements of high point density and high point precision.

The registration was performed by using spheres since high accuracy is guaranteed, cf. Section 3.1.5. They were placed on tripods using tribrachs and well-distributed around the area to be scanned to avoid the need for extrapolation. The spheres can also be replaced by prisms. The advantage is these tie points can be surveyed with a total station, when using the prisms, and high accuracy can be achieved. Thus, these control points can be included in a reference frame and can be aligned with respect to gravity. The orientation regarding gravity is of importance for water flow. The total station and the tribrachs can be levelled and referenced to gravity. Thus, the control points are geo-referenced. The gradients in height can be interpreted for water flow. The measurement setup and the road area can be seen in Figure 6.1. The accuracy of the control points surveyed with a total station are less than 2 mm. The center points of the spheres derived, as precisely as possible from the point cloud, can be estimated using the 'fix' adjustment. The resulting accuracy of the registration shows that the residuals for all control points are less than 6 mm and therefore, sufficiently high.

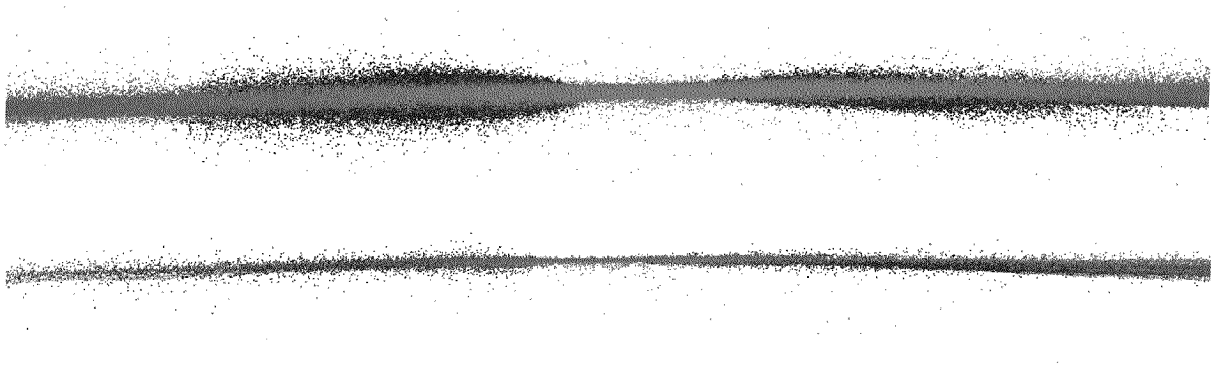


Figure 6.2: Cross section of one lane of the road. The upper part shows the noise of the skidmarks and the lower part the reduced noise after applying the noise reduction.

According to the introduced noise reduction technique, cf. Section 4.1.5, the biased data were optimized. The angle of incidence and the dark surface colour of the road are especially influential on the accuracy. The noise is aligned along the direction of the measurement. The result of noise reduction is a reduced and smoothed point cloud. An example of a cross section of the road surface is shown in Figure 6.2 and represents one lane including skid marks. The smoothed road surface in the lower part in comparison with the original point cloud in the upper part can be seen. After registration, the point clouds are registered and aligned with respect to gravity. The road section described by the point cloud can be seen in Figure 6.3. The intensity values simplify the interpretation of objects. The lane-markers at the borders and at the middle of the road are clearly visible, as well as the varying colours of the tarmac caused by wheel abrasion. The brighter the colours, the higher the intensity values.

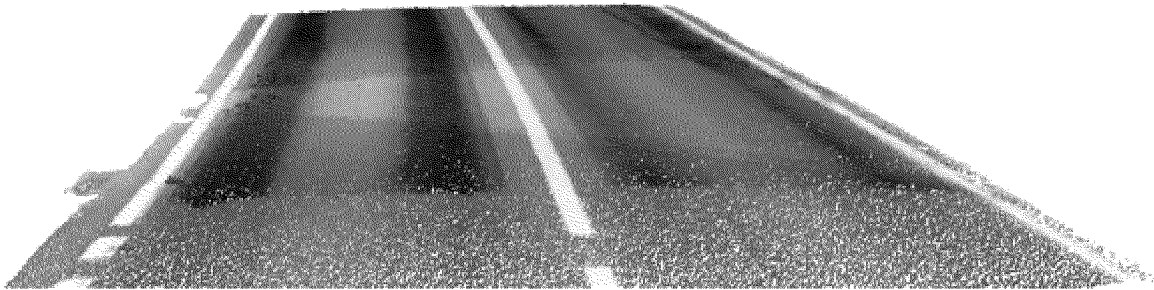


Figure 6.3: Point cloud of road section. Noise is reduced by applying the developed filter algorithm. The intensity values ease the identification of details of the surface of the road, e.g. lane-markers, different types of tarmac.

6.1.3 Results

Overview

Generally, to calculate mass balances for heavy metals in the vegetated road shoulder as a function of the road distance, the part of the heavy metal load that is in the road runoff to be drained directly and to be infiltrated into the vegetated road shoulder and the part of runoff which is distributed diffusively with spray, have to be known. The total heavy metal load in the road runoff can be calculated by multiplying the average heavy metal concentration and the total runoff volume. The total runoff volume is calculated by multiplying the rainfall height with the catchment area, minus 20 % of losses caused by wetting effects and evaporation [Gujer, 1999]. In summary, the catchment area, the runoff volume and the rainfall height must be measured or calculated.

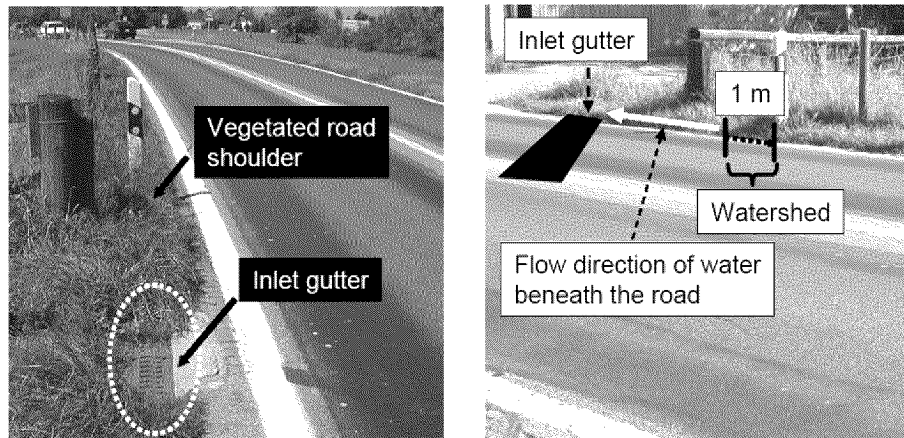


Figure 6.4: Inlet gutter and vegetated road shoulder (left), watershed and initially assumed catchment area (right). Flow direction due to preferential flow beneath the road is indicated.

In the pilot plant, the road runoff was collected in a storage tank using a 0.5 m long gutter located directly beneath the road. The volume was read periodically, cf. Figure 6.4, left. The rainfall height was measured at a distance of 6 m from the road. The first calculations for a catchment area of 1.5 m^2 , 0.5 m gutter length times 3 m road width, were not meaningful because too much water was collected in the sampling tank relative to the road surface of 1.5 m^2 . The catchment area must be much larger than assumed. This would be the case if the road would have a slight slope in the longitudinal direction or other effects would occur, such as preferential flow. In order to assess the latter, simple tracer experiments were conducted. These revealed significant water flow from the area adjacent to the road into the inlet gutter of the water storage tank. The length of this section is 2.5 m to 3.5 m and the watershed can be located within a range of 1 m, cf. Figure 6.4, right. Although this tracer experiment answered the question that there is some preferential flow, the question of the size of the catchment area is still unsolved.

Calculation of Catchment Areas

The catchment area was calculated by using the noise-reduced and geo-referenced laser scanning data. Based on these data, a grid with a sampling interval of 8 cm, the streams leaving the road, cf. Figure 6.5, as well as the different catchment areas for the inlet gutter, cf. Figure 6.6, were derived. These calculations showed that water flow is almost perpendicular to the road alignment. In addition, sensitivity analyses showed the point density for deriving the grid is sufficient and a decreased point spacing of the grid does not significantly affect the size of the different catchment areas.

As measured by the tracer experiments, the assumed location of the watershed lies within a range of about 1 m. Based on the coloured tracer experiment it was not possible to estimate the watershed more accurately. For this reason, it was assumed that the watershed is located in the middle of the range at 0.5 m. Consequently, the two different catchment areas number 1 and 2 lead to the catchment area of 14.1 m^2 , as shown in Figure 6.6.

Based on the catchment area of 14.1 m^2 , the maximal runoff was calculated and was compared with the collected road runoff. As a result, 36 % of the maximal runoff drains directly into the storage tank and therefore would infiltrate into the vegetated road shoulder. The other 64 % of the road runoff are dispersed mostly through diffusion within a distance of the road of 25 m [Steiner et al., 2005]. As the heavy metal load can be assumed to be nearly proportional to the water flow, about 36 % of the pollutant load in the road runoff infiltrate the vegetated road shoulder directly below the road. During infiltration, many pollutants such as heavy metals and organic substances are accumulated. Thus, accumulation results in a high concentration

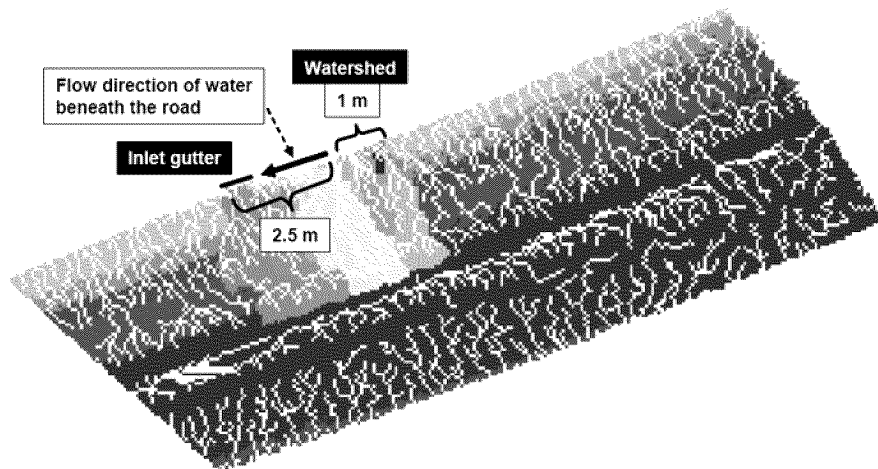


Figure 6.5: Calculated streams based on the topological model. Flow direction due to preferential flow beneath the road is indicated.

of pollutants in the topsoil of the vegetated road shoulder. Considering other treatment possibilities, such as centralised on-site options, 36 % of the pollutant load in the road runoff were collected with a gutter beneath the road. However, further calculations showed the percentage of collectable road runoff could be increased significantly if an additional impermeable surface such as a sidewalk or an emergency lane would exist beside the road [Steiner et al., 2005].

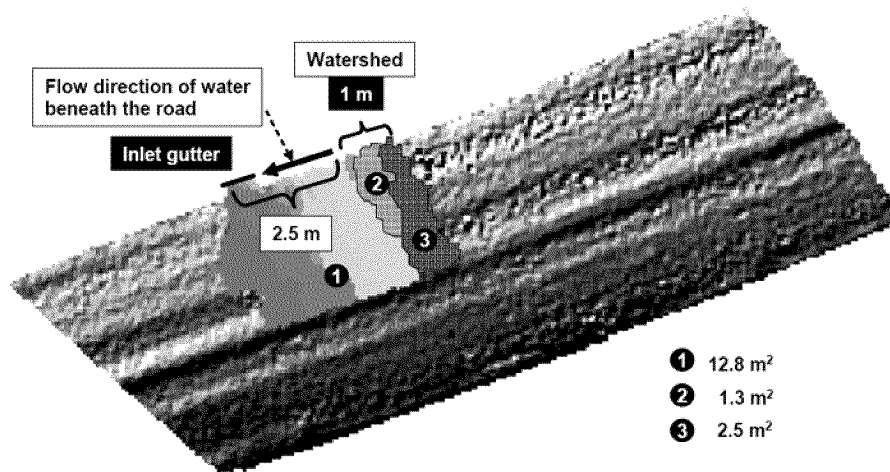


Figure 6.6: Calculated catchment areas for the inlet gutter. Flow direction due to preferential flow beneath the road is indicated.

Conclusion

Terrestrial laser scanning was revealed as a best method for acquiring 3D coordinates for small surface areas of max. 50 m^2 . Compared to GPS, tacheometry and levelling laser scanning is superior considering the sampling rate, the accuracy and the point density. The accuracy of the data is strongly dependent on the angle of incidence, the structure and the colour of the surface. Noise in the data result in extensive post-processing, including special filtering and noise reduction.

In this project, a surface model of a road segment was derived using 3D data acquired by terrestrial laser scanning. The surface model was applied subsequently to derive the catchment area of a pilot plant collecting road runoff. Based on the calculated catchment area, the rainfall data and the measured road runoff

volume, the percentage of road runoff that drains directly into the vegetated road shoulder was calculated as 36 %, while 64 % of road runoff is dispersed diffusively. As the pollutant load may be considered to be proportional to the water distribution, about 36 % of the pollutant load in the runoff would infiltrate the vegetated road shoulder immediately below the road. Thus, infiltration leads to high accumulation rates and high concentrations of heavy metals and organic substances in the topsoil.

This new method for the calculation of small scale catchment areas can be assessed as a success. However, it is recommended to control the results at critical parts of the surface drain, e.g. inlet with small scale tracer experiments, which only require a few minutes.

6.2 Static Application: Rock Engineering Applications

6.2.1 Introduction

Engineering works in rocks induce disturbances in the original state of equilibrium in which rock masses are found. The response of a particular rock mass to these disturbances is greatly influenced by its internal structure resulting from the occurrence of geological discontinuities with different preferential orientations. This response usually involves rock mass deformations that can be observed by recording the displacements of points located within the rock or on excavation surfaces. In practice, the monitoring of such displacements is of great interest as it allows for the understanding of the mechanisms through which rock masses react to excavation-induced perturbations and for predicting potential stability problems that may occur in the future. As a consequence, *in situ* characterization of the rock mass structure and displacement monitoring are two important operations that are routinely carried out during rock engineering projects.

Appropriate characterization of the rock mass structure is a time-consuming process as a sufficient number of features have to be sampled to achieve a reliable description of rock mass fracturing. Moreover, production constraints and installation of rock support systems, such as steel meshes or concrete linings, usually leave very little time to undertake an extensive survey of geological structures. On the other hand, discontinuity surveying requires safe access to rock surfaces that can only be guaranteed if adequate support is installed beforehand. Displacement monitoring is a common practice that is used to track the evolution of the rock mass behaviour. However, this operation is traditionally achieved by measuring the displacement of a limited number of points. Displacement monitoring of points located within the rock mass requires the drilling of boreholes and the installation of specific equipment. Therefore, the measurement of surface displacements is more frequently performed in practice. In this case, arrays of object points have to be installed firmly anchored within the first centimeters behind the rock surface at different locations along the surface. In both cases, it is necessary to monitor a sufficient number of points to achieve reliable interpretation of the actual rock mass behaviour.

The use of 3D laser scanners allows for effective management of the practical constraints encountered in rock engineering since it quickly provides a realistic and permanent representation of excavation surfaces that requires the installation of a reduced number of physical targets used only for data referencing purposes. This is of great importance in the study of inaccessible and potentially unstable surfaces, which are, thus, mapped at any time from a safe location regardless of the lighting conditions. Because of the high spatial resolution of the data, these tools can also be used for topographical surveys and the documentation of excavation surfaces, which are two additional procedures carried out routinely throughout construction work. Finally, the direct collection of digital data results in speeding up processing work through the use of modern computer resources. Therefore, terrestrial laser scanning has a high potential since it can be used as an efficient tool to record data required for various routine rock engineering applications and analyses.

The laser scanner has been used to measure the characteristics of geological structures as well as the surface displacements in an experimental tunnel in the Mont Terri Rock Laboratory, Switzerland. Several exper-



Figure 6.7: *Laser scanner inside the excavated niche including object points signaled by spheres.*

iments are currently undertaken in this laboratory to understand the behaviour of a rock formation, i.e. Opalinus clay, that has been identified as a potential host for a radioactive nuclear waste repository. The excavation is a 5 m long and 3.8 m diameter circular tunnel, cf. Figure 6.7, which was extended in seven steps with pauses for several investigations including total station surveying and laser scanning. Figure 6.8 shows different views of the point cloud that resulted from the surveying of the tunnel at the end of its excavation. The main objective of the work was to assess the potential of laser scanning in quantifying accurately geometrical characteristics of geological structures and in deriving time lapse surface displacement maps of object points as well as of rock surfaces with a high spatial resolution.

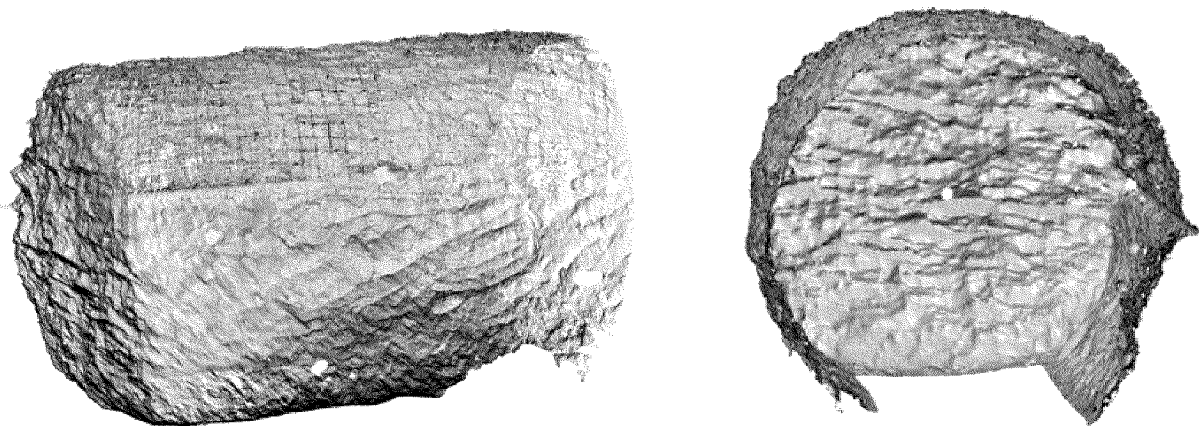


Figure 6.8: *Point cloud representing the final geometry of the tunnel: exterior view of the tunnel, as seen from inside the rock mass (left) and interior view of the tunnel (right).*

6.2.2 Method

A major concern when measuring displacement data is the installation of an appropriate and stable reference system. This reference frame is defined by reference points, which are fixed in regions that are not influenced by the excavation of the tunnel during the observation period. Based on previous displacement measurements made at the Mont Terri laboratory, i.e. convergence measurements, the zones that were not

influenced by the excavation of the tunnel were identified. Four control points (1, 2, 3, 4), defining a local reference frame, were installed in these regions. The left part of Figure 6.9 illustrates the location of the control points with respect to the location of the niche. Displacement monitoring was carried out with respect to the local reference system. This procedure is necessary for calculating absolute displacements with a higher order of accuracy. Furthermore, it facilitates the interpretation of the displacement data as it allows for the alignment of one horizontal coordinate axis with the tunnel axis.

Five arrays (100, 200, 300, 400, 500) of object points were installed during and after the tunnel excavation to assess the performance of displacement monitoring. The configuration of the first four arrays normal to the tunnel axis is illustrated in the right part of Figure 6.9. Each array has been oriented so that it is aligned with the assumed directions of the principal stresses. It was expected that the largest displacements, related to elastic response of the rock mass to the excavation, would be aligned with the direction of the major principal stress (σ_1). Object points were installed every 45° to cover uniformly each investigated tunnel cross-section. For practical reasons, no object point was installed in the tunnel floor. Bolts were utilized for both the reference points and the object points. These bolts were fixed in concrete and rock using mechanical anchors. Finally, additional points (1000, 1001) belonging to the surveying test field of the Mont Terri laboratory were included to transform the local coordinates into the reference frame of the laboratory, i.e. the Swiss Projection System, since the characterization of rock mass structure has to be performed with respect to a north-oriented reference system.

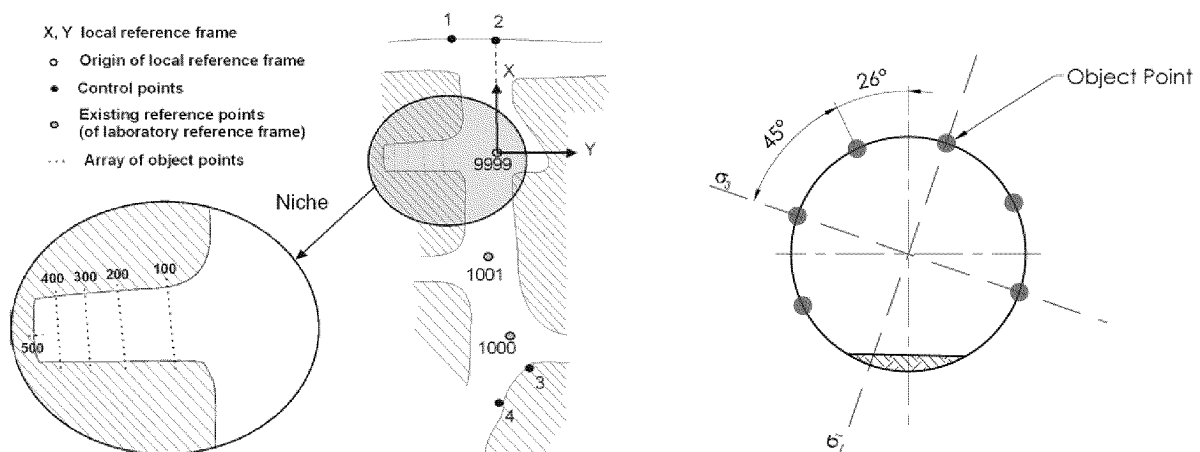


Figure 6.9: Location of the experimental tunnel, the reference points and the arrays of object points (left), configuration of the object point of the first four arrays normal to the tunnel axis (right).

Total station surveying of a number of object points installed on the tunnel surface was first carried out to assess the accuracy of utilizing the laser scanner as an alternative for the measurement of absolute displacements. The main focus during the excavation of the experimental tunnel was the identification of zones in the rock mass where the development of fractures sub-parallel¹ to the surface is occurring. It is assumed that the propagation and the opening of such fractures produce local displacements of the surface towards the inside of the tunnel. The detection of these zones requires the construction of maps showing the distribution of the displacements along the rock surface. Such maps were derived from the comparison of different scans of the excavation taken at different stages of its construction. Subtracting different scans of the same surface is in reality a relative measurement of the displacements, which allows for the identification and the quantification of local variations in the volume of the excavation.

The object points of the arrays, cf. Figure 6.9, were equipped with prisms and were surveyed after each excavation step using an automated total station. The use of the total station within the setup allowed for achieving an accuracy of less than 1 mm. All prisms were surveyed in two faces and in several sets.

¹Sub-parallel means, that it is not perfectly parallel but close to being parallel or slightly oblique.

Each free positioning of the total station was determined by surveying all four reference points, cf. Figure 6.9. The calculation of 3D coordinates of the object points was carried out in an adjustment. The achieved accuracy was less than 0.3 mm. The first measurement of the object points was used as an initial or reference measurement (session 0). Displacements that occurred between the initial and the i^{th} measurement session were calculated by subtracting the coordinates of session i from the initial coordinates of session 0. The resulting accuracy of the derived displacements of the object points in each coordinate direction (x, y, z) was quantified with less than 0.5 mm. Therefore, the accuracy of 3D displacements for each point of session i , with respect to session 0, were specified with less than 1 mm.

The object points can also be defined by spheres, instead of prisms, attached on the bolts installed, cf. Figure 6.7. Spheres are well-adapted for laser scanning because of their attractive properties regarding visibility and deriving center points, cf. Section 3.1.5. Each sphere was scanned and, based on the resulting point cloud, the coordinates of the center point of the spheres were calculated. This approach results in an accuracy of the center point of less than 3 mm, cf. Section 3.6.2. In addition, the center points have to be referred to the local reference frame. Nevertheless, it is not always possible in practice to scan both the reference points and the object points from the same scanner position. First, the distances from the laser scanner to the reference points are usually too long to achieve the required accuracy. Second, the reference points are not always visible from the position of the laser scanner. Looking at Figure 6.9, it can be seen that these problems occurred during the surveying work in the laboratory, which required positioning the laser scanner inside the niche. To solve this problem, intermediate reference points were set up temporarily and close to the laser scanner using tripods. These reference points were also surveyed by the total station and were included in the local reference frame. The accuracy of the position of the laser scanner can be specified within 3 mm. The resulting accuracy of the derived displacements in one coordinate direction was less than 5 mm. Consequently, the accuracy of 3D displacements for each object point is within 9 mm.

Understanding the actual rock mass behaviour can be greatly improved if the distribution of the displacements along the excavation surface is investigated instead of considering the displacements of a few discrete points. For that purpose, point clouds representing surfaces scanned at different phases of the excavation can be used. Several software packages allow for the 3D comparisons of point clouds and surfaces. In this case study, the software Geomagic by Raindrop Geomagic Inc. was used. The generation of time-lapse displacement maps requires some processing beforehand. First, points representing blunders have to be detected and deleted automatically or manually. Then, the noise is reduced by means of a filtering process. This is an essential step as the noise due to the natural limits of scanning affects greatly the quality of the point cloud, by making sharp edges dull and making smooth surfaces rough. The result is a more uniform arrangement of points. Subsequently, the processing entails the conversion of the initial or reference point cloud into a surface model that consists of small triangles (TIN, Triangular Irregular Network). This surface model represents the reference object that can be further processed, if required, e.g. by deleting non-contiguous intersecting triangles, filling holes or surface smoothing. Finally, the residuals of a test object described by a point cloud or a TIN representing the same region at a different time can be computed by comparing this test object with respect to the reference object. This operation is possible only if the test object has been transformed previously into the same reference system as the reference object.

As another possibility, the use of the least squares 3D surface and curve matching algorithm, developed by [Grün and Akca, 2005], may help the interpretation and detection of surface displacements based on 3D point clouds. Therefore, the possible displacements of objects, described by 3D point clouds, can be characterized by a 3D translation vector and a 3D rotation vector. Thus, new insights into the behaviour of rock masses can be obtained.

6.2.3 Results

Rock Mass Structure Characterization

The point cloud resulting from scanning the area of the tunnel, which is found to be intersected by several geological discontinuities, is shown in Figure 6.10. The figure is a close-up of the point cloud illustrating one of these discontinuities in the upper part of the tunnel face. In this example, the average point spacing of the point cloud is about 5 mm. Comparing the image generated by the laser scanner with a digital image representing the same area, cf. lower part of Figure 6.10, it can be seen that in this case, the density of the point cloud is sufficient to produce a realistic rendering of the surface, thereby allowing for the identification of geological features of interest.

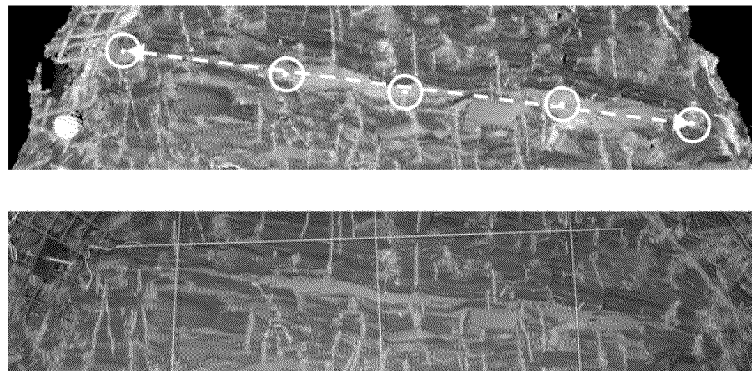


Figure 6.10: Geological discontinuity intersecting the tunnel face, selected points on the discontinuity surface, measurement principle of the discontinuity trace length (up) and corresponding digital image (below).

Furthermore, points that were selected to define and locate the discontinuity plane can also be seen in Figure 6.10. The orientation of the discontinuity was then determined by calculating the orientation of the best-fit plane minimizing the mean square distance to all the selected points. Dip values of 50° and 46° and dip direction values of 146° and 156° were obtained through the analysis of the point cloud and on-site manual measurement, respectively. The measurements based on the laser point cloud are actually more representative of the overall orientation of the structure since manual measurements using a compass are directly influenced by local variations of the surface morphology. The geometry of these variations, which correspond to the large-scale roughness of the discontinuity surface, can be quantified easily using the distance between the best-fit plane and the selected points. Finally, the trace length, e.g. the length of the linear feature resulting from the intersection between the rock face and the discontinuity, is quantified by measuring the distance between two points selected on both extremities of the trace. By repeating this process with other discontinuities visible in the image it is possible to produce a database that can be further utilized to characterize and model the structure and the behaviour of the rock mass around the excavation.

Displacement Monitoring

The expected accuracy of displacement data both for total station and for laser scanner has been discussed previously. Total station surveying was used to provide a high order of accuracy, within 1 mm for both coordinate differences and 3D point differences, while the expected accuracy of laser scanning was 5 mm for the coordinate differences and 9 mm for the 3D point differences. For example, the coordinate differences in z-direction of some points (points 1 and 6 of the arrays 100, 200, 300 and 400) located at the top of the niche are presented in Figure 6.11 and in Figure 6.12. The upper parts show the results obtained by total station and the lower parts show the results obtained by laser scanning. In all the figures, an upward trend of the coordinate differences in z-direction between sessions 10 and 11 are visible. The coordinate differences are defined by subtracting session i from session 0. Thus, the upward trend of the coordinate differences

means a downward trend of the absolute coordinate of the point at session i . Considering the location of these points in the roof of the niche, the behaviour is logical since the roof is deforming downwards. A time period of half a year is represented between sessions 10 and 11. Surprisingly is the trends were also detected by laser scanning and suggest that the accuracy has to be smaller than the estimated value of 9 mm.

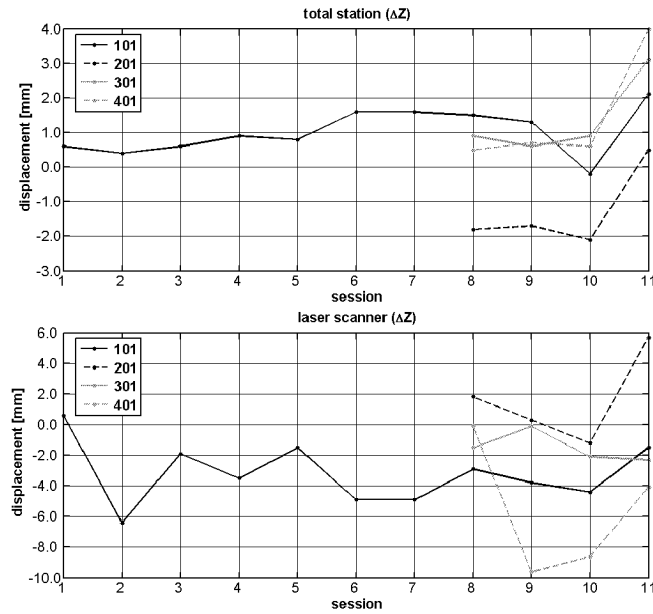


Figure 6.11: Displacements in height for point 1 for arrays 100, 200, 300, 400. Total station (top) and laser scanner (bottom).

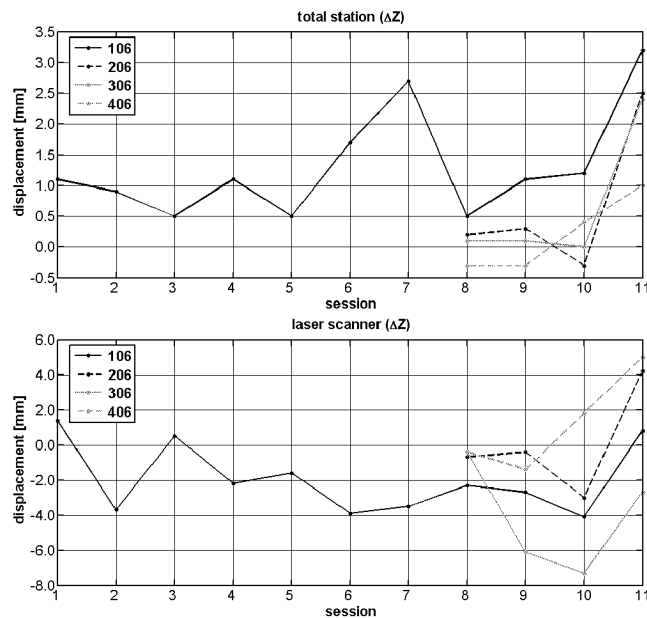


Figure 6.12: Displacements in height for point 6 for arrays 100, 200, 300, 400. Total station (top) and laser scanner (bottom).

A displacement map of the upper part of the final tunnel face is shown to demonstrate the potential of using the laser scanning point clouds. The displacements calculated were based on measurements carried out after the end of the excavation (session 8), two days later (session 9) and six days later (session 10). A TIN was created using the data of session 8, which represents the reference object. The residuals of the point clouds for sessions 9 and 10 were then computed with respect to the reference object. Figure 6.13 shows

the displacements, which occurred between sessions 8 and 10, did not exceed 10 mm. Therefore, they are of the same order of magnitude as the accuracy of the laser scanning for the determination of the object point displacements. However, changes in the concentration of the areas characterized by displacements greater than ± 2 mm suggest that displacements increased with time and with distance from the center of the tunnel face.

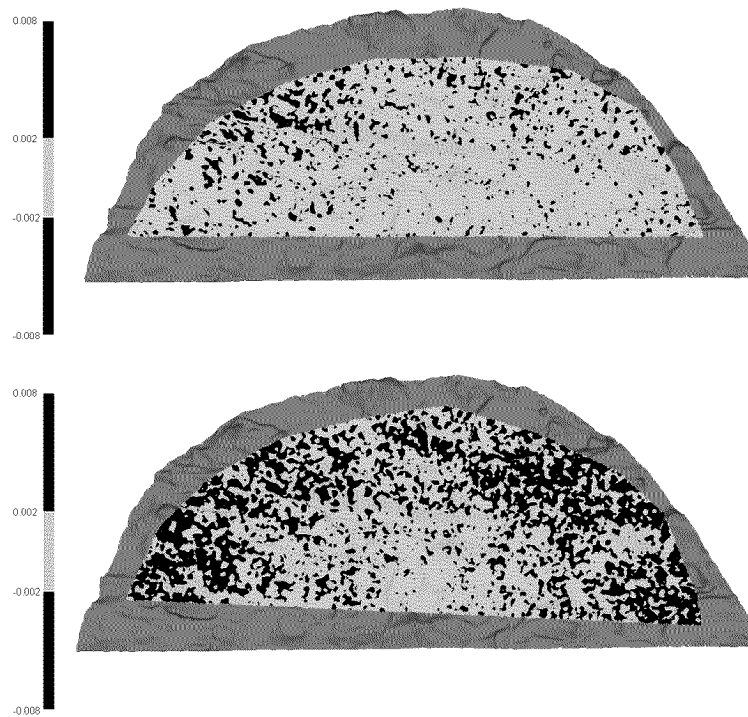


Figure 6.13: Surface displacements (in [m]) obtained from comparing the point clouds acquired during sessions 9 (up) and 10 (down), with the surface model corresponding to session 8.

Conclusion

Laser scanning is considered as a promising technique in the field of rock engineering since it has the potential to be used for the collection of data required for several routine tasks. However, it is essential to select the most appropriate laser scanner according to project-specific constraints such as range, excavation geometry, time available for scanning as well as point accuracy and point density. The Imager 5003 of Zoller+Fröhlich was used in an experimental tunnel in the Mont Terri Rock Laboratory for the characterization of geological discontinuities and displacement monitoring. This scanner was found to be particularly well-suited for rock mass characterization in underground excavations while yielding an accuracy of less than 1 cm in the determination of the displacement of object points. Nevertheless, preliminary results suggested that displacement maps with a higher order of accuracy can be produced by taking advantage of the large quantity of spatial data provided by the laser scanner. Therefore, the construction of accurate displacement maps would greatly improve the understanding of the rock mass behaviour. Crucial issues identified for this application included referencing to a stable reference system, coordinate transformation, noise reduction and smoothing of point clouds.

Regarding rock mass characterization, efforts should be made to automate the recognition of discontinuities so that the time required for data analysis can be significantly decreased. Future work will focus on the development and comparison of processing algorithms to improve the accuracy of the displacement mapping. The resulting maps will be further compared with the results of other field investigation meth-

ods and numerical models simulating the rock mass behaviour around the tunnel. The aim of this study will be to better assess the capability of laser scanning in monitoring geomechanical processes occurring in rocks.

6.3 Kinematic Application: Test Tunnel

6.3.1 Introduction

Due to the fast acquisition rate and the high point density, laser scanning is not only suitable for static applications but also for kinematic applications. This is especially the case for profile measurements, which are useful for generating an area-wide surveying of objects by means of a moving platform.

The following example of a kinematic application refers to the surveying of tunnel surfaces. The goal is to prove that, with kinematic laser scanning, a sufficient absolute accuracy can be achieved. Tunnel surfaces are either scanned with static applications, using consecutive viewpoints, or with relative kinematic applications with respect to the rail axis. Relative surveying with respect to the rail axis is appropriate for detecting objects dangerous to trains, i.e. railway loading gauge. However, the interpretation of deformations is difficult since the object, i.e. the tunnel surface, or the rails could be changed or moved with time.

The kinematic application is performed on a test tunnel, i.e. the calibration track line at the IGP of the ETH Zurich. The laser scanner is mounted on the test trolley, which moves along the track. A total station tracks the moving platform so that the absolute trajectory can be obtained. The laser scanner surveys vertical 2D profiles normal to the moving direction. During the motion, control points installed on both sides of the track at different heights are scanned. The 3D coordinates of the control points visualized by spheres can be calculated. The performance and accuracy are assessed by comparing the calculated center points of the spheres with the reference coordinates based on surveying with a total station. The experimental setup was already shown in Section 5.1, cf. Figure 5.1, and the test field of control points along the test tunnel was discussed in Section 3.1.2.

The test trolley was forced to run with a constant velocity along the test tunnel. The control software for the encoder, causing the rotation of the wheels of the test trolley, allows a maximum velocity of $0.7 \frac{\text{m}}{\text{s}}$. The test tunnel and constant velocities are chosen to minimize errors for calculating the trajectory of the test trolley. Thus, the trajectory can be approximated by a regression line implying a constant velocity. A more general method is the approximation of the trajectory by a Kalman filter. The Kalman filter can respond to varying system states such as variation in the velocity. Applying both mathematical tools allow for comparing the results and assessing the potential of kinematic laser scanning for absolute geo-referencing.

The test runs for this kinematic application include

- different velocities of the test trolley,
- different rotation times of the rotating mirror of the laser scanner, and
- different scanning resolutions.

The point-spacing along the moving direction can be defined by the velocity of the test trolley and by the rotation time of the rotating mirror of the laser scanner. The point-spacing within each vertical profile has to be controlled by means of the scanning resolution according to the scanning modes supported by the manufacturer of the laser scanner.

6.3.2 Kinematic Model: Regression Line

The velocity of the test trolley is estimated with a mathematical model of the regression line, cf. Section 5.3.3. Since the test tunnel can be sufficiently approximated by a straight line and since the tracking total station is set up in extension from this line, cf. Section 3.1.1 and Section 5.1, the reference frame is oriented so that the trolley moves along the x -axis whereas the y - and z -components are set to zero. The azimuthal orientation is defined by surveying a control point with an azimuth that is given with respect to the global reference frame of the test tunnel.

Before calculating the regression line, the data acquired by the total station have to be pre-processed. First, the spherical coordinates in terms of the angular directions hz and v and the distance s are filtered by applying a median filter with a window size of five. The distance data may show blunders that have to be eliminated beforehand. Second, the spherical coordinates are transformed to Cartesian coordinates with

$$\begin{aligned}x_a &= s \cdot \cos(v) \cdot \cos(hz) \\y_a &= s \cdot \cos(v) \cdot \sin(hz) \\z_a &= s \cdot \sin(v)\end{aligned}\tag{6.1}$$

According to Equation (5.1), the moving trolley is defined by the vector \vec{x}_a with respect to the absolute coordinate system. The rotation matrix R for a possible rotation of the local coordinate system defined by the moving trolley can be replaced by the identity matrix due to the experimental setup, cf. Section 5.1. The local coordinates acquired by the laser scanner are described by

$$\begin{aligned}x_l &= 0 \\y_l &= y_s \\z_l &= z_s\end{aligned}\tag{6.2}$$

whereas y_s and z_s are the coordinates supported by the laser scanner. Due to the orientation of the vertical profiles normal to the moving direction, the coordinates in the x -direction are set to zero and are only defined by the tracking total station. Based on the internal time tag given by the rotation time T , cf. Section 5.2, each point measured by the laser scanner has a relative time reference. Knowing the absolute time tag for the first point of the first vertical profile, the absolute time tags for all other points of the following vertical profiles can be derived, cf. Section 5.4. Thus, all laser points are time-referenced and the absolute position and orientation are determined by a mathematical model for the motion of the trolley. The motion model introduced is defined by the following parameters:

- $v_y = v_z = \text{const} = 0$
- $v_x = \text{const}$

The velocity along the x -axis is assumed to be constant and is computed by applying the regression line on the data of the x -components. Since the motion of the trolley is not changed during the data set, additional blunders can be identified within the adjustment algorithm using normalized residuals or a distance offset. The missing coordinates in the x -direction of the points acquired by the laser scanner can be obtained by using the regression line. Since the time tag of each laser point as well as the motion of the trolley are known, the position vectors \vec{p} of the interpolated points are obtained by

$$\begin{aligned} p_x &= x_a + x_l + \Delta t \cdot v_x \\ p_y &= y_a + y_l + \Delta t \cdot v_y \end{aligned} \quad (6.3)$$

$$\begin{aligned} p_z &= z_a + z_l + \Delta t \cdot v_z \\ \Delta t &= j \cdot \frac{T}{nr_{\text{profile}}} \end{aligned} \quad (6.4)$$

whereas the time interval Δt is defined by the rotation time T , the number of points within each vertical profile nr_{profile} (depending on the scanning mode) and the current point number j of the whole point cloud.

Table 6.1: Characteristics of one total station data set.

tracking time [s] :	410
number of measurements :	3278
measured velocity [m/s] :	0.100216
standard deviation of velocity [m/s] :	0.000001

Several data series varying in length, rotation time and scan resolution were acquired and processed. For example, the calculation of one regression line is presented. The characteristics of the data set are given in Table 6.1. The residuals to the regression line are shown in Figure 6.14. It can be seen that the velocity is estimated within high accuracy and the residuals do not to exceed ± 5 mm. Therefore, blunders were eliminated within the adjustment algorithm.

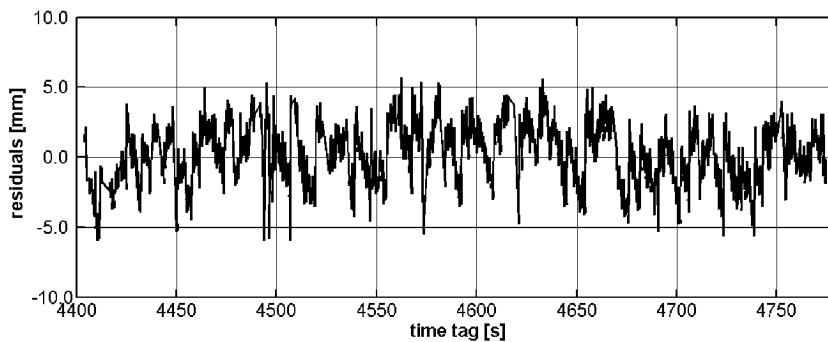


Figure 6.14: Residuals of total station data to regression line.

The quality of the mathematical model is verified by comparing the coordinates of the calculated center points of the control points, i.e. spheres, with their nominal values. Therefore, the center points can be derived using the 'free' adjustment and the 'fix' adjustment, cf. Section 3.1.5. The results of a complete data set for the velocity $v = 0.1 \frac{\text{m}}{\text{s}}$ are given in Table 6.2. The 3D accuracy is about 3 mm for the center points derived by the 'free' adjustment. In addition, the use of the well-known diameter of the spheres increases the 3D accuracy to 2 mm. The data sets differ in the rotation time, length, scan resolution and number of control points. The table shows that neither the rotation time nor the scan resolution influenced the accuracy significantly. Only treatment of the diameter of the spheres increased the accuracy. Changing the velocity to $v = 0.2 \frac{\text{m}}{\text{s}}$ and $v = 0.3 \frac{\text{m}}{\text{s}}$, the results are similar to the results shown in Table 6.2.

6.3.3 Kinematic Model: Kalman Filter

The system state of the moving test trolley along the track line is estimated by a Kalman filter. The total station data defining the absolute reference frame are pre-processed in two steps. First, blunders are

Table 6.2: Results of kinematic laser scanning based on the mathematical model of a regression line. The time, the rotation per second (RPS), the scanning resolution, the velocity, the number of control points and the 3D accuracy are shown.

Time [s]	RPS	Scanning Resolution	Velocity [m/s]	# Control Points	3D Accuracy [mm]	
					'free'	'fix'
100	25	middle	0.10020	5	3.4	1.8
		high	0.10021		2.9	1.6
	33	middle	0.10020		3.4	2.0
		high	0.10021		3.9	2.4
200	25	middle	0.10020	8	3.3	1.8
		high	0.10021		3.2	2.1
	33	middle	0.10020		2.3	1.9
		high	0.10021		2.9	2.0
300	25	middle	0.10022	13	3.0	1.8
		high	0.10021		3.6	2.2
	33	middle	0.10021		2.9	2.1
		high	0.10022		2.3	1.9

eliminated by applying a median filter. Second, the Kalman filter requires equidistant data sets. Based on the acquired and median filtered data, the equidistance is derived by polynomial interpolation. The polynomial interpolation may influence the equidistant data set to be generated. The influence of different polynomials were not compared in detail. Due to the motion of the test trolley, a third order polynomial presented a good approximation. If higher orders of the polynomial are chosen, the significance of the coefficients can be tested.

The interpolated and equidistant data provide the input for the Kalman filter. The mathematical model for the motion of the test trolley is a motion with a constant velocity and accelerations in the form of disturbances with

$$\vec{x}_k = \vec{x}_{k-1} + \Delta t \cdot \vec{v}_{k-1} + \frac{1}{2} \Delta t^2 \cdot \vec{a}_{k-1}. \quad (6.5)$$

According to the dynamic model described by Equation (5.21), the first two terms of Equation (6.5) define the system state and are summarized in the transition matrix Φ . The accelerations are disturbances and defines the disturbance input matrix Γ . The system state can be expressed by the parameters

- position: x, y, z and
- velocity: $\dot{x}, \dot{y}, \dot{z}$.

The disturbances are characterized by

- acceleration: $\ddot{x}, \ddot{y}, \ddot{z}$.

Based on the mathematical model and the parameters for the motion, the matrices can be determined. The transition matrix Φ contains the derivatives of the variables describing the system state with respect to the variables of the system state. The disturbance input matrix Γ consists of the derivatives of the disturbance variables with respect to the system state variables:

$$\Phi_k = \begin{pmatrix} 1 & 0 & 0 & \Delta t & 0 & 0 \\ 0 & 1 & 0 & 0 & \Delta t & 0 \\ 0 & 0 & 1 & 0 & 0 & \Delta t \\ 0 & 0 & 0 & 1 & 0 & 0 \\ 0 & 0 & 0 & 0 & 1 & 0 \\ 0 & 0 & 0 & 0 & 0 & 1 \end{pmatrix} \quad (6.6)$$

$$\Gamma_k = \begin{pmatrix} \frac{1}{2}\Delta t^2 & 0 & 0 \\ 0 & \frac{1}{2}\Delta t^2 & 0 \\ 0 & 0 & \frac{1}{2}\Delta t^2 \\ \Delta t & 0 & 0 \\ 0 & \Delta t & 0 \\ 0 & 0 & \Delta t \end{pmatrix} \quad (6.7)$$

The observation of the system state is carried out by the tracking total station. Since the original observations are spherical coordinates, the Cartesian coordinates have to be derived using Equations (6.2). The given coordinates allow for the introduction of indirect observation of the velocity with respect to the coordinate axes. The observation vector z is then defined by the (indirect) observations of the six variables of the system state:

$$z_k = \begin{pmatrix} x_k \\ y_k \\ z_k \\ (x_k - x_{k-1})/\Delta t \\ (y_k - y_{k-1})/\Delta t \\ (z_k - z_{k-1})/\Delta t \end{pmatrix} \quad (6.8)$$

The covariance matrix of the deduced observations is not only a diagonal matrix because the Cartesian coordinates are correlated with each other. The relation between the observations and the system state variables is described by the matrix H , which contains the derivatives of the system state variables with respect to the observations and results in an identity matrix.

The error covariance matrix for the input disturbances Q and the error covariance matrix for the observations R have to be derived. Covariances have to be eventually considered for dependent variables, e.g. the deduced observations. The covariance matrices can be easily obtained by applying the error propagation. Furthermore, the system noise has to be considered by forming the vector w .

The recursive Kalman filter requires the initialization of the system state x_0 and the error covariance matrix of the system state P_0 . The better the initial values, the better the estimation of the system states and the error covariances of the system states for the following epochs. Bad initial values result in the need for more epochs for the filtering process and therefore, iterations to properly estimate the system state including the error covariances. In any case, the filter algorithm converges rapidly.

The Kalman filter describes a powerful tool for estimating the system state and the error covariances of a moving object. The filter algorithm allows for tuning of the mathematical model for the movement individually. The implemented algorithm is defined by a simple algorithm due to the motion of the test trolley along the track line. The system state as well as the error covariances can be adapted in many ways, according to that best-suited for the present application. The Kalman filter is used to model the motion of the test trolley not only for constant motion but also for arbitrary motion.

The trajectory resulting from applying the Kalman filter in a forward and a backward direction are used to calculate the object points scanned by the laser scanner during motion. The quality of the estimated

trajectory is assessed by control points with coordinates derived analogous to the procedure described for the use of the regression line, cf. Section 6.3.2.

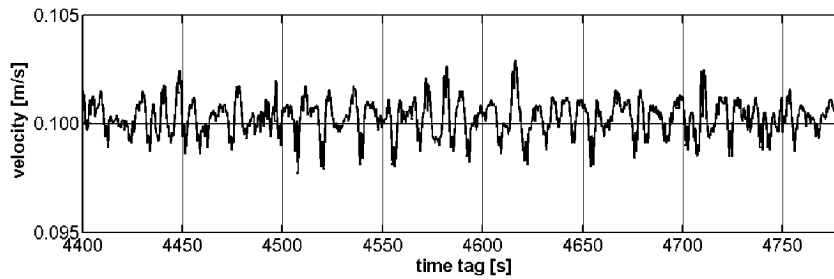


Figure 6.15: Velocity of moving trolley estimated by Kalman filter for one data set.

For example, the velocity of the test trolley of one data set estimated by the Kalman filter is shown in Figure 6.15. It can be seen that the motion of the trolley oscillates. These oscillations are based either on the noise produced by the tracking total station or by the variations of the encoders controlling the velocity of the test trolley. Considering a distance error of $\Delta s = 1 \text{ mm}$ by a time interval of $\Delta t = 0.1 \text{ s}$, a variation in the velocity of $v = 0.01 \frac{\text{m}}{\text{s}}$ results. Thus, the oscillations of the velocity are relatively small in comparison with the distance accuracy of the total station. The accuracy of the trajectory and the scanned point cloud is assessed by control points. The same parameters for the data sets are chosen compared to the example where the regression line was used. Table 6.3 summarizes the results and shows the 3D accuracy for the control points. The accuracy is sufficiently high since the 3D accuracy is within 5 mm. Surprisingly, the accuracy decreases with the time and therefore, with the length of the trajectory. One possibility is that the equidistant time tags of the total station measurements, derived for the Kalman filter, show deviations. Another reason can be found in the Kalman filter. The tuning of the filter, e.g. mathematical model of the system state, covariance matrices, offers several ways of deriving the trajectory. Considering the given accuracy of the used total station² in the tracking mode (5 mm + 2 ppm), the 3D accuracy, given in Table 6.3, fits the manufacturer's specification.

Furthermore, the same conclusion, as for the regression line, can be drawn: neither the rotation time nor the scan resolution significantly influence the 3D accuracy. Only the treatment of the diameter of the spheres increases the accuracy. Changing the velocity to $v = 0.2 \frac{\text{m}}{\text{s}}$ and $v = 0.3 \frac{\text{m}}{\text{s}}$ have similar results, which are shown in Table 6.3.

6.3.4 Results

Kinematic laser scanning has become an alternative to static laser scanning. The advantage is a higher performance of scanning objects characterized by a fast acquisition rate. For linear objects, e.g. tunnels or roads, kinematic applications are especially superior to static applications.

The accuracy that can be achieved is not only limited by the laser scanner used. The acquisition of the position and the orientation of the parameters describing the moving trolley is also essential. Finally, the trajectory that establishes the base for calculating the object points acquired by the laser scanner has to be estimated. Mainly, the pre-processing of the data required for the trajectory can be completed with several methods and yield different results. Thus, processing of the data from the example of a kinematic application was completed in different ways. The trolley was forced to run with a nearly constant velocity. The mathematical models applied to the motion of the trolley were described by a regression line and a Kalman filter.

²TPS1201 from Leica Geosystems

Table 6.3: Results of kinematic laser scanning based on the mathematical model of a Kalman filter. The time, the rotation per second (RPS), the scanning resolution, the number of control points and the 3D accuracy are shown.

Time [s]	RPS	Scanning Resolution	# Control Points	3D Accuracy [mm]	
				'free'	'fix'
100	25	middle	5	2.7	2.4
		high		3.5	2.4
	33	middle		2.6	2.3
		high		3.2	2.1
200	25	middle	8	3.3	2.8
		high		3.1	2.9
	33	middle		3.5	3.0
		high		4.1	3.5
300	25	middle	13	4.4	4.5
		high		4.9	4.3
	33	middle		4.3	4.0
		high		4.6	4.1

The regression line represents optimal processing of the data since errors produced by processing the data are minimized. The total station data were only pre-processed with a median filter to eliminate blunders. The algorithm of the regression line allows for the calculation of a constant velocity of the trolley. The residuals of the data used for calculating the regression line confirm that the motion can be assumed to be constant. The combination of both the test tunnel and the constant velocity of the test trolley allows for an assessment of the stability of the rotation time of the rotating mirror of the laser scanner. The results can be interpreted as sufficient regarding the 3D accuracy of the control points, which do not exceed 3 mm for the 'fix' adjustment.

The Kalman filter is a powerful tool for estimating the trajectory of arbitrarily moving objects. Due to the characteristics of the sensors acquiring the required data for calculating the system state, additional pre-processing algorithms have to be applied, such as polynomial interpolation and smoothing. The Kalman filter requires an appropriate mathematical model for the motion and the influencing variables disturbing the motion. The filter tuning becomes a key factor and plays an important role. The results obtained by Kalman filtering refers to the filter settings. The implemented algorithm shows the feasibility of the Kalman filter. The obtained 3D accuracy is slightly worse than the 3D accuracy obtained by applying the regression line. The accuracy can be increased by testing more sophisticated filter settings, such as error and covariance models.

Nevertheless, the kinematic application of the laser scanner using the profile mode has been successful. The obtained 3D accuracy of modeled objects does not exceed 5 mm. Thus, kinematic laser scanning is also conceivable for deformation monitoring in tunnel applications. The laser scanner and its derived rotation time offers a powerful instrument for the generation of a dense point cloud for kinematic applications. For example, the point cloud of the test tunnel along the calibration track line is shown in Figure 6.16. The calculated point clouds have to be treated analogous to the point clouds based on static applications. This means data processing and filter algorithms have to be applied to eliminate blunders and to reduce the noise within the data, e.g. blunder detection and mixed pixels, cf. Section 4.1.

The following figures show views of the processed laser scanning data. Figure 6.16 gives an impression of a view inside the test tunnel. The track line on which the laser scanner moved runs along the right side. Since the laser scanner cannot acquire data below itself, due to the housing, the floor or objects lying under the scanner were not captured by the laser beam. The control points were visualized by spheres on the

left and right sides. The shadows produced by the objects show the scanning direction and homogeneous orientations. The visualized section has a length of nearly 37 m, the width is about 5 m and the height is about 3 m. The varying grayscale values of the point cloud are based on the intensity values acquired by the laser scanner. The intensity values are influenced by several parameter, e.g. the range, the reflectivity of the object, and the angle of incidence between the surface normal of the object and the laser beam.



Figure 6.16: *Point cloud of test tunnel based on kinematic surveying (inside view).*

In Figure 6.17, the ceiling was faded out to catch a better view from outside to inside of the test tunnel. The objects as well as the object shadows can be roughly recognized. The left side of the tunnel was equipped with some geodetic installations, e.g. pillars, granite tables and instruments. The right side shows only a wall and some posters. Ten posters at the right side can be seen.

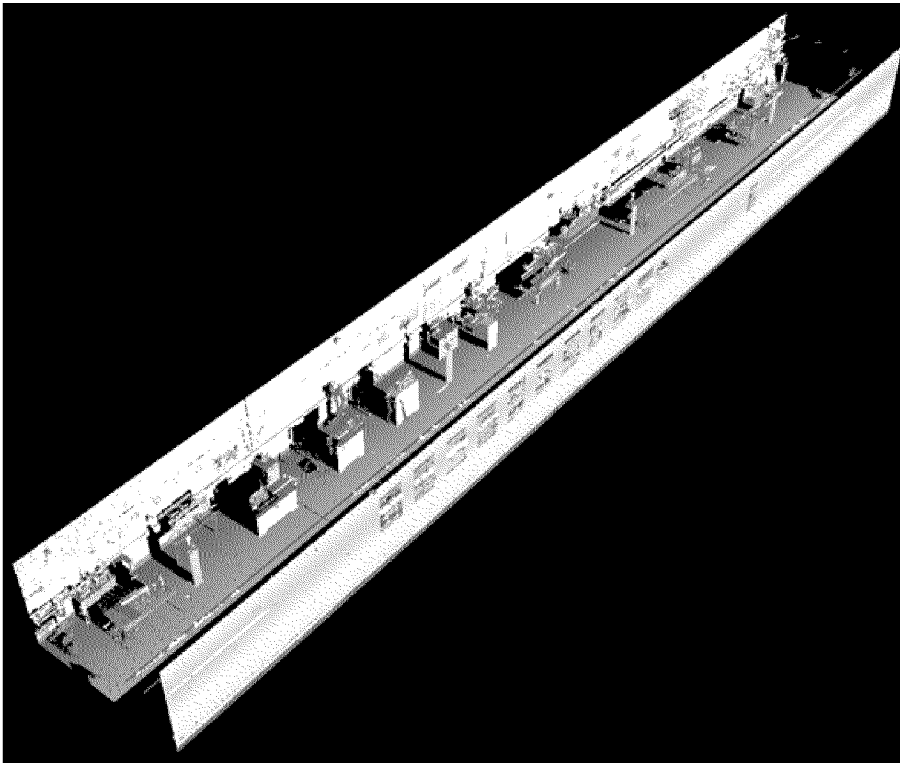


Figure 6.17: *Point cloud of test tunnel based on kinematic surveying (outside view).*

Figure 6.18 shows an example of one control point which was used to assess the accuracy of the kinematic laser scanning. The sphere was already modeled by the point cloud to demonstrate the location of the control point. The spheres were attached on bolts which were drilled in the concrete walls. The point shadow produced by the sphere can be seen on the wall. Furthermore, the high resolution of the acquired point cloud is obvious since the headlines of the posters hung on the walls are readable. The settings for this data set show a velocity of the test trolley of $v = 0.3 \frac{\text{m}}{\text{s}}$, the scan resolution was 'middle' and the rotation time was $T \approx 0.04 \text{ s}$. The vertical profiles show a regular grid based on the orientation of the laser scanner normal to the motion direction. The point spacing in the vertical direction is only based on the scanning mode, the point spacing in horizontal direction can be adapted by changing the velocity of the test trolley or by choosing a different rotation time.

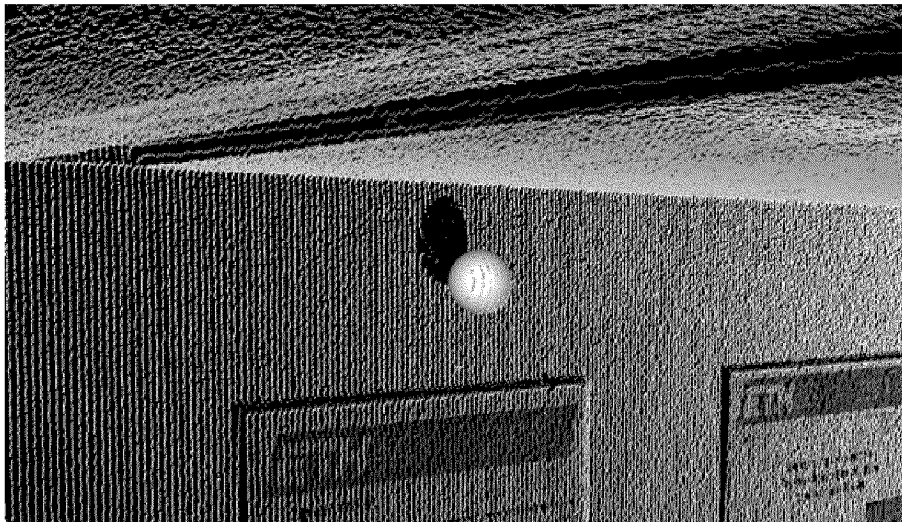


Figure 6.18: Point cloud of test tunnel based on kinematic surveying (detailed view).

Summary

7.1 Conclusions

Terrestrial laser scanning is a promising technique and has the potential to be adapted as an equal surveying technique. Laser scanners are now in the second to third generation of development and fulfill several geodesists' needs. Investigation regarding potentials and limitations have been launched some years ago. Independent examinations from different institutions have established a comprehensive knowledge regarding properties, influencing parameters, performance and limitations. The collaboration between geodesists and manufacturers results in improvements, which ease the use of laser scanners and significantly improve the accuracy.

The calibration and investigation of the laser scanner 'Imager 5003' of Zoller+Fröhlich was carried out regarding several aspects, such as:

- distance precision and accuracy
- angle precision and accuracy
- instrumental errors
- non-instrumental errors

The results have shown that laser scanners offer a high potential regarding high accuracy within the millimeter-scale. The most critical factor is thereby defined by the distance measurement system. Since the distance measurement is based on prismless measurements, the signal-to-noise ratio influences the precision significantly. The signal-to-noise ratio is generally affected by three parameters: the range, the reflectivity of the object and the angle of incidence. This thesis showed that the noise related to the distance can be reduced by an adequate filtering technique, which takes into account the orientation of the noise along the measurement direction.

Systematic effects produced by methodological errors may also affect the data significantly. The investigation regarding the wobble of the vertical axis and the errors of the collimation axis showed that there are indeed systematic effects, especially for short ranges below ten meters. Furthermore, the verification of the laser scanner system and its performance, i.e. measurement noise and instrumental errors, over time are recommended either with a system calibration or with a component calibration.

The two discussed applications regarding static laser scanning showed the potential for applications in the field of engineering geodesy. Point clouds defining objects in a high point resolution achieved results from the whole object and also in only discrete points. The flow directions of a road section or the displacements on a tunnel face after excavation establish a new method of interpretation, especially in the related engineering fields of urban water management and engineering geology. The accuracy in the millimeter

range, achievable by the laser scanning data, has established laser scanning as an alternative to traditional surveying techniques, i.e. tachymetry, GPS, levelling, photogrammetry.

The third example involves a kinematic application. Kinematic applications are of greatest interest in tunnel applications, railways and roads. The surveying in three dimensions, including intensity information, in a kinematic way significantly increases the performance of surveying objects. An example of kinematic laser scanning in a test tunnel showed that laser scanners can provide a sufficient absolute 3D accuracy. Concerning deformation monitoring during and after tunnel excavations, laser scanning seems to offer an alternative to static convergence measurements. The limiting factor is not the accuracy of the laser scanner, but the accuracy of the required 3D trajectory acquired by additional sensors for an absolute positioning fixing, e.g. total station, inclinometers, GPS, INS. The calculation of the 3D trajectory becomes an important aspect. However, laser scanners also offer the possibility of capturing the environment quickly and precisely in kinematic applications.

7.2 Outlook

Terrestrial laser scanning is a part of geodesy and offers a high potential for fast, nearly continuous and precise data capturing. The improvements regarding accuracy, range, sampling interval and the implementations of inclinometers, levels and digital cameras define a powerful surveying instrument. Sensor fusion between GPS and total station in recent years have allowed for the development of an all-in-one instrument in the near future that will consist of a GPS-based scanning total station, thus combining the advantages of each individual instrument in one. The lack of staking out, surveying discrete points and other tools have yet to be resolved. Furthermore, the possibility of operating laser scanners in harsh climatic conditions, e.g. low and high temperatures, humidity (rain or snow), and the reliability in the operation of laser scanners will help to extend the field of applications.

The first steps for combining a laser scanner with a total station were carried out at ETH Zurich. A laser scanner, LMS200 of Sick (Germany), is mounted on a total station to benefit from the advantages of both instruments. Figure 7.1 shows the sensor fusion first published by [Schulz and Zogg, 2006].



Figure 7.1: *Sensor Fusion: Laser scanner mounted on total station.*

The acceptance is not only dependent on improvements on the side of hardware, but also a standardization is recommended to assess and compare the different types of terrestrial laser scanners. An international guide including information regarding standardized parameters for distance accuracy, angle accuracy, 3D

accuracy of single points, 3D accuracy of objects, e.g. spheres, would help users to distinguish between available laser scanner systems. Since laser scanning also means the processing of point clouds, the data transfer and exchange between laser scanners and software packages is essential and should be simplified. Furthermore, the processing of point clouds has to be supported by fully-automatic algorithms to reduce the time for post-processing work. The limiting time factor is not only the data acquisition, but also the processing of the huge numbers of point clouds.

In the past three years another promising technique has been developed and may revolutionise the world of 3D data capturing methods. It is called range-imaging (RIM) and is based on CMOS¹ image sensors. So called range-imaging cameras acquire, with each single pixel of the CMOS chip, slope distances between objects and the camera. The camera-like operation mode allows for directly deriving 3D coordinates by spatial resection using the camera characteristics, i.e. focal length and pixel coordinates, and the measured slope distance. The intensity or amplitude of the demodulated signal complement the 3D coordinates with a fourth dimension analogous to laser scanning. The data acquisition rate is extremely high, with frame rates up to 50 frames per second, the range is limited to several meters, i.e. close-range applications, and the accuracy is within the centimeter-scale [Kahlmann and Ingensand, 2005]. An example of one range-imaging camera is shown in Figure 7.2, the SwissRanger SR-2 by CSEM (Switzerland). The lens is located in the middle for acquiring the data, the visible array of LEDs is used as the emitting system for the distance measurement. The CCD/CMOS sensor is behind the lens. RIM cameras are small in dimensions, i.e. centimeters, light in mass, i.e. some hundreds of a kilogram, and low in cost, i.e. below 1000 CHF. Thus, they are well-adapted for several applications, e.g. automotive, safety, security and surveillance, telemonitoring, robot vision, autonomous vehicles, and surveying.

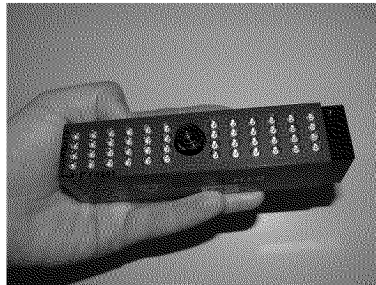


Figure 7.2: *SwissRanger*TM SR-2 by CSEM.

¹CMOS: complementary metal-oxide-semiconductor

Imaging System of Imager 5003 of Zoller+Fröhlich

Figure A.1 shows schematically the principle of the imaging system of the laser scanner adapted from [Fröhlich et al., 2000]. The spot laser system in the lower part consists of a laser head, receiver optics, and an avalanche photodiode (APD). The receiver optics cause that the reflected laser light is focussed towards the APD. The deflection unit in the upper part consists of a mirror and of a motor for high-speed rotations. The whole system additionally rotates about a vertical axis to capture the environment in 3D.

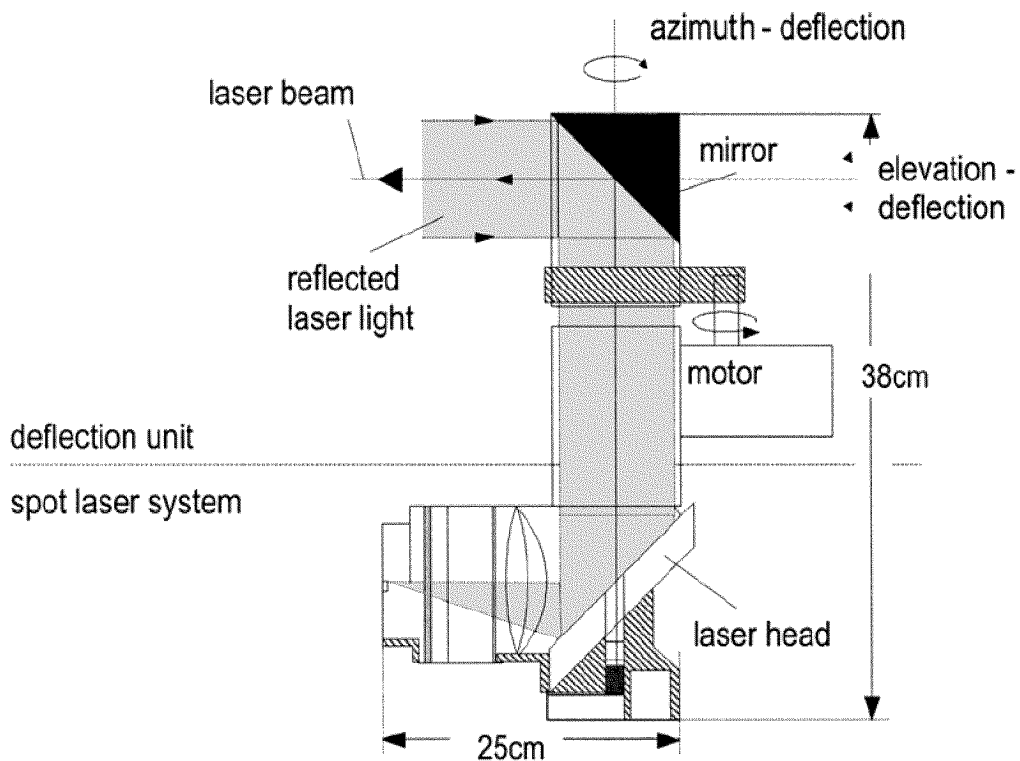


Figure A.1: Imaging System adapted from [Fröhlich et al., 2000].

B

Technical Data of Imager 5003 of Zoller+Fröhlich

Laser measurement system	LARA 35200	LARA 33500
Ambiguity interval:	25.2 m	53.5 m
Min. range:	1.0 m	1.0 m
Resolution Range:	16 Bit 1.0 mm/lsb	16 Bit 1.0 mm/lsb
Data acquisition rate:	625,000 px/sec.	500,000 px/sec.
Typical data acquisition rate:	125,000 px/sec.	125,000 px/sec.
Linearity error: ¹⁾	≤ 3 mm	≤ 5 mm
Range noise at 10 m: ¹⁾²⁾		
> Reflectivity 20% (dark grey):	1.6 mm rms	3.0 mm rms
> Reflectivity 100% (white):	0.9 mm rms	1.3 mm rms
Range noise at 25 m: ¹⁾²⁾		
> Reflectivity 20% (dark grey):	4.5 mm rms	9.0 mm rms
> Reflectivity 100% (white):	1.6 mm rms	3.0 mm rms
Range drift over temp. (0–40°C):	negligible due to internal reference	
Optical transceiver		
Laser output power (CW):	23 mW (red)	
Beam divergence:	0.22 mrad	
Beam diameter at 1 m distance:	3 mm circular	
Laser safety class:	3R (DIN EN 60825-1)	
Deflection unit		
Field of view vertical:	310°	
Field of view horizontal:	360°	
Resolution vertical:	0.018°	
Resolution horizontal:	0.01°	
Accuracy vertical: ¹⁾	0.02° rms	
Accuracy horizontal: ¹⁾	0.02° rms	
Max. scanning speed vertical:	2,000 rpm	
Typ. scanning speed vertical: ²⁾	1,500 rpm	
Max. no. of pixels vertical:	20,000 360°	
Max. no. of pixels horizontal:	20,000 360°	
Scanning time: (image field of view total at middle resolution): ²⁾	100 sec.	
Miscellaneous		
Data interface:		
> Max. output data rate:	5 MB/sec.	
> Host interface:	IEEE1394 ("Firewire"/"i-Link")	
Power supply:		
> Input voltage:	24V DC (scanner) 90–260V AC (power unit)	
> Power consumption (total):	50–70 W	
Ambient conditions:		
> Calibrated temperature range:	0–40°C	
> Humidity:	non-condensing	
> Target reflectivity:	no retro-reflectors	
> Illumination:	all conditions from darkness to daylight	
Dimensions and weights		
Scanner (w x d x h):	30 x 18 x 50 cm	16 kg
Tripod:		
> Height:	approx. 80–140 cm	9 kg
> Diameter:	approx. 120 cm	

Adjustment of Sphere

A sphere can be described mathematically by [Bronstein and Semendjajew, 1999]

$$x^2 + y^2 + z^2 - r^2 = 0, \quad (\text{C.1})$$

where x, y, z are the 3D coordinates and r is the radius. Equation (C.1) requires that the center of the sphere equals the origin of the coordinate system. Implementing an arbitrary oriented sphere, with an undefined center point, the following equation is obtained

$$(x - x_M)^2 + (y - y_M)^2 + (z - z_M)^2 - r^2 = 0. \quad (\text{C.2})$$

The unknowns of the sphere in Equation (C.2) are the three coordinates of the center point x_M, y_M, z_M and, depending on whether the sphere is calibrated or not, the radius. The resulting equation system is unambiguous if at least three points are given by their coordinates x, y, z . If more than three 3D points are given, an adjustment problem can be formulated, which is either based on

- an observation model: radius is known (Gauss-Markov Model), or
- a mixed model: radius is unknown (Gauss-Helmert Model).

A detailed mathematical description of the adjustment models is given in [Leick, 2004]. Since in surveying the number of observations and thus, the redundancy is often far below 1000, adjustment problems can be easily solved without computational problems. Considering laser scanning, the number of observations, i.e. the number of points of a point cloud, increases significantly. The number of points can reach several thousands up to hundreds of thousands. Such huge observations lead to both computational and storage problems since the matrices for solving the adjustment become too large. This necessitates the adjustment equations to be formed in such a way that they can be solved by a computer without any difficulties.

The unknowns of the adjustment problems introduced are based on the following relations [Leick, 2004]

$$f(x, l) : \quad x = (A^T P A)^{-1} A^T P l \quad (\text{observation model}) \quad (\text{C.3})$$

$$f(x, l) : \quad x = [A^T (B^T P^{-1} B)^{-1} A]^{-1} A^T (B^T P^{-1} B) w \quad (\text{mixed model}) \quad (\text{C.4})$$

where x is the vector of unknowns, l is the vector of observations, P denotes the weight matrix and w is the discrepancies vector. The matrices A and B are based on linearization of the nonlinear mathematical models, cf. Equation (C.2), around the known point of expansion (x_0) [Leick, 2004]:

$$A = \left. \frac{\partial f}{\partial x} \right|_{x_0, l} \quad (\text{C.5})$$

$$B = \left. \frac{\partial f}{\partial l} \right|_{x_0, l} \quad (\text{C.6})$$

The dimensions of the matrices and vectors are given by the number of observations n and by the number of unknowns u . The redundancy r is obtained generally by

$$r = n - u. \quad (\text{C.7})$$

Thus, the following dimensions are obtained for the required matrices:

- $P = \dim(n, n)$
- $A = \dim(n, u)$
- $B = \dim(r, n)$
- $w = \dim(r, 1)$

The implemented equations for the adjustment are well-known and can be found in various scientific publications and books, e.g. [Großmann, 1961], [Höpcke, 1980], [Leick, 2004], [Welsch et al., 2000].

The weight matrix P is a diagonal matrix since the coordinates acquired by the laser scanner are independent of each other. This assumption is only conditionally valid since the Cartesian coordinates x, y, z are derived by the spherical coordinates h, v, s , which are independent of each other. However, the Cartesian coordinates are correlated and the covariances have to be considered in a strict sense. Nevertheless, for simplification reasons, the assumption of uncorrelated coordinates is adhered to. The weight of observations is controlled by the weight matrix P . In the case of blunders, the weight can be reduced to eliminate the influence of the blunder on the unknowns. A blunder is detected by data snooping. The normalized residual, which equals the distance of one point to the sphere surface, is a reliable criterion for eliminating blunders.

The a posteriori variance of the unit weight σ_0^2 estimates the variance of one single observation. Here, it is the variance of one single coordinate represented by x or y or z . Based on σ_0^2 , one obtains the variance of a 3D point σ_p^2 by

$$\sigma_p^2 = 3\sigma_0^2. \quad (\text{C.8})$$

The required matrices for calculating the unknowns can result in large dimensions due to the number of observations n . To avoid huge matrices, the given matrices have to be summarized for obtaining new matrices, which only depend on the parameters unknowns u and redundancy r . Another crucial aspect is the inversion of matrices necessary to estimate the unknowns in the vector x . The inversion of matrices requires non-singular matrices. The implemented algorithm for a stable inversion of a matrix is based on [Press et al., 2002], which includes a decomposition of the matrix in a lower and an upper triangular matrix called LU decomposition.

Due to the implemented algorithm, the adjustment of spheres can be performed nearly independently of the number of input points. The algorithm is fast und reliable. Also, files consisting of more than 100,000 points can be processed in seconds. Figure C.1 shows the Microsoft Windows® application that calculates a sphere based on a given data set of 3D points. A limit for the recognition of blunders in terms of a maximum

distance between points and the sphere surface can be chosen. As mentioned before, this parameter equals a normalized residual. Considering a single point precision of 3.3 mm, a maximum distance of 10 mm from one point to the sphere surface means a normalized residual of 3. Furthermore, the operator can define if the diameter of the sphere has to be estimated during the adjustment procedure or if the diameter is well-known. Depending on the diameter, either the observation model or the mixed model is run for estimating the unknowns. After a successful calculation, the application shows the results of the unknowns including precision terms as well as other parameters.

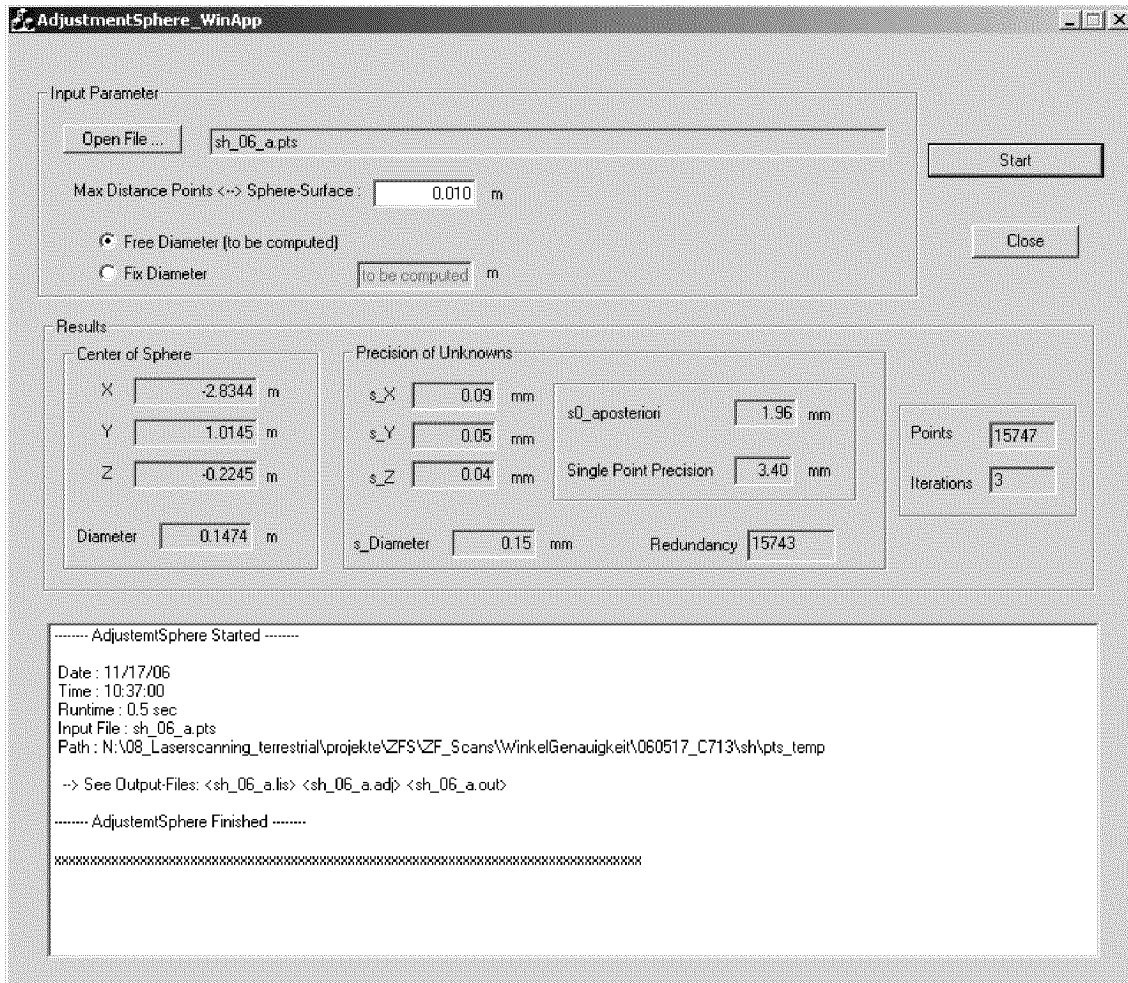


Figure C.1: Microsoft Windows[®] application for adjustment of spheres.

D

Electronic Circuit for Determining Rotation Time

The implemented oscillator in the electronic circuit defines the time base. The rotating laser beam hits the two diodes and the time that this takes is stored by using the time base of the oscillator. The measured time can then be read out by the parallel port using the data bits and three different registers. The complete electronic circuit can be seen in Figure D.1.

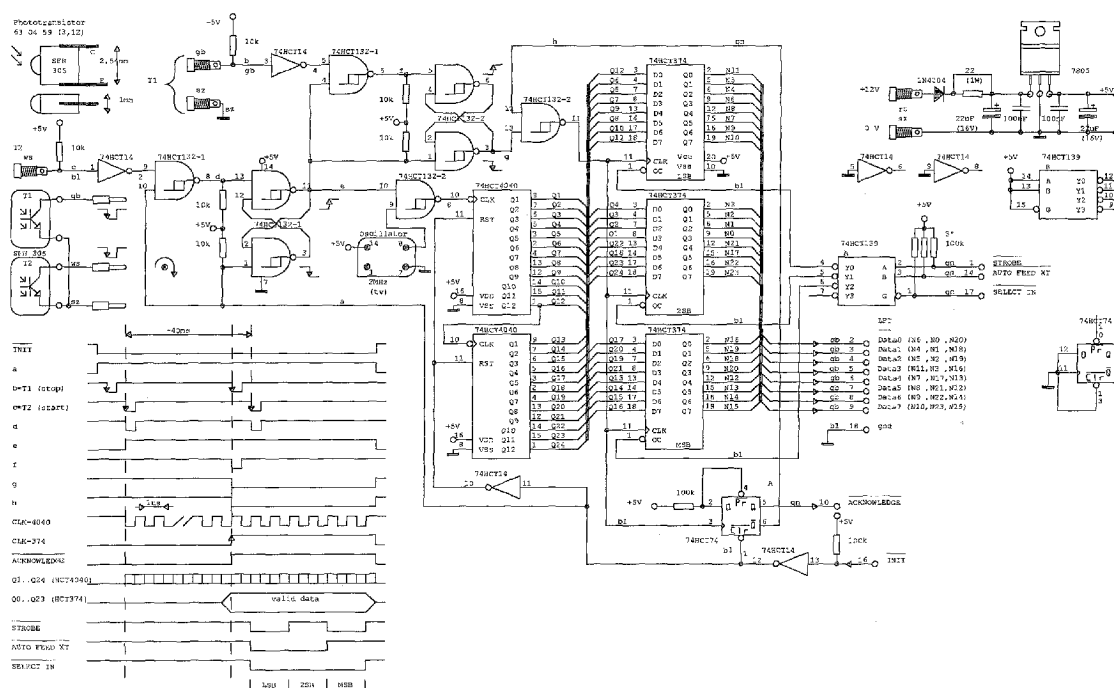


Figure D.1: Circuit diagram of the developed electronic circuit. How the registers of the parallel port are used for controlling the time measurement process of the rotation time of the rotating laser beam can be seen.

Depending on the chosen oscillator frequency, the data bits of the data register have a different time resolution. Table D.1 shows the relation between the three registers and the data bits in terms of time values in $[\mu\text{s}]$ for all four oscillator frequencies used. The oscillators used are hybrid oscillators, AQO 14 of Auris GmbH, Germany. The stability of the oscillator frequency is defined by 25 ppm, which means a time precision of $25 \mu\text{s}$ for a 2 MHz oscillator and $3 \mu\text{s}$ for a 16 MHz oscillator.

Data bit	Register 1 [μs]				Register 2 [μs]				Register 3 [μs]			
	2 MHz	4 MHz	8 MHz	16 MHz	2 MHz	4 MHz	8 MHz	16 MHz	2 MHz	4 MHz	8 MHz	16 MHz
0	64	32	16	8	1	0.5	0.25	0.125	1048576	524288	262144	131072
1	16	8	4	2	2	1	0.5	0.25	262144	131072	65536	32768
2	32	16	8	4	4	2	1	0.5	524288	262144	131072	65536
3	2048	1024	512	256	8	4	2	1	65536	32768	16384	8192
4	128	64	32	16	131072	65536	32768	16384	8192	4096	2048	1024
5	256	128	64	32	2097152	1048576	524288	262144	4096	2048	1024	512
6	512	256	128	64	4194304	2097152	1048576	524288	16384	8192	4096	2048
7	1024	512	256	128	8388608	4194304	2097152	1048576	32768	16384	8192	4096

Table D.1: Time values in [μs] of the data bits for the three registers and the different oscillator frequencies.

Bibliography

- Amann, M.-C., Bosch, T., Lescure, M., Myllyla, R. and Rioux, M. [2001], *Laser Ranging: a Critical Review of Usual Techniques for Distance Measurement*, in 'Optical Engineering', Vol. 40, No. 1, SPIE, pp. 10–19.
- American Heritage Dictionary [2004], *The American Heritage® Dictionary of the English Language*, fourth edn, Houghton Mifflin Company.
- Andrews, L. C. and Phillips, R. L. [1998], *Laser Beam Propagation through Random Media*, SPIE Optical Engineering Press, Bellingham, Washington.
- ASTM E456-02 [2002], 'Standard Terminology for Relating to Quality and Statistics', ASTM International.
- Aussems, T. [1999], *Positionsschätzung von Landfahrzeugen mittels Kalman-Filterung aus Satelliten- und Koppelnavigationsbeobachtungen*, PhD thesis, RWTH Aachen, Geodätisches Institut.
- Axelsson, J. [1997], *Parallel Port Complete*, Lakeview Research, Madison, WI.
- Baarda, W. [1968], *A Testing Procedure for Use in Geodetic Networks*, Netherlands Geodetic Commission, Publications on Geodesy, Vol. 2, No. 5, Delft.
- Beland, R. R. [1993], *Propagation Through Atmospheric Optical Turbulence*, in F. G. Smith, ed., 'The Infrared and Electro-Optical Systems Handbook', Vol. 2, Atmospheric Propagation of Radiation, SPIE, Bellingham, Washington, pp. 157–232.
- deBerg, M., van Kreveld, M., Overmars, M. and Schwarzkopf, O. [2002], *Computational Geometry - Algorithms and Applications*, second edn, Springer, New York, Berlin.
- Bergevin, R., Soucy, M., Gagnon, H. and Laurendeau, D. [1996], *Towards a General Multi-View Registration Technique*, in 'IEEE Transactions on Pattern Analysis and Machine Intelligence', Vol. 18, No. 5, pp. 540–547.
- Besl, P. J. and McKay, N. D. [1992], *A Method for Registration of 3D Shapes*, in 'IEEE Transactions on Pattern Analysis and Machine Intelligence', Vol. 14, No. 2, pp. 239–256.
- Blinn, J. F. [1977], *Models of Light Reflection for Computer Synthesized Pictures*, in 'SIGGRAPH '77: 4th Annual Conference on Computer Graphics and Interactive Techniques, San Jose (California)', ACM Press, New York, NY, pp. 192–198. Proc.
- Blug, A., Baulig, C., Wölfelschneider, H. and Höfler, H. [2005], *Novel Geometry for a High Speed Outdoor Laser Scanning System*, in A. Grün and H. Kahmen, eds, 'Optical 3-D Measurement Techniques VII', Vol. I, Vienna (Austria), pp. 154–163. Proc.
- Böhler, W., Bordas Vicent, M. and Marbs, A. [2003], *Investigating Laser Scanner Accuracy*, in 'The International Archives of the Photogrammetry, Remote Sensing and Spatial Information Sciences', Vol. XXXIV (Part 5 / C 15), pp. 696–701.
- Bosch, T. and Lescure, M., eds [1995], *Selected Papers on Laser Distance Measurement*, SPIE Milestone Series, Vol. MS 115, SPIE Optical Engineering Press, Bellingham, WA.
- Bronstein, I. N. and Semendjajew, K. A. [1999], *Taschenbuch der Mathematik*, 4th edn, Verlag Harri Deutsch, Frankfurt a. M.
- Carr, J. C., Beatson, R. K., Cherrie, J. B., Mitchell, T. J., Fright, W. R., McCallum, B. C. and Evans, T. R. [2001], *Reconstruction and Representation of 3D Objects with Radial Basis Functions*, in 'SIGGRAPH '01: Proceedings of the 28th Annual Conference on Computer Graphics and Interactive Techniques', ACM Press, New York, NY, USA, pp. 67–76.
- Chen, Y. and Medioni, G. [1991], *Object Modeling by Registration of Multiple Range Images*, in 'Image and Vision Computing', Vol. 10, No. 3, pp. 145–155.
- Chui, C. K. and Chen, G. [1999], *Kalman Filtering with Real-Time Applications*, third edn, Springer, New York.

- Clark, J. and Robson, S. [2004], *Accuracy of Measurements With a Cyrax 2500 Laser Scanner Against Surfaces of Known Colour*, in 'Survey Review', Vol. 37, No. 294, pp. 626–638.
- Cooper, M. A. R. [1982], *Modern Theodolites and Levels*, second edn, Granada Publishing, London.
- Dam, E. B., Koch, M. and Lillholm, M. [1998], *Quaternions, Interpretation and Animation*, Department of Computer Science, University of Copenhagen, Technical Report DIKU-TS-98/5.
- Deakin, R. E. and Kildea, D. G. [1999], *A Note on Standard Deviation and RMS*, in 'The Australian Surveyor', Vol. 44, No. 1, pp. 74–79.
- Deumlich, F. and Staiger, R. [2002], *Instrumentenkunde der Vermessungstechnik*, 9th edn, Herbert Wichmann, Heidelberg.
- Dijkman, S. T. and van den Heuvel, F. A. [2002], *Semi Automatic Registration of Laser Scanner Data*, in 'ISPRS-Congress, Commission V, Close-Range Imaging, Long-Range Vision', Corfu (Greece), pp. 12–17. Proc.
- Dünisch, M. and Kuhlmann, H. [2001], *Investigation on Accuracy of Tracking Motorized Tacheometers*, in A. Grün and H. Kahmen, eds, 'Optical 3-D Measurement Techniques V', Vienna (Austria), pp. 218–225. Proc.
- Feng, Q. H. and Röshoff, K. [2004], *In-situ Mapping and Documentation of Rock Faces Using Full Coverage 3D Laser Scanning Technique*, in 'SINOROCK 2004 Symposium', Yichang (China), pp. 139–144. Proc.
- Foppe, K., Schwieger, V. and Staiger, R. [2004], *Grundlagen kinematischer Mess- und Auswertverfahren*, in V. Schwieger and K. Foppe, eds, 'Kinematische Messmethoden "Vermessung in Bewegung"', Beiträge zum 58.DVW Seminar, 2005, Stuttgart', Vol. 45 (2004), Schriftenreihe des DWV, Wißner, Augsburg, pp. 3–18.
- Fraser, D. [1967], *A New Technique for the Optimal Smoothing of Data*, Report No. T-474, M.I.T. Instrumentation Lab, Cambridge, Massachusetts.
- Fröhlich, C. [1996], *Aktive Erzeugung korrespondierender Tiefen- und Reflektivitätsbilder und ihre Nutzung zur Umgebungserfassung*, PhD thesis, Technische Universität München.
- Fröhlich, C., Mettenleiter, M. and Härtl, F. [1998], *Imaging Laser Radar for High-Speed Monitoring of the Environment*, in 'Intelligent Transportation Systems', SPIE Vol. 3207, pp. 50–64. Proc.
- Fröhlich, C., Mettenleiter, M., Härtl, F., Dalton, G. and Hines, D. [2000], *Imaging Laser Radar for 3-D Modelling of Real World Environments*, in 'Journal of Sensor Review; Volume 20, Issue 4', pp. 273–282.
- Gaich, A., Schubert, W. and Pötsch, M. [2004], *Reproducible Rock Mass Description in 3D Using the Joint-netrix 3D System*, in 'EUROCK 2004 & 53rd Geomechanics Colloquium', Salzburg (Austria), pp. 61–64. Proc.
- Gelb, A. [1974], *Applied Optimal Estimation*, written by Analytical Sciences Corporation, The M.I.T. Press, Cambridge, Massachusetts and London, England.
- Gerstbach, G. [1976], *Zur Azimutmessung mit Sekundentheodoliten*, in 'Österreichische Zeitschrift für Vermessungswesen und Photogrammetrie', Vol. 1, Österreichischer Verein für Vermessungswesen und Photogrammetrie.
- Gerthsen, C. and Vogel, H. [1993], *Physik*, 17th edn, Springer, Berlin.
- Gläser, A. and Schollmeyer, R. [2004], *Messwert-erfassung und -synchronisation in Multisensorsystemen*, in V. Schwieger and K. Foppe, eds, 'Kinematische Messmethoden "Vermessung in Bewegung"', Beiträge zum 58.DVW Seminar', Vol. 45 (2004), Schriftenreihe des DWV, Wißner, Augsburg, pp. 35–58.
- Glaus, R. [2005], *Kinematic Track Surveying by Means of a Multi-Sensor Platform*, PhD thesis, Institute of Geodesy and Photogrammetry, Swiss Federal Institute of Technology Zurich.
- Großmann, W. [1961], *Grundzüge der Ausgleichungsrechnung*, second edn, Springer, Berlin, Göttingen, Heidelberg.
- Grün, A. and Akca, D. [2005], *Least Squares 3D Surface and Curve Matching*, in 'ISPRS Journal of Photogrammetry and Remote Sensing', Vol. 59, No. 3, pp. 151–174.

- Gühring, J. [2002], *3D-Erfassung und Objektrekonstruktion mittels Streifenprojektion*, PhD thesis, DGK Reihe C, Nr. 560.
- Gujer, W. [1999], *Siedlungswasserwirtschaft*, Springer, New York.
- Hancock, J., Langer, D., Hebert, M., Sullivan, R., Ingimarsen, D., Hoffman, E., Mettenleiter, M. and Fröhlich, C. [1998], *Active Laser Radar for High-Performance Measurements*, in 'IEEE International Conference on Robotics & Automation', Leuven (Belgium), pp. 1465–470. Proc.
- Hancock, J. A. [1999], *Laser Intensity-Based Obstacle Detection and Tracking*, PhD thesis, The Robotics Institute, Carnegie Mellon University, Pittsburgh, Pennsylvania.
- Hebert, M. and Krotkov, E. [1992], *3D Measurements From Imaging Laser Radars: How Good are They?*, in 'Image and Vision Computing', Vol. 10, No. 3, pp. 170–178.
- Heister, H. [2006], *Zur standardisierten Überprüfung von terrestrischen Laserscannern (TLS)*, in W. Niemeier and M. Schäfer, eds, "Terrestrisches Laser-Sanning (TLS 2006), Beiträge zum 72.DVW Seminar, 2006, Fulda", Vol. 51 (2006), Schriftenreihe des DVW, Wißner, Augsburg, pp. 35–44.
- Henderson, A. R. [1997], *A Guide to Laser Safety*, Springer.
- Hennes, M. [1999], *Grundlegende Aspekte zur Bestimmung der Leistungsfähigkeit von Robottachymetern*, in 'Allgemeine Vermessungsnachrichten (AVN)', Vol. 11-12/1999, pp. 374–385.
- Hennes, M. and Ingensand, H. [2000], *Komponentenkalibrierung versus Systemkalibrierung*, in 'XIII. Kurs für Ingenieurvermessung', München. Proc.
- Heunecke, O. [1995], *Zur Identifikation und Verifikation von Deformationsprozessen mittels adaptiver Kalman-Filterung (Hannoversches Filter)*, PhD thesis, Wissenschaftliche Arbeiten der Fachrichtung Vermessungswesen der Universität Hannover, Nr. 208.
- Hinderling, J. [2004], *Distanzmesser - Funktionsprinzipien und Demonstration von EDM*, in 'Skript Geodätische Sensorik', ETH Zürich, Institut für Geodäsie und Photogrammetrie, Prof. Dr. H. Ingensand.
- Hofmann-Wellenhof, B., Legat, K. and Wieser, M. [2003], *Navigation - Principles of Positioning and Guidance*, Springer, Wien, New York.
- Holst, G. C. [1998], *Sampling, Aliasing, and Data Fidelity for Electronic Imaging Systems, Communications, and Data Acquisition*, SPIE Optical Engineering Press, Bellingham, Washington.
- Höpcke, W. [1980], *Fehlerlehre und Ausgleichsrechnung*, Walter de Gruyter, Berlin, New York.
- Hoppe, H., DeRose, T., Duchamp, T., McDonald, J. and Stuetzle, W. [1992], *Surface Reconstruction from Unorganized Points*, in 'SIGGRAPH '92: Proceedings of the 19th annual conference on Computer graphics and interactive techniques', ACM Press, New York, NY, USA, pp. 71–78.
- Horn, B. K. P. [1987], *Closed-Form Solution of Absolute Orientation Using Unit Quaternions*, in 'Optical Society of America A: Optics, Image Science, and Vision', Vol. 4, pp. 629–642.
- Hoscheck, J. and Lasser, D. [1992], *Grundlagen der geometrischen Datenverarbeitung*, Teubner, Stuttgart.
- Hovenbitzer, M. [2003], *Zur Automation berührungsloser 3D-Objekterfassung im Nahbereich*, PhD thesis, DGK Reihe C, Nr. 556.
- IEC [2001], *International Standard: Safety of Laser Products - Part 1: Equipment Classification, Requirements and User's Guide*, International Electrotechnical Commission, Geneva, Switzerland.
- Ingensand, H. and Böckem, B. [1997], *Automatic Location and Pointing Techniques in Local Positioning Systems*, in A. Grün and H. Kahmen, eds, 'Optical 3-D Measurement Techniques IV', Zurich (Switzerland). Proc.
- Ingensand, H. [1998], *Elektronische Teilkreisabgriffsysteme und Teilkreisprüfung*, in 'Skript Messtechnik und Sensorik', ETH Zürich, Institut für Geodäsie und Photogrammetrie, Prof. Dr. H. Ingensand.
- Ingensand, H., Ryf, A. and Schulz, T. [2003], *Performances and Experiences in Terrestrial Laser Scanning*,

- in A. Grün and H. Kahmen, eds, 'Optical 3-D Measurement Techniques VI', Vol. I, Zurich (Switzerland), pp. 236–243. Proc.
- Ingensand, H. [2006], *Metrological Aspects in Terrestrial Laser-Scanning Technology*, in '3rd IAG & 12th FIG Symposium', Baden (Austria). Proc.
- ISO [1998], *ISO 5725-1*, International Organization for Standardization, Geneva, Switzerland.
- ISO [2002], *ISO 5725-2*, International Organization for Standardization, Geneva, Switzerland.
- Janser, A., Luther, W. and Otten, W. [1996], *Computergraphik und Bildverarbeitung*, Vieweg Verlag, Braunschweig, Wiesbaden.
- Jazwinski, J. A. [1970], *Stochastic Processes and Filtering Theory*, Academic Press, New York.
- Jekeli, C. [2001], *Inertial Navigation Systems with Geodetic Applications*, Walter de Gruyter, Berlin, New York.
- Joekel, J. and Stober, M. [1991], *Elektronische Entfernungs- und Richtungsmessung*, second edn, Konrad Wittwer, Stuttgart.
- Kahlmann, T. and Ingensand, H. [2005], *Calibration and Improvements of the High-Resolution Range-Imaging Camera Swiss RangerTM*, in 'Videometrics VIII, part of the IS&T/SPIE Symposium on Electronic Imaging', Vol. 5665, San Jose, CA (USA), pp. 139–144.
- Kahmen, H. [1997], *Vermessungskunde*, 19th edn, Walter de Gruyter, Berlin.
- Kalman, R. E. [1960], *A new Approach to Linear Filtering and Prediction Problems*, in 'Transactions of the ASME-Journal of Basic Engineering', Vol. 82, No. Series D, pp. 35–45.
- Kern, F. [2003], *Automatisierte Modellierung von Bauwerksgeometrien aus 3D-Laserscanner-Daten*, PhD thesis, Geodätische Schriftenreihe der Technische Universität Braunschweig, Nr.19.
- Kersten, T., Sternberg, H., Mechelke, K. and Acevedo Pardo, C. [2004], *Terrestrial Laserscanning System Mensi GS100 - Accuracy Tests, Experiences and Projects at the Hamburg University of Applied Sciences*, in 'The International Archives of the Photogrammetry, Remote Sensing and Spatial Information Sciences', Vol. XXXIV (Part 5 / W 16).
- Kersten, T., Sternberg, H. and Mechelke, K. [2005], *Investigations Into the Accuracy Behaviour of the Terrestrial Laser Scanning System Mensi GS100*, in A. Grün and H. Kahmen, eds, 'Optical 3-D Measurement Techniques VII', Vol. I, Vienna (Austria), pp. 122–131. Proc.
- Kneubühl, F. [1982], *Repetitorium der Physik*, second edn, Teubner, Stuttgart.
- Kopacik, A. and Wunderlich, T. [2004], *Usage of Laser Scanning Systems at Hydro-Technical Structures*, in 'INGEO 2004 and FIG Regional Central and Eastern Conference on Engineering Surveying', Bratislava (Slovakia). Proc.
- Kraus, K. [1994], *Photogrammetrie - Grundlagen und Standardverfahren*, fifth edn, Ferdinand-Dümmler, Bonn.
- Kraus, K. [2002], *Laser-Scanning - ein Paradigma-Wechsel in der Photogrammetrie*, in 'Vermessung Photogrammetrie Kulturtechnik', Vol. 10/2002, pp. 620–624.
- Kuhlmann, H. [2004], *Mathematische Modellbildung zu kinematischen Prozessen*, in V. Schwieger and K. Foppe, eds, 'Kinematische Messmethoden "Vermessung in Bewegung"', Beiträge zum 58.DVW Seminar, 2005, Stuttgart', Vol. 45 (2004), Schriftenreihe des DWV, Wißner, Augsburg, pp. 19–33.
- Kuipers, J. B. [2002], *Quaternions and Rotation Sequences - A Primer with Applications to Orbits, Aerospace, and Virtual Reality*, Princeton and Oxford, Princeton University Press.
- Langer, D., Mettenleiter, M., Härtl, F. and Fröhlich, C. [2000], *Imaging Ladar for 3-D Surveying and CAD Modeling of Real-World Environments*, in 'The International Journal of Robotics Research', Vol. 19, No. 11, pp. 1075–1088.
- Leica Geosystems [1988], *Handbuch Nivel 20*. Leica Geosystems AG, Heerbrugg.
- Leica Geosystems [2004], *GeoCOM Reference Manual. TPS1200 - Version 1.00*. Leica Geosystems AG, Heerbrugg.

- Leick, A. [2004], *GPS Satellite Surveying*, third edn, Wiley, New Jersey.
- Lemy, F. and Hadjigeorgiou, J. [2004], *A Field Application of Laser Scanning Technology to Quantify Rock Fracture Orientation*, in 'EUROCK 2004 & 53rd Geomechanics Colloquium', Salzburg (Austria), pp. 435–438. Proc.
- Li, W. X. and Mitchell, L. D. [1995], *Laser Scanning System Testing - Errors and Improvements*, in 'Measurement', Vol. 16, No. 2, pp. 91–101.
- Lichti, D. D., Gordon, S. J. and Stewart, M. P. [2002a], *Ground-Based Laser Scanners: Operation, Systems and Applications*, in 'Geomatica', Vol. 56, No. 1, pp. 21–33.
- Lichti, D. D. and Harvey, B. [2002b], *An Investigation Into The Effects of Reflecting Surface Material Properties on Terrestrial Laser Scanner Measurements*, in 'Geomatics Research Australasia', Vol. 76, pp. 1–21.
- Lichti, D. D., Gordon, S. J. and Tipdecho, T. [2005a], *Error Models and Propagation in Directly Georeferenced Terrestrial Laser Scanner Networks*, in 'Journal of Surveying Engineering', Vol. 131, No. 4, pp. 135–142.
- Lichti, D. D. and Franke, J. [2005b], *Self-Calibration of the IQSun 880 Laser Scanner*, in A. Grün and H. Kahmen, eds, 'Optical 3-D Measurement Techniques VII', Vol. I, Vienna (Austria), pp. 112–121. Proc.
- Lichti, D. D. and Jamtsho, S. [2006], *Angular Resolution of Terrestrial Laser Scanners*, in 'The Photogrammetric Record - An International Journal of Photogrammetry', Vol. 21, No. 114, pp. 141–160.
- Löffler et al. [2002], *Maschinen- und Anlagenbau*, in Möser, Müller, Schlemmer and Werner, eds, 'Handbuch Ingenieurgeodäsie', second edn, Herbert Wichmann, Heidelberg.
- Luhmann, T. [2003], *Nahbereichsphotogrammetrie*, 2nd edn, Herbert Wichmann, Heidelberg.
- Luhmann, T., Robson, S., Kyle, S. and Harley, I. [2006], *Close-Range Photogrammetry*, Whittles Publishing, Caithness, Scotland.
- Masuda, T. and Yokoya, N. [1996], *A Robust Method for Registration and Segmentation of Multiple Range Images*, in 'Computer Vision and Image Understanding', Vol. 61, No. 3, pp. 540–547.
- Matthias, H. [1961], *Umfassende Behandlung der Theodolitachsenfehler auf vektorieller Grundlage unter spezieller Berücksichtigung der Taumelfehler der Kippachse*, in F. Kobold, ed., 'Mitteilungen aus dem geodätischen Institut an der Eidgenössischen Technischen Hochschule in Zürich', Vol. 10, Verlag Leemann Zürich.
- Meschede, D. [2004], *Optics, Light and Lasers: The Practical Approach to Modern Aspects of Photonics and Laser Physics*, Wiley-VCH.
- Mettenleiter, M. [2004], *Understanding IMAGER 5003 Accuracy Specifications*. Zoller+Fröhlich GmbH, Wangen.
- Mikhail, E. M., Bethel, J. S. and McGlone, J. C. [2001], *Introduction to Modern Photogrammetry*, John Wiley & Sons, Inc., New York.
- Möser, M., Müller, G., Potthoff, H., Schulz, H.-U., Hoffmeister, H., Wanniger, L. and Ingensand, H. [2000], *Grundlagen*, in Möser, Müller, Schlemmer and Werner, eds, 'Handbuch Ingenieurgeodäsie', 3rd edn, Herbert Wichmann, Heidelberg.
- Niemeier, W., Thomsen, S. and Schäfer, M. [2002], *3-D Geometrieerfassung mit terrestrischen Laserscannern*, in T. Luhmann, ed., 'Photogrammetrie und Laserscanning - Anwendungen für As-Built-Dokumentation und Facility Management', Herbert Wichmann, Heidelberg, pp. 15–26.
- NIST [2002], *'LADAR Calibration Facility Workshop'*, NIST Technology Administration, U.S. Department of Commerce. Proc.
- Phong, B. T. [1975], *Illumination for Computer Generated Pictures*, in 'Communications of the ACM', Vol. 18, No. 6, pp. 311–317.
- Piegl, L. [1991], *On NURBS: A Survey*, in 'IEEE Computer Graphics and Applications', Vol. 11, No. 1, pp. 55–71.
- Pope, A. J. [1975], *The Statistics of Residuals and the Detection of Outliers*, in 'XVII. General Assembly of the IUGG', Grenoble (France). Proc.

- Press, W. H., Teukolsky, S. A., Vetterling, W. T. and Flannery, B. P. [2002], *Numerical Recipes in C++*. *The Art of Scientific Computing*, second edn, Cambridge University Press.
- Przybilla, H.-J. [2005], *Fusion von terrestrischem Laser-scanning und digitaler Photogrammetrie*, in W. Barth, K. Foppe and T. Schäfer, eds, 'Terrestrisches Laser-scanning (TLS): Ein geodätisches Messverfahren mit Zukunft, Beiträge zum 65.DVW Seminar, 2005, Fulda', Vol. 48 (2005), Schriftenreihe des DWV, Wißner, Augsburg, pp. 95–105.
- Reshetyuk, Y., Horemuž, M. and Sjöberg, L. E. [2005], *Determination of the Optimal Diameter for Spherical Targets Used in 3D Laser Scanning*, in 'Survey Review', Vol. 38, No. 297, pp. 243–253.
- Reshetyuk, Y. [2006a], *Investigation of the Influence of Surface Reflectance on the Measurements with the Terrestrial Laser Scanner Leica HDS3000*, in 'Zeitschrift für Vermessungswesen (ZfV)', Vol. 131, No. 2, pp. 96–103.
- Reshetyuk, Y. [2006b], *Calibration of Terrestrial Laser Scanners for the Purposes of Geodetic Engineering*, in '3rd IAG & 12th FIG Symposium', Baden (Austria). Proc.
- Rhinoceros[®] [2006], *NURBS Modeling for Windows*. <http://www.rhino3d.com> (accessed 27th September 2006).
- Richter, R. [1985], *Some Aspects of the Atmospheric Radiance Model of LOWTRAN 6*, in 'International Journal of Remote Sensing', Vol. 6, pp. 1773–1777.
- Riesenfeld, R. F. [1973], *Applications of B-Spline Approximation to Geometric Problems of Computer-Aided Design*, PhD thesis, Syracuse University, N.Y.
- Rietdorf, A., Gielsdorf, F. and Gründig, L. [2004], *A Concept for the Calibration of Terrestrial Laser Scanners*, in 'INGEO 2004 and FIG Regional Central and Eastern Conference on Engineering Surveying', Bratislava (Slovakia). Proc.
- Rietdorf, A. [2005], *Automatisierte Auswertung und Kalibrierung von scannenden Messsystemen mit tachymetrischem Messprinzip*, PhD thesis, DGK Reihe C, Nr. 582.
- Rüeger, J. M. [1996], *Electronic Distance Measurement*, fourth edn, Springer, Berlin.
- Runne, H., Niemeier, W. and Kern, F. [2001], *Application of Laser Scanners to Determine the Geometry of Buildings*, in A. Grün and H. Kahmen, eds, 'Optical 3-D Measurement Techniques V', Vienna (Austria), pp. 41–48. Proc.
- Sachs, L. [1984], *Angewandte Statistik*, Springer, Berlin, Heidelberg, New York.
- Saleh, B. E. A. and Teich, M. C. [1991], *Fundamentals of Photonics*, John Wiley & Sons, New York, NY.
- Schlemmer, H. [1996], *Grundlagen der Sensorik*, Herbert Wichmann, Heidelberg.
- Schlemmer, H. [2004], *Einführung in die Technologie des Laserscannings*, in 'XIV. Kurs für Ingenieurvermessung, Tutorial Laserscanning', ETH Zürich, Institut für Geodäsie und Photogrammetrie, Prof. Dr. H. Ingensand.
- Schulz, T. and Ingensand, H. [2004a], *Laserscanning – Genauigkeitsbetrachtungen und Anwendungen*, in T. Luhmann, ed., 'Photogrammetrie Laserscanning Optische 3D-Messtechnik', Herbert Wichmann, pp. 90–97. Beiträge der Oldenburger 3D-Tage 2004.
- Schulz, T. and Ingensand, H. [2004b], *Terrestrial Laser Scanning – Investigations and Applications for High Precision Scanning*, in 'FIG Working Week – The Olympic Spirit in Surveying', Athens (Greece). Proc.
- Schulz, T. and Ingensand, H. [2004c], *Influencing Variables, Precision and Accuracy of Terrestrial Laser Scanners*, in 'INGEO 2004 and FIG Regional Central and Eastern Conference on Engineering Surveying', Bratislava (Slovakia). Proc.
- Schulz, T., Ingensand, H. and Steiner, M. [2005], *Laser Scanning and Noise Reduction Applied to 3D Road Surface Analysis*, in A. Grün and H. Kahmen, eds, 'Optical 3-D Measurement Techniques VII', Vol. I, Vienna (Austria), pp. 135–143. Proc.
- Schulz, T., Lemy, F. and Yong, S. [2005], *Laser Scanning Technology for Rock Engineering Applications*, in A. Grün and H. Kahmen, eds, 'Optical 3-D Measurement Techniques VII', Vol. I, Vienna (Austria), pp. 50–59. Proc.

- Schulz, T. and Zogg, H. M. [2006], *Terrestrisches Laserscanning in der Geomatik*, in 'Geomatik Schweiz', Vol. 8/2006, pp. 420–424.
- Stahlberg, C. [1997], *Eine vektorielle Darstellung des Einflusses von Ziel- und Kippachsenfehler auf die Winkelmessung*, in 'Zeitschrift für Vermessungswesen (ZfV)', Vol. 122, No. 5, pp. 225–235.
- Staiger, R. [2003], *Terrestrial Laser Scanning – Technology, Systems and Applications*, in '2nd FIG Regional Conference, Marrakech (Morocco)'. Proc.
- Staiger, R. [2005], *Terrestrisches Laserscanning – Eine neue Universalmessmethode?*, in W. Barth, K. Foppe and T. Schäfer, eds, 'Terrestrisches Laserscanning (TLS): Ein geodätisches Messverfahren mit Zukunft, Beiträge zum 65.DVW Seminar, 2005, Fulda', Vol. 48 (2005), Schriftenreihe des DVW, Wißner, Augsburg, pp. 3–15.
- Steiner, M., Langbein, S. and Boller, M. [2005], *Schadstoffe einer stark befahrenen Strasse und deren Retention mit neuartigen Filterpaketen*. EAWAG Dübendorf (Schweiz).
- Stempfhuber, W. V. [2004], *Ein integritätswahrendes Messsystem für kinematische Anwendungen*, PhD thesis, Institut für Geodäsie und Landmanagement, Technische Universität München.
- Stempfhuber, W. and Wunderlich, T. [2004], *LEICA System 1200: Auf dem Weg zur Sensorsynchronisation von GPS und TPS für kinematische Messaufgaben*, in 'Allgemeine Vermessungsnachrichten (AVN)', Vol. 5/2004, pp. 175–184.
- Sternberg, H. [2000], *Zur Bestimmung der Trajektorie von Landfahrzeugen mit einem hybriden Messsystem*, PhD thesis, Schriftenreihe der Universität der Bundeswehr München, Studiengang Geodäsie und Geoinformation, Heft 67, Neubiberg.
- Tatarskii, V. I. [1971], *The Effects of the Turbulent Atmosphere on Wave Propagation*, Keter Press, Jerusalem.
- Taubenheim, J. [1969], *Statistische Auswertung geophysikalischer und meteorologischer Daten*, in Buchheim, Fanselau, Hiller and Menzel, eds, 'Geophysikalische Monographien, Band 5', Akademische Verlagsgesellschaft Geest & Portig K.-G., Leipzig.
- Teunissen, P. J. G. and Salzmann, M. A. [1988], *Performance Analysis of Kalman Filters*, in 'Report 88.2, Faculty of Geodesy, Delft University of Technology'.
- Teutsch, C., Berndt, D., Trostmann, E. and Weber, M. [2005], *Efficient Reconstruction of NURBS Surfaces for Shape Analysis and Surface Inspection*, in A. Grün and H. Kahmen, eds, 'Optical 3-D Measurement Techniques VII', Vol. I, Vienna (Austria), pp. 144–153. Proc.
- Tönnies, K. D. and Lemke, H. U. [1994], *3D-Computergrafische Darstellungen*, R. Oldenburg Verlag, München.
- Torrance, K. and Sparrow, E. [1967], *Theory for Off-Specular Reflection From Roughened Surfaces*, in 'Journal of the Optical Society of America', Vol. 57, pp. 1105–1114.
- Tukey, J. W. [1977], *Exploratory Data Analysis*, Addison-Wesley, Reading, MA.
- Versprille, K. J. [1975], *Computer-Aided Design Applications of the Rational B-Spline Approximation Form*, PhD thesis, Syracuse University, N.Y.
- VIM [1993], *International Vocabulary of Basic and General Terms in Metrology (VIM)*, second edn, International Organization for Standardization (ISO).
- Weichel, H. [1990], *Laser Beam Propagation in the Atmosphere*, SPIE Optical Engineering Press, Bellingham, Washington.
- Weisstein, E. W. [2003], *CRC Concise Encyclopedia of Mathematics*, 2nd edn, Chapman & Hall/CRC.
- Welch, G. and Bishop, G. [2004], *An Introduction to the Kalman Filter*, Department of Computer Science, University of North Carolina at Chapel Hill.
- Welsch, W., Heunecke, O. and Kuhlmann, H. [2000], *Auswertung geodätischer Überwachungsmessungen*, in Möser, Müller, Schlemmer and Werner, eds, 'Handbuch Ingenieurgeodäsie', Herbert Wichmann, Heidelberg.
- Wikipedia [2006], *The Free Encyclopedia*. <http://en.wikipedia.org> (accessed 29th September 2006).

- Wunderlich, T. A. [2001], *Operational and Economic Prospects of Terrestrial Laser Scanning*, in A. Grün and H. Kahmen, eds, 'Optical 3-D Measurement Techniques V', Vienna (Austria), pp. 18–25. Proc.
- Young, M. [1984], *Optics and Lasers*, second edn, Springer, Berlin, Heidelberg, New York, Tokyo.
- Zetsche, H. [1979], *Elektronische Entfernungsmessung (EDM)*, Konrad Wittwer, Stuttgart.
- Zhang, Z. [1994], *Iterative Point Matching for Registration of Freeform Curves and Surfaces*, in 'International Journal of Computer Vision', Vol. 13, No. 2, pp. 119–152.

List of Figures

1.1	Overview of terrestrial laser scanners	2
1.2	Distance measurement technologies in LiDAR systems	3
2.1	Optical distance measurement methods in terrestrial laser scanners	8
2.2	Transmission of electromagnetic waves	9
2.3	Casing and structure of a laser diode	10
2.4	Beam waist	11
2.5	Eye transmission	12
2.6	Direct Time-of-Flight Principle	13
2.7	Amplitude-modulated continuous wave (AMCW)	14
2.8	Zoller+Fröhlich: amplitude-modulated continuous wave (AMCW)	15
2.9	Frequency-Modulated Continuous Wave (FMCW)	15
2.10	Layout of silicon photodiodes	16
2.11	Types of reflection	17
2.12	Phong model	18
2.13	Torrance and Sparrow model	19
2.14	Encoder overview	19
2.15	Binary encoding	20
2.16	Different types of terrestrial laser scanners classified by field of view	21
2.17	Oscillating mirrors	21
3.1	Calibration of terrestrial laser scanners	23
3.2	Calibration track line including the test trolley moving on the track line	26
3.3	Trajectory of the calibration track line	27
3.4	Configuration of the control points	28
3.5	Situation of the observation pillars	28
3.6	Electronic unit for frequency measurement	29
3.7	Sphere used as target for laser scanning	30
3.8	Targets with varying reflectivity values	32
3.9	Kern theodolite DKM1 used as target holder	33
3.10	Calibration setup for the distance measurement system in the 'static mode'	34
3.11	Repeatability of the distance measurement system based on the 'static mode'	34
3.12	Accuracy of the distance measurement system based on the 'static mode'	35
3.13	Precision of the distance measurement system based on the 'static mode'	36
3.14	Calibration setup for the distance measurement system in the 'scanning mode'	36
3.15	Residuals between estimated diameter and nominal diameter	37
3.16	Residuals between derived horizontal distances and the nominal distances	37
3.17	Development of the number of points defining a sphere	38
3.18	Points on a sphere	39
3.19	Development of the distance measurement system over a time period	40
3.20	Development of the frequency and the internal temperature	41
3.21	Experimental setup for determining the accuracy of the angle measurement system	43

3.22	Residuals of the horizontal encoder	45
3.23	Residuals of the vertical encoder	47
3.24	Angular Resolution	48
3.25	Principle of the laser scanner and the axes of rotation	49
3.26	Adjusting Circle	51
3.27	Aliasing effects based on sampling	53
3.28	Laser scanner mounted on a granite table directly without using a tribrach	55
3.29	Inclination values of three data series	56
3.30	Amplitude spectrum derived by Fourier analysis	57
3.31	Inclination values of a data series including the sine curve of the levelling error	58
3.32	Collimation error applied to the laser scanner	59
3.33	Eccentricity of the collimation axis	60
3.34	Influence of the errors of the collimation axis in horizontal direction	61
3.35	Eccentricity of the collimation axis in horizontal direction	62
3.36	Influence of the errors of the collimation axis in vertical direction	63
3.37	Intensity of reflected laser beam	65
3.38	Influence of the angle of incidence on the size of the footprint of the laser beam	66
3.39	Influence of the angle of incidence to the distance precision	66
3.40	Influence of the angle of incidence to the distance accuracy	67
3.41	Influence of the angle of incidence	68
3.42	Surface backscattering and refractive effects	68
3.43	Distance accuracy of materials	69
3.44	Distance accuracy of metal	69
3.45	3D single point precision	71
3.46	3D object point accuracy	71
4.1	Geometrical interpretation of mixed pixels	75
4.2	Mixed pixels occurred near objects	75
4.3	Effect of multipath	76
4.4	Noise in laser scanning data oriented along the measuring direction	77
4.5	Types of artificial targets used for laser scanning	81
4.6	Examples for NURBS modeling	84
4.7	CAD	85
5.1	Laser scanner mounted on the test trolley of the calibration track line	89
5.2	Azimuthal orientation of the laser scanner	90
5.3	Installation of a prism on top of the laser scanner	91
5.4	Experimental setup for deriving the rotation time T directly	93
5.5	Mathematical relations for deriving center angle α (method 1)	94
5.6	Influence of a deflection angle δ of the autocollimation mirror.	96
5.7	Arrangement of the two photo diodes	97
5.8	Measured time delay Δt for 12.5 rps, 25 rps and 33 rps	98
5.9	Work flow for total station data	103
5.10	Sampling interval of total station	104
5.11	Polynomial interpolation	105
5.12	The Kalman Filter cycle	107
6.1	Road section to be investigated	110
6.2	Cross section of one lane of the road	111
6.3	Point cloud of road section	111

6.4	Inlet gutter, vegetated road shoulder and road	112
6.5	Calculated streams based on the topological model	113
6.6	Calculated catchment areas for the inlet gutter	113
6.7	Laser scanner inside excavated niche	115
6.8	Point cloud representing the final geometry of the tunnel	115
6.9	Location of the experimental tunnel, the reference points and the arrays of object points . . .	116
6.10	Geological discontinuity intersecting the tunnel face	118
6.11	Displacements in height for point 1 for arrays 100, 200, 300, 400	119
6.12	Displacements in height for point 6 for arrays 100, 200, 300, 400	119
6.13	Surface displacement maps	120
6.14	Residuals of total station data to regression line	123
6.15	Velocity of moving trolley estimated by Kalman filter	126
6.16	Point cloud of test tunnel based on kinematic surveying (inside view)	128
6.17	Point cloud of test tunnel based on kinematic surveying (outside view)	128
6.18	Point cloud of test tunnel based on kinematic surveying (detailed view)	129
7.1	Sensor Fusion: Laser scanner and total station	132
7.2	SwissRanger™ 2 by CSEM	133
A.1	Imaging System of Imager 5003 of Zoller+Fröhlich	135
C.1	Microsoft Windows® application for adjustment of spheres	141
D.1	Circuit diagram of the developed electronic circuit	143

List of Tables

2.1	Overview of Laser Safety Classes	12
2.2	Overview of distance measurement techniques in terrestrial laser scanners	16
2.3	Overview of deflection techniques in terrestrial laser scanners	22
3.1	Specifications of the terrestrial laser scanner Imager 5003 of Zoller+Fröhlich	24
3.2	Parameters of the hyperbola showing the development of the number of points	39
3.3	Precision for the horizontal encoder of the angle measurement system	44
3.4	Accuracy for the horizontal encoder of the angle measurement system	44
3.5	Precision for the vertical encoder of the angle measurement system	46
3.6	Accuracy for the vertical encoder of the angle measurement system	46
3.7	Angular resolution of the deflection unit	48
3.8	Residuals of observations	50
3.9	Unknowns of the adjustment including their precisions	50
3.10	Results of the calculation of the levelling error	54
3.11	Results from the Fourier analysis of the the vertical axis wobble	55
3.12	Influence of the eccentricity of the collimation axis	60
3.13	Results of the adjusting hyperbola concerning the error of the collimation axis	62
3.14	Error of the horizontal axis	64
4.1	Software for processing laser scanning data	83
5.1	3D translation vector	92
5.2	Influence of time resolution on the precision of center angle σ_α	95
5.3	Precision of center angle σ_α by using autocollimation	95
5.4	Resolution of autocollimation in dependence of different radii	96
5.5	Difference $\Delta\alpha$ between 'desired' center angle α and 'falsified' center angle β	97
5.6	Results of the derived mean value for the time delay Δt	99
5.7	Results for the measured rotation time T	99
5.8	Results of both types of adjustment for deriving the rotation time T	100
5.9	Comparison of the results of both methods deriving the rotation time T	101
5.10	Kalman filter equations	107
6.1	Characteristics of one total station data set	123
6.2	Results of kinematic laser scanning (regression line)	124
6.3	Results of kinematic laser scanning (Kalman filter)	127
D.1	Time values of the data bits	144

Acknowledgement

This dissertation was carried out at the Institute of Geodesy and Photogrammetry (IGP) of ETH Zurich. I am greatly indebted to all those who contributed to its realization. In particular, I would like to express my sincere thanks to:

- *Prof. Dr. Hilmar Ingensand* who gave me the opportunity to work on interesting projects and provided me with excellent research environment. He supported and encouraged my work all the time.
- *Prof. Dr.-Ing. Thomas Wunderlich* who kindly accepted to co-examine this thesis and made very valuable suggestions to it.
- My colleagues at IGP, especially (in alphabetical order)
Ralph Glaus, Maja Haberecht, Timo Kahlmann, Jürg Lüthy, Adrian Ryf and Hans-Martin Zogg for the fruitful discussions and ideas during this work,
Jules Fenner, Hanspeter Oesch and Paul Sorber for the support, construction, realization and implementation of various devices required for my laboratory experiments and in computer matters, and
Susanna Naldi who helped me in so many ways.
- *Dr. Michele Steiner* (EAWAG) for the challenging project and collaboration.
- *Prof. Dr. Simon Löw, Dr. Frank Lemy, Salina Yong* for the challenging project and collaboration.
- All students who provided small pieces of the whole puzzle in writing their seminar theses, bachelor theses, or master theses (in alphabetical order):
Urs Aebi, Hannes Eugster, Marcel Koller, Stefan Münch, Thomas Pfarrwaller, Marzio Righitto, Matthieu Stevens, Marius Schütuble and Hans-Martin Zogg.
- *Salina Yong* who proof-read the thesis regarding grammar and style.
- My family and my close friends who gave me life richness in so many ways that I cannot list them all here.

Curriculum Vitae

Personal Data

Name Thorsten Schulz
Date of Birth 24 February 1977
Nationality German

Education

1997 - 2002 Study of Geodesy
Technical University of Berlin, Germany
Graduation with Diploma in Geodesy
Diploma Thesis: Entwicklung eines Algorithmus zur Ableitung von
Geometrie-Information aus 3D-Punktwolken

Work Experience

2003 - 2007 Research and Teaching Assistant
Institute of Geodesy and Photogrammetry, ETH Zurich
Geodetic Metrology and Engineering Geodesy (Prof. Dr. H. Ingesand)
PhD Thesis: Calibration of a Terrestrial Laser Scanner for Engineering Geodesy

2002 Trainee
GI Consult GmbH (Berlin, Germany)

2002 Student Employee
FPK Ingenieurgesellschaft mbH (Berlin, Germany)

2000 - 2002 Student Assistant
Technical University of Berlin, Germany
Institute of Geodesy and Geoinformation Techniques
Division of Engineering Surveying and Adjustment Techniques (Prof. Gründig)

Languages

German native language
English fluently

